UNIVERSITAT POLITÈCNICA DE CATALUNYA BARCELONATECH

Study on the shear and punching-shear strength of reinforced concrete slabs subjected to point loads and in-plane tensile forces

Pablo Gonzalo Fernández Sánchez

UNIVERSITAT POLITÉCNICA DE CATALUNYA
Departament d'Enginyeria Civil i Ambiental

STUDY ON THE SHEAR AND PUNCHING-SHEAR STRENGTH OF REINFORCED CONCRETE SLABS SUBJECTED TO POINT LOADS AND IN-PLANE TENSILE FORCES

Doctoral Program in Construction Engineering
Doctoral Thesis by:
Pablo G. Fernández Sánchez

Supervisors:
Prof. Antonio Marí Bernat
Prof. Eva Oller Ibars

Barcelona, November 2021

..

Summary

Reinforced concrete members, especially when subjected to concentrated loads, can fail in shear. This is an undesirable and brittle failure mode preventing the structure from deforming and reaching higher load levels. It is therefore important to investigate and understand the nature of shear failures in RC beams and slabs, which are typically not provided with shear reinforcement. Despite the exhaustive research work carried out since the beginning of the XXth century, the shear behavior of reinforced concrete elements is still not fully clear. The complex kinematics and the different contribution of the widely accepted shear resisting actions, which depend, among other parameters, on the load level and the geometry of the specimens, are part of those uncertainties that have provoked the lack of consensus that currently exist around the shear problem in structural engineering.

In this context, this thesis focuses on the shear behavior of reinforced concrete slabs without shear reinforcement subjected to point loads. On the one hand, part of the work carried out during this investigation deals with shear in one way slabs supported on linear supports. Thanks to the experimental work conducted in the last two decades, a significant database of test results is now available, which has allowed to develop and verify a new mechanical model to predict the shear strength of RC one-way slabs without shear reinforcement. It takes into account a significant number of variables involved in the phenomenon and is applicable to simply supported slabs, cantilever slabs and situations with partial restraint to the rotation. The model is divided into two sub-models. One for loads applied close to supports, where the direct transmission of the load to the support plays an important role in the shear strength and a second one for loads applied away from supports where the possibility of a shear failure is assumed to coexist with the possibility of a local punching failure.

On the other hand, the second part of the investigation deals with the shear behavior of reinforced concrete slabs subjected to the simultaneous action of in plane tensile stresses and out-of-plane point loads. This load case has not been exhaustively studied throughout the years, and in order to contribute to gain insight into this aspects of shear design, the mechanical model recently developed at UPC for the prediction of the punching-shear strength of two-way slabs has been extended to the case of simultaneous in-plane tensile forces. A set of experimental test for the validation of the model for the particular case of uniaxial in-plane tension is also presented. In addition to that, the particular case of one-

way simply supported slabs subjected to transverse tensile stresses has also been experimentally studied. This is a seldom studied load case and the conducted set of test will help to understand the overall behavior of these elements under this particular loading condition.

Keywords

Shear; One-way slabs; Reinforced concrete; Mechanical model; Concentrated loads, Punching-shear, Tension, Yielding, Cracking.

Resumen

Los elementos de hormigón armado, especialmente cuando están sometidos a la acción de cargas puntuales, pueden alcanzar su resistencia última a esfuerzo cortante, lo cual limita su capacidad para deformarse y resistir valores de carga mayores. Este es un modo de fallo frágil y repentino, por lo que debe ser evitado. Así pues, es importante seguir investigando y comprender la naturaleza de la respuesta de vigas y losas de hormigón armado ante solicitaciones de este tipo, sobre todo cuando no están provistas de armadura de cortante. A pesar de la gran cantidad de campañas experimentales llevadas a cabo desde principios del siglo XX, el comportamiento a cortante y punzonamiento de los elementos estructurales de hormigón armado no está todavía del todo claro. La compleja cinemática y la diferente contribución de los mecanismos resistentes ampliamente aceptados, la cual depende, entre otros factores, del nivel de carga y de la geometría de los especímenes, son parte de esas incertidumbres que han provocado la falta de consenso que existe actualmente dentro del campo de la ingeniería estructural.

En este contexto, esta tesis se centra en el comportamiento a cortante de losas de hormigón armado sin armadura de cortante sometidas a la acción de cargas puntuales. Por un lado, parte del trabajo realizado durante esta investigación está orientado al cortante en losas unidireccionales apoyadas sobre apoyos lineales. Gracias a todas las campañas experimentales realizadas en las últimas dos décadas, una significativa base de datos de resultados experimentales se encuentra disponible en la literatura, lo que ha permitido desarrollar y verificar un nuevo modelo mecánico para predecir la resistencia última a cortante de este tipo de elementos. Dicho modelo tiene en cuenta un número importante de variables involucradas en el fenómeno y es aplicable a losas simplemente apoyadas, en ménsula, y apoyadas en apoyos con restricción parcial al giro. El modelo se ha dividido en dos sub-modelos para facilitar su desarrollo. Uno para cargas aplicadas cerca de los apoyos, donde la transmisión directa de la carga al apoyo juega un papel importante, y un segundo para cargas aplicadas lejos de los apoyos, en donde se asume que la posibilidad del fallo por cortante coexiste con la posibilidad de un fallo local por punzonamiento.

Por otro lado, la segunda parte de la investigación está focalizada en el comportamiento a cortante de losas de hormigón armado sometidas simultáneamente a la acción de cargas puntuales y tracciones en su plano. Este caso de carga no ha sido demasiado investigado a lo largo de las últimas décadas,

y con la intención de contribuir a comprender esta compleja interacción, el modelo mecánico recientemente desarrollado en la UPC, para la predicción de la resistencia a punzonamiento en losas bidireccionales, ha sido extendido a este caso particular de cargas y validado con los resultados de campañas experimentales disponibles en la literatura y el conjunto de ensayos realizados como parte de esta investigación para el caso particular de tracciones unidireccionales. Adicionalmente, el efecto de las tracciones transversales en el plano en la resistencia a cortante de losas unidireccionales también ha sido estudiado experimentalmente. Esta combinación de cargas no ha sido apenas investigada y un nuevo grupo de ensayos experimentales puede contribuir a comprender el comportamiento global de este tipo de elementos ante este caso particular de carga.

Palabras clave

Cortante; Losas unidireccionales; Hormigón armado; Modelo mecánico; Cargas puntuales, Punzonamiento, Tracción, Plastificación, Fisuración.

Acknowledgements

Despite the doctorate is an individual award, the development of this thesis would have been impossible without the help of the outstanding group of people that have encouraged, helped and supported me during the process. Here in these line I would like to express my sincere gratitude to of all them.

First of all I would like to thank my supervisors Prof. Antonio Marí and Prof. Eva Oller for their guidance throughout the whole process. Thank you for giving me the opportunity of collaborating with you in this research, for your confidence since the beginning, your support and all the time kindly dedicated to me during these four years. Without you, this thesis would not have been possible.

I would like to express my sincere gratitude to all the members of the staff of the Laboratory of Technology of Structures of the Universitat Politècnica de Catalunya. Tomás, Carlos, Jordi C., Robert and Jordi L.: Thank you for your friendship, patience, collaborative attitude, dedication and help. I have spent plenty of good times with you and some of them I will remember forever.

I am grateful to all my colleagues of the structural concrete research group at UPC. In addition to Prof. Marí and Prof. Oller, I faithfully thank Prof. Bairán, Noemi, Mauro and Ulric for their support and help. I would like to do a special mention to Montse Bernaus. Thank you for your affection from the beginning, for taking care of me and for your invaluable help with all the administrative paperwork.

Finally, I want to thank my family. Thank you for being always by my side, for your unconditional support, for encouraging me during my whole life and specially these years. Thank you for your phone calls when I was down, for your always useful advices, for your confidence and for your love. I cannot find words to express my gratitude. I would like to conclude with a special mention to my girlfriend Maru. You have always been beside me in the hard times during the doctorate. Thank you for your hugs, your good words and your infinite patience. I cannot think of the way I can give back all of that love that you have given to me.

This thesis was carried out within the framework of the research project BIA-2015-64672-C4-1-R, financed by the Ministry of Economy and Competitiveness (MINECO) of Spain.

Barcelona, November 2021

Pablo G. Fernández Sánchez

Content_Toc87040365

List of Tables

List of Figures

Chapter 1

Introduction and objectives

1.1 Motivation

In the past century, many research works have been carried out on concrete elements trying to understand how they behave and fail under different types of loading. All these works have provided some, but in some cases incomplete, insight in the mechanics behind the load carrying and failure mechanisms. A widely accepted physical model for shear in one-way elements or punching-shear in two-way slabs is still not found. Experience shows that current code provisions provide safe designs for the general cases, despite they are often based on empirical or semi-empirical models but, due to the lack of a physical model behind those formulations, it may be often not straightforward to use the codes for situations that are not within those cases for which the codes formulations were developed.

For instance, in the last decades, some European countries started to assess the capacity of different categories of reinforced concrete bridges, with a significant amount of them built in the 1960s and 1970s, subjected to traffic loads bigger than those at the time of design. The results of the initial studies indicated that, in the case of reinforced concrete solid slab bridges without stirrups, the shear strength requirements set by the current regulations were not met by a significant number of structures. However, no shear failure or excessive cracking had been observed, which may indicate that the current simplified design rules are not taking all load-bearing mechanisms into account. Often design formulas are rather conservative, and may lead to unnecessary retrofitting or replacement of this kind of structures, with the corresponding cost in terms of money, time and traffic delays. Shear provisions in codes are generally based on statistical analysis of laboratory tests carried out on beams subjected to three or four-point bending, and may not be very suitable for other types of specimens or loading conditions. Such is the case of one-way slabs subjected, either to a concentrated load close to a support, or to the simultaneous action of out-of-plane loads and in-plane tensile stresses.

In the last decade, extensive research has been done at Universitat Politècnica de Catalunya (UPC) developing mechanical models for the prediction of the shear strength of reinforced concrete elements. First model was developed for rectangular beams, showing good accuracy and low scatter when applied to the available shear test databases. Thanks to the rational nature of these models, and to the significant number of shear tests carried out with different configurations, it was successfully extended to T or I-shaped beams, prestressed beams, deep beams, fibre-reinforced concrete beams, punching-shear strength of axisymmetric slabs, etc. However, until the beginning of the XXIst century, shear tests on one-way slabs under concentrated loads were scarce. This circumstance changed when some European countries started to assess the adequacy of their road networks to the current traffic conditions as mentioned above. Large experimental campaigns were carried out in the Netherlands, Germany and France, increasing the number of recorded laboratory test and opening the possibility of developing or extending new mechanical models, as the derived for shear in beams at the UPC. The main strength of mechanical models is their adaptability to new geometries, loading and support conditions, materials properties or reinforcement layouts. Due to their rational basis, new inputs can be introduced into the model, which is usually the most difficult task, and the governing equations may be rearranged and solved in order to obtain new expressions for daily design that are often more reliable than empirical expressions modified by the addition of some statistical parameters.

In this context, special attention has been paid to the effects of in-plane tensile forces on the shear and punching-shear strength of one-way and two way slabs respectively. Concentrated loads and in-plane tensile forces can be found acting simultaneously in top slabs of box girder bridges subjected to hogging bending moments, decks of tied arch bridges, floor slabs under seismic loads, restrained shrinkage or thermal effects, etc. (Fig. 1.1). However, this phenomenon has not been exhaustively studied throughout the last decades. First widely known studies on the effect of tension on the shear strength of RC beams were carried out in the United States, after the partial collapse of a military warehouse in 1955, and few research has been carried out since then. Codes usually incorporates the effect of normal stresses as an additive term to the shear strength, sometimes assuming that the increment of shear strength due to a compression force is equal to the reduction in shear

strength due to a tensile force of the same magnitude, despite the response of concrete in one case or in the other one is radically different. Furthermore, in the particular case of one-way shear, code provisions are intended mostly for beams, where axial stresses are always applied in longitudinal (spanning) direction. However, if these expressions are used to calculate the shear strength of a one-way slab, axial loads may exist in the longitudinal and in the transverse direction. If the latter is the case, it is not clear whether those axial stresses have to be taken into account or neglected.

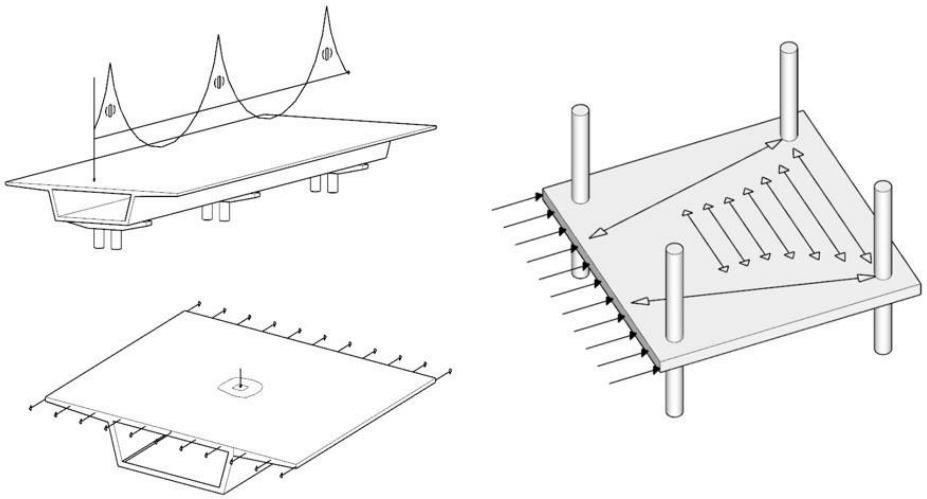

Figure 1.1: Common situations where in-plane tensile stresses and a concentrated load may act together.

To contribute to gain insight into these aspects of shear design, extending the mechanical model recently developed at UPC for the prediction of the punching-shear strength of two-way slabs to the case of in-plane tensile forces was a feasible option. A significant amount of punching tests on slabs subjected to bi-axial in-plane tension was available thanks to two different experimental campaigns carried out at Cornell University in the early 80's, allowing the validation of a new model. In addition to that, an experimental campaign was designed to study the particular case of uniaxial in-plane tension, since there were almost no similar experimental tests reported in literature, and the initial intention was to develop a flexible model that may adapt to both situations providing simplified expressions in both cases. This campaign was subsequently extended incorporating a set of shear tests on simply supported one-way slabs subjected to transverse tensile stresses. Only

a single test of these characteristics was available in literature and, despite much more research is needed in order to study this particular case with a mechanical model, a new set of tests will help to understand the overall behavior of these elements under this particular loading condition.

1.2 Objectives

1.2.1 General objectives

The main objectives of this thesis are two: on the one hand, this research is aimed to develop a new mechanical model for the prediction of the shear strength of one-way slabs subjected to concentrated loads, to validate them using the shear tests databases available in literature and, whenever possible, provide simplified expressions suitable for the daily engineering design or assessment. On the other hand, it is aimed to study the influence of in plane tensile forces on the shear and punching-shear strength of RC slabs. With this purpose, it is desired to extend the punching-shear mechanical model recently developed at UPC to incorporate in-plane tension into it, and to validate it with available tests in literature and with the results of a set of tests carried out as part of this research, for the particular case of uniaxial in-plane tension. In addition to that, another set of shear tests on simply supported one-way slabs subjected to transverse in-plane tension was conducted, with the goal of providing experimental background for this barely investigated load case.

1.2.2 Specific objectives

In order to achieve the main goals of this thesis, the following set of specific objectives are stated:

- To carry out a thorough analysis of the available literature related to this research topic, finding as much experimental campaigns as possible that could be useful for the validation of the mechanical models.

- To develop a new mechanical model for the prediction of the shear strength of one-way slabs subjected to concentrated loads,

validating it using the available databases and providing simplified expressions for the daily engineering design.

- To extend the recently developed punching-shear mechanical model to the case of in-plane tension, validating it using the available databases and providing simplified expressions for the daily engineering design.

- To conduct an experimental campaign on axisymmetricaly supported RC slabs subjected to a point load and uniaxial in-plane tension, in order to help in the development and validation of the mechanical model mentioned in the previous point.

- To carry out a set of shear tests on one-way RC slabs subjected to transverse in-plane tension, providing some experimental background for this particular load case.

1.3 Research significance

Currently, sustainability and the rational use of construction materials are some of the major concerns in the building sector. Manufacturing of construction materials is a highly polluting process, with cement being the source of about 8% of the world's carbon dioxide (CO_2) emissions. Global warming is a reality and solutions must be provided in order to tackle such a big problem. In the last decades, exhaustive research is being done in the concrete manufacturing field, trying to find new mixes and additions that allow to decrease the content of cement of this material, thus decreasing its carbon footprint, without changing its basic properties, such as strength, permeability, stiffness, fire protection, etc. However, this is not the only way this issue can be tackled. A better knowledge of the load-carrying capacity and failure mechanics of concrete structures leads to a more rational and optimized designs, which is directly related to the amount of material required. In this regard, a significant number of code provision for the shear and punching-shear design are based on empirical or semi-empirical models that often yield conservative results that lead to either poorly optimized designs, with an excess of materials, or unnecessary retrofitting or

replacement of structures, with the corresponding cost in terms of sustainability and debris generation. This thesis is aimed to give a better insight into shear mechanics and provide optimized expressions for the calculation of the shear strength of RC slabs subjected to concentrated loads and for the punching-shear strength of RC slabs subjected to in-plane tension.

The model developed for one-way slabs takes into account a significant number of variables involved in the phenomenon, such as the clear shear span, the concrete compressive strength, the reinforcement ratio, the effective depth, the load spreading angle, the size effect and the size of the loaded area. It is applicable to simply supported slabs, cantilever slabs and situations with partial restraint to the rotation, such as intermediate supports. It has been divided into two sub-models for the sake of simplicity. One for loads applied close to supports, where the direct transmission of the load to the support plays an important role in the shear strength and a second one for loads applied away from supports where the possibility of a shear failure is assumed to coexist with the possibility of what has been called one-way punching failure. Both sub-models showed good accuracy when compared to the available test results.

The punching-shear model has been extended incorporating the main effects of in plane tension, such as the neutral axis depth reduction, the decrement of the normal stresses in the compression head or the increment of the stresses in the reinforcement. The amount of flexural reinforcement parallel to the external tension proves to be a differential factor in the punching-shear strength. If in-plane tensile stresses crack the concrete cross-section, stresses in the reinforcement may increase significantly if not enough bars are provided, which may lead to a premature flexural-punching failure. The model was validated with available tests in literature and a set of test carried out as part of this research for the particular case of uniaxial in-plane tension, showing good accuracy in both cases. In addition to the developed models, a set of experimental tests on simply supported slab subjected to transverse axial tension have been carried out in order to provide some additional background for this investigated load case.

1.4 Contents of the document

This thesis is divided into six chapters. The first one is the current introduction. Chapter two contains a literature review. Various failure

mechanisms are explained, existing models for one-way shear and punching-shear are analyzed, with special attention to those ones developed at the UPC, and finally the design formulas from various building codes are treated.

Chapter three presents de derivation of the mechanical model for the shear strength or RC slabs without transverse reinforcement subjected to concentrated loads. Firstly, the case of point loads close to the supports is presented. The model is based on equilibrium and special attention is paid to the effects of the proximity between the load and the support. Validation of the model has been done using a database of 90 shear test in slabs subjected to a single concentrated load in different supporting conditions. This chapter also includes parametric analysis, detailing how the different involved variables affect the shear strength, and a set of simplified equations for shear assessment.

Secondly, the case of concentrated loads away from support is analyzed. In this case the possibility of two different types of failure is accepted: shear failure, where the critical section is considered to be placed between the load and the support, parallel to the last, and punching-shear failure, considered as a local failure around the load along a control perimeter. Derivation of the models for both types of failure modes is detailed and the resulting equations are validated against a database of 43 laboratory tests. A parametric analysis is also presented, detailing how the different involved variables affect the shear strength and the predicted failure mode, helping to gain insight into this phenomenon.

Chapter four deals with the extension of the punching-shear mechanical model, recently developed at the UPC, to take into account in-plane tension. First, the experimental campaign carried out as part of this research for the particular case of uniaxial tension is described. Tests set-up, procedures, materials characterization and instrumentation are detailed. Results are presented, analyzed and compared with numerical predictions. Secondly, the extended model is developed. Main assumptions and how they have been incorporated into the model are explained, and a new set of simplified equations is obtained. The results are interpreted and validated against a database of 31 punching-shear tests on slabs subjected to biaxial tension and 7 tests on slabs subjected to uniaxial tension.

Chapter five presents the experimental campaign carried out on simply supported slabs subjected to transverse axial tension. The experimental

campaign is detailed similarly to the one presented in the previous chapter. Results are interpreted and compared with numerical predictions. A comparison between tests results and code predictions is also included, with a discussion on the suitability of code provisions for this particular load case.

Finally, chapter six summarizes all the work carried out and conclusions are drawn. Furthermore, suggestions for future work that could lead to an improvement or extension of the proposed mechanical models are addressed.

1.5 Publications

During the development of the research detailed in the following chapters, four publications were generated and published in indexed scientific journals:

- Punching-shear strength of reinforced concrete slabs subjected to unidirectional in-plane tensile forces. Structural Concrete. 2020. 22(2). 1223-38. Published online at https://doi.org/10.1002/suco.202000112
- Theoretical prediction of the punching shear strength of concrete flat slabs under in-plane tensile forces. Engineering Structures. 2021. 229(3). 1116-32. Published online at https://doi.org/10.1016/j.engstruct.2020.111632
- Theoretical prediction of the shear strength of reinforced concrete slabs under concentrated loads close to linear supports. Structure and Infrastructure Engineering. 2021. Published online at https://doi.org/10.1080/15732479.2021.1988990
- Experimental investigation of the shear strength of one-way reinforced concrete (RC) slabs subjected to concentrated loads and in-plane transverse axial tension. Structural Concrete. 2021. Published online at https://doi.org/10.1002/suco.202100447

Chapter 2

State of the art

2.1 Introduction

It is widely known that RC members, especially when subjected to concentrated loads, can fail in shear. This is an undesirable and brittle failure mode preventing the structure from deforming and reaching higher load levels. It is therefore important to investigate and understand the nature of shear failures in RC beams and slabs, which are typically not provided with shear reinforcement. This chapter starts with an overview of the evolution of knowledge on this topic, followed by a review of the shear resisting actions and of some mechanical models developed in the past for shear in beams and one-way slabs, including the ones developed at the Universitat Politècnica de Catalunya. Then, the experimental campaigns conducted throughout the last 60 years in order to study the influence of axial tension on the shear strength of RC elements are summarized. To conclude, the shear provisions presented in some of the most accepted international codes such as EN CEN (2005), CEB-*fib* (2010) and ACI Committee 318 (2019) are analyzed.

The behavior of concrete during loading and at failure is a complex three dimensional problem influenced by numerous different parameters. The reason it is called shear failure was explained by Kani (1964) in this way:

"*When testing reinforced concrete beams, simply supported at both ends and loaded at two locations, the beams failed due to severe (diagonal) cracking outside the central part of the beam* (Fig. 2.1). *In this case the failure could not be caused by the bending moment, because the maximum bending moment was in the middle of the span. However, at the failure locations of the beam there is a shear force present. It was concluded that shear force or shear stress caused this type of failure. Hence the name shear failure*".

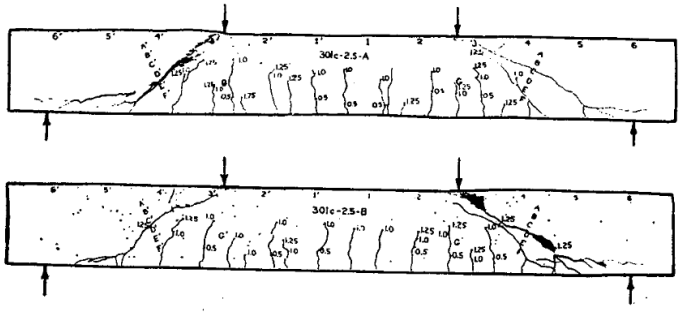

Figure 2.1: Beam failure caused by diagonal cracking reported by Kani (1964).

In general, two different types of shear related failures are considered when designing reinforced concrete slabs: one-way shear and two-way or punching-shear. The term "two-way" refers to the situation where lines representing the flow of shear forces do not run parallel to each other but rather in a radial way around the load. It is often found in slabs supported on isolated columns or under concentrated loads at some distance from the supports. One-way shear, on the contrary, is found in beams, cantilever slabs or simply supported slabs on two parallel sides. In this case shear lines run parallel from the load to the support. This is well illustrated in Fig. (2.2).

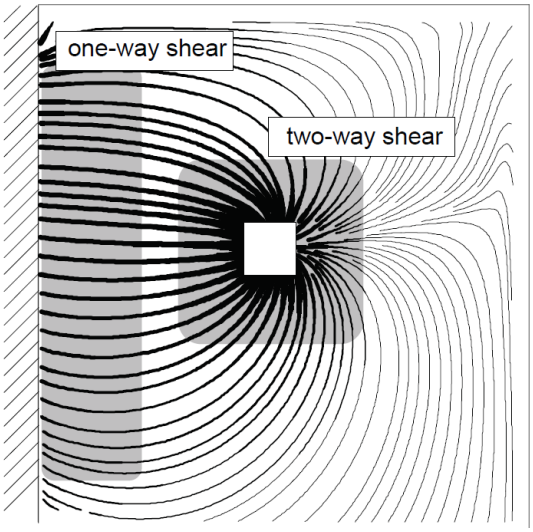

Figure 2.2: Shear flow in a slab showing the difference between one-way and two-way shear. Vaz Rodriguez (2007)

2.2 Overview of knowledge until 1960

2.2.1 Early stages

Reinforced concrete members were used long before the basic principles were understood or a rational design theory was developed. During the XIX century it was wrongly believed that shear failure in RC elements was caused by pure horizontal shear, as had been experienced with web rivets in steel and wood girders. Fortunately, concrete was assumed to have a low horizontal shear strength and vertical steel stirrups were used, supposedly acting as shear-keys, against high horizontal shear stresses (Fig 2.3). First formula for the calculation of the distribution of shear stresses τ in a beam subjected to a shear force V was first derived by the Russian engineer Dimitri Zhuravskii in 1855 for a homogeneous and elastic material.

$$\tau = \frac{V \cdot S}{I \cdot b} \tag{2.1}$$

Where b is the width of the member at the considered fiber, I is the moment of inertia of the cross-section, and S is first moment of the area enclosed by the top fiber and the considered fiber.

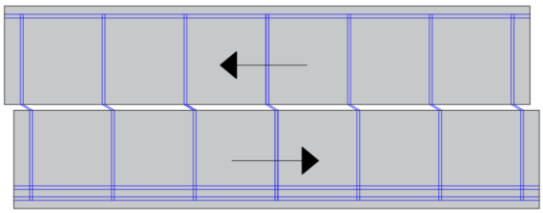

Figure 2.3: Shear failure mechanism accepted in the early stages of reinforced concrete.

First rational approach was presented by Ritter in 1899. It consisted on what is known as the "45º truss analogy", in which a cracked RC beam with stirrups is compared to a parallel chord truss with compression diagonals inclined at 45º (Fig. 2.4). Ritter assumed the following hypothesis:

- The concrete compression zone acts as the top chord of the truss and only carries horizontal compressive flexural stresses.

- The longitudinal reinforcement acts as the bottom chord and only carries horizontal tensile flexural stresses.
- The stirrups or bent-up bars in tension, and concrete struts in compression act as the web members, carrying all inclined or vertical stresses.

Ritter was the first to understand that inclined web cracks in linear elements were caused by tensile stresses orthogonal to them, introducing the concept of diagonal tension as a mechanism of shear failure of RC elements. He also defended, according to his truss model, that the stirrups worked resisting vertical tensile stresses instead of horizontal shear stresses. On that basis, Ritter proposed the following design formula for the spacing s of the stirrups, which is still the basis of several current design codes.

$$s = \frac{A_v f_y jd}{V} \tag{2.2}$$

where A_v is the cross-sectional area of the stirrups, f_v its yield strength, V the design shear force and jd is the lever, assumed as j times the effective depth d.

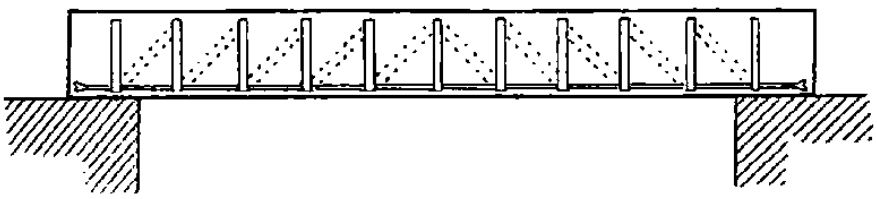

Figure 2.4: Reproduction of Ritter's original truss model (Ritter 1899)

Major contribution to the understanding of RC members in shear was made by Mörsch in the first decade of the XXth century. Mörsch demonstrated that when a concrete beam is subjected to bending and shear, principal tensile stresses in the web exists inclined at certain angle from the longitudinal axis of the element. He also highlighted that, in the hypothesis of pure shear, a maximum tensile stress exists inclined at 45º. Thus, inclined cracks and shear failures where consequence of diagonal principal tensile stresses in the web, corroborating the theories proposed by Ritter a few years before.

He also derived a model for the shear stress distribution in the cross-section of a cracked RC beam. He predicted that the shear would be zero at

the top compression fiber and would increase until reaching its maximum at the neutral axis, remaining constant beyond that point to the flexural reinforcement (Fig. 2.5). He provided Eq. (2.3) for the calculation of the maximum shear stress, where *jd* is the flexural lever arm and b_w the web width. This expression, which is still universally used today with the minor change of omitting *j*, was derived by considering the equilibrium of a body of concrete enclosed by two flexural cracks. Mörsch was the first one who used the tangential stresses as a measure of the diagonal tension in the web, setting the tone for the following decades.

$$\tau = \frac{V}{b_w \cdot jd} \tag{2.3}$$

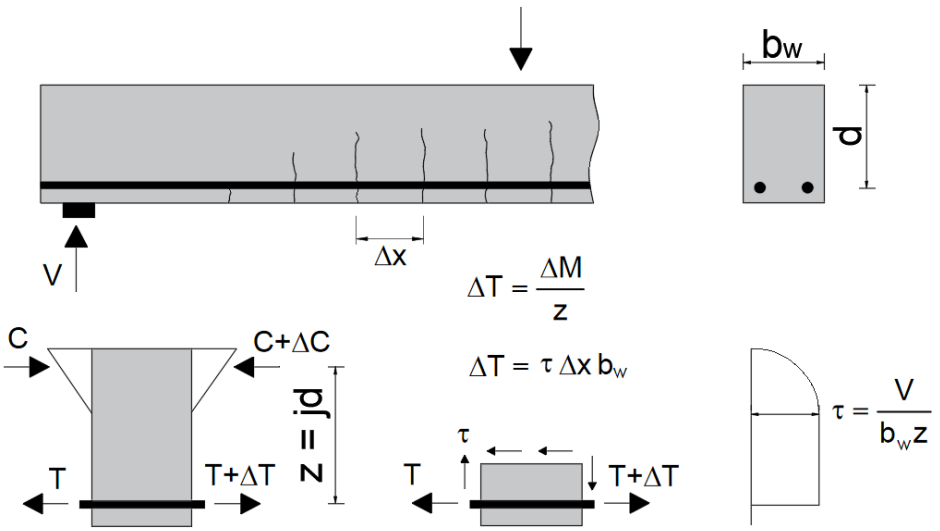

Figure 2.5: Shear stress distribution derived by Mörsch in a cracked RC beam. Adapted from Cladera (2003).

After several experimental work, Mörsch reaffirmed the truss model proposed by Ritter, pointing out that the stirrups worked resisting tensile stresses instead of horizontal shear stresses, highlighting its effectiveness once they were crossed by an inclined crack. However Mörsch always believed that the concrete's ultimate shear capacity was a characteristic of the material itself, related only to the concrete compressive strength. This assumption

would be later proved incorrect after experimental works conducted in the United States.

First codes that appeared in Europe, such as the Swiss Code of 1903, the German code of 1904 or the French code released in 1906, adopted limiting values for the maximum ultimate shear stress of concrete. If design stresses were lower than the maximum allowed values, shear reinforcement could be removed. French code adopted a limiting value of $0.028f_c$, being f_c the concrete compressive strength, whereas the German and Swiss codes adopted a constant value of 0.45 MPa. When shear reinforcement was necessary, German and Swiss codes recommended to design it to resist the total shear force, without considering any concrete contribution, whereas French code allowed a certain reduction in the design shear force. These values did not have a solid experimental background due to the technical difficulties in that period of time.

In the same decade, first research on diagonal tension was carried out in the United States at the University of Illinois. Talbot (1909) conducted more than one hundred tests in reinforced concrete rectangular beams without stirrups. He observed that the shear strength not only depended on the concrete compressive strength, as Mörsch thought, but also on the age of concrete, the amount of longitudinal reinforcement, the effective depth and the length of the specimens. He found that bent-up bars were most advantageous when distributed over the region of high shear and recommended that the stirrups should be dimensioned for two-thirds of the external shear, being the remaining one-third carried by concrete in the compression zone. Unfortunately, Talbot never provided mathematical expressions or theoretical models based on his research, and all this knowledge was barely taken into account until many years later.

At the same time, Withey (1907, 1908) presented two reports in which Eq. (2.2) was introduced into the American literature for the first time. In his experiments conducted on RC beams, he observed that this equation gave too high stirrup stresses for the values of the ultimate shear obtained experimentally and concluded that the concrete of the compression zone carried considerable shear stresses. He also highlighted the contribution of the dowel action, defined as the resistance of a reinforcing bar crossing a crack to shear displacement. By the end of that decade, the horizontal shear

approach was practically abandoned in favor of the diagonal tension as the cause of shear failure of RC beams. In 1910, the first American concrete code was issued by the National Association of Cement Users (NACU 1910), limiting the maximum shear strength in concrete to 0.02 f_c.

2.2.2 1910-1960

In the period from 1910 to about 1950 relatively few contributions were made towards the shear problem. The usual way of proceeding when dimensioning the shear reinforcement of an RC element was to compare the maximum design shear stress, obtained using Eq. (2.2), to the maximum stress allowed by the corresponding code. If the design stress was lower, no shear reinforcement would be provided. Otherwise stirrups and bent-up bars would be dimensioned using Eq. (2.1) to resist totally or partially the design shear force, depending on the code. For the particular case of Spain, first code was released in 1939 (MOP 1939). The maximum shear stress allowed was that given by Eq. (2.4). If design tangential stresses were greater than the limit value, stirrups and bent-up bars should be provided to resist the total shear force.

$$\tau \leq \frac{1}{2}\sqrt[3]{f_c} \tag{2.4}$$

It is interesting to note that some of the early researchers in the first decade of XXth century, such as Ritter, Mörsch and Talbot, developed most of the basic ideas that are currently widely accepted.

After World War II much effort was put into obtaining a mathematical expression for the shear strength of RC beams, especially in the United States. According to ASCE-ACI Committee 445 (1998), the limit value for the maximum shear stress in concrete had been modified throughout the years, adopting each time less conservative approaches. In ACI Committee 318 (1951), the maximum shear stress allowable in concrete was $0.03f_c$, which represents a 50% increment with respect to the 1910 provisions. Several large experimental campaigns where carried out. Clark (1951) pointed out the influence of the longitudinal reinforcement, the *a/d* ratio and the concrete compressive strength on the shear strength, as Talbot had done forty years

before. Clark also reported redistribution of forces between adjacent stirrups after the first yielding of one of them.

Laupa *et al.* (1953) published an extensive analytical report analyzing earlier investigations carried out at the University of Illinois, making some interesting contributions. On the one hand, they concluded that Eq. (2.2) could not be used for the calculation of the maximum shear stress in concrete. They considered that transfer of stresses across cracks did not occur and only the compression area above the flexural neutral axis contributed to resist shear, neglecting the dowel action as well. The neutral axis to effective depth ratio x/d was included for the first time in the calculation of the shear strength of concrete. On the other hand, they studied beams failing in shear under distributed loads. The influence of a/d ratio was known but it presented a problem when incorporating it to the formulations. The shear span a had only physical meaning for the particular case of point loads and the way of proceed for other load cases, such as distributed loads, was not clear. They presented an empirical formulation in which the shear span a was replaced by the moment to shear ratio M/V for the first time. Moody *et al.* (1954, 1955a, 1955b, 1955c) published a four-part report on RC beams tested under different types of loading and supporting conditions, including the term M/V in the empirical formulation provided. However, no special conclusions on the influence of the supporting conditions on the shear strength were reported.

In 1955, the partial collapse of a military warehouse in Ohio, USA, brought ACI shear design provisions into question. Roof beams failed in shear under the action of the permanent load, with an estimated shear stress of less than 0.5 MPa, lower than the maximum allowed by the ACI provisions of that time. Beams were 914 mm depth and presented an amount of reinforcement of 0.45%, without stirrups. An investigation was carried out by the Portland Cement Association (Elstner *et al.* 1957) in smaller specimens of 305 mm depth that in normal conditions resisted shear stresses up to 1.0 MPa. Based on the laboratory observations, failure was considered to be caused by axial tensile stresses due to restrained shrinkage that drastically reduced the shear strength, and new provisions were incorporated to the ACI code (ACI 1963), such as a minimum amount of shear reinforcement, an increment in the anchorage length of flexural reinforcement, the incorporation of the axial

tensile stresses in the provisions and the consideration of the interaction between shear and flexure by detailing rules for the flexural reinforcement cutoff points for the first time. Nevertheless, the size effect, defined as the decrement in the shear strength of geometrically similar beams of different sizes as the beam depth increases, was probably the main reason for this failure (Cladera 2003). However, this phenomenon will not be widely studied until Kani (1967) laboratory tests.

By the end of the 1950s, first shear-compression failures theories where developed in Europe. Probably the most known is the model presented by Walther as part of his studies on the shear strength of prestressed concrete beams. This theory suggested that failure may occur due to crushing of concrete in the compression zones if a shear crack reduces sufficiently their depth. He also commented the possible reduction of the limiting compressive stresses induced by shear in the compression zone. Leonhardt and Walther (1961) conducted a large experimental campaign on rectangular and T-beams failing in shear, developing a model combining beam and arch effects, whose contribution depended on the slenderness of the beam. It was also observed that stresses in the stirrups were always lower than predicted after diagonal cracking, regardless the load level. Based on that, the usual additive expression of the concrete and steel contribution for the calculation of the total shear strength was progressively adopted.

2.3 One-way shear in RC elements without stirrups

In this section, an overview of the development and the current state-of-the-art on shear strength models for one-way RC elements without stirrups is presented. First, widely accepted shear resisting actions are introduced, followed by a brief discussion on the size effect. Then, different mechanical approaches for the shear strength of RC beams without stirrups are reviewed, finishing with an overview of the current knowledge on the shear behavior of one-way slabs.

2.3.1 Shear resisting actions

In RC beams, the external shear forces must be always in equilibrium with the internal shear forces of the beam. Several different internal shear transfer actions are currently widely accepted. However, its quantification and contribution is still subject of research. These resisting mechanisms were firstly introduced by the ASCE-ACI Committee 426 (1973), in a report of the state-of-art in the knowledge of shear strength at that time, and further completed by 1998 ASCE-ACI Committee 445 (1998). Five basic mechanism of shear transfer in concrete beams without stirrups where introduced (Fig. 2.6):

V_{cc}: Arching action. Direct strut action from the load to the support.

V_d: Shear resisted in the longitudinal reinforcement by dowel action.

V_a: Shear resisted at the crack interface by friction and aggregate interlock.

V_w: Shear resisted in the crack processing zone.

V_c: Shear resisted in the uncracked compression zone.

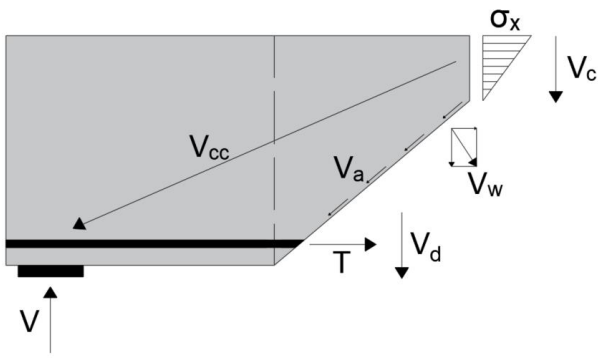

Figure 2.6: Shear resisting actions in a RC beam.

Arching action (direct strut)

This resisting action usually predominates in non-slender beams. In slender beams arching action, which implies a constant tensile force in the reinforcement, is less likely unless the reinforcement is unbonded or partially yielded in advanced load stages after redistribution of internal forces, as observed by Leonhardt and Walther (1961) and Kani (1964). For loads applied close to the supports, it results in a significant increment in the shear

capacity. One of the most accepted approaches to the arching action consist on considering the total shear force V as the sum (Eq. (2.4)) of the beam action (constant flexural lever arm z with varying tension T in the reinforcement thanks to bond stresses) and arching action itself (constant tension in the reinforcement with varying flexural lever arm) (Fig. 2.7). The contribution of the arching action may be estimated by based on trajectories of stresses (Kani, 1966) or by reinforcement strain measurements in laboratory tests, as those carried out by Olonisakin and Alexander (1999) in wide beam specimens, concluding that yielding of the reinforcement forces a shift from beam action to arching action thus a plastic hinge may precipitate a shear failure. They also observed that, even though simplified design methods based on beam action accurately predicted the shear failure load, beam action only accounted for a small fraction of the shear strength, according to their measurements. Rational models were also developed by Kim *et al.* (1999, 2011) based on similar approaches and laboratory measurements.

$$V = \frac{d(T.z)}{dx} = \frac{d(T)}{dx} z + \frac{d(z)}{dx} T \tag{2.4}$$

Dowel action (direct strut)

Dowel action was defined as the resistance of a bar of the flexural reinforcement, crossing a crack, to shear deformation. Due to the flexural deformations of the compression zone, the parts on either side of a diagonal crack would have to rotate causing the dowel action of the longitudinal reinforcement (Fig 2.7). The contribution of this basic mechanism, which was first mentioned by Mörsch, is typically small in RC element without stirrups since it is limited by splitting of concrete cover supporting the dowel. Some models for the dowel action have been presented throughout the years, based on linear elastic approaches (Fenwick and Paulay, 1968) or plastic approaches (Bhide and Collins, 1989). Vintzeleou and Tassios (1986) presented a mechanical model for the prediction of the dowel strength subjected to monotonic and cyclic loading, assuming two possible failure modes: Yielding of the bar accompanied of crushing of surrounding reinforced concrete and concrete splitting.

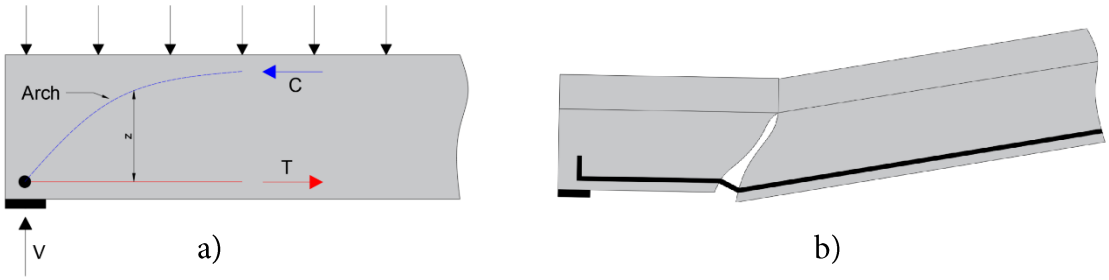

Figure 2.7: a) Arching carrying the compressive force C; b) dowel action resulting from diagonal cracking.

Interface shear (Aggregate interlock)

The interface shear results from the friction between the two faces of a diagonal crack due to the roughness of the surfaces. In normal strength concrete, the strength of the hardened cement paste is usually lower than the strength of the aggregate. Therefore, cracks generally run through the cement paste and along the edges of the aggregate particles. This way, when crack forms, this aggregate particles protruding from the crack surface interlock with the opposite face resisting shear displacements. Extensive research was carried out between 1960 and 1980 (Kani, 1964; Fenwick and Paulay, 1968; Taylor, 1974). Walgreen (1981) made a significant amount of tests and developed a model that idealized the aggregate particles as spheres and the cement matrix as perfectly plastic. Based on experimental evidence, it was considered that both normal stresses σ and tangential stresses τ were functions of the crack width w and shear displacement Δ. The equations of the model are based in a probabilistic analysis of the crack structure and contact areas between protruding aggregates and crack surfaces (Fig. 2.8). Significant research has been done in factors influencing the aggregate interlock, such as the type and nature of the aggregate (Regan et al. 2005), aggregate size (Sherwood et al. 2007) and the type of concrete (Walraven, 1995; Hassan et al. 2010).

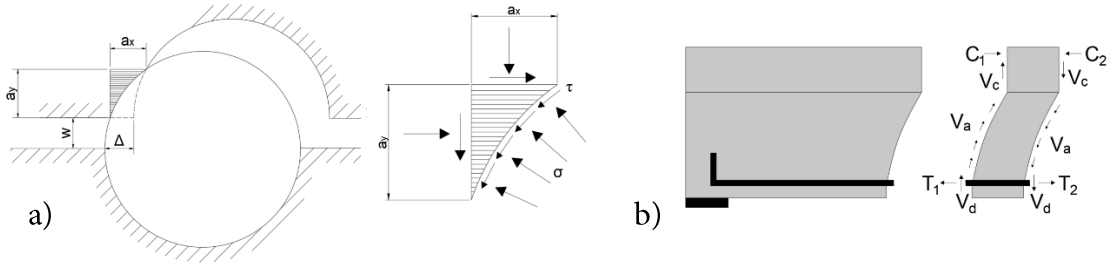

Figure 2.8: Models for interface shear: a) Walraven (1981); b) Fenwick and Paulay (1968)

Shear resisted in the crack processing zone

The consideration of the residual tensile stresses at the crack tip was a consequence of the development and application of the fracture mechanics for the analysis of quasi-brittle materials. Noticeable work was initially carried out by Hilerborg (1976, 1983) and Gustafsson *et al.* (1988). With this approach, it is possible to estimate the length over which the concrete is still able to transfer stresses across an open inclined crack (Fig. 2.9). In fracture mechanics, this resisting action is seen as the primary shear transfer mechanism (ACI Committee 445, 1998). Its importance is greater in smaller beams than in larger elements (Reineck, 1991) due to the increased overall crack widths, what could be a possible explanation for the size effect.

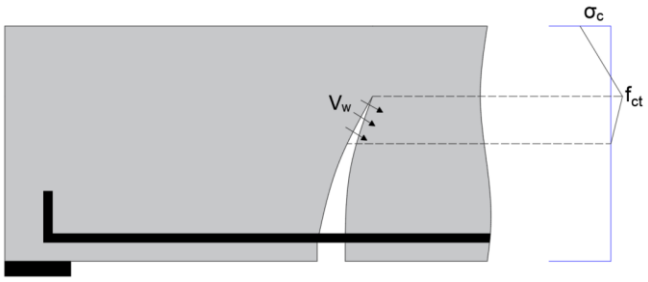

Figure 2.9: Residual stresses transferred across the crack.

Shear resisted in the uncracked compression zone

From the early stages, the shear resisted in the compression zone was considered part of the contribution of the concrete to the shear strength. First mechanical models considered this resisting mechanism closely related to the arching action (Kani, 1964). Throughout the years, new approaches have been

developed. Reineck (1991) determined the contribution of this mechanism integrating the shear stresses over the depth of the compression zone, whereas Zararis and Papadakis (2001) related the shear strength of the element to the splitting strength of the concrete in this zone. The models developed at the UPC for the prediction of the shear strength of slender and non-slender beams consider this action as the main resisting mechanism, and it will be explained in detail in section 2.3.3.4.

While the general shear transfer actions can be understood separately, the difficulty has been and still is the quantification of the contribution of each one to the shear strength. This has been investigated throughout the years (Taylor, 1974; Sarkar *et al.* 1999; Campana *et al.*, 2016; Bairan *et al.*, 2017) comparing different shear models with experimental measures, and a variety of ranges for the contribution of each resisting action have been provided, usually agreeing in the special importance of the aggregate interlock and shear resisted in the compression zone. This is a big challenge due to the huge amount of variables involved in the phenomenon and the internal redistribution of stresses that take place for different loading stages. In general, mechanical models that attempt to account to all the resisting actions yield complex equations that have to be solved iteratively, as they depend in the external forces, internal forces and sectional deformations. Thus, the problem also lies within the task of providing simple, sound and safe equations suitable for the daily use.

2.3.2 Size effect

It has been known from many years that the size effect ζ in shear leads to relatively smaller nominal shear capacities for larger cross-sectional depths (Kani, 1967; Shioya et al., 1989; Collins and Kuchma, 1999). This issue was pointed out by Kani (1967) after his experimental campaign in beams with depths ranging from 150 to 1200 mm (Fig. 2.10). Prior to that, most of the experimental testing had been carried out in beams ranging in depth from 250 to 400 mm and size effect had not been observed. One rational approach, based on fracture mechanics of quasi-brittle materials (Bazant and Kim, 1984; Bazant and Yu, 2005; Carmona and Ruiz, 2014), defends that cracks in larger elements are generally wider, which leads to a reduction of the contribution

of residual tensile stresses. In 1984 Bazant proposed the well-known expression Eq. (2.5) of the energetic size effect ζ, where d_0 is a parameter depending on the material. Other theories defend that what is actually affected by the greater width of cracks in larger elements is the aggregate interlock (Bentz 2005, 2019; Fernández-Ruiz *et al.* 2015). The current size effect law (Eq. (2.6)) adopted in the Model Code 2010 (*fib* 2010) was derived from this approach (Sigrist 2013) and includes the term k_{dg} depending on the aggregate size d_g for Level of Approximation II. It is noticeable that ACI 318-19 code has introduced for the first time a size effect factor in its shear formulation (Kuchma *et al.* 2019), in this case adopting Eq. (2.5) considering d_0 = 250 mm (Eq. (2.8)). In general, size effect is included in the codes formulae for the calculation of the shear strength V_R as a factor multiplying the nominal shear strength v ($V_R = \zeta \cdot v \cdot b_w \cdot d$)

$$\zeta = \frac{1}{\sqrt{1 + \frac{d}{d_0}}} \tag{2.5}$$

$$LoA\ I: \zeta = \frac{0.18}{1 + \frac{z}{800}}; \qquad LoA\ II: \zeta = \frac{1.3}{1 + \frac{k_{dg} z}{1000}} \quad (z\ in\ mm) \tag{2.6}$$

$$k_{dg} = \frac{32}{16 + d_g} \geq 0.75 \quad (d_g in\ mm) \tag{2.7}$$

$$\zeta = \sqrt{\frac{2}{1 + 0.004d}} \leq 1 \quad (d\ in\ mm) \tag{2.8}$$

With the increasing amount of experimental evidence generated throughout the years, in addition to mechanical approaches, the size effect phenomenon has been also investigated from an empirical point of view. Initially, studies were based on regression analysis and size effect laws were usually written in additive form, as Eq. (2.9), introduced in the Model Code 78 (CEB-FIP 1978). This equation was subsequently replaced by Eq. (2.10), which is still in use today since it was introduced into Eurocode 2 and current Spanish code, with the minor change of limiting its maximum value to 2. With the huge increment in computational capabilities within the last decades, more complex data analysis have been carried out, no longer limited

to regression analysis. Artificial Neural Networks (ANNs) were for example used by Cladera and Mari (2004) to gain deep insight into factors influencing the shear strength. The ANN was fed with input data from selected shear test and learnt to predict the shear capacity as accurate as possible. Genetic programming, a technique usually used for the optimization of parametric problems, has been also applied in this field (Perez *et al.* 2012; Cladera *et al.* 2014). The current expression for the size factor used in the mechanical models developed at the UPC (Eq. (2.11)) was derived from this work, which includes a term for the shear span *a*. A comparison of some of the expressions provided herein is presented in Fig. 2.11. One of the problems of the statistical and data analysis approaches is that databanks may be biased due to the usual overrepresentation of smaller members.

$$\zeta = 1.75 - 1.25d \geq 1.0 \quad (d \; in \; mm) \tag{2.9}$$

$$\zeta = 1 + \sqrt{\frac{200}{d}} \quad (d \; in \; mm) \tag{2.10}$$

$$\zeta = \frac{2}{\sqrt{1 + \frac{d_0}{200}}} \left(\frac{d}{a}\right)^{0.2} \geq 0.45 \quad (d_0 = d \geq 100 \; in \; mm) \tag{2.11}$$

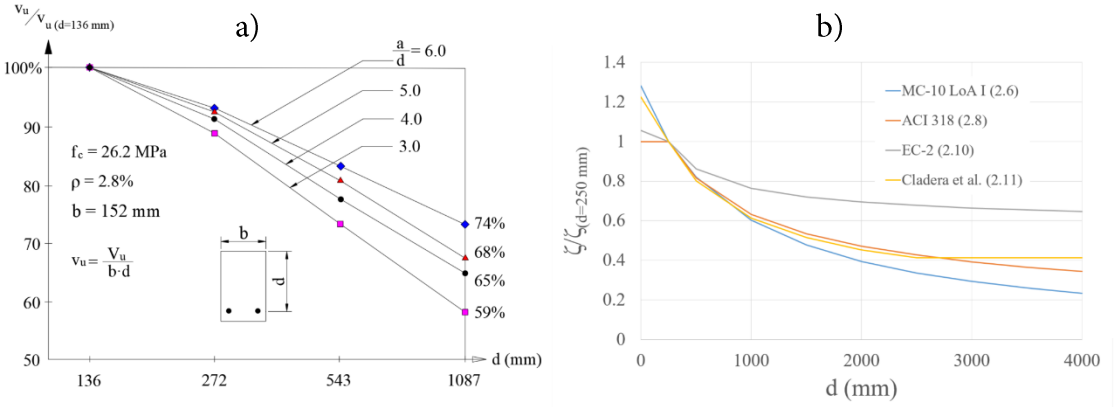

Figure 2.10: a) Variation of relative beam strength versus depth. Adapted from Kani (1967); b) Comparison of normalized size effect (z = 0.9*d* in Eq. (2.6) as suggested in MC-10 and *a*/*d* = 2.5 in Eq. (2.11)).

2.3.3 Mechanical models for the shear strength of RC beams without stirrups

In this section different shear strength mechanical models applicable to RC beams without stirrups are presented. They have been sorted according to the basis theory behind their rational approach. For the sake of simplicity, and considering that this thesis deals with behavior rather than design, no differentiation will be made between the various types of concrete strengths (f_c, f_{ck}, $f_{cm,cil}$, etc) used in different approaches. Therefore average values of the concrete shear strength will be provided.

2.3.3.1 Tooth Models

In an attempt to provide a rational theory for the effects of shear and diagonal tension on the behavior of reinforced concrete members, Kani developed what he called the "Tooth Model" (Kani 1964). According to his research, a beam subjected to an increasing load can be represented as a comb-like structure. In the tensile zone of the beam, more or less vertical cracks appear due to insufficient concrete tensile strength, showing concrete between cracks a resemblance with teeth. In this area the tensile forces are carried by the flexural reinforcement, whilst the compression zone of the beam can be seen as the backbone of the comb (Fig. (2.11)).

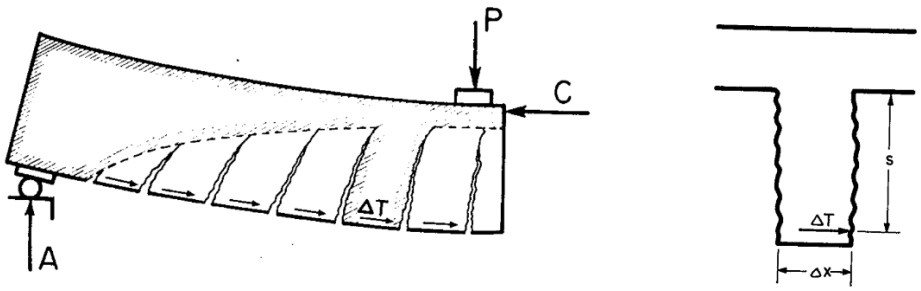

Figure 2.11: Comb-like shape and concrete teeth of a RC beam subjected to an increasing load. Kani (1964).

The vertical concrete teeth can be seen as cantilevers clamped in the compression zone and subjected to a horizontal load ΔT, transmitted by the bond between the concrete and the reinforcement, acting at the end of each

tooth (Fig. 2.12). After some calculations, Kani derived the failure moment of the concrete teeth M_{CR} for rectangular beams as:

$$M_{CR} = M_0 \frac{\Delta x}{s} \cdot \frac{a}{d} \tag{2.12}$$

$$M_0 = 0.0013 \cdot bd^2 f_{ct} \tag{2.13}$$

where M_0 is a constant depending on the geometry of the section (in mm) and the concrete tensile strength f_{ct} (in MPa), a is the shear span, d is the flexural reinforcement effective depth, s is the height of the teeth and Δx is the average crack spacing. For a beam with constant cross-section and reinforcement layout over its whole length, M_{CR} is a linear function of the shear span to effective depth ratio a/d. When this ratio increases, M_{CR} will increase as well, until the flexural capacity of the cross-section is reached. After failure of the teeth, no bond can be transmitted between the reinforcement and the concrete, so the tensile force in the reinforcement becomes constant over the whole length of the beam. A new equilibrium can be attained in the form of a tied arch (Fig (2.12)).

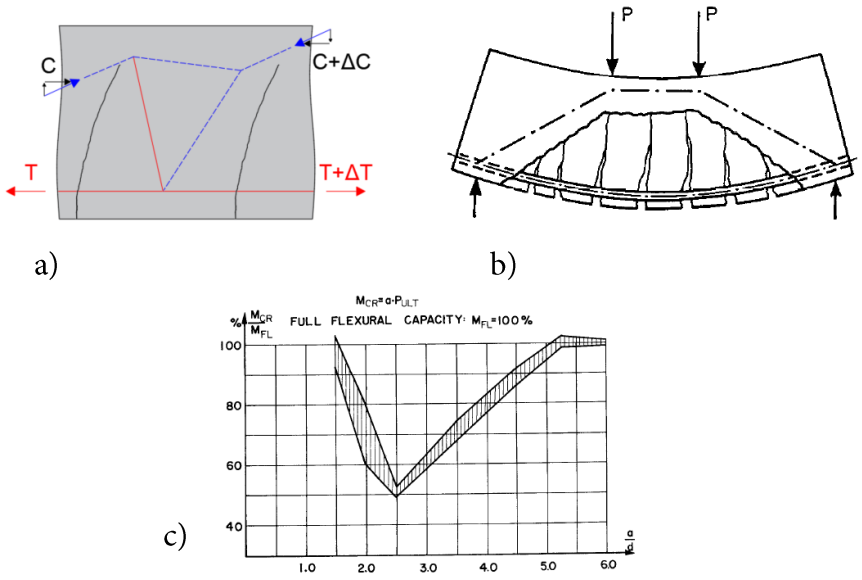

Figure 2.12: a) Internal resisting mechanism of teeth; b) Remaining concrete tied arch after failure of the teeth; c) Beam capacities versus a/d ratios of the beams tested by Kani (1964).

Kani found in his experiments three characteristic stages in the shear behavior for different values of *a/d*. For values smaller than 2.5, the concrete teeth will fail before the tied arch, so the load carrying capacity of the beam is limited by the capacity of the arch, given by the following expression derived by Kani, where M_{FL} represent de ultimate bending moment of the cross-section of the beam.

$$M_{CR} = \frac{M_{FL}}{0.9} \cdot \frac{d}{a} \tag{2.14}$$

For *a/d* between 2.5 and 5.2, the capacity of the concrete teeth is higher than the capacity of the tied arch, resulting in sudden collapse of the beam after their failure. For *a/d* values greater than 5.2, the load carrying capacity is limited by the flexural strength of the beam. These stages can be clearly distinguished in Fig. 2.12c in what is known as Kani's valley.

Kani's model assumes that the concrete teeth can rotate freely but this is not completely true due to the restriction coming from the dowel effect of the longitudinal reinforcement and friction between the rough surfaces of the inclined cracks. Fenwick and Paulay (1968) commented that the internal resisting action of the teeth would generate too high tensile stresses to be resisted entirely by concrete and refined Kani's model (Fig. 2.8b) including interface shear and dowel action. Taylor (1974) carried out experimental investigations to study each resisting action separately and derived a mathematical model with which analyzed the contribution of each internal resisting mechanisms. It was estimated a 20-40 % for the contribution of the compression zone, 33-50 % for the aggregate interlock and 15-25 % for the dowel effect.

A complete mechanical model that considers the equilibrium of the concrete tooth was developed by Reineck (1991). The model is based on a free-body cut of a concrete tooth assuming that flexural cracks are inclined at an angle of 60º (Fig. 2.13). The tooth width (or crack spacing) s_{cr} was assumed to be given by Eq. (2.15). In each tooth, the variation of the forces in the chords is equilibrated by the friction in cracks V_a, dowel action V_d and cantilevering action of the tooth from the compression zone, which is small and may be neglected. These actions, along with the shear resisted in the compression chord V_c, must equilibrate the external acting shear force.

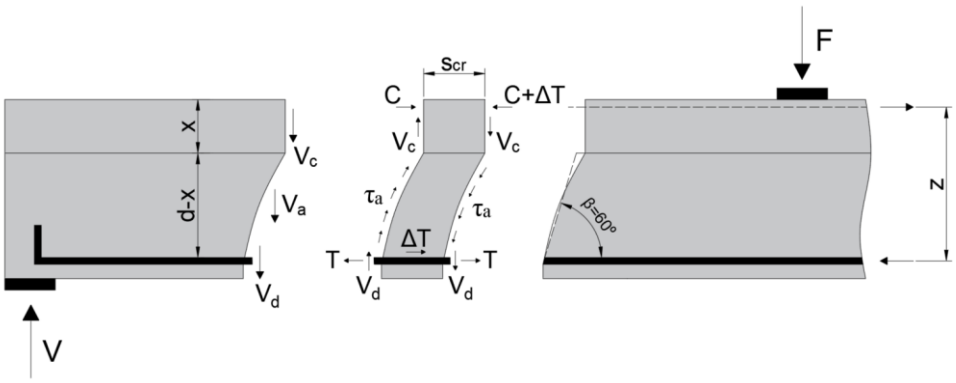

Figure 2.13: Tooth model according to Reineck (1991).

The stress distribution in the compression zone, shown in Fig. 2.14a isolated from the tension zone, is obtained using linear elastic theory. Since the variation ΔT of the force in the tension chord must be equilibrated by an equal force in the compression zone, the shear stress in the neutral axis must be equal to the nominal shear stress v_n (Eq. (2.16)). Integrating shear stresses over the depth x, V_c is obtained (Eq. (2.17)). Following from this approach, for a beam with an amount of reinforcement within the usual range in practice, at most a maximum of about 30% of the total shear force will be transferred in the compression zone. The dowel action is introduced as a parabolic distribution of stresses acting between crack faces (Fig. 2.14b). Since the value V_d depends on the diameter of the bars of the longitudinal reinforcement a lower limit for the dowel effect was given (Eq. 2.18), based on the work carried out by Vintzeleou and Tassios (1986). Finally, friction stresses τ_a in the cracks generated by aggregate interlock are considered constant along the crack depth (Fig 2.15a) and depending linearly on the crack slip Δs for a constant crack width w following Walraven's (1981) proposal. The component V_a is obtained from integrating friction stresses along the crack.

$$s_{cr} = 0.7(d - x) \tag{2.15}$$

$$v_n = \frac{\Delta T}{b_w s_{cr}} = \frac{V}{b_w \cdot z} \tag{2.16}$$

$$V_c = \frac{2}{3} \frac{x}{\left(d - \frac{x}{3}\right)} V \tag{2.17}$$

$$V_d = 1.4\,\frac{\rho^{8/9}\cdot f_c^{1/3}}{d^{1/3}} b_w d \quad (f_c \text{ in } MPa, d \text{ in } m) \tag{2.18}$$

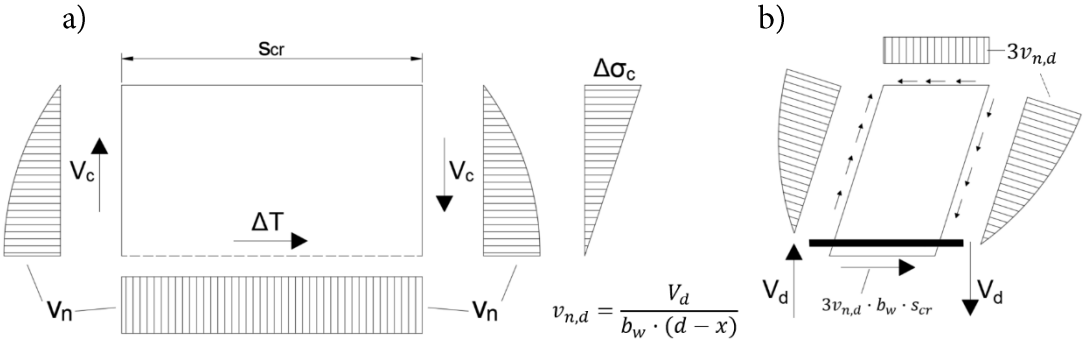

Figure 2.14: a) stresses in compression zone of tooth; b) friction stresses induced by dowel action. Reproduced from Reineck (1991).

The ultimate shear strength of the element is associated with the maximum value of the total friction stresses τ_{fu} (from aggregate interlock and dowel action) acting at mid-depth of the crack. This value, according to Walraven (1981), depends on the tensile strength of concrete and is assumed to decrease linearly with increasing crack width (Eq. 2.19). This maximum value for the friction stress is associated with a critical deformation state of the tooth, whose corresponding slip is given by Eq. (2.20). Crack width may be related to the deformation of the longitudinal reinforcement based on the kinematic consideration given in (Fig. 2.15b). The horizontal displacement at the mid-depth of the crack Δu is considered to be exactly half of the value at the level of the longitudinal reinforcement $\Delta u_L = \varepsilon_s \cdot s_{cr}$. The strains in the reinforcement ε_s, given by Eq. (2.21), are calculated from the moment equilibrium of the free body on the left hand side of Fig. 2.14 and this way the ultimate friction stress can be obtained. Since the crack spacing s_{cr} and the crack width at mid-depth of the shear crack depend directly on the depth of the crack (d-x), the friction capacity is reduced with increasing depth of the member, which is predominantly responsible for the size effect on the shear capacity.

A simplified expression for the ultimate shear strength of RC elements without axial force derived in the model is given in Eq. (2.22).

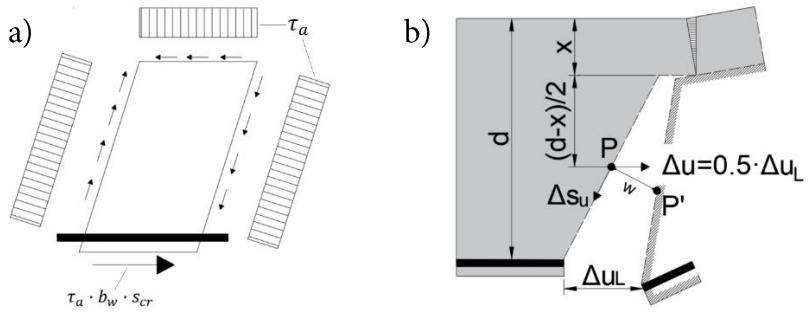

Figure 2.15: a) friction stresses induced by aggregate interlock; b) kinematic consideration for the crack width at mid-depth of the crack. Reproduced from Reineck (1991).

$$\tau_{fu} = 0.45 f_{ct}\left(1 - \frac{w}{0.9}\right) \quad (w \; in \; mm) \tag{2.19}$$

$$\Delta s_u = 0.336w + 0.01 \quad (w \; in \; mm) \tag{2.20}$$

$$\varepsilon_s = \frac{1}{E_s A_s z}\left(V\left(a - 1.5d + \frac{d-x}{\tan\beta}\left(1 + \frac{2}{3}\frac{x}{z}\right)\right) - V_d \frac{z}{\tan\beta}\right) \tag{2.21}$$

$$V_R = 0.4\frac{b_w \cdot d \cdot f_{ct} + V_d}{1 + 0.054\lambda} \tag{2.22}$$

$$\lambda = \frac{f_c}{E_s \rho} \cdot \frac{d}{0.9} \quad (d \; in \; mm) \tag{2.23}$$

As shown in this section, tooth models have been important to the understanding of the basic shear transfer mechanisms. However, the work performed in this area has not been yet adopted in a design code.

2.3.3.2 Models based on the strain-state and crack width

The modified Compression Field Theory (MCFT).

The Modified Compression Field Theory (Vecchio and Collins 1986) is a general model for the post-cracking load-deformation behavior of two-dimensional RC elements subjected to combined shear and axial stresses. In this model, the cracked concrete is treated as a new material with empirically

defined strain-stress behavior (Fig. 2.16a). One of the main assumptions of the MCFT is that principal strain directions coincide with principal stress directions in cracked concrete. The compatibility conditions relating the strains in cracked concrete with the strains in the reinforcement are expressed in terms of average strains, measured experimentally over base lengths that included several cracks. Equilibrium conditions, which relate the external applied load to the stresses in cracked concrete and reinforcing steel, and strain-stress relationships of each material are also expressed in terms of average stresses. The equilibrium equations, the compatibility conditions, and the constitutive equations of cracked concrete and reinforcement enable to obtain, through an iterative process, the average stress, the average strain and the angle θ of inclination of the cracks for any load level up to failure. Failure of the RC element may be governed not by average stresses but rather by the local stresses occurring at a crack. Cracks are considered to be normal to the principal tensile stress direction of cracked concrete. However, locally, at a crack, it is assumed that only shear and compression can be transmitted (Fig. 2.17). During the solution process, it has to be checked after every step that the steel at crack does not yield and that the crack surface is able to resist the corresponding shear stresses.

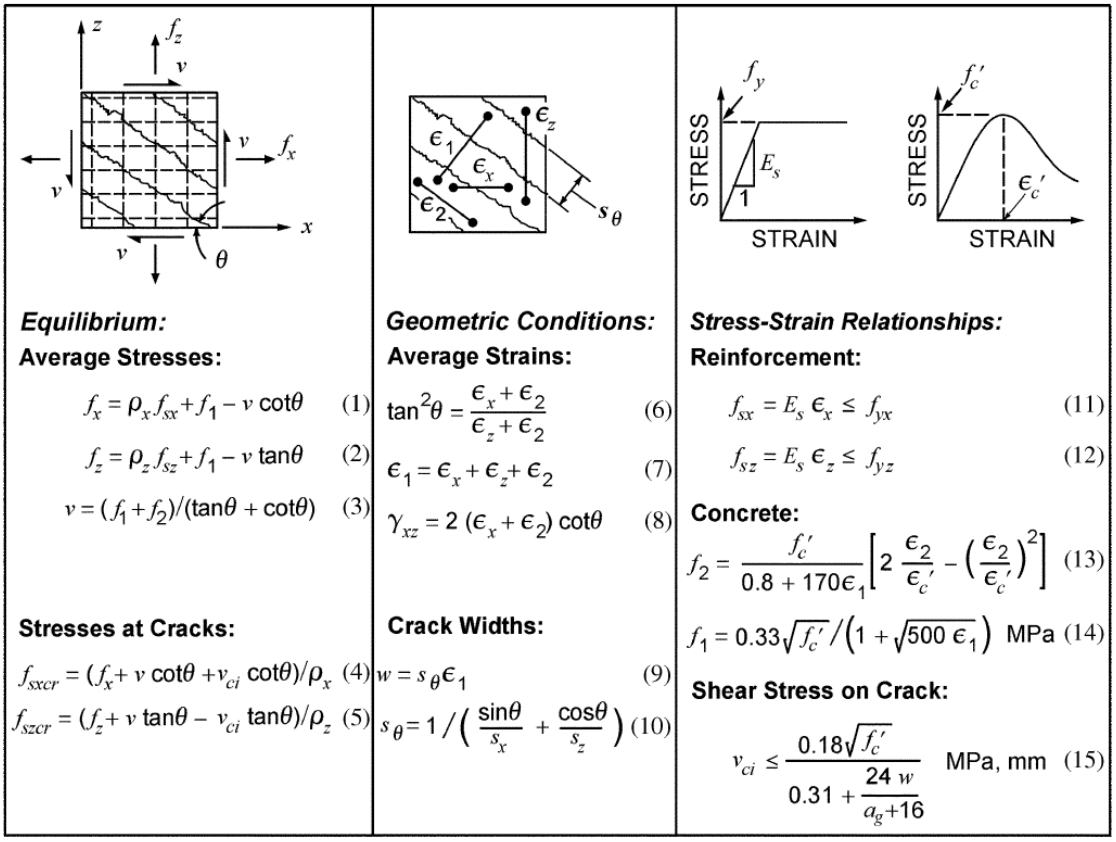

Figure 2.16: Equations of the MCFT. Bentz *et al.* (2006).

As the applied external stresses f_x, f_z and v are fixed, if equilibrium exists, both the average stresses and the stresses at a crack must be statically equivalent (Fig. 2.17). Equilibrium equations are shown in Fig. 2.16 (1)-(5). Shear is resisted by the principal average compressive stresses f_2 together with the diagonal principal tensile stress f_1. If the three strain components (ε_x, ε_z, γ_{xz}) are known, the strain in any other direction can be found from geometry through the Mohr's circle (Fig. 2.18). Based on experimental investigations, the principal compressive stress f_2 in concrete was found to be a function not only of the principal compressive strain ε_2 but also of the co-existing principal tensile strain ε_1 (Fig. 2.16 (13)). Thus cracked concrete subjected to high tensile strains in the direction normal to the compression is softer and weaker than concrete in a standard cylinder tests. Regarding the principal tensile strength f_1, the post-cracking relationship given in Fig. 2.16 (14) was

proposed. A typical bilinear diagram was used for the constitutive equation of the reinforcement.

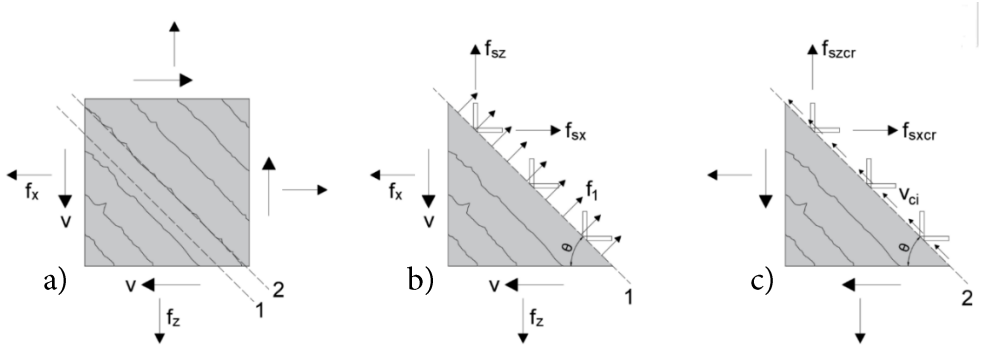

Figure 2.17: Comparison of local stresses at a crack with calculated average stresses a) element analyzed; b) average stresses in concrete; c) local stresses at a crack. Reproduced from Vecchio and Collins (1986).

The ability of the crack interface to transmit shear stresses is given in Fig. 2.16 (15) based on Walraven's (1981) work, where a_g is the aggregate size. Shear stresses in the crack depends on the crack width, which was related to the crack spacing (Fig. 2.16 (6)-(8)). Horizontal and vertical crack spacing (s_x and s_z) were initially estimated as 1.5 times the separation of the bars in each direction respectively. A deeper study analyzing possible expressions for these parameters was presented in Adebar and Collins (1996). A solution technique for determining the complete response of bi-axially stressed element is explained in Vecchio and Collins (1986).

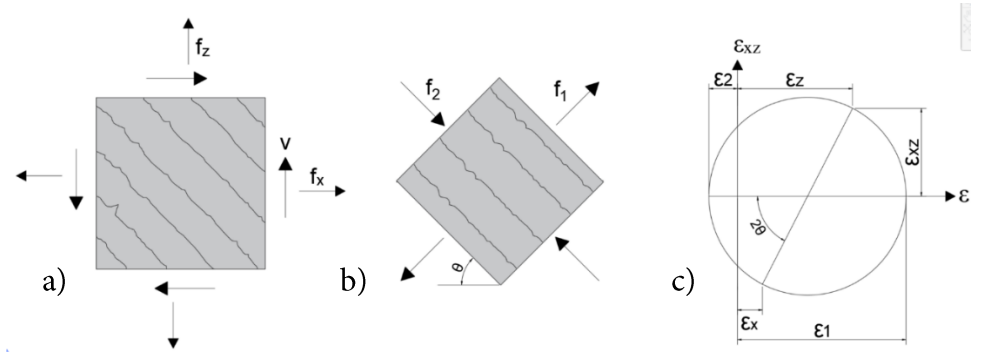

Figure 2.18: a) Average concrete stresses; b) principal stresses in concrete; c) Mohr's circle for the average concrete stresses. Reproduced from Vecchio and Collins (1986).

Rearranging the equilibrium equations of Fig. 2.16, shear stresses v can be expressed as an addition of the contribution of concrete v_c and the contribution of the shear reinforcement v_s (Eq (2.24)). If no shear reinforcement is provided ($\rho_z = 0$), the shear strength is given by Eq. (2.25), limited by the maximum shear that can be transmitted at the crack surface. This model was further extended (Vecchio 2000,2001) incorporating rigid slipping along crack surfaces into compatibility equations, thus allowing for a divergence of the angles of inclination of average principal stress and average principal strain in concrete. A simplified version was presented by Bentz *et al.* 2006, incorporating simplified expressions for the angle of inclinations of the cracks θ and for the contribution of concrete to the shear strength β (Eq. (2.26) and Eq. (2.27) respectively). In Eq. (2.26), the two factors were considered as a strain effect factor and the size effect factor respectively. The strain ε_x may be considered as the strain in the longitudinal reinforcement. Simplified approaches of this theory have been adopted by some codes, as the Canadian code (CSA 1994) and the AASHTO (2000) code.

$$v = v_c + v_s = f_1 \cot\theta + \rho_z f_y \cot\theta \tag{2.24}$$

$$v = v_c = \frac{0.33\cot\theta}{1+\sqrt{500\varepsilon_1}}\sqrt{f_c} = \beta\sqrt{f_c} \le \frac{0.18}{0.31+\frac{24w}{a_g+16}}\sqrt{f_c} \quad (f_c in\ MPa) \tag{2.25}$$

$$\beta = \frac{0.4}{1+1500\varepsilon_x}\cdot\frac{1300}{1000+s_x} \quad (s_{xe} in\ mm) \tag{2.26}$$

$$\theta = (29\ deg + 7000\varepsilon_x)\left(0.88+\frac{s_x}{2500}\right) \le 75 deg \tag{2.27}$$

The Critical Shear Crack Theory (CSCT).

This model (Muttoni and Fernández-Ruiz 2008a) assumes that after the development of the critical shear crack, the response of a member is controlled by arching action. Two possibilities for the development of this resisting mechanism are considered, an elbow-shaped strut that deviates from the line connecting the load and the support to avoid cracks, and a direct strut that develops thank to the aggregate interlock in the critical shear crack (Fig. 2.19).

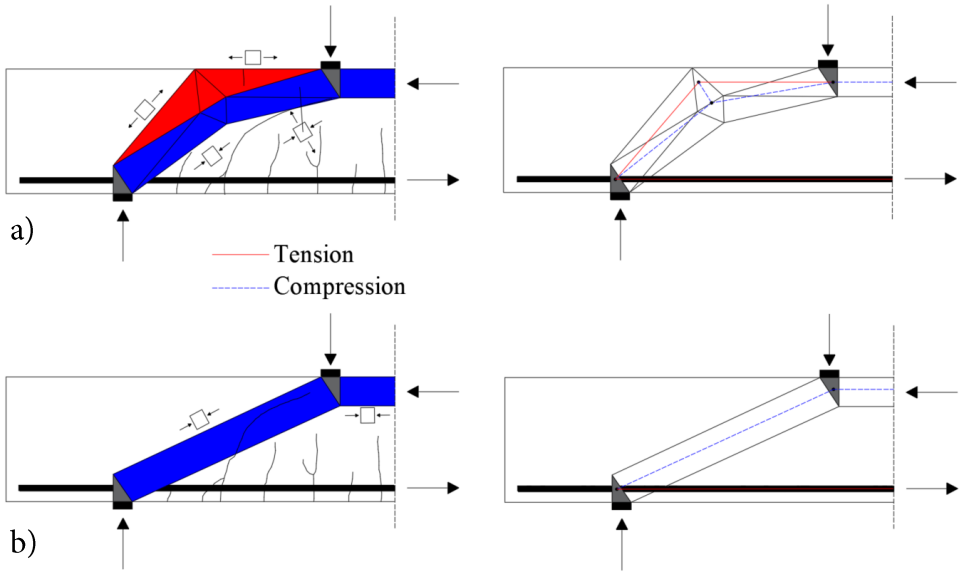

Figure 2.19: Load carrying mechanisms after development of the critical shear crack: a) elbow shaped strut; b) straight strut (enabled by aggregate interlock). Reproduced from Muttoni and Fernández-Ruiz (2008a).

The shear strength V_R of members without stirrups is considered to be strongly dependent on the critical shear crack width and on its roughness. For the calculation of the shear strength, the following hypothesis were accepted:

- The shear strength is checked in a section where the width of the critical shear crack can be adequately represented by the strain ε at depth $0.6d$ from the compression face (Fig 2.20a).
- The critical crack width w is proportional to the product of the longitudinal strain in the control depth ε times the effective depth of the element. ($w \propto \varepsilon d$) (Muttoni and Schwartz 1991; Reineck 1991; Collins *et al.* 1996). Based on previous work (Walraven 1981; Vecchio and Collins 1986), the amount of shear that can be transferred across the critical shear crack is accounted for by dividing the nominal crack width εd by the quantity ($d_{g0} + d_g$), where d_g is the maximum aggregate size and d_{g0} is a reference size equal to 16 mm.

After analyzing a database of almost 170 shear tests, the analytical expression given by Eq. (2.28) was derived. If no axial forces are applied, the strain in the control depth may be based on the bending moment M in the

critical section (Eq. (2.29)). The proposed expression fitted very well the experimental results of the available databank (Fig. 2.20b). Is important to highlight that all test results correspond to values of $a/d > 2.9$. A simplified expression for ε was also provided Eq. (2.30), assuming that the depth of the compression zone x was equal to $0.35d$ and proportionality between the acting bending moment M strains at the reinforcement ε_s.

$$V_R = \frac{1}{6}\frac{2}{1+120\dfrac{\varepsilon d}{16+d_g}}\, bd\sqrt{f_c}\ \ (MPa\ and\ mm) \tag{2.28}$$

$$\varepsilon = \frac{M}{bd\rho E_s(d-x/3)}\frac{0.6d-x}{d-x} \tag{2.29}$$

$$\varepsilon = \varepsilon_s \frac{0.6d-x}{d-x} \cong 0.41\varepsilon_s \tag{2.30}$$

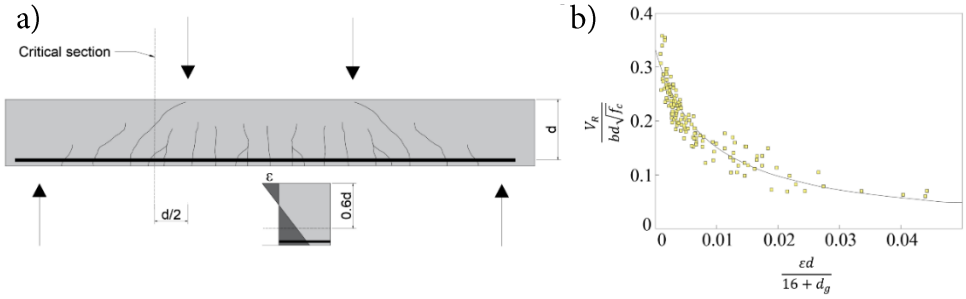

Figure 2.20: a) Critical section and control depth for the longitudinal strain; b) Comparison of Eq. (2.28) with test results for concentrated loading. Reproduced from Muttoni and Fernández-Ruiz (2008a).

This model was slightly modified to its inclusion as part of the Model Code 2010 provisions. Based on the Simplified Modified Compression Field Theory (Bentz *et al.* 2006), Eq. (2.31) and Eq. (2.32) were provided, for levels of approximation (LoA) I and II respectively. In Eq. (2.31), the first factor is considered to represent the strain effect whereas the second factor is considered to represent the size effect. According to Yu et al. (2016) this size effect factor is unrealistic. This can be shown on the asymptote of the curve of $V_R = v_R \cdot b_w \cdot d$ versus d. In contrast to other size effect curves, this asymptote

is horizontal (Fig. 2.21a). Thus, if a beam is sufficiently deep, the doubling of its depth, for example, would not lead to any increase in the load capacity.

$$V_R = \frac{0.18}{1 + \frac{z}{800}} z b_w \sqrt{f_c} \quad (MPa \text{ and } mm) \tag{2.31}$$

$$V_R = \frac{0.4}{1 + 1500\varepsilon_x} \cdot \frac{1300}{1000 + k_{dg} z} z b_w \sqrt{f_c} \tag{2.32}$$

In the last decade, CSCT underwent further development. Fernández-Ruiz *et al.* (2015) investigated the various potential shear-transfer actions in RC beams, discussing their role on the shear strength and providing some analytical expressions for its calculation, comparing the results to the shear strength criteria of the CSCT (Fig. 2.21b). Cavagnis *et al.* (2018) carried out a similar but more refined study, using measures of the crack kinematics obtained through Digital Image Correlation (DIC) (Cavagnis *et al.* 2015; Huber *et al.* 2016).

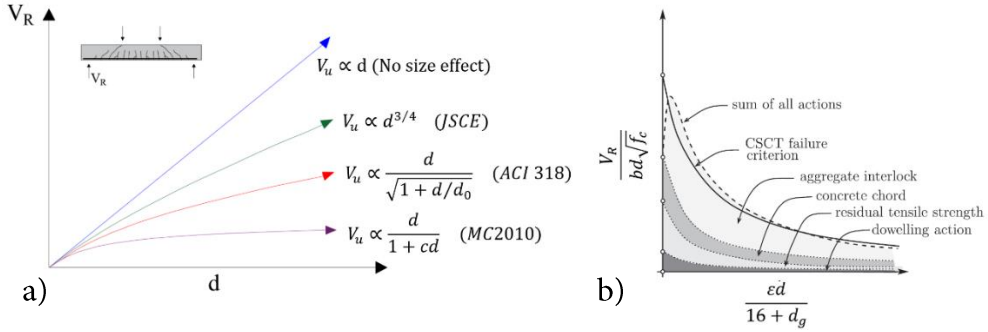

Figure 2.21: a) Comparison of the load capacity asymptotes based on different size effects. Reproduced from Yu *et al.* (2016); b) qualitative comparison of the shear transfer actions contributions and the CSCT failure criterion. Fernández-Ruiz *et al.* (2015).

2.3.3.3 Models based on theory of plasticity

The theory of plasticity is a branch of the study of the strength of materials. In its simplest form (perfect plasticity), it deals with materials that can deform plastically under constant stresses when the load has reached a sufficient high value, namely the yield strength. Drucker, who was one of the first researchers to develop a general formulation for this theory (Drucker and Prager 1952),

studied its implementation to RC members subjected to shear (Drucker 1961). He proposed several stress fields in which the load is carried directly by inclined struts or arches (Fig. 2.22) considering that failure was governed by yielding of longitudinal reinforcement. However, proposed stress fields were not found suitable for RC beams, usually leading to unsafe designs (Muttoni and Fernández-Ruiz 2008a). One of the approaches that uses the lower bound theorem of plasticity for design purposes is the strut and tie method (S&T) (Schlaich *et al.* 1987). S&T models represent the flow of forces in a concrete member by statically admissible compressive struts and tension ties that must equilibrate the external actions. They are usually applied to RC elements with shear reinforcement, but may be also applied to beams without stirrups, considering that the concrete ties represent the shear resisting actions developed in the beam after diagonal cracking (Reineck 1991, 2002). According to this theory, shear failure occurs either due to yielding of the stirrups or due to crushing of concrete in the web of the element (Nielsen 1984).

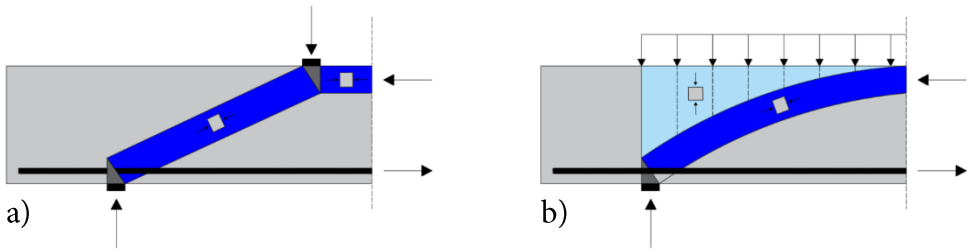

Figure 2.22: Stress fields according to theory of plasticity for one-way elements a) concentrated load; b) distributed load.

If a simply supported beam symmetrically loaded by two concentrated forces (Fig. 2.23a) is considered, the compression and tension zones may be idealized as stringers, carrying the forces C and T respectively. The shear force V is resisted by the web. In general, the depth of the web is considered equal to the flexural lever arm z for design purposes. The shear force V generates a shear stress in the cross-section given by Eq. (2.33). A statically admissible stress field in the web can be constructed considering that concrete is in a plane-stress state subjected to uniaxial compression σ_c at an angle θ with the horizontal axis. The horizontal component of this stress field is transferred to the stringers, generating and increment in the force resisted by the

longitudinal reinforcement equal to $V/2 \cdot cot\theta$, and the vertical component is carried out by vertical stirrups (Fig. 2.23b).

The ultimate shear capacity of the beam will be reached in the following way: at a certain load stirrups will yield. Once this happens, increasing shear force can only be carried by increasing the compression stress σ_c which at the same time rotates to smaller angles θ. The concrete stress may increase until it reaches the effective compression strength νf_c, where ν is the effectiveness factor, which accounts for the softening of unconfined concrete after cracking. The shear stress that can be resisted if stirrups are allowed to yield is given by Eq. (2.34), where ψ is the degree of shear reinforcement and A_{sw} the area of one stirrup. If concrete is considered to be perfectly plastic, the maximum shear stress is given by Eq. (2.36). This formula is usually provided in codes as an upper limit of the shear strength of RC elements with stirrups. Equalizing these two expressions, the shear capacity of the beam is given by Eq. (2.37), which is known as the web crushing criterion. Based on the results of a large number of tests, it was found that the effectiveness factor ν could be determined with sufficient accuracy by Eq. (2.38). In practice ν is usually considered equal to 0.6, which is a conservative assumption.

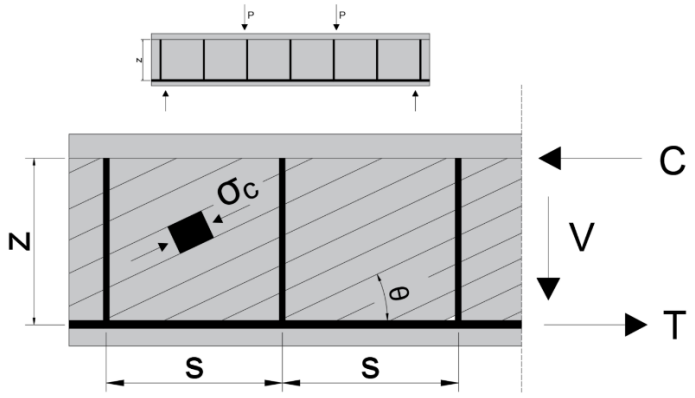

Figure 2.23: Diagonal compression field in the web. Reproduced from Hoang and Nielsen (1998).

$$\tau = \frac{V}{bz} \tag{2.33}$$

$$\tau = \psi f_c \cot\theta \tag{2.34}$$

$$\psi = \frac{A_{sw} f_y}{b \cdot s \cdot f_c} = \rho_w \frac{f_y}{f_c} \tag{2.35}$$

$$\tau = \frac{\nu f_c}{\tan\theta + \cot\theta} \tag{2.36}$$

$$\frac{\tau}{\nu f_c} = \begin{cases} \sqrt{\frac{\psi}{\nu}\left(1 - \frac{\psi}{\nu}\right)} & \psi \leq \frac{\nu}{2} \\ 0.5 & \psi > \frac{\nu}{2} \end{cases} \tag{2.37}$$

$$\nu = 0.8 - \frac{f_c}{200} \quad (f_c in\ MPa) \tag{2.38}$$

The web crushing criterion do not agree well with test results when the degree of shear reinforcement becomes small. If ψ is small, θ must be also small before web crushing can take place. Hence, the diagonal stress field must cross cracks with many different directions, which provokes that the cracked web region becomes instable, resulting in sliding failure along cracks before is vf_c reached. This is one of the reasons why codes usually introduce a minimum amount of shear reinforcement and limit the choice of the maximum value of cot θ. Since the 45º angle truss model was presented by Ritter, it has been widely used to the design of RC elements with stirrups. Further developments or modifications, based on the joint application of a truss analogy and principles from the MCFT are the Rotating Angle Truss Model (Belarbi and Hsu 1995), the Fixed Angle Softened Truss Model (Pang and Hsu 1996), the Cracked Membrane Model (Kaufmann and Marti 1998) or the Disturbed Stress Field Model (Vecchio 2000). RC elements with transverse reinforcement are out of the scope of this thesis and will not be analyzed in detail.

Alternatively, in an upper bound plasticity approach, the critical shear crack is seen as a yield line (Fig. 2.24a). Some models have been presented, as the Crack Sliding Model (Hoang and Nielsen 1998), which may be applicable to RC beams without stirrups. It considers that failure takes place when the element experiences sliding along the critical crack. Based on a simplified derivation for the internal work, the failure load of the element is given by Eq. (2.39). More recently, a new approach based also on the yield line theory was presented by Fisker and Hagsten (2016). In this case a yield line with three

sections is assumed, as shown in Fig. (2.24b). Resisting mechanism is related to the sliding of plain concrete in the compression zone, sliding along the already existing shear crack and separation of the concrete layer along the longitudinal reinforcement. A modified version of Walraven's (1981) law for interface shear stresses is used to obtain the maximum shear that can be resisted. The main disadvantage of this model is that the failure location is a priori unknown and should be determined by finding the minimum capacity based on the position of the critical crack.

$$P_u = 2\frac{0.059\nu_0 f_c}{l/h}bh \quad (f_c \; in \; MPa) \tag{2.39}$$

$$\nu_0 = \frac{0.88}{\sqrt{fc}}\left(1+\frac{1}{\sqrt{h}}\right)(1+26\rho) \quad (h \; in \; m) \tag{2.40}$$

$$\left(\frac{l}{h}\right)^3 + \frac{l}{h} - 1.51\nu_0 f_c^{1/3}\left(\frac{h}{0.1}\right)^{0.3}\frac{a}{h} = 0 \tag{2.41}$$

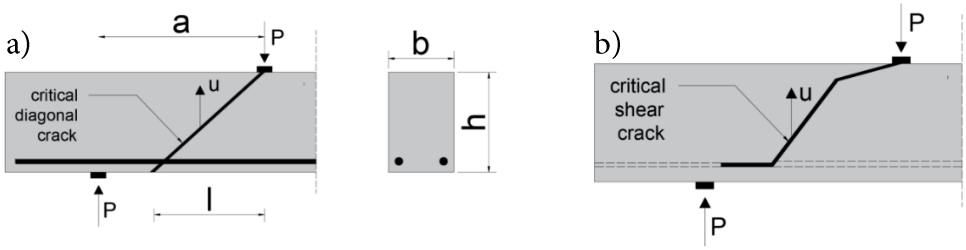

Figure 2.24: Yield lines: a) Crack Sliding Model (Hoang and Nielsen 1998); b) Fisker and Hagsten (2016)

2.3.3.4 Models based on Linear Elastic Fracture Mechanics (LEFE)

Since the phenomenon of diagonal shear cracking is generally considered a brittle mode of failure, principles from LEFE may be adopted to predict the shear strength of reinforced concrete elements. This theory leads to the conclusion that a strong size effect is associated with the failure stress of the specimen (Bazant and Chen 1997). According to principles of linear fracture mechanics, the nominal shear strength of a beam decreases proportional to $\lambda^{1/2}$ in which λ represents the scale factor. In RC beams the effective depth d is

usually used as the scale factor. The counter part of the linear approach is that it is assumed that materials behave in a linear elastic way until reaching failure, which is not true in the particular case of concrete. Bazant and Kim (1984) developed a model considering concrete as a quasi-brittle material, since it possesses a large fracture process zone relative to its crack size, and proposed a structural size effect law to describe the quasi-brittle nature of concrete according to non-linear fracture mechanics given by Eq. (2.42), where d_0 is a constant depending on the material. Fig. 2.25 shows in double logarithmic scale that it provides a smooth transition between a plastic strength criterion and LEFE. Another well-known model based on non-linear fracture mechanics is the Fictitious Crack Model (Hillerborg 1983)

$$\tau_n = \frac{1}{\sqrt{1 + d/d_0}} \tag{2.42}$$

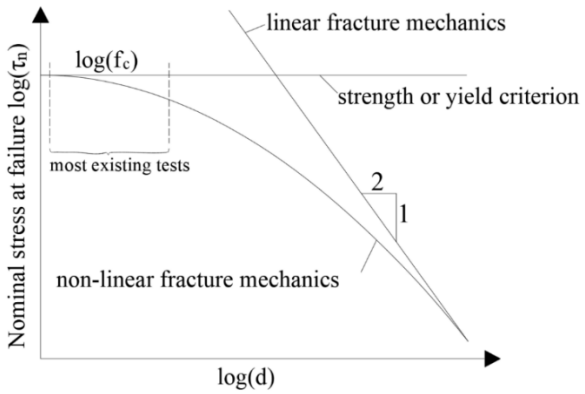

Figure 2.25: Size effect according to non-linear fracture mechanics compared to a simple tield criterion. Reproduced from Bazant and Kim (1984).

Gasteblad and May (2001) presented a model based on the idea that the extra moment due to the rotation at the tip of the diagonal shear crack is equal to the fracture energy necessary to extend the unbounded part of the longitudinal reinforcement. This way the fracture mechanics approach was linked with the effects of the strain in the longitudinal reinforcement. More recently, the so-called Universal Size Effect Law was introduced (Bazant and Yu, 2009; Hoover and Bazant, 2014). This law tries to link the six simple and easily modeled asymptotic cases in cohesive fracture of quasi-brittle materials.

Although there are many principles involved in models based on fracture mechanics, the rational approach does not go beyond the explanation of the size effect. Influence of other parameters, such as the amount of longitudinal reinforcement, or shear slenderness, are mostly considered on an empirical basis.

2.3.3.5 Models based on the critical shear crack displacement

Recently, Yang *et al.* (2015, 2017) developed a model to evaluate the shear capacity of reinforced concrete beams without shear reinforcement showing flexural shear failure. Based on experimental observations, it was proposed that the opening of the critical inclined crack can be considered as the lower bound for the shear capacity of a structural member. This model assumes that the unstable opening of the critical inclined crack is triggered when the shear displacement reaches a critical value Δ_{cr} (Fig. 2.26a). Thus the critical shear displacement is used as a failure criterion, and based on that, a new shear evaluation method was proposed.

The critical crack comprises a part representing an existing flexural crack and two secondary crack branches, one propagating to the compressive zone and one developing along the tension reinforcement (Fig. 2.26a). The development of the secondary crack branches, which is considered to be governed by the shear displacement of the flexural crack, reduces the confinement of the flexural crack, which results in a loss of shear resistance due to the loss of aggregate interlock along the crack faces. This opening process of such a crack is therefore considered as the criterion for the initiation of the final shear failure of the structure. As mentioned above, the theoretical model provides a lower bound prediction of shear capacity.

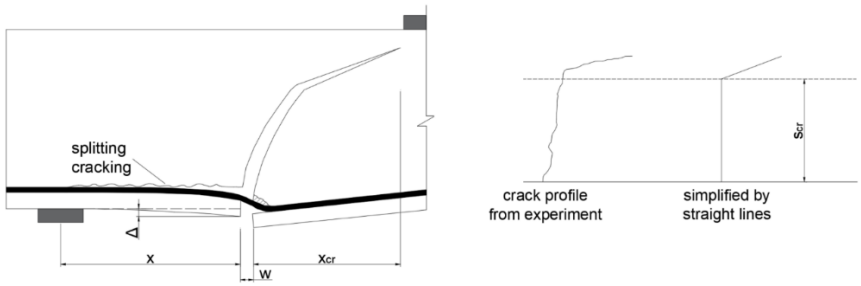

Figure 2.26: a) Free body formed by a flexural crack and two secondary crack branches; b) crack profile simplification. Adapted from Yang *et al.* (2015).

The shear displacement of a flexural crack depends on the external shear force, the bending moment acting on the cracked section and the profile of the flexural crack. However, only the cracks that reach the neutral axis, defined as "major cracks" in the model, can develop into a critical shear crack. The spacing between these major cracks, $l_{cr,m}$, is related to the stress redistribution that takes place after the formation of a previous crack. In a simplified way, for structural members reinforced with ribbed bars and having a realistic effective depth (d > 200 mm), is considered to be given by Eq. (2.43). A bilinear crack profile is assumed, as shown in Fig. 2.26b. Using this simplified profile, the normal crack opening and the tangential shear displacement can be considered independent. Hence, the normal crack opening distributes linearly, whereas the shear displacement becomes constant. Ignoring the tensile stresses in the secondary branch, the crack's contribution to the shear resistance of the structural member is mainly due to aggregate interlock in the main crack branch.

The crack width at the level of the longitudinal reinforcement, given by Eq. (2.44), is estimated from the average crack spacing $l_{cr,m}$ and the steel strain ε_s, determined by the moment at the cross section with = $M/(A_s{\cdot}E_s{\cdot}z)$. The relative shear displacement between the crack faces is related to the shear force and the crack opening. The value of the critical shear displacement was determined by an inverse analysis of a large collection of test results taking into account the simplified crack profile. Thus, it also implicitly corrects the inaccuracy introduced by the simplified crack profile. The critical shear displacement is given by Eq. (2.45), where Φ is de diameter of the longitudinal reinforcement.

$$l_{cr,m} = \frac{s_{cr}}{1.28} \tag{2.43}$$

$$w = l_{cr,m}\varepsilon_s \tag{2.44}$$

$$\Delta_{cr} = \frac{25d}{30610\Phi} + 0.0022 \leq 0.025 \tag{2.45}$$

At the cracked cross-section, the shear force is transferred by three load-carrying mechanisms: direct shear transfer in the concrete compression zone V_c, aggregate interlock V_{ai} and dowel action V_d (Fig. 2.27). In the proposed

simplified model, the total shear force V reached upon the opening of the critical flexural shear crack is:

$$V = V_c + V_{ai} + V_d \tag{2.46}$$

$$V_{ai} = \int_0^{s_{cr}} \tau_{ai}(\Delta, w) \cdot b \cdot ds \tag{2.47}$$

If the cross-section is rectangular, Eq. (2.47) can be further simplified to Eq. (2.48), with $w \geq 0.04$ mm. For V_c, an expression based on the Mörsch's approach was used (Eq. (2.49)) and for the dowel action V_d, Eq. (2.50) was adopted. The value of f_c used in this set of expressions should not be larger than 60 MPa.

$$V_{ai} = f_c^{0.56} s_{cr} b \frac{0.03}{w - 0.01}(-978\Delta^2 + 85\Delta - 0.27) \tag{2.48}$$

$$V_c = \frac{d - s_{cr}}{d + 0.5 s_{cr}} V \tag{2.49}$$

$$V_d = 1.64 b \Phi^3 \sqrt{f_c} \tag{2.50}$$

In the generalized expression for the aggregate interlock component, V_{ai} depends on the crack width and the relative shear displacement between the crack faces. For the determination of the crack width, the bending moment at the cracked section is required. Hence, when the magnitude of the load applied to the specimen is not known, iteration is needed to solve the maximum shear force V. The calculation process is illustrated in Fig. 2.27.

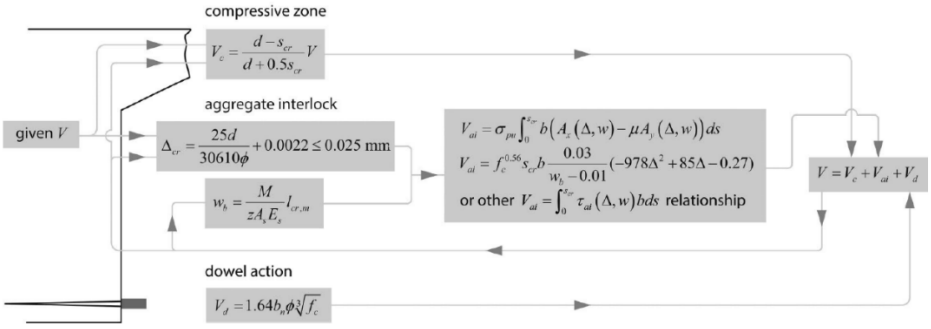

Figure 2.27: Solution scheme for the critical shear displacement theory. Yang *et al.* (2015).

The method shows agreeable accuracy when compared with test results in literature.

2.3.3.6 Models based on the strength of the compression zone

In general, models based on this approach assume that in slender beams without shear reinforcement under two-point loading, the critical shear crack typically involves two branches. The first branch is an inclined shear crack, which usually develops after flexural cracking at some section between the load and the support (the higher the reinforcement amount, the closer to the support) and whose height is similar to that of the flexural cracks. The second branch of the critical crack initiates from the tip of the first branch and propagates abruptly toward the loading point, crossing the compression zone and causing the failure of the specimen (Fig. 2.28). The opening of the first branch of the critical crack is assumed to be orthogonal to the line of the crack, being the result of a rotation around its tip. The compression zone above the tip prevents any meaningful contribution of shear slip along the crack interface, thus the contributions of aggregate interlock and dowel action are considered small and may be neglected (Kostovos *et al.* 1987; Ruddle *et al.* 1999; Khuntia and Stojadinovic 2001)

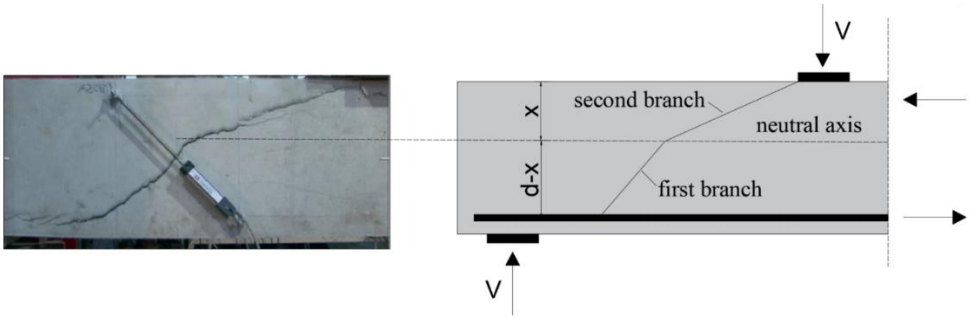

Figure 2.28: Critical shear crack evolution.

Zararis and Papadakis (2001) presented a model considering that shear failure was governed by the splitting strength of concrete in the compression zone. The geometry of the splitting surface was assumed to be a disk whose diameter is in the line joining the support and the point of the application of the resultant of the compression stresses at the section of application of the load. The disk passes through that point and through the through the tip of

the first branch of the critical crack (Fig. 2.29). The height of the first branch of the critical crack is derived from the equilibrium of the cross-section considering a parabolic distribution of normal stresses in the compression zone (Eq. (2.51)). The size effect factor ζ was incorporated as a multiplier of the shear strength obtained by the model. It was empirically derived, based on results from test conducted on cylindrical disks of broad size ranges and constant thickness, and incorporates a term accounting for the shear span (Eq. (2.52)). Finally, the shear strength of the element is given by Eq. (2.53).

$$\left(\frac{x}{d}\right)^2 + 600\frac{\rho}{f_c}\frac{x}{d} - 600\frac{\rho}{f_c} = 0 \tag{2.51}$$

$$\zeta = 1.2 - 0.2a \geq 0.65 \quad (d \; in \; meters) \tag{2.52}$$

$$v_R = \frac{V_R}{bd} = (1.2 - 0.2a)\frac{x}{d}f_{ct} \tag{2.53}$$

$$\tan^2\theta - \frac{a/d}{1 - x/d}\tan\theta + \frac{2.5 - x/d}{1 - x/d} \tag{2.54}$$

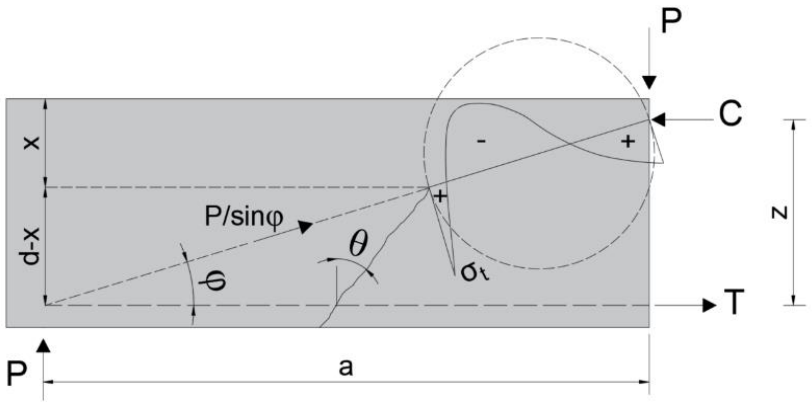

Figure 2.29: Distribution of normal stresses along line of second branch of critical crack. Reproduced from Zararis and Papadakis (2001).

Park *et al.* (2006) and Choi *et al.* (2007) developed a model in which the shear strength of the compression zone is evaluated considering the influence of the normal stresses, developed by the flexural moment, on the shear capacity. The failure mechanism of the compression zone was considered to vary from a tension failure to a compression failure as the *a/d* ratio decreases so the model is suitable for both slender and non-slender beams. To define

the failure mechanism of the compression zone subjected to combined normal and tangential stresses, Rankine's failure criteria were used, so material failure is considered to occur when the principal stress reaches material strength. When the principal tensile stress reaches the tensile strength of concrete f_{ct}, a failure controlled by tension occurs. On the other hand, when the principal compressive stress reaches the compressive strength f_c, failure controlled by compression occurs (Fig. 2.30a). Based on these criteria and assuming a parabolic distribution of normal stresses in the compression zone, the shear strength along an inclined crack was studied, concluding that the shear capacity reaches its minimum value when tensile cracking reaches the neutral axis (Fig. 2.30b). Eq. (2.55) was provided as a simplified expression, in which the second term is related to the compression crushing in non-slender beams and is equal to zero if a/d >2.3. The factor λ_s in the first term correspond to the size effect and was taken equal to Zararis and Papadakis (2001) expression.

$$V_c = 0.52\lambda_s\sqrt{f_c}\cdot b(x - c_c) + 0.45 f_c \cdot b \cdot c_c \tag{2.55}$$

$$\lambda_s = 1.2 - 0.2\frac{a}{d} \geq 0.65 \quad (d \; in \; meters) \tag{2.56}$$

$$c_c = (1 - 0.43\, a/d)x \geq 0 \tag{2.57}$$

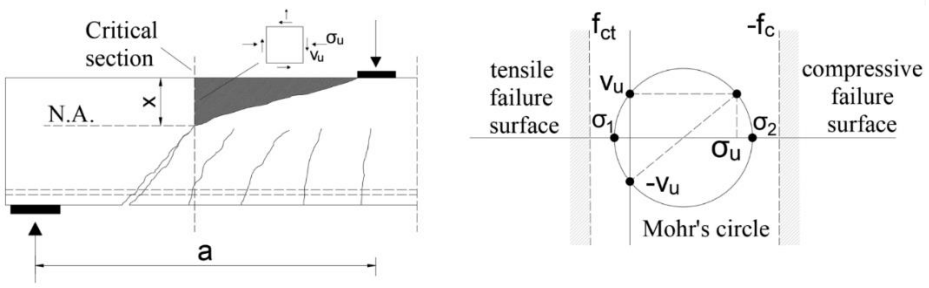

Figure 2.30: Rankine failure criteria. Reproduced from Choi *et al.* (2007).

The Multi-Action Shear Model (MASM).

As part of the models developed at the UPC, the Multi-Action Shear Model is a mechanically-based model for the prediction of the shear-flexure strength of RC slender beams, with and without stirrups, which incorporates the most important shear transfer actions that take place in beams (Marí *et al.*

2014). For beams without stirrups, in a simplified manner, this model assumes that the global shear resisting mechanism of a RC beam can be represented by a truss model in which equilibrium is guaranteed by the existence of inclined concrete ties which may cross cracks up to a certain load levels. These ties represent the resultant of residual tensile stresses and frictional stresses along the crack and its inclination depends on the capacity of the crack to transmitting both type of stresses, which is directly related to the crack width (Fig. 2.31a). As the load increases, the crack width also increases, hence tensile and frictional stresses concentrate in the upper part of the crack, where the crack opening is smaller, reducing both the contribution of the shear resisted along the crack and the increment of force at the longitudinal reinforcement. The reduction in shear resisted across the crack is compensated with an increment in the inclination of the compression chord or, in other words, by a certain arching action, which increases the shear taken by the compression zone. As a consequence, the actual shear stress distribution in a section of a beam will be similar to that schematically shown in Fig. 2.31b, which results from a combination of pure bending action and pure arch action (Bairán and Mari 2006; Mohr *et al.* 2010).

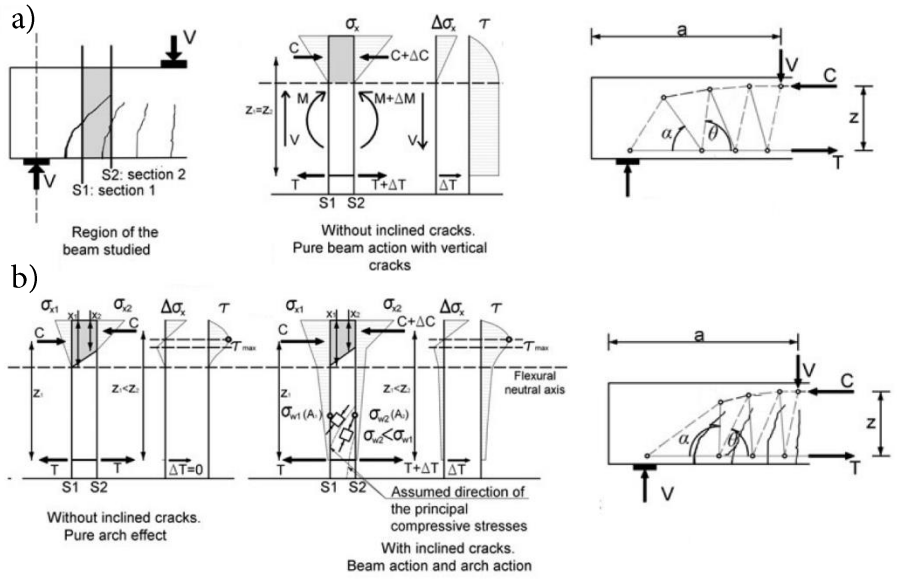

Figure 2.31: distribution of stresses in diagonally cracked R members: a) slightly cracked; b) heavily cracked. Marí *et al.* (2014).

Main assumptions of the model

At ultimate load level, shear in a beam without stirrups is considered to be resisted by the joint contributions of the uncracked concrete zone (V_c), the tensile stresses transferred along the crack (V_w) and the dowel action the longitudinal reinforcement can transfer (V_l), which is neglected if no stirrups are provided (Fig 2.32).

The distributions of stresses along the compression zone shown in Fig. 2.32 are assumed: (a) a linear distribution of normal stresses σ_x; (b) a parabolic distribution of the shear stresses, with $\tau = 0$ at the top fiber and at the neutral axis and with its maximum at mid-depth of the compression zone. This is not strictly truth since certain value of the shear stress at the neutral axis must exist and therefore, the maximum of the parabola should be closer to the neutral axis. However, the shear stress resultant obtained by the simplified distribution is very similar to the actual one; (c) No vertical normal stresses are considered in slender beams without stirrups ($\sigma_y = 0$). Tensile stresses are considered positive.

The depth of the uncracked zone is equal to the neutral axis depth in pure bending (x). It can by calculated by standard analysis of cracked reinforced concrete sections under pure flexure, neglecting both the effects of compression reinforcement and the contribution of concrete in tension.

$$\frac{x}{d} = n\rho\left(-1 + \sqrt{1 + \frac{2}{n\rho}}\right) \tag{2.58}$$

$$n = \frac{E_s}{E_c} \tag{2.59}$$

The horizontal projection of the first branch of the critical crack is considered equal to $0.85d$, as indicated in Fig. 2.32. This value is in accordance with experimental observations made by the authors (Cladera and Marí 2004; Marí *et al.* 2014). In general, the inclination of the cracks is affected by the longitudinal and transverse reinforcement ratios, which influence the strain state of the beam. However, as observed by other researches, this influence is moderate (Collins *et al.* 2008; Karayannis and Chalioris 2013)

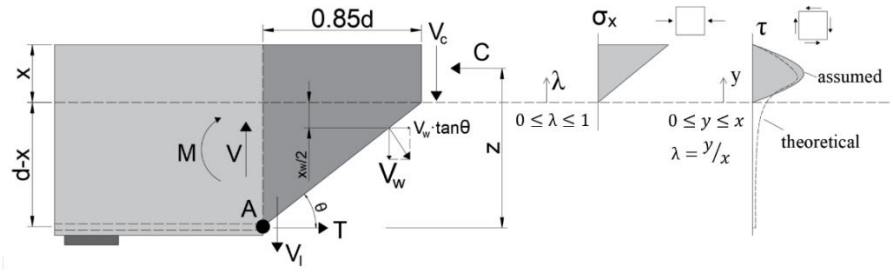

Figure 2.32: Shear transfer mechanisms considered and distribution of stresses at the uncracked compression zone. Marí *et al.* (2014).

Failure criteria

It is considered that failure occurs at a point of the compression zone, at the critical section, when the principal stresses (σ_1, σ_2) at that point reach the Kupfer's biaxial failure envelope (Kupfer and Gerstle 1973) in the compression-tension branch (Fig. 2.33). In this branch, the envelope is considered to be a straight line for compression stresses lower than $0.8f_c$. This straight line passes through the point corresponding to uniaxial tensile stress $(0, f_{ct})$, has a slope m = - 0.8 and is given by Eq. (2.60), where the left hand side is named the damage existing at any point subjected to principal stresses (σ_1, σ_2) and is equal to 1 for any point pertaining to the failure envelope.

$$\frac{\sigma_1}{|f_{ct}|} + 0.8\frac{\sigma_2}{|f_c|} = 1 \tag{2.60}$$

For $\sigma_2 > 0.8f_c$, the envelope is a curved line connecting the straight line with the point corresponding to the uniaxial compressive strength (f_c, 0). However, since failure usually takes place for principal compressive stresses lower than $0.5f_c$, the equation of this part is not relevant for the model.

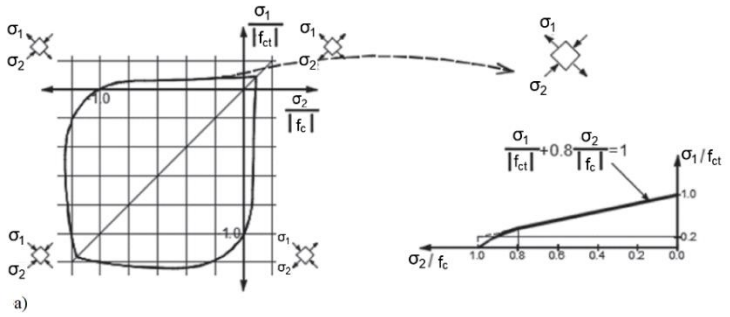

Figure 2.33: Kupfer's failure envelope for the tension-compression sector. Adapted from Kupfer and Gerstle (1973).

Position of the critical section and of the point of maximum damage within the compression zone

For beams with constant geometry and reinforcement layout along their length, the weakest section is considered to be placed at the tip of the first branch of the critical diagonal crack (Fig. 2.34a). Actually, any other section closer to the zero bending moment point has a bigger depth of the compression zone, produced by the inclination of the crack, and therefore, it will resist a higher shear force. In addition to that, any other section placed farther from the support will have the same depth of the compression zone but will be subjected to higher normal stresses, hence will have a greater shear capacity. In order to obtain the position of the critical section, the critical crack is assumed to start where the bending moment diagram at failure reaches the cracking moment of the section ($s_{cr} = M_{cr}/V_u$), which is a conservative assumption. Then, taking into account the assumption made for the horizontal projection of the crack, the critical section will be placed at a distance from the support equal to $s_{cr} = M_{cr}/V_u + 0.85d$. This position of the critical section was also obtained by Park et al. (2006) assuming an angle of the crack inclination in the tensile zone of 45º and relating the bending moment at sections B and C (Fig. 2.34a) by estimating the increment of shear needed to make the tensile crack reach the neutral axis.

The critical point inside the compression chord will be that with the maximum damage, given by the left hand side of Eq. (2.60), and will depend on the distributions of normal and shear stresses along the concrete compression zone. Its position is obtained through the relative damage index, given by the ratio between the damage at any fiber of the compression chord and the damage at the compression top fiber. For the linear and parabolic distributions assumed for normal and shear stresses respectively, the principal stresses at any point at a distance *y* from the neutral axis (Fig. 2.32) are given by the following expressions, based on Mohr's circle, where $\sigma_{x,max}$ refers to the normal stress at the compression top fiber:

$$\sigma_1 = \left[-\frac{y}{x} + \sqrt{\left(\frac{y}{x}\right)^2 + \frac{9(d - x/3)}{(M/V)^2}\left(\frac{y}{x} - \frac{y^2}{x^2}\right)^2} \right] \sigma_{x,max} \qquad (2.61)$$

$$\sigma_2 = \left[-\frac{y}{x} - \sqrt{\left(\frac{y}{x}\right)^2 + \frac{9(d - x/3)}{(M/V)^2}\left(\frac{y}{x} - \frac{y^2}{x^2}\right)^2} \right] \sigma_{x,max} \qquad (2.62)$$

Fig. 2.34b shows that the critical point is placed at a distance from the neutral axis around $y = 0.425x$ for $M/V < 3d$, which are ratios of $s/d = M/(Vd)$ where usually the critical crack develops.

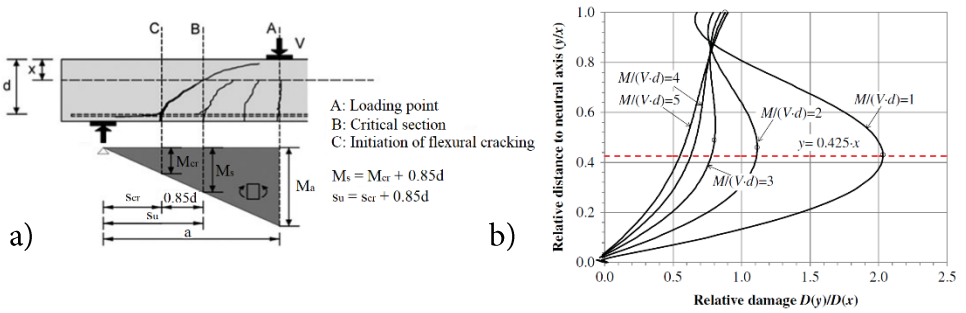

Figure 2.34: a) Position of the shear critical section; b) Position of the critical point inside the compression concrete chord. Marí *et al.* (2014).

Formulation of the model

Shear transferred across the crack

The shear transferred across the crack is due to the residual tensile stresses and the frictional stresses, both related to the three-dimensional irregularities of the crack surface. In this model, both types of stresses are considered jointly in a simplified manner, by assuming that the resulting principal stress is normal to the average crack surface. This assumption is consistent with the Disturbed Stress Field Model (Vecchio 2000, 2001), which sets that such principal direction cannot deviate more than 15º, approximately, from the crack direction, unless another crack is formed.

In order to evaluate the total force transferred across the crack, compatibility of strains normal to the crack is set by assuming that the plane section hypothesis is valid for the plane of inclination of the crack (Fig. 2.35b). A tensile stress-strain relationship with a linear softening branch for concrete in tension is considered, in which the ultimate tensile strain $\varepsilon_{ct,u}$ depends on the fracture energy. The expression for the shear resisted along the crack is:

$$V_w = \int_0^{l_w} \sigma_w \cdot b \cdot \cos\theta \cdot dl \approx \frac{x_w}{\sin\theta} \cdot b \cdot \cos\theta = x_w \cdot \sigma_w \cdot b \cdot \cot\theta \qquad (2.63)$$

where $\sigma_w = f_{ct}/2$ is the adopted constant concrete tensile stress, extended to the length l_w along the crack, which is energetically equivalent to the triangular distribution of Fig. 2.35c. The depth of the tensile zone x_w, given by Eq. (2.64), is obtained by setting the compatibility of deformations in the direction normal to the crack and taking into account the geometrical relationships indicated in Fig. 2.35b, where ε_s is the strain in the longitudinal reinforcement.

$$x_w = (d - x)\frac{\varepsilon_{ct,u}}{\varepsilon_s}\sin^2\theta \qquad (2.64)$$

The ultimate tensile strain can be expressed as a function of the fracture energy G_f and the concrete cracking strain, $\varepsilon_{ct,cr} = f_{ct}/E_c$, as follows:

$$G_f = \int_0^w \sigma_w(w) \cdot dw \approx \frac{1}{2} \cdot f_{ct} \cdot w_{max} = \frac{1}{2} \cdot f_{ct} \cdot \left(\varepsilon_{ct,u} - \varepsilon_{ct,cr}\right) \cdot s_{m\theta} \qquad (2.65)$$

The maximum crack opening has been assumed equal to $w_{max} = (\varepsilon_{ct,u} - \varepsilon_{ct,cr}) \cdot s_{m\theta}$, In which $s_{m\theta}$ is the average spacing of the inclined cracks. This value varies from one point to the other of the crack and is affected by the bond of the longitudinal reinforcement. Because not all flexural cracks develop into shear cracks, the distance between shear cracks, especially when stirrups do not exist, is greater than the distance between flexural cracks (Fig. 2.35a). For this reason, in this model $s_{m\theta}$ is considered equal to the effective depth d, which is a conservative value. Thus, the following expression is obtained for the ultimate tensile strain:

$$\varepsilon_{ct,u} = \frac{f_{ct}}{E_c} \cdot \left(1 + \frac{2 \cdot G_f \cdot E_c}{f_{ct}^2 \cdot d}\right) \qquad (2.66)$$

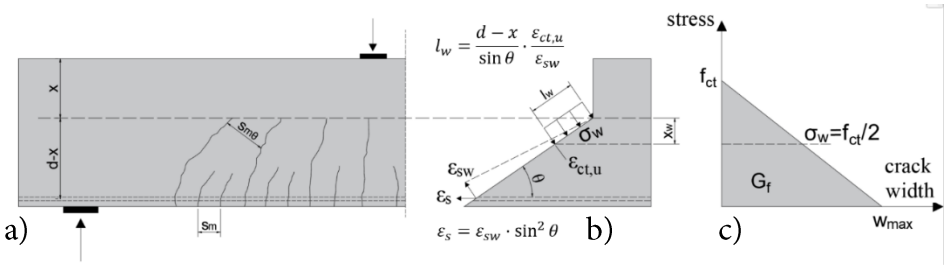

Figure 2.35: a) Diagonal crack spacing; b) compatibility of strains in a direction normal to the crack; c) assumed tensile stress-crack width diagram. Marí *et al.* (2014).

Substituting these parameters into Eq. (2.63), an expression for V_w is obtained, given by Eq. (2.67), which was subsequently simplified in Eq. (2.68a), considering average values of some of the involved parameters, such as ε_s = 0.0009, that is between service and yielding strains, or θ = 36º, which corresponds to x/d = 0.38 assuming an amount of longitudinal of reinforcement ratio ρ = 1.5%.

$$V_w = \frac{0.425 \sin^2\theta \cdot f_{ct}}{E_c \cdot \varepsilon_s} \cdot \left(1 + \frac{2 \cdot G_f \cdot E_c}{f_{ct}^2 \cdot d}\right) b \cdot d \tag{2.67}$$

$$V_w = 167 \frac{f_{ct}}{E_c} \left(1 + \frac{2 \cdot G_f \cdot E_c}{f_{ct}^2 \cdot d}\right) b \cdot d \tag{2.68a}$$

For the calculation of the fracture energy G_f, a new expression was developed by the authors which takes into account the influence of the concrete compressive strength f_c and the maximum aggregate size d_g (Marí *et al.* 2014).

$$G_f = 0.028 \cdot f_c^{0.18} \cdot d_g^{0.32} \quad (f_c \, in \, MPa; \; d_g in \, mm; \; G_f in \, N/mm) \tag{2.68b}$$

Shear resisted in the un-cracked compression zone

According to the Mohr's circle of stresses, the shear stress τ that takes place at any point of the compression zone can be related to the normal and principal stresses by:

$$\sigma_{1,2} = \frac{\sigma_x + \sigma_y}{2} \pm \sqrt{\left(\frac{\sigma_x - \sigma_y}{2}\right)^2 + \tau^2} \tag{2.69a}$$

$$\tau = \sigma_1 \cdot \sqrt{1 - \frac{\sigma_x + \sigma_y}{\sigma_1} + \frac{\sigma_x \cdot \sigma_y}{\sigma_1^2}} \rightarrow \sigma_y = 0 \rightarrow \tau = \sigma_1 \cdot \sqrt{1 - \frac{\sigma_x}{\sigma_1}} \tag{2.69b}$$

If the value of the of the shear stress at the point of maximum damage, located at a distance $\lambda \cdot x$ (λ=0.425 as explained previously) from the neutral axis, is considered to be known and equal to τ_λ, the shear stress distribution $\tau(y)$ (Fig. 2.32) along the uncracked zone (y measured from the neutral axis) can be obtained by imposing the boundary conditions $\tau(0) = 0$, $\tau(x) = 0$ and $\tau(\lambda x) = \tau_\lambda$, resulting in:

$$\tau(y) = \frac{\tau_\lambda}{\lambda(1-\lambda)}\left(\frac{y}{x} - \frac{y^2}{x^2}\right) \tag{2.70}$$

The resultant shear force at the concrete chord V_c, assuming a constant width b, is obtained by integration of the shear stresses along the compression zone:

$$V_c = \int_0^x \tau(y) \cdot b \cdot dy = \frac{\tau_\lambda \cdot b \cdot x}{6 \cdot \lambda(1-\lambda)} \tag{2.71}$$

The value of τ_λ in Eq. (2.70) can by replaced by the normal and principal stresses acting at the point of maximum damage, according to Eq. (2.69). This way, V_c can be expressed in terms of σ_x, σ_y and σ_1 (Eq. (2.72)). The maximum shear capacity will be reached when the principal stresses at the point of maximum damage satisfy the Eq. (2.60) of the tension-compression branch of the Kupfer's failure envelope.

$$V_c = \frac{\sigma_1 \cdot b \cdot x}{6 \cdot \lambda(1-\lambda)}\sqrt{1 - \frac{\sigma_x}{\sigma_1} + \frac{\sigma_x \cdot \sigma_y}{\sigma_1^2}} \tag{2.72}$$

Since σ_y is considered equal to zero in beams without stirrups, the last step is to relate the normal compressive stresses σ_x to the internal forces acting at the critical section. This can be done by setting the equilibrium of moments (Eq. (2.73)), at Point A, of the forces acting on the free body of the Fig. 2.32 and taking into account that, according to the linear distribution of normal stresses, the normal stress at the point of maximum damage is given by Eq. (2.74). Thus, combining these two equations with Eq. (2.72), an expression for V_c is finally obtained. (Eq. (2.75)), where $v_w = V_w/(f_{ct} \cdot b \cdot d)$, R_t is given by Eq. (2.76) and μ_{cr} is the non-dimensional cracking moment, given by Eq. (2.77) for the particular case of rectangular sections.

$$C \cdot z = M_{cr} + 0.85d \cdot V_c + V_w \frac{0.85\mathrm{d} - 0.5\mathrm{x}_w \cot\theta}{\cos^2\theta} \tag{2.73}$$

$$\sigma_x = -2\frac{C \cdot z \cdot \lambda}{bx\left(d - {}^{x}/_{3}\right)} = -2\frac{\lambda\left(M_{cr} + 0.85d \cdot V_c + V_w \frac{0.85\mathrm{d} - 0.5\mathrm{x}_w \cot\theta}{\cos^2\theta}\right)}{bx\left(d - {}^{x}/_{3}\right)} \tag{2.74}$$

$$v_c = \frac{V_c}{f_{ct} b d} = \frac{R_t}{6\lambda(1-\lambda)}\frac{x}{d}\sqrt{1 - \frac{2\lambda\left(\mu_{cr} + 0.85v_c + v_w \frac{0.85 - 0.5 \cdot {}^{x_w}/_{d} \cot\theta}{\cos^2\theta}\right)}{{}^{x}/_{d}\left(1 - {}^{x}/_{3d}\right)R_t}} \tag{2.75}$$

$$R_t = \frac{\sigma_1}{|f_{ct}|} = 1 - 0.8\frac{\sigma_2}{|f_c|} \tag{2.76}$$

$$\mu_{cr} = \frac{M_{cr}}{f_{ct} \cdot b \cdot d} = \frac{b \cdot h^2 \cdot f_{ct}}{6 \cdot f_{ct} \cdot B \cdot d^2} = \frac{1}{6}\left(\frac{h}{d}\right)^2 \approx 0.2 \tag{2.77}$$

To obtain the ultimate shear resisted by the compression zone V_c, the following iterative procedure may be followed:

- **Input data**: Geometry, materials and reinforcement data.
- **Step 1**: Calculate V_w and its non-dimensional form $v_w = V_w/(f_{ct} \cdot b \cdot d)$ using Eq. (2.68).
- **Step 2**: Assume a starting value for R_t. Typically $R_{t0} = 1$.
- **Step 3**: Calculate v_c and V_c using Eq. (2.75) by means of an iterative procedure.
- **Step 4**: Calculate τ, σ_x and σ_y at the point of maximum damage using Eq. (2.71) for τ and Eq. (2.74) for σ_x. ($\sigma_y = 0$ in slender beams without stirrups).
- **Step 5**: Calculate the principal stresses σ_1 and σ_2 at the point of maximum damage using Eq. (2.69a).
- **Step 6**: Calculate R_t using Eq. (2.76)
- **Step 7**: If $|R_t - R_{t0}| \leq tol \rightarrow END$. Else, go to Step 3 using the value of R_t obtained in the previous step.

The shear resisted by the compression chord must be modified to account for the size effect ζ due to the brittle character of the failure that takes place when the second branch of the critical crack develops. For this purpose, the empirical model proposed by Zararis and Papadakis (Eq. (2.56)) was adopted, and V_c must be multiplied by this factor. In the particular case of distributed loads, the shear span a should be considered equal to the ratio M_{max}/V_{max} in the section of the beam being analyzed. Taking this into account, if the equilibrium of vertical forces is set on the free body of Fig. 2.32, the ultimate shear strength of the element is given by:

$$V_R = \zeta V_c + V_w = (1.2 - 0.2a)V_c + V_w \tag{2.78}$$

After a parametric study, it was observed that the shear transferred by the uncracked concrete chord linearly depended on the neutral axis depth, as had been obtained by Tureyen and Frost (2003) using a similar approach and by Zararis and Papadakis (2001) using the splitting test analogy. Thus, a simplified expression for V_c was derived:

$$\zeta \cdot V_c = (1.2 - 0.2a)\left(0.88\frac{x}{d} + 0.02\right) f_{ct} \cdot b \cdot d \qquad (2.79a)$$

If for any reason, the strength verification is to be done at intermediate sections, the bending moment M used in Eq. (2.73) will not be the cracking moment M_{cr}. Thus, the simplified equation for the concrete chord contribution have to be modified as follows:

$$\zeta \cdot V_c = (1.2 - 0.2a)\left(0.88\frac{x}{d} + 0.02\right)(0.94 + 0.3\mu_{cr}) f_{ct} \cdot b \cdot d \qquad (2.79b)$$

The Compression Chord Capacity Model for beams without stirrups (CCCM)

The Compression Chord Capacity Model (Cladera *et al.* 2016) is a simplification but also an extension of the MASM introduced above, with the goal of making the model easier to use in daily engineering practice and suitable for a wider range of cases. The basic idea was that, since the contributions of the web V_w and the dowel action V_l are much smaller than that of the compression chord, to adopt average values for V_w and V_l and to incorporate them into the contribution of the compression chord.

T and I-beams

Initially derived for rectangular beams, the model was extended to T and I-beams (Cladera *et al.* 2015) by incorporating the influence of the compression flange by means of the effective shear width, which depends on the section geometry and on the longitudinal reinforcement ratio. The neutral axis depth of a T-shaped section is closer to the top compressed fiber. Therefore, for the same reinforcement area and effective depth, the crack opening is higher than in a rectangular beam of the same web width, so the aggregate interlock is lower and shear resisted in the compression chord becomes very relevant. Thus, once the shear stresses concentrate on the concrete flange, the contribution to the shear strength of the compression

chord is higher than in a rectangular section of $b = b_w$, resulting in higher total shear strength. This phenomenon had been also observed experimentally (Fig. 2.36a), indicating that there exists some contribution of the compression flange being ignored. For that reason, the following expressions for the effective depth were proposed (see also Fig. 2.36b):

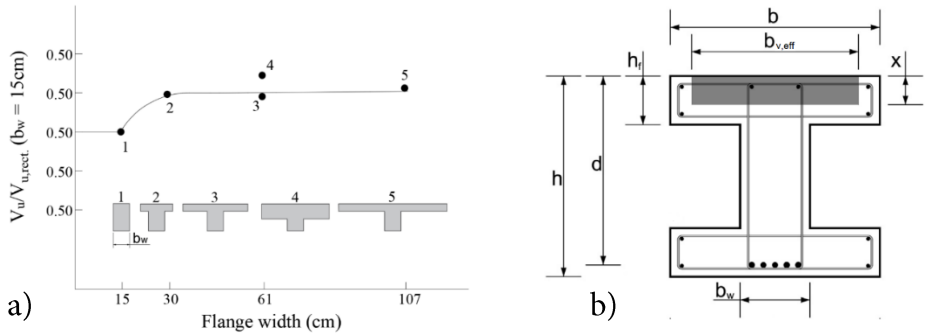

Figure 2.36: a) Effect of flange width on the shear strength. Adapted from *ASCE-ACI Committee 426 (1973)*; b) schema for the calculation of the effective flange width. Cladera *et al.* (2015).

$$if\ x \leq h_f \ \rightarrow\ b_{v,eff} = b_w + 2h_f \leq b \tag{2.80}$$

$$if\ x > h_f \ \rightarrow\ b_{v,eff} = b_w + (b_v - b_w)\left(\frac{h_f}{x}\right) \tag{2.81}$$

Size effect

According to the empirical factor adopted in the MASM, derived from splitting tests (Zararis and Papadakis 2001), the size effect on the shear failure of slender beams only depends on the length of the shear span (Eq. (2.56)). However, it had been observed experimentally that both the effective depth d of the element and the a/d ratio were involved on the size effect. For that reason, a new empirical size effect term was proposed which depends on both parameters separately. The factor depending on d was taken the same as the factor proposed by ACI Committee 446 (Bazant *et al.* 2007). The factor depending on a/d was taken from empirical work with genetic programming (Pérez *et al.* 2012; Cladera *et al.* 2014) where it was seen that the term $(a/d)^{0.21}$ correctly predicted the influence of this variable. The new combined size

effect factor is given by Eq. (2.82). Fig. 2.37 shows a comparison between the size effect adopted in the MASM and the new expression.

$$\zeta = \frac{2}{\sqrt{1+\frac{d_0}{200}}}\left(\frac{d}{a}\right)^{0.2} \geq 0.45 \quad d_0 = d \geq 100\,mm \tag{2.82}$$

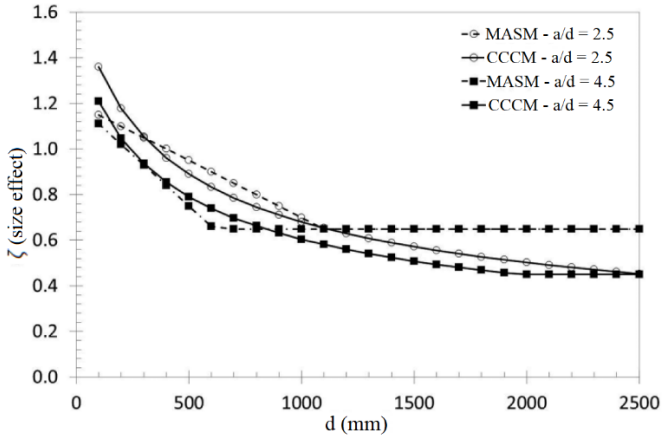

Figure 2.37: Comparison between the size effect law used in the MASM and in the CCCM. Cladera *et al.* (2016).

Axial loads

The effect of an axial load on the shear strength was introduced in the model taking into account its influence on the neutral axis depth. Based on non-linear analyses of reinforced concrete sections carried out by the authors (Mari *et al.* 2016) the following expressions where derived for the cases of axial compression (N < 0) and axial tension (N > 0) respectively, where x_0 represents the neutral axis depth of the cracked section in pure bending. The factor of 0.8 included in the expression for compressed members is needed to correct the fact that in the derivation of the simplified expression for the shear strength (Eq. 2.85), a mean value of the shear resisted in the web was added to V_c. However, V_w should not be affected by the variation of the neutral axis depth and for this reason the reduction factor is needed. It is also important to highlight that the increase of the neutral axis depth depends on the ratio $\sigma_N/(\sigma_N+fct)$ and not only on σ_N.

$$if\ N \geq 0 \rightarrow x = x_0 + 0.8(h - x_0)\left(\frac{d}{h}\right)\frac{\sigma_N}{\sigma_N + f_{ct}} \leq h \tag{2.83}$$

$$if\ N < 0 \rightarrow x = x_0\left(1 + 0.1\frac{N \cdot d}{M}\right) \geq 0 \tag{2.84}$$

$$\sigma_N = \frac{N}{A_c} \tag{2.85}$$

Simplified expression for the shear strength

Taking into account that when shear failure takes place the residual stresses V_w are small compared to the shear resisted in the compression zone, a new compact expression was derived by incorporating V_w into V_c, resulting in Eq. (2.86). However, in some members without stirrups and low levels of reinforcement ratio, this expression may lead to over-conservative results, as the contribution due to residual stresses along the crack may be comparable to the contribution of the uncracked zone, since x/d is small. In this situation, an equation for the minimum shear strength $V_{R,min}$, that takes explicitly into account the residual tensile stresses was derived as a lower bound of the shear strength of RC beams without stirrups (Eq. (2.87)), where $K_c = x/d > 0.2$ and $d_0 = d > 100$mm.

$$V_R = 0.3 \cdot \zeta \cdot \frac{x}{d} f_c^{2/3} \cdot b_{v,eff} \cdot d \geq V_{R,min} \tag{2.86}$$

$$V_{R,min} = 0.25 \cdot \left(\zeta \cdot K_c + \frac{20}{d_0}\right) f_c^{2/3} \cdot b_w \cdot d \tag{2.87}$$

The Compression Chord Capacity Model for Non-Slender beams without stirrups (CCCM-NS)

Non-slender beams are usually defined as beams in which the shear span to effective depth ratio a/d is less than 2.5. This situation may occur in deep beams or in geometrically slender beams when there are point loads applied near the supports. In these cases, the shear strength is enhanced by arch action, so the lower the a/d the higher the shear resisted. To adapt the described shear models to non-slender beams (Bairan *et al.* 2020), the following aspects of the structural response of non-slender beams were considered in the formulation:

The strain deformations are not planar and the neutral axis depth x increases as a/d decreases (Fig. 2.38a). This affects the contribution to the shear strength because it is directly dependent on the size of the uncracked zone. To account for this increment of the neutral axis depth, a parabolic variation of x is assumed between $a/d = 2.5$ ($x = x_0$, B region) and $a/d = 0$ ($x = d$), resulting:

$$\frac{x}{d} = \frac{x_0}{d} + \left(1 - \frac{x_0}{d}\right)\left(1 - 0.4\frac{a}{d}\right)^2 \tag{2.88}$$

As a consequence, the flexural lever arm is assumed to vary linearly from $z = d - x/3$ for $a/d = 2.5$ to $z = 0.6d$ for $a/d = 0.5$. The same way, the force due to bending in the compression chord approximately varies from $C = 0.5 \cdot \sigma_{xmax} \cdot b \cdot x$ for $a/d = 2.5$ to $C = 0.8\ \sigma_{xmax} \cdot x$ for $a/d = 0.5$.

Due to the distribution of stresses in the D-region between the load and the support, the critical crack is considered to develop as a straight crack connecting both points. Therefore, in the modified non-slender model, the critical crack inclination is taken as:

$$\cot\theta \approx \frac{a}{d} \geq 0.5 \tag{2.89}$$

Furthermore, the shear transferred across the crack has to be calculated using the angle of the critical crack given by Eq. (2.89), so the simplified expression cannot be used and Eq (2.67) must be used instead. The reinforcement strain can be estimated by the following expression, where v is the dimensionless shear ($v = V/(f_{ct} \cdot b \cdot d)$). The free body considered for the equilibrium equations is shown in Fig. 2.38b.

$$\varepsilon_s = \frac{V \cot\theta}{A_s E_s} \tag{2.90}$$

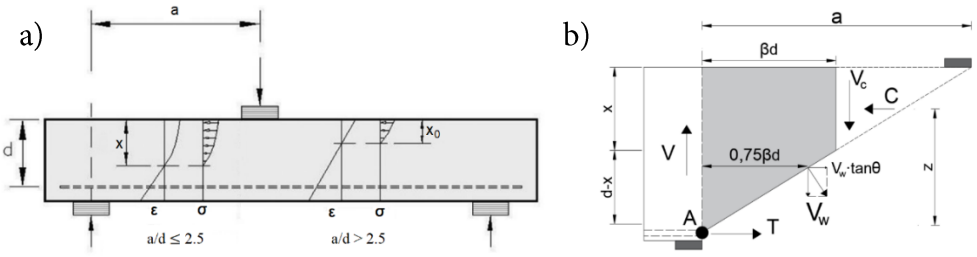

Figure 2.38: a) Stresses and strain distributions in slender and non-slender beams; b) Forces acting on the free body part of the beam. Adapted from Bairán *et al.* (2020).

When the point load is applied on top of the beam, vertical compression stresses σ_y are generated in the compression chord, producing a confining effect that may increase the shear capacity of the fibers of this zone. At the critical point, an assumed average value is obtained by distributing the applied point load in a surface of width equal to the width of the beam b, and length equal to $l = c + x \cdot a/d$ (Fig. 2.39), resulting in:

$$\sigma_y \cong \frac{\lambda \cdot V}{b \cdot \left(c + x \cdot {}^{a}/_{d}\right)} \psi_{ad} \tag{2.91}$$

where ψ_{ad} is a stress interpolation factor in terms of a/d given by the following expression. It varies from 0 to 1, and provides continuity between slender and non-slender beams. The factor $\lambda = Q/V$ is the ratio between the applied load and the shear at the considered support.

$$\psi_{ad} = 1.25\left(1 - 0.4\frac{a}{d}\right) \quad 0 \leq \psi_{ad} \leq 1 \tag{2.92}$$

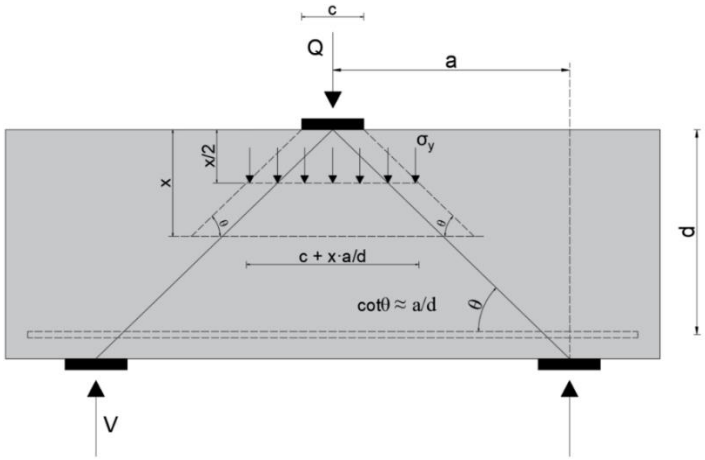

Figure 2.39: Compressive vertical stresses introduced by point load. Adapted from Bairán *et al.* (2020).

According to the critical crack geometry assumptions, the distance from the starting section of the critical crack to the resultant of the force transferred by the uncracked compression chord V_c is $\beta d = (d\text{-}x)\cdot a/d$. For the sake of

simplicity, the resultant of the force transferred by the cracked web V_w is assumed to be placed at a distance $\beta_w d = 0.75\beta d$ (Fig. 2.38b).

Taking into account all these assumptions, if the equilibrium of moments at the starting point of the critical crack is considered (Fig. 2.38b), the longitudinal normal stress at the point of maximum damage is given by:

$$\sigma_x = 0.75\frac{(d-x)}{b\cdot x}\left(V_c\frac{a}{d} + 0.75V_w(1+\tan^2\theta)\right) \tag{2.93}$$

Following a similar procedure to that explained for the MASM, the maximum shear capacity can be obtained. After a parametric study, a simplified design expression was provided, which includes the size effect factor ζ adopted in the CCCM.

$$V_R = \zeta\cdot\frac{x}{d}\left(1+\left(2.5-\frac{a}{d}\right)^2\right)b\cdot d\cdot f_{ct} \tag{2.94}$$

The rational and mechanical models described in this section are just a few. A big amount of models for the calculation of the shear strength of RC beams without stirrups is available in the literature, and some compendiums have been published, such as ASCE-ACI Committee 445 (1998) or *fib* (2018), where a significant number of references may be found.

2.3.4 Shear in one-way slabs

The occurrence of one-way shear failure or punching-shear failure in one-way RC slabs without shear reinforcement depends on several parameters, such as the dimensions of the element, the shape and the position of the load, material properties, reinforcement ratio and layout, etc. Pure one-way shear failure only occurs if the conditions are such that the shear forces flow from the load to the support parallel to each other. This may be the case of simply supported on two parallel sides or cantilever slabs subjected to a line load over their whole width (Fig. 2.40). In this situation, it has been observed that the width of the element is not of significant influence on the shear strength (Sherwood *et al.* 2006; Guruzteaga *et al.* 2015). Thus the behavior is 'beam

like' and the slab can be checked only for one-way shear using shear models developed for beams.

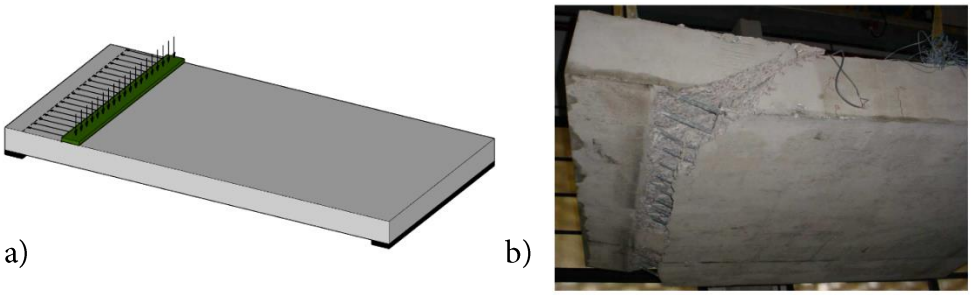

Figure 2.40: One way shear failure on a simply supported slab subjected to a line load over its full width: a) flow of shear forces; b) failure surface. Guruzteaga *et al.* (2015).

Punching-shear is generally associated with concentrated loads on slabs, especially with slabs supported on a more or less regular grid of isolated columns, where the column reaction is assumed to be introduced into the slab by radially developing shear forces (Fig. 2.41a). One of the simplifications that is often applied is the assumption of axis-symmetrical conditions. This means that for both orthogonal directions of the slab, the loading, the reinforcement layout and the geometry of the column and the slab are considered to be the same. However, the assumption of axis-symmetrical conditions is not always justified, as is the case of edge or corner columns, slabs supported on two opposite sides, unbalanced loading, etc. This phenomenon was seldom studied until around 1990. Elstner and Hognegstad (1956) included two tests of slabs supported at two opposite edges in their work on punching, and their strengths were about a 12% below those for comparable slabs supported at all four edges. Leonhardt and Walther (1961) tested one-way slabs subjected to two loads placed symmetrically in the span. One was a concentrated load and the other a full-width line load. Shear failures generally occurred near the concentrated loads, but the slabs were relatively narrow and no real reduction of the strength could be expected. Alexander and Simmons (1987) conducted a series of punching tests in non- axis-symmetrical conditions and observed that when one side of the loading area was subjected to a heavier load, the punching region was confined to the area on that side of the loading plate whereas the opposite side showed a considerable lower stress. Same behavior was observed in the case of edge columns (Fig 2.41b).

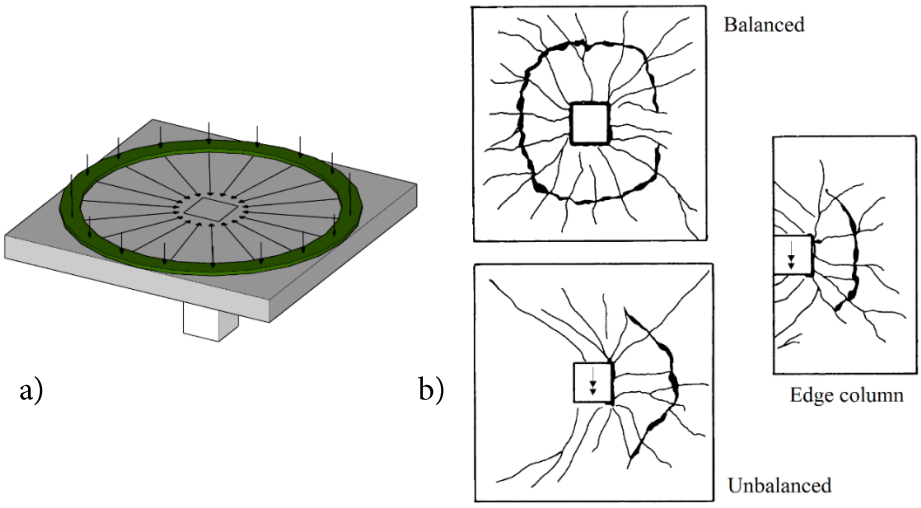

Figure 2.41: a) Axis-symmetric punching-shear; b) punching failure under different load conditions. Alexander and Simmons (1987).

For one-way slabs, like bridge deck slabs, subjected to a concentrated load very close to the support, it is generally accepted that the shear failure mechanism is directly related to one-way shear. However, when the concentrated load is far away from the support, the shear failure is more related to punching-shear. Thus, as the distance from the concentrated load to the support increases, the shear failure mechanism changes. According to Vaz Rodrigues *et al.* (2008) also intermediate situations may be found in practice, where the shear forces develop neither parallel nor radially, since the transition in failure mechanism is not sudden. When the load is applied close to the support, shear strength is usually assessed by means of one-way shear models developed for beams using an effective width. On the contrary, when the concentrated load is not close to the support, according to most of the building codes, both the one-way shear and the punching-shear capacities have to be calculated to see which failure mode is governing. A transition failure mode is in general not considered.

2.3.4.1 Parameters influencing the shearing behavior on one-way slabs

There are a lot of parameters influencing the shear capacity and behavior of RC one-way slabs. The parameters briefly described below are widely accepted as the most significant ones.

Effective shear width and width of the slab

For slabs subjected to a concentrated load, spanning in only one direction, building codes usually assess the shear capacity by assuming that shear is carried by only a portion of the slab, the so-called effective width. Within this strip, the shear distribution is assumed to be constant. The effective width was initially defined (Goldbeck 1917) as the width over which the resultant force due to the maximum stress equals the resisting action due to the variable stress over the entire width (Fig. 2.42). For flexure, the effective width associated to a concentrated load applied over a certain area can be calculated using the theory of elasticity (Westergaard 1930, AASHTO 2007) or estimated based on field testing (Amer et al. 1999). However, regarding shear, very little information on the distribution across the width of the element is available, and the design methods to determine the effective width result from local practice.

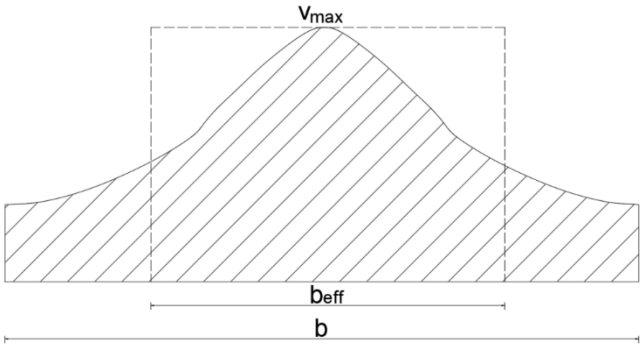

Figure 2.42: Definition of effective width. The area below the curve of the shear stresses over the width b equals the area of the maximum shear stress v_{max} over b_{eff}.

A method of load spreading recommended in the French code (FD-P 2013) is shown in Fig. 2.43a. The load spreading is assumed under an angle of

45º from the far corners of the loading plate and the effective width is measured at the closest support. This approach indirectly takes into account the effect of the size of the load in the effective width. Another approach is provided by the Dutch code (NEN 6720 (1995)), where the load is assumed to spread at an angle of 45º from the center of the loading plate (Fig. 2.43b). The effective width is also measured at the closest support but a minimum effective width equal to two times the effective depth *d* of the flexural reinforcement is considered. A third example are the guidelines for the determination of the effective width given in the Model Code 2010 (CEB-*fib* 2010), where the load is considered to spread from the far corner of the loading plate at an angle of 60º for simply supported slabs and 45º for cantilever slabs (Fig. 2.41c), based on the Swiss code (SIA 1962) provisions.

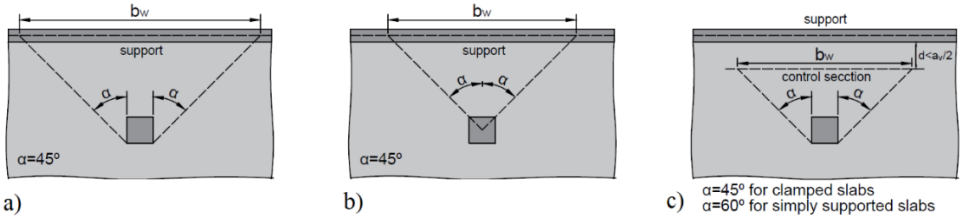

Figure 2.43: Effective width for the shear strength calculation according to different codes: (a) French Code (FD-P 2013); (b) Dutch Code (NEN 6720 (1995)); (c) Model Code 2010 (CEB-*fib* 2010).

During the last decades, different researchers have proposed expressions for the definition of the effective shear width, and many of them have been compiled and can be consulted in Lantsoght *et al.* (2015a). This work also includes a comparison of the three schemas described above to determine the effective width with experimental results, highlighting that the French proposal is the best approximation, which has been recently confirmed by Havolnik *et al.* (2020). The shear effective width has been also studied by means of non-linear finite element models (Doorgest 2012; Belleti *et al.* 2014), analyzing the distribution of the reaction at the support. Both studies concluded that the numerically obtained effective width was a bit greater than the effective width calculated using the French proposal, and would corresponding to a spreading angle slightly over 50 degrees.

The influence of the width of the slab on the shear strength has been experimentally investigated throughout the last decades. Regan and Rezai-

Jorabi (1988) tested a set of slabs made of the same concrete and with the same reinforcement ratio and effective depth and a/d = 5.42, but with different values for the width b, ranging from 400 to 1200 mm. The study was repeated for different sizes of the loading plate. Similar trends were obtained in all cases, with a rate of increase slightly less than linear for widths up to 1000 mm, but no further increase when b = 1200 mm (Fig. 2.44a). A similar experimental study was carried out by Reissen and Hegger (2012), where slabs of widths ranging from 0.5 to 3.5 meters were tested under a concentrated load with a/d = 4.16 using a square loading plate of 0.4 x 0.4 m. The full width of the slabs was activated when $b \leq$ 1.5 m. For b = 2.5 and 3.5 m, the experimentally measured effective width was smaller than the specimen width, but a threshold value was not observed (Fig. 2.44b).

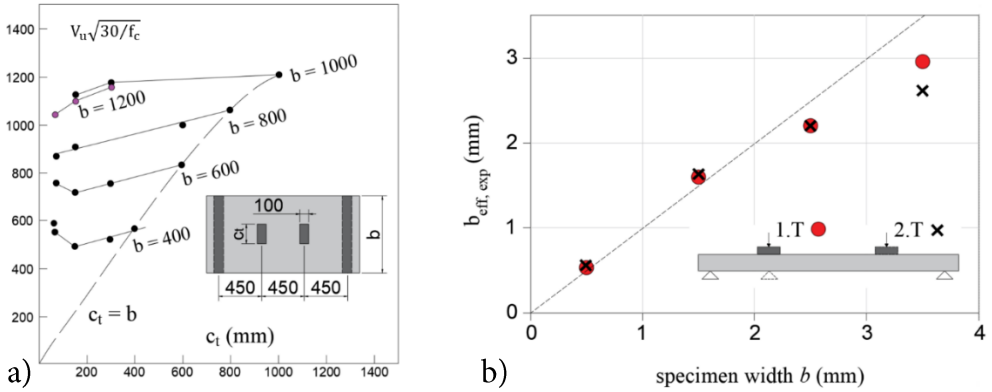

Figure 2.44: a) Shear strengths as function of slabs widths. Regan and Rezai-Jorabi (1988); b) experimental effective width $b_{eff,exp}$ for different specimen widths. Reissen and Hegger (2012).

Lantsoght *et al.* (2015a) performed a comprehensive study on this topic which included different a/d ratios, supporting conditions (Simply support and continuous support) and loading plate sizes. It was observed that, for slab strips with a small width, an increase in the specimen width leaded to an increase in the shear capacity, since the full width of the specimen carried the load at the support. For larger widths, a threshold value was observed, above which no further significant increase of the shear strength takes place with an increasing specimen width (Fig. 2.45). This threshold value corresponded to the effective width that carries the load to the support. The following conclusion were made based on this study:

- Slightly lower effective widths were found at the continuous support compared to the simple support.
- A larger loading area leads to a larger effective width, which is in line with the French load spreading method.
- The effective width threshold becomes smaller as the *a/d* ratio decreases, which correspond to the idea of horizontal load spreading at a certain angle

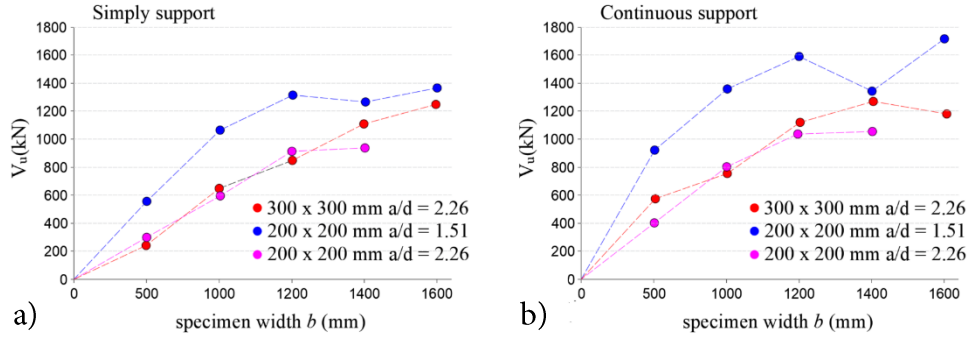

Figure 2.45: Influence of overall width on shear capacity: a) Simply support; b) continuous support. Adapted from Lantsoght *et al.* (2015a).

Reissen *et al.* (2017) carried out an experimental campaign in which the distribution of the reactions at the support was measured for different degrees of restraint to the rotation, amounts of transverse reinforcement and *a/d* ratios. In general, the measurements indicated a more pronounced load transfer to the middle of the slabs decreasing toward the outer edges, which is in agreement with the idea of an effective width. The concentration of the support reaction in the middle of the slab was more pronounced with decreasing shear span to depth ratios. However, the degree of restraint and the transverse reinforcement ratio had only small influence on the distribution of reaction forces.

Shear span to effective depth ratio

The shear span *a* is usually defined as the distance between the point of application of the load and the axis of the closest support. However, in some publications, the clear shear span a_v, defined as the distance between the inner face of the support and the inner face of the loading plate (Fig. 2.46), is used instead of the shear span. This is because the effective depth *d* is in general

smaller in slabs than in beams, and depending on the size of the loading plate, there may be a significant difference between the a/d and a_v/d ratios. Regarding shear in one way slabs, this parameter is directly related with two phenomena: The failure mode and the enhancement of the shear strength due to the arching action.

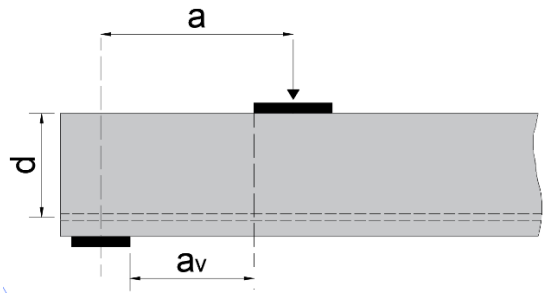

Figure 2.46: Shear (a) and clear shear (a_v) span definitions.

As mentioned above, when the concentrated load is applied very close to the support, the failure mechanism is related to one-way shear. However, when the load is far away from the support, the shear failure is more related to punching-shear. A thorough numerical investigation was carried out by Doorgest (2012), where the influence of the a/d ratio and the slab width to effective depth ratio b/d was investigated, keeping constant other parameters such as the reinforcement ratio, concrete strength, the size of the loading plate or the span length. Results are showed in Fig. 2.47, where three different areas, corresponding to shear failure (S), punching failure (P) and a transition between both failure modes (S + P) were identified. Rombach and Henze (2017) conducted an experimental campaign on cantilever slabs subjected to concentrated loads for a_v/d ratio ranging from one to six. It was observed that the critical shear crack shifted away from the support for $a_v/\mathrm{d} \geq 4$ (Fig. 2.48a). All slabs exhibited shear failures except for the value of $a_v/d = 6$, where the diagonal crack spread around the loaded area and punched out a part of the slab. Is important to highlight that in that case, the load was applied close to the free edge of the cantilever. The shifting of the critical crack was also observed by Reissen *et al.* (2017) in simply supported slabs (Fig. 2.48b).

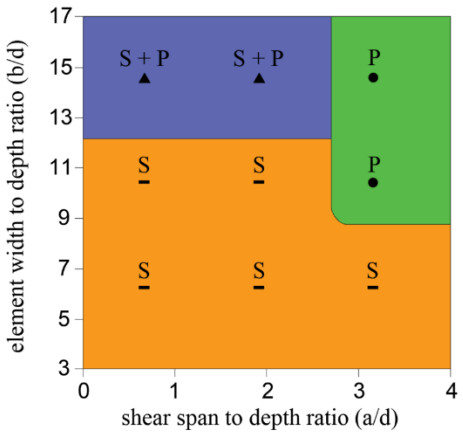

Figure 2.47: Failure mechanism as a function of the shear span to depth ratio (*a/d*) and the element width. Reproduced from Doorgest (2012).

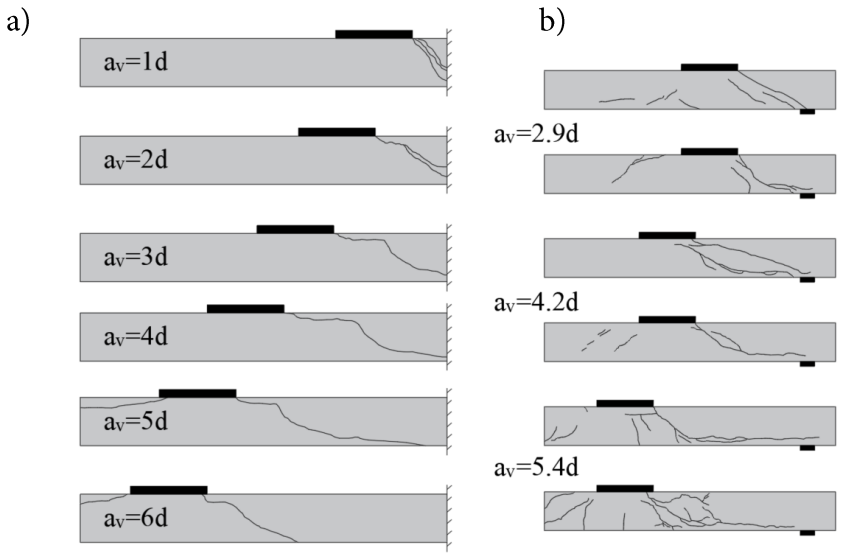

Figure 2.48: Crack pattern for different load positions: a) Cantilever slabs. Rombach and Henze (2017); b) simply supported slabs. Reissen *et al.* (2017).

Regarding the enhancement of the shear strength, Lantsoght *et al.* (2013b) clearly observed an increment in the shear strength when the a/d ratio decreased from 2.16 to 1.51. However, the increase in the shear capacity with decreasing *a/d* ratios was less in slabs than it was in beams (Fig. 2.45). It was concluded that when the element width is relatively big, the horizontal spreading of the load generates a fan of struts which are in general longer than the straight strut generated in narrow elements like beams. Hence, the average

length of the struts is not a but $a^* > a$. This way, if a^* is used instead of a, the shear span to effective depth ratio will increase, which might suggest a horizontal shift to the left in the Kani's valley of shear (Fig. 2.12c) when applied to slabs instead of beams. Reissen and Hegger (2012) carried out a similar study with a/d equal to 2.91, 4.16 and 5.41 concluding that a clear influence of the a/d ratio on the shear strength was not clear due to contrasting effects. While the shear capacity decreases with increasing a/d, the simultaneously increasing effective width increases the capacity, so both effects offset. Natario *et al.* (2014) tested cantilever slabs subjected to concentrated loads placed at $a = 2d$, $3d$ and $4d$, observing a 50% increment in the shear capacity when a/d was equal to two with respect to the other two positions of the point load.

Building codes such as Eurocode-2 proposes a reduction factor β for the design load ($V_{ED,red} = \beta \cdot V_{ED}$) due to the partial load transfer to the support by a direct compression strut. The value of β depends on the clear shear span a_v. $\beta = a_v / 2d$ for $0.5d \leq a_v \leq 2d$. EC-2 limits the value of this reduction factor to $0.25 \leq \beta \leq 1$. This factor was determined by Regan (1998) from beam shear tests and provides a lower bound for the increase in capacity as a_v/d decreases. In the experimental campaign conducted by Rombach and Henze (2017) commented before, a clear influence of the arching action was observed for values of $a_v/d \leq 3$. It was concluded that a higher proportion of the external force can be transferred by means of direct struts between the load and the support, for points loads placed within that range of distances. Fig. 2.49 shows a comparison of test on RC slabs without shear reinforcement. The maximum shear force V_u achieved in the tests is shown in relation to the shear capacity calculated according to EC-2 assuming $\beta = 1$. As can be observed, arching action effects seems to start enhancing the shear strength for values of $a_v/d \leq 3$.

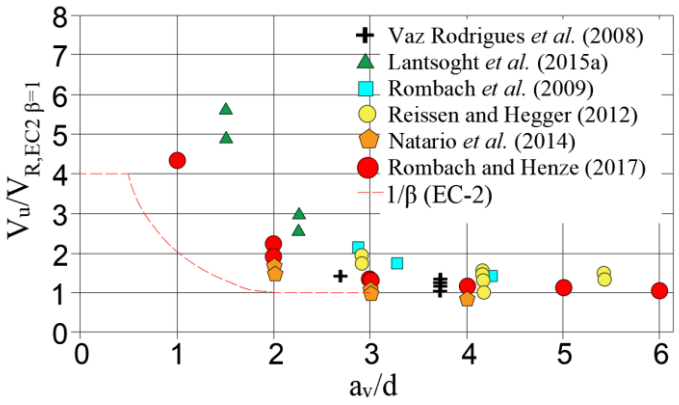

Figure 2.49: Tests of reinforced concrete slabs under point loads depending on shear slenderness a_v/d. Rombach and Henze (2017).

Size effect

Another relevant aspect related to the geometry of the specimens is the size effect. Sherwood *et al.* (2006) investigated the influence of the element width on the size effect and concluded that it is not of significant influence, and that the well-established size effect of decreasing shear stress at failure as the member depth increases also applies to wide beams and thick one-way slabs. In general, slabs are shallow elements, so the size effect is not as important as it may be in beams, where elements are deeper and cracks may be wider.

Reinforcement ratio and layout

The influence of the reinforcement ratio on the punching-shear strength of RC slabs was highlighted more than 50 years ago by Kinnunen and Nylander (1960). When this ratio is low ($\rho \approx 0.5\%$), the reinforcement yields and the slabs behave ductile. The shear capacity is then limited by the flexural capacity. After large plastic deformations, punching failure occurs. For intermediate reinforcement ratios ($\rho \approx 1\%$), the behavior tends to be more brittle and limited yielding of the reinforcement occurs before punching. For higher reinforcement ratios, the flexural capacity is much higher than the shear capacity, and sudden brittle punching failure will occur. Increasing the reinforcement ratio results in a higher punching capacity, but limits the ductility of the element prior to failure (Fig. 2.50a).

Regarding one-way slabs, the influence of the longitudinal (parallel to the span) reinforcement layout was studied by Guruzteaga *et al.* (2015) by testing slabs with the same reinforcement ratio but different spacing (*s*) between the bars. No significant changes were observed on the ultimate load, but the failure surface obtained was quasi-cylindrical and uniform along the breadth of the slabs with a short longitudinal bar spacing whereas it was irregular and curled in slabs with $s/d \approx 1.5$. In the same research the influence of bottom transverse reinforcement was also investigated. After comparing the experimental results obtained by the authors with a database of 79 tests, it was concluded that the bottom transverse reinforcement did not significantly modify the shear response of the specimens. This behavior was also observed by Reissen and Hegger (2012) and Lantsoght *et al.* (2015a). The influence of compression reinforcement has also been observed to be insignificant (Reissen and Hegger 2015).

As far as the tensile longitudinal reinforcement concerns, Lubell *et al.* (2009) tested six RC slabs without shear reinforcement with different effective depths and reinforcement ratios, comparing the results with data available in literature. They concluded that the shear capacity of the specimens increased with increasing reinforcement ratios, as can be seen in Fig. 2.50b. Bui *et al.* (2017a) tested 5 slabs with longitudinal reinforcement ratios ranging from 0.9% to 1.5%, but its influence on the shear strength could not be fully determined, since no clear dependencies were obtained.

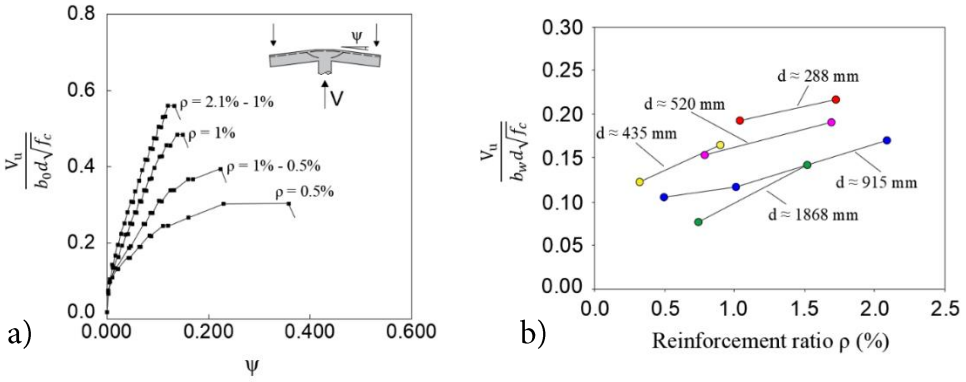

Figure 2.50: Influence of shear reinforcement on the shear response of RC slabs: a) Load rotation curves in axis-symmetric punching tests. Kinnunen and Nylander (1960); b) Shear stress at failure in one-way slabs. Lubell *et al.* (2009).

Concrete compressive strength

Traditionally, the concrete tensile strength was considered the most important factor influencing the shear capacity of RC elements, However, for design purposes, the tensile strength is calculated from the concrete compressive strength f_c, with a relationship usually comprised between the square root and the cubic root, depending on the code. Moody *et al.* (1955a) tested 16 small ($d \approx 0.27$ m), heavily reinforced ($\rho = 1.89\%$) RC beams without stirrups with values of f_c ranging between 10 and 40 MPa. It was observed that the shear strength increased by a factor of approximately 2 when the concrete strength increased by a factor of approximately 4. However, Kani (1967) studied the influence of f_c on the shear strength of RC rectangular beams without stirrups and concluded that its influence is negligible and can be omitted in strength analysis. More recently, Angelakos *et al.* (2001) conducted an experimental campaign on 14 large ($d \approx 1$ m), lightly reinforced ($\rho \leq 1\%$) beams without stirrups, with values of f_c ranging from 21 to 98 MPa and observed almost no influence on the shear strength.

Regarding slabs, Lantsoght (2013b) compared the ultimate load of shear tests carried out in 3 slabs produced with normal strength concrete (NSC) to tests on slabs made of high strength concrete (HSC). The measured average increase in shear resistance for (HSC) versus (NSC) was a 0.6% for an increase in concrete cube compressive strength of 54% (Fig. 2.51a). Thus, the influence of f_c on the shear strength was considered negligible. On the contrary, Bui *et al.* (2017a) tested 5 equal slabs with different concrete compressive strengths ranging from 18 to 35 MPa, observing a significant influence on the shear strength of f_c (Fig. 2.51b), the same way as Moody *et al.* It is noticeable that when the concrete compressive strength is moderate ($f_c \leq 40$), it has been observed that it significantly influences the shear strength, whereas for higher values, no meaningful influence has been observed.

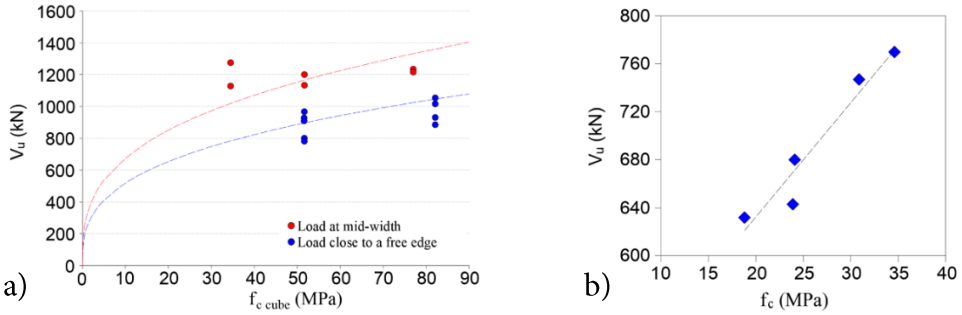

Figure 2.49: Influence of concrete compressive strength on the shear capacity of one-way slabs: a) Lantsoght (2013b); b) Bui *et al.* (2017).

Size of the loading plate

Depending on the selection of the horizontal load spreading schema adopted to address the shear capacity in the design of a one-way slab, the size of the loading plate may play an important role in the determination of the effective width. Regan and Rezai-Jorabi (1988) tested a set of slabs with equal reinforcement arrangement and effective depth, but varying the transverse dimension of the slabs and the loading plates. Regardless the width of the element, a more or less linear increment with increasing loading plate widths was obtained (Fig. 2.44a). Lantsoght *et al.* (2015a) reported a 40% load capacity increase in 2.5 m wide slabs when the loading plate was increased from 200 x 200 mm to 300 x 300 mm. For elements with a width of 2.0 meters, the average increase in capacity was 24.2% when applying a bigger loading plate. For elements of 1.0 m or 1.5 m in width the average increase was under 1%. If the effective width is accepted to be related to the size of the loading plate, these results can be explained by the limited element width. When the load plate is wider, the effective width increases, but this increase is limited by the actual width of the element. When the element width is not limiting, the effective width can increase further (Fig. 2.52). The size of the loading area also influences the failure mode. Wider loading plates usually lead to shear failures, whereas narrower plate may lead to a punching-shear failure (Fig. 2.47).

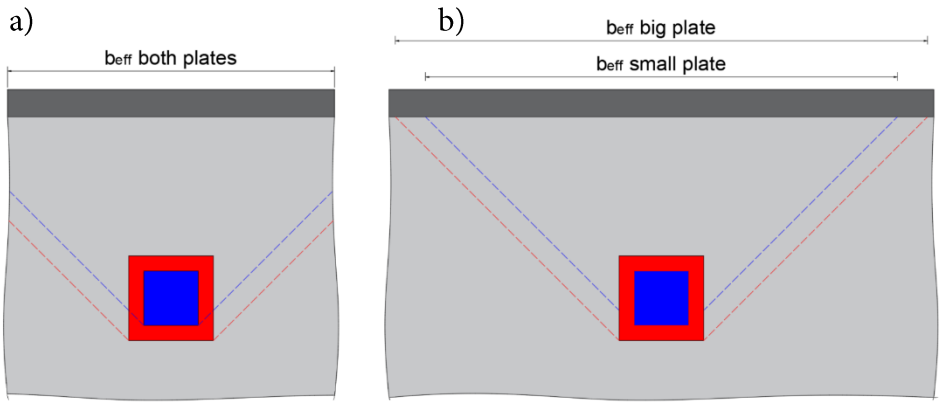

Figure 2.50: a) Effective width in strip limited by the element width; b) Effective width in slab not limited by element width.

Support conditions

The type and the conditions at the support influence the shear strength and the failure mode. Slabs supported on isolated columns are very likely to fail in punching-shear, even if they are one-way slabs (Sagaseta *et al.* 2011). Wide beams or slabs may be also supported along the full width or only along a part of it. Lubell *et al.* (2008) investigated the effect of the element width to support width ratio on the shear capacity and concluded that the ultimate load decreases when the supported width is narrower than the width of the member. The degree of rotational restraint at the support is also an important factor. Islam *et al.* (1998) tested a significant amount of beams with different concrete strength f_c and reinforcement ratio ρ, using a test configuration that allowed to apply different degrees of restraint at the considered support. It was observed that, regardless the value of f_c or ρ, the presence of a contraflexure point within the shear span could increase the capacity of a beam by as much as 100%. The maximum increase occurred in all cases when the contraflexure point was at the middle of the shear span (Fig. 2.53). The contraflexure point within the shear span provokes that the critical shear crack cannot start close to the support nor close to the point load, since the top and bottom fibers respectively at this sections are compressed. Thus, this phenomenon may be seen as if the contraflexure point divides the shear span into two shorter shear spans, and it is this shortening which leads to the increase in the shear strength.

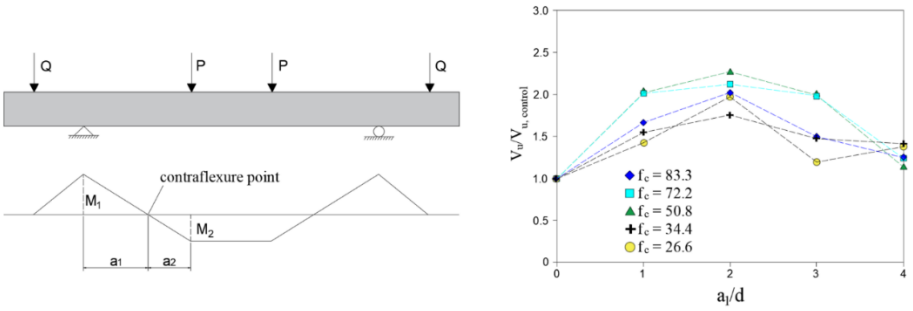

Figure 2.53: Effect of the position of the contraflexure point on the shear strength. Adapted from Islam *et al.* (1998).

Reissen *et al.* (2017) conducted a similar study in one-way slabs supported on two opposite sides. Beginning with simply supported, single-span slabs, the rotational restraint at the closest support to the load was stepwise increased to a 100%, representing a fully clamped support, for different a/d ratios. No influence of the degree of restraint was found for medium and large shear-span-to-depth ratios (a/d = 4.2 and 5.4 respectively). In these two cases the shear strength of the tests remained almost constant. However, for a/d = 2.9, the highest capacity was attained for the point of contraflexure lying in the middle of the distance between the load and the support (degree of rotational restraint of 50%).

2.3.4.2 Rational models

As have been commented in the previous sections, the usual way to proceed when assessing the shear strength of a one-way slab is to use the shear provisions developed for beams replacing the web width b_w of the beam by the shear effective width of the slab. When the point loads are applied far from the support, the punching-shear strength is usually assessed by means of mechanical models developed assuming axis-symmetrical conditions. However, throughout the last decades, some rational models have been developed for intermediate situations that may be suitable for the shear assessment of one-way slabs. Some of them are presented in this section.

Regan's model

P.E. Regan (1982) developed a pseudo-empirical model for the calculation of the punching-shear strength of one-way slabs under concentrated loads close to supports ($a_v/d_l \leq 2$). It was based on the definition of a critical perimeter around the concentrated load (Fig. 2.54). The punching-shear strength P_R is given by:

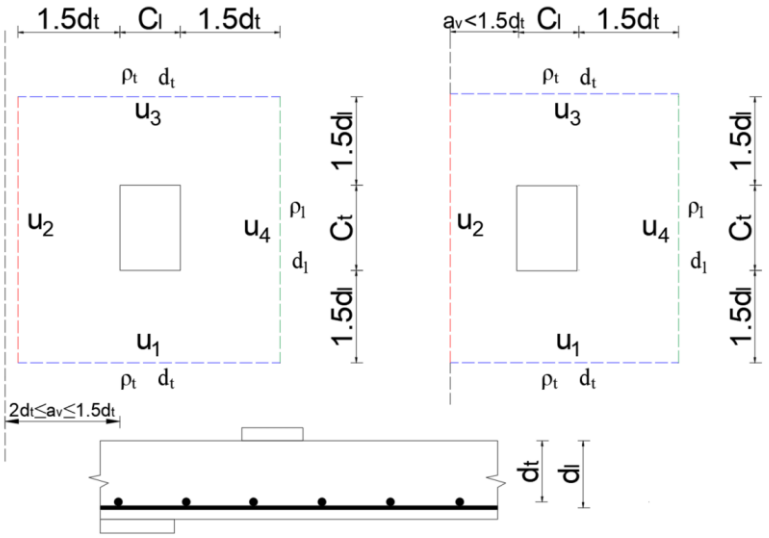

Figure 2.54: Regan's Model. Adapted from Regan (1982).

$$P_R = P_{R1} + P_{R2} \tag{2.95}$$

$$P_{R1} = \sum_i \zeta_s v_c u_i d_i \quad i = 1, 3, 4 \tag{2.96}$$

$$P_{R2} = \left(\frac{2d}{a_v}\right) \zeta_s v_c u_2 d < \frac{\sqrt{f_{cube}}}{\gamma_m} u_2 d \tag{2.97}$$

Where:

- P_{R2} is the shear resistance of the part of the control perimeter faced to the closest support (u_2).
- P_{R1} is the sum of the shear resistance of the remaining parts (u_1, u_3 and u_4) of the perimeter.

- a_v is the clear shear span between the load and the support.
- ζs is a size effect factor: $\zeta_s = \sqrt[4]{500/d}$.
- v_c is the maximum shear stress of concrete, based on the British standard in force at that time: $v_c = \frac{0.27}{\gamma_m}\sqrt[3]{100\rho f_{cube}}$.
- u_i is the length of the part of the perimeter considered (i= 1, 2, 3, 4).
- γ_m is the partial material safety factor.
- f_{cube} is the concrete cube compressive strength.
- d is the average effective depth of the slab: $d = \frac{d_t+d_l}{2}$.
- ρ is the average reinforcement ratio of the slab: $\rho = \frac{\rho_t+\rho_l}{2}$.
- d_l, d_t, ρ_l, ρ_t, are the longitudinal and transverse effective depth and reinforcement ratio respectively, used depending on which part of the perimeter is considered.

In case of a continuous support, Regan incorporated the effect of the degree of restraint by multiplying the punching shear capacity P_R by a factor α given by the following expression, where M_1 represents the positive bending moment under the point load and M_2 the negative bending moment at the support.

$$\alpha = \sqrt{\frac{M_1 + M_2}{M1}} \tag{2.98}$$

Critical Shear Crack Theory (CSCT)

The Critical Shear Crack Theory (Muttoni 2008b) is a mechanical model for the assessment of the axis-symmetric punching-shear strength of RC slabs without shear reinforcement. This model was subsequently extended to the case of non-axis-symmetrical conditions (Sagaseta *et al.* 2011). In a similar way than the CSCT for shear in beams, the CSCT considers that after the development of the critical shear crack, the response of a member is controlled by a direct strut whose ultimate strength is closely related to the aggregate interlock. As the critical crack widens, the strut deviates to avoid flexural cracks while the aggregate interlock capacity decreases, ultimately leading to punching-shear failure (Fig. 2.55a). The crack width is assumed to

be proportional to the product ψd, where ψ is the rotation of the slab. After analyzing a database of almost 100 punching tests from literature (Fig. 2.55b), the analytical expression for the failure criterion was derived (Eq. (2.99)), where b_0 is the length of the control perimeter at a distance $0.5d$ from the column face and d_g is the maximum aggregate size. Punching failure occurs at the intersection of the failure criterion with the load-rotation (V-ψ) curve of the slab. The load-rotation curve of a slab may be predicted by using a non-linear finite element analysis or estimated by the simplified expression given by Eq. (2.100), where r_s is the radius of the circular isolated slab element ($r_s \approx 0.22L$, where L is the span of the slab) and V_{flex} is the value of the load that causes the yielding of the reinforcement.

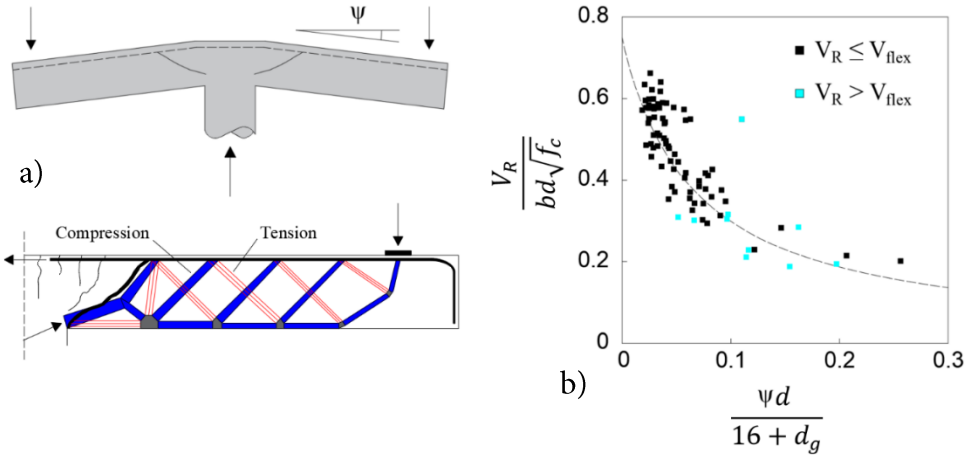

Figure 2.55: CSCT for axis-symmetric punching-shear: a) elbow-shaped strut; b) Failure criterion. Adapted from Muttoni (2008).

$$\frac{V_R}{b_0 d\sqrt{f_c}} = \frac{3/4}{1 + 15\frac{\psi d}{16 + d_g}} \tag{2.99}$$

$$\psi = 1.5\frac{r_s}{d}\frac{f_y}{E_s}\left(\frac{V}{V_{flex}}\right)^{3/2} \tag{2.100}$$

Sagaseta *et al.* (2011) presented a new approach to account for the shear redistributions along the control perimeter due to non-axis-symmetrical conditions, the so called CSCT(ψ_x - ψ_y) method. In this situation, the slab rotations depend on the considered direction and are uneven along the

control perimeter. This means that some parts of the slab reach their ultimate shear strength while others still have a potential shear capacity. However, this do not imply the collapse of the slab, as the areas that reached its ultimate strength develop a softening process (side A of Fig. 2.56a) while others continue increasing their shear force (side B of Fig. 2.56a), as was observed experimentally. This redistribution results in higher punching shear strengths and higher rotations when compared with the CSCT(ψ_{max}) method, which in a conservative approach only considers the load rotation curve of the weakest reinforced direction, provided that the shear increase in side B balances the shear softening in side A.

Based on these considerations, in a simplified way, the control perimeter is divided into four segments (Fig. 2.56b), assuming constant rotations ψ_x - ψ_y and unitary shear strengths v_{Rx} - v_{Ry} for each segment, so the punching shear strength V_R is given by:

$$V_R = \frac{V_{Rx}}{b_0} b_x + \frac{V_{Ry}}{b_0} b_y \tag{2.101}$$

Where V_{Rx} and V_{Ry} are calculated according to the CSCT using the corresponding load rotation curves and $b_0 = b_x + b_y$. Lengths b_x and b_y are generally taken as $b_0/2$ in square columns, but reduced lengths are recommended of b_x and b_y if the punching load is close to the flexural load, as wide crack opening may limit the redistribution capacity of the slab, with a minimum value equal to twice the length corresponding side of the loading plate.

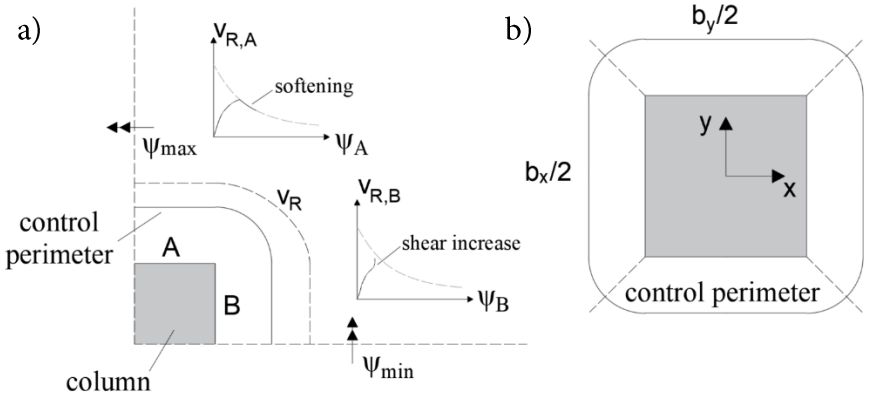

Figure 2.56: CSCT(ψ_x - ψ_y) for non-axis-symmetric punching-shear: a) shear redistributions; b) discretization of control perimeter. Adapted from Sagaseta *et al.* (2011).

The (Modified) Bond Model

The Bond Model (Alexander and Simmons 1992) was originally develop for concentric punching shear. It is a mechanical model that combines radial arching action and the concept of a critical shear stress, as used for beam shear. Shear results where the magnitude of the tension in the reinforcement T or the lever arm z varies along the length of the member, as shown in Fig. 2.7 and Eq. (2.4). Based on experimental observations, the arching action is considered to be the dominant mechanism in the radial direction, so it was assumed that the load is distributed in the radial directions from the column in strips working by arching. Four strips branching out from the column and parallel to the reinforcement are considered, separating the column from the slabs quadrants (Fig. 2.57a).

These strips are loaded in shear on their side faces only and are considered as cantilever beams, fixed into the column (Fig. 2.57b). These cantilevers have negative and positive moment capacities of M_{neg} and M_{pos} that are summed into M_s, the total flexural capacity of the strip. The length l_w is the loaded length of the strip, and the loading term q is an estimate of the shear that can be delivered by the adjacent quadrant of the slab to one side face of the strip. For a strip with two side faces, the total uniformly distributed load on the strip is $2q$. Using force and moment equilibrium of the cantilever strip results in the following expressions for the total flexural capacity M_s and the concentrated load at the column $P_{AS,1}$. To find the maximum capacity of the slab P_R, the contribution of the four strips are added. The maximum value of the loading term q was set after a parametrical analysis based on the inclined cracking load given in ACI 318 codes.

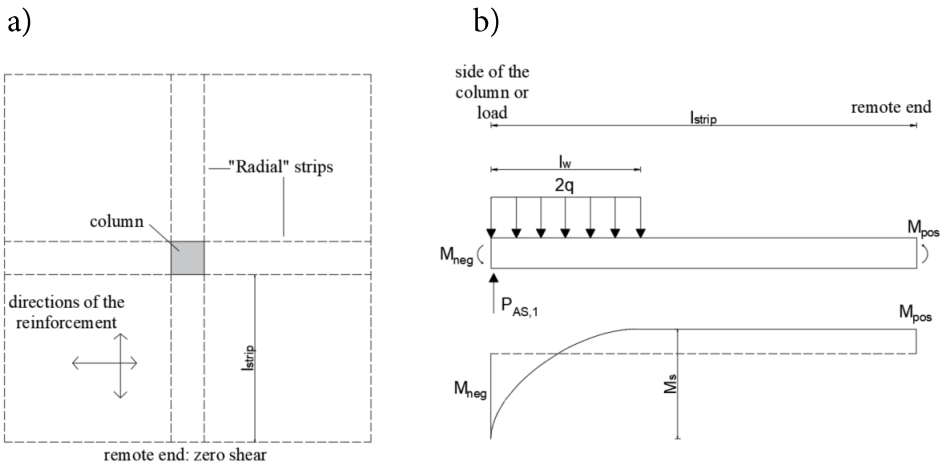

Figure 2.57: Bond Model for axis-symmetric punching-shear: a) slab-column connection: division into radial strips and quadrants; b) loading of a strip over loaded length l_w and resulting moment diagram. Adapted from Alexander and Simmons (1992).

$$M_s = \frac{2ql_w^2}{2} \tag{2.102}$$

$$P_{AS,1} = 2ql_w = 2\sqrt{M_s q} \tag{2.103}$$

$$P_R = 4 \cdot P_{AS,1} = 8\sqrt{M_s q} \tag{2.104}$$

$$q_{ACI} = 0.1667 d\sqrt{f_c}; \quad (q \text{ in } {}^{kN}/_{m} \text{ and } f \text{ in } MPa) \tag{2.105}$$

This model was extended to the case of one-way slabs subjected to concentrated loads close to supports (Lantsoght 2013a). For the x-direction strip between the concentrated load and the support (Fig. 2.58), direct transfer of the load from its point of application to the support needs to be taken into account. Based on the Regan's model, the capacity of this side of the punching perimeter parallel to the closest support was enhanced by a factor $2d_x/a_v$, in which d_x is the effective depth of the reinforcement in the x-direction and a_v is the face-to-face distance between the load and the support. The different shear transferred to the closest support than to the farthest support was also taken into account. If v_{2x} reaches the inclined cracking load q_{ACI} failure of the section is reached. At that moment, the shear at v_{1x} will be less. The ratio between the shears v_{1x} and v_{2x} at the strip is given by Eq. (2.106). As a result, the total load on the y-direction strip at failure is given by Eq. (2.107). Following similar assumptions than in the original Bond Model, the capacity

of the strips P_{y1}, P_{y2}, P_x and P_{sup} (Fig. 2.58) is obtained, so the total capacity is given by the sum of the capacities of the strips.

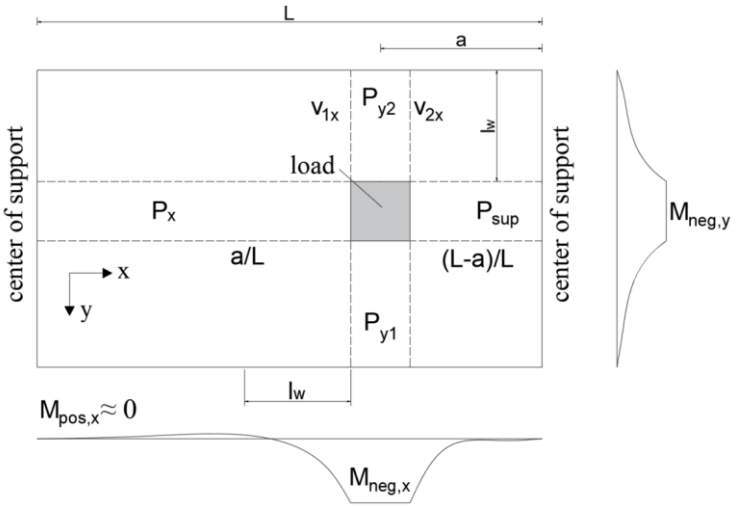

Figure 2.58: Modified Bond Model for one-way slabs under concentrated loads close to support. Adapted from Lantsoght (2013a).

$$\frac{v_{1x}}{v_{2x}} = \frac{a}{L-a} \tag{2.106}$$

$$v_{1x} + v_{2x} = \left(1 + \frac{a}{L-a}\right) q_{ACI} = \frac{L}{L-a} 0.1667 d_x \sqrt{f_c} \tag{2.107}$$

$$P_{y1} = P_{y2} = (v_{1x} + v_{2x}) l_w = \sqrt{2M_{neg,y}(v_{1x} + v_{2x})} \tag{2.108}$$

$$P_x = 2\sqrt{2M_{neg,x} \cdot 0.1667 d_y \sqrt{f_c}} \tag{2.109}$$

$$P_{sup} = \frac{2d_x}{a_v} 2\sqrt{2M_{neg,x} \cdot 0.1667 d_y \sqrt{f_c}} \tag{2.110}$$

The Modified Bond Model was extended to be suitable for loads applied close to a continuous support, in which the negative moment reinforcement can increase the total flexural capacity. As the positive and negative moment capacities are not activated in the same cross-sections of the strips and because yielding of the hogging reinforcement is not assumed in the model,

the following expression is proposed to take into account the effect of the negative moment reinforcement:

$$M_s = M_{neg} + \lambda M_{pos} \tag{2.111}$$

$$\lambda = \frac{M_1}{M_2} \leq 1 \quad (see\ Fig.\ 2.53) \tag{2.112}$$

The factor λ ranges from 0 (no restrain) to 1 (full restrain). When the concentrated load is placed close to a continuous support, two quadrants experience the change in moment from hogging moment M_1 to sagging moment M_2. As a result, the combined effect of the top and bottom reinforcement should be taken into account on the three strips that border these two quadrants. The resulting strip capacities are then:

$$P_{y1} = P_{y2} = \sqrt{2M_{s,y}\frac{L}{L-a}0.1667 d_x \sqrt{f_c}} \tag{2.113}$$

$$P_x = 2\sqrt{2M_{neg,x} \cdot 0.1667 d_y \sqrt{f_c}} \tag{2.114}$$

$$P_{sup} = \frac{2d_x}{a_v} 2\sqrt{2M_{s,x} \cdot 0.1667 d_y \sqrt{f_c}} \tag{2.115}$$

The Compression Chord Capacity Model for axis-symmetric punching (CCCM-Punching)

As part of the collection of mechanical models developed at the UPC, the CCCM-punching (Marí *et al.* 2018) is a mechanical model for the prediction of the punching-shear strength of RC flat slabs with and without shear reinforcement under concentric loading. Since this model is used as a starting point for some of the work presented in this thesis, its development and application for RC slabs without shear reinforcement are explained in detail in this section. This punching-shear model is an adaption of the MASM and the CCCM (see section 2.3.3.6), in which the relevant differences between shear in beams and axis-symmetric punching-shear in slabs have been identified and accounted for into the governing equations and into the failure criteria.

Phenomenology

If a RC flat slab without shear reinforcement supported on an interior isolated column is considered (Fig. 2.59a), two families of orthogonal bending moments, m_r producing radial stresses, and m_φ producing tangential stresses, take place around the column. The normal stresses, σ_r and σ_φ, produced respectively by both families of moments, compress the bottom and stretch the top of the slab. When these stresses exceed the concrete tensile strength f_{ct}, flexural cracks, noticeable normal and parallel to the column perimeter, appear. Under increasing load, damage tends to concentrate in a tangential crack that develops inclined through the slab depth, crossing the compressed chord and reaching the slab bottom at its intersection with the column face, thus producing a punching-shear failure. Along the loading process, redistributions between radial and tangential bending moments take place due to changes in the stiffness produced by cracking and eventually yielding of the flexural reinforcement.

An important aspect is that the concrete placed at the bottom of the slab is compressed by both the radial and tangential moments. Furthermore, in the vicinity of the column, the slab is also subjected to vertical compressive stresses, since the forces transmitted from the slab to the column concentrate on the column periphery, which enhances the capacity of this region to resist shear stresses (Fig. 2.59b).

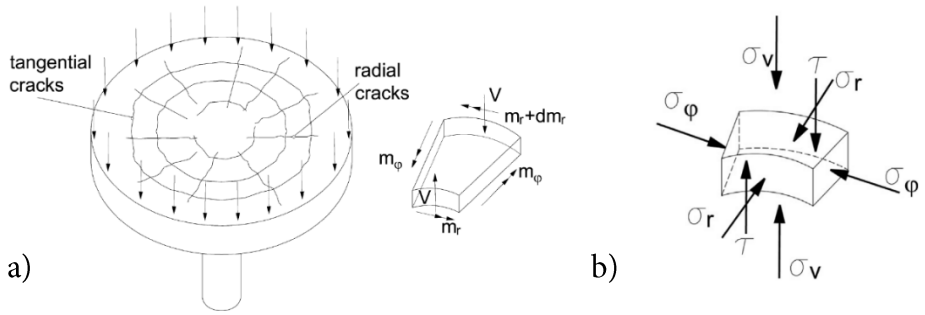

Figure 2.59: Punching-shear around an internal column: a) cracking and internal forces; b) Stress state in the compression zone in the vicinity of the column. Marí *et al.* (2018).

Position and inclination of the critical crack

In a slab supported on isolated columns, the radial bending moment per unit width law $m_r(r)$ is different than that of the bending moments in a beam or a one-way slab. As a result, the distance from the column face to the point where $m_r(r)$ reaches the cracking moment, which is considered the section where the critical crack initiates, is generally less than $1.5d$, so the compressed concrete zone of the slabs lies close enough to the column to be considered a D-region (Fig. 2.60). In addition to that, the previously mentioned vertical compressive stresses makes the critical crack inclination steeper than in beams so that unlike what happens in slender beams or one-way slabs, the punching critical crack around a column follows almost and straight path from its initiation to the intersection of the bottom of the slab with the column face. Then, the perimeter where the critical crack reaches the compression zone of depth x (Fig. 2.60), the so-called critical perimeter, will be placed at a distance s_{crit} from the column face, given by:

$$s_{crit} = x \cdot \cot\theta = s_{crack} \cdot \frac{x}{d} \quad (\cot\theta \leq 2.5) \tag{2.116}$$

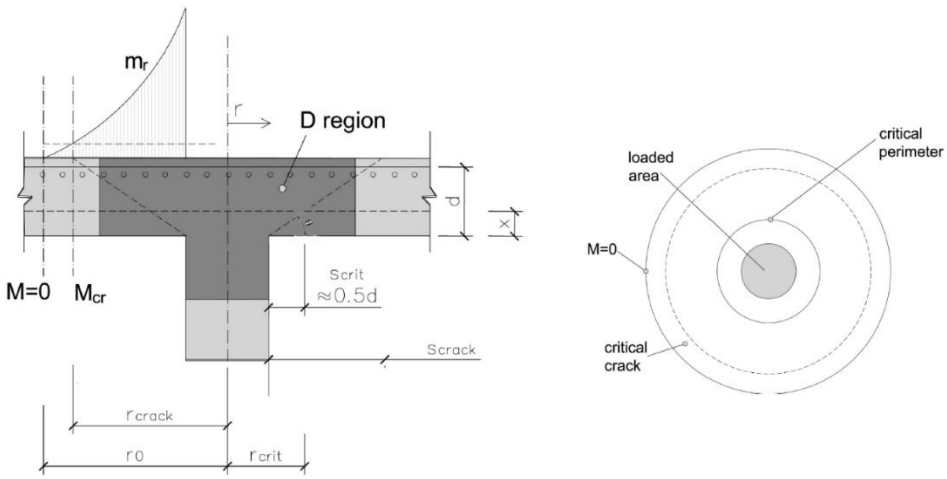

Figure 2.60: Position of the critical crack and the critical perimeter. Marí *et al.* (2018).

According to the elastic theory of plates (Timoshenko and Woinowsky-Krieger 1959), for a simply supported circular slab of radius r_0, subjected to a concentrated load V on its center, $m_r(r)$ is given by Eq. (2.117), where ν is

Poisson's coefficient. If, for the particular case of a slab supported on an isolated column, r_0 is considered to be the distance from the column axis to the point of zero radial bending moment, the position of the critical perimeter can be obtained by equaling $m_r(r)$ to the cracking moment per unit width m_{crack} and taking into account the geometrical assumptions for the inclination of the crack. The position of the critical perimeter is then given by Eq. (2.118).

$$m_r(r) = \frac{V}{4\pi}(1+\nu) ln\left(\frac{r_0}{r}\right) \tag{2.117}$$

$$\frac{s_{crit}}{d} = \frac{s_{crack}}{d}\frac{x}{d} = \frac{r_{col}}{d}\left(\frac{r_0}{r_{col}} e^{\frac{-4\pi m_{crack}}{V(1+\nu)}} - 1\right)\frac{x}{d} \tag{2.118}$$

Since for design purposes it is desirable a simpler way to define the position of the critical perimeter, Eq. (2.118) was evaluated using a database of over 500 axis-symmetric punching tests, obtaining values of s_{crit} between $0.4d$ and $0.7d$. The slabs with higher values of s_{crit}/d are those with lower ratio d/u_0, where u_0 is the perimeter of the column, and higher reinforcement ratios, since the cracking moment is smaller due to the lower effective depth and the relative neutral axis depth x/d is higher. However, in order to avoid flexural failures, the longitudinal reinforcement ratio in tests is greater than usual in practice, so as a conservative assumption, the distance from the critical perimeter to the side of the column adopted was $s_{crit} = 0.5d$, which is in line with the punching provisions of ACI code (ACI Committee 318 (2019)) and Model Code 2010 (CEB-*fib* 2010)

Effect of the multi-axial stress state in the slab compressed chord

Vertical stresses σ_z in the vicinity of the column enhance the capacity of the concrete of the compression zone to resist shear, as indicated in Eq. (2.66). Note that in general, in axis-symmetric problems, *r-z* plane is used, whereas in 2D planar problems, *x-y* plane is used. In order to estimate the value of the vertical stresses, a parametric numerical study was conducted, varying the d/u_0 ratio and the reinforcement ratio ρ. It was obtained that the maximum vertical stress between the column face and the critical perimeter ranged between 1.25 and 1.50 times the average vertical stress in the area enclosed by the critical perimeter. Then, a value of 1.25 was adopted so the vertical stresses

in concrete are given by Eq. (2.119), where $v = V/(u_{crit} \cdot d \cdot f_{ct})$ is the non-dimensional shear resisted by the concrete.

$$\frac{\sigma_z}{f_{ct}} = 1.25 \frac{V}{f_{ct} \pi r_{crit}^2} = 2.5 \frac{v}{r_{crit}/d} \tag{2.119}$$

Normal stress σ_φ is estimated assuming that it is proportional to the radial stress, as the slab is cracked in both radial and tangential directions and the reinforcement ratios in both orthogonal directions are similar in interior columns with similar span lengths. Then, the tangent normal stress can be obtained by multiplying the radial stress by the ratio between the tangential and the radial moments m_φ / m_r:

$$\frac{\sigma_\varphi}{\sigma_r} \approx \frac{m_\varphi}{m_r} = \frac{\frac{V}{4\pi}\left[(1+\nu) ln \frac{r_0}{r} + 1 - \nu\right]}{\frac{V}{4\pi}\left[(1+\nu) ln \frac{r_0}{r}\right]} = 1 + \frac{1-\nu}{(1+\nu) ln \frac{r_0}{r}} \tag{2.120}$$

A value of $r_0 = 0.15L$ was adopted, which takes into account the redistribution of radial bending moments due to cracking and partial yielding of the reinforcement. Considering $\nu = 0.3$ and common values for the distance between interior columns L, a conservative value of $m_\varphi / m_r = 1.5$ can be estimated.

Both tangential stresses σ_φ and vertical stresses σ_z confine the concrete in the tangential-vertical (φ-z) plane, thus increasing its compressive strength in the radial direction. However, the effect of such confining stresses is moderate, since a tri-axial compressive stress is never reached, because the normal stresses in the bottom region of the slab are always accompanied by shear stresses, generating always a tensile principal stress. Consequently, failure will take place in a compression-compression-tension state of principal stresses (Fig. 2.61a). In order to account for this phenomenon, a modified tension-compression branch of the Kupfer's (Kupfer and Gerstle 1973) biaxial failure envelope is adopted (Fig. 2.61b), in which the confined concrete compressive strength f_{cc} is used instead of the regular compressive strength f_c, so that a higher shear stress is needed to reach failure. The Eurocode-2 (EN-CEN 2005) provision for f_{cc} is adopted (Eq. (2.121)), where for the confinement stress σ_{cc} the mean value between the vertical and tangential stresses is used.

$$f_{cc} = f_c\left(1.125 + 2.5\frac{\sigma_{cc}}{f_c}\right) \quad if \ \frac{\sigma_{cc}}{f_c} \geq 0.05 \tag{2.121}$$

$$\sigma_{cc} = \frac{\sigma_\varphi + \sigma_z}{2} \tag{2.122}$$

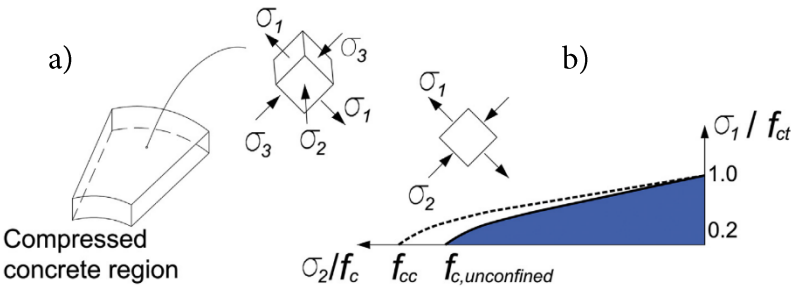

Figure 2.61: a) Principal stresses at the uncracked slab region: b) modified Kupfer's biaxial failure envelope. Marí *et al.* (2018).

Equilibrium and design equations

From the equilibrium of a portion of the slab around the column shown in Fig. 2.61, the radial normal stress can be related to the forces acting in the free body by considering the equilibrium of moments at point A (Eq. (2.123)), where the differential term $m_\varphi \cdot d\varphi \cdot \beta d$ can be neglected. Following the original assumption of the MASM of a linear behavior in the uncracked concrete zone, the radial stress at the point of maximum damage is then given by Eq. (2.124). The distance βd is the horizontal projection of the first branch of the critical crack. According to the assumptions made, it is equal to $0.5d(d-x)/x$, being x the neutral axis depth. V_w represents the resultant of the residual stresses crossing the crack and can be calculated using the simplified expression given by Eq. (2.68). Its point of application is close to the crack tip, so the distance $\beta_w d$ to the crack initiation is slightly lower than βd. $\beta_w d = 2/3\beta d$ was conservatively adopted. Following the iterative procedure detailed in the explanation of the MASM (section 2.3.3.6), the value of the shear resisted in the compression zone V_c can be obtained. Note that σ_x, σ_y and b must be replaced by σ_r and σ_z and u_{crit} (length of the critical perimeter) in the set of equation provided for the MASM to fit the notation of the CCCM-punching.

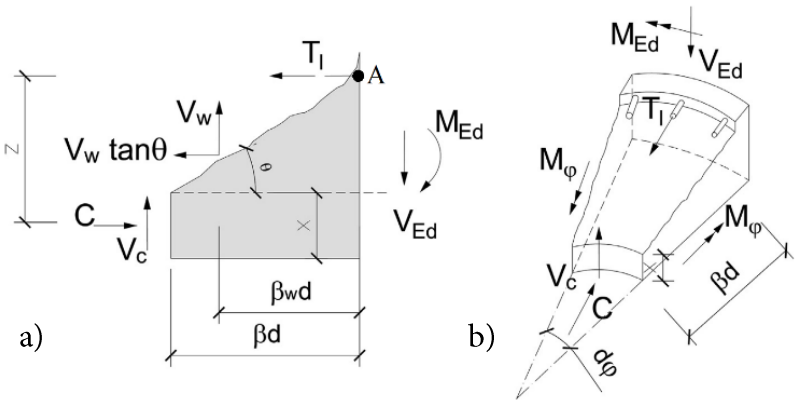

Figure 2.62: a) Forces in a portion of the slab above the critical crack. Marí *et al.* (2018).

$$Cz + d\varphi \cdot m_{\varphi} \cdot \beta d = m_{crack}\frac{r_{crack}}{r_{crit}} + V_c\beta d + V_w\beta_w d(\tan\theta + \cot\theta) \quad (2.123)$$

$$\sigma_r(\lambda) = \frac{2\lambda C}{xz} = \frac{2\lambda\left(m_{crack}\frac{r_{crack}}{r_{crit}} + V_c\beta d + V_w\beta_w d(\tan\theta + \cot\theta)\right)}{x\left(d - {}^{x}/_{3}\right)} \quad (2.124)$$

According to the equilibrium of vertical forces, the total shear resisted is equal to the addition of V_w and V_c, which have to be scaled by a factor ζ (Eq. (2.76)) that takes into account the size effect $V_R = (\zeta \cdot V_c + V_w)$. The shear span a, to be used in the size effect parameter, can be estimated as the average distance from the position of the line of zero radial bending moment to the edge of the column. This model neglects dowel action contribution V_l in specimens without shear reinforcement due to spalling of the concrete cover.

The maximum punching-shear capacity is always limited by the yielding of the reinforcement, which may occur for reinforcement ratios less than 0.75% approximately (Fig. 2.50). Due to the internal redundancy of slabs, when yielding in the tangential direction occurs, a redistribution of moments take place. Assuming perfect plasticity, the radial moment will also reach the plastic moment under increasing load. The associated load V_y can be obtained in a simplified way considering $\nu = 0.3$, $r_0/r_{crit} = 5$ and using the rectangular diagram for the concrete in compression (Eq. (2.126)).

$$m_r = \frac{V}{4\pi}\left[(1+\nu) ln \frac{r_0}{r}\right] \approx \frac{V_y}{2\pi} = m_y = \rho f_y d^2 \left(1 - \frac{\rho f_y}{2 f_c}\right) \quad (2.125)$$

$$V_R = (\zeta \cdot V_c + V_w) \leq V_y \approx 2\pi \rho f_y d^2 \left(1 - \frac{\rho f_y}{2 f_c}\right) \quad (2.126)$$

After a parametric study, V_c resulted to be an almost linear function of the relative neutral axis depth x/d, the tensile concrete strength f_{ct}, the effective depth of the slab d and the column dimensions (through the critical perimeter u_{crit}). A simplified expression for the punching-shear strength was derived assuming average values of the material properties and a conservative minimum value of $\nu_w = V_w/(f_{ct} \cdot u_{crit} \cdot d) = 0.05$:

$$V_R = (\zeta \cdot V_c + V_w) = \zeta \left(1.125 \frac{x}{d} + 0.425\right) f_{ct} u_{crit} d \quad (2.127)$$

For slabs, where both the depth and reinforcement ratio are small, the portion of shear transferred along the crack is higher than in the case of beams, as x/d is small and ν_w is inversely proportional to the effective depth d. Therefore, similarly to what was done in the CCCM for beam shear, a minimum punching strength was defined, that incorporates a simplified form of the component ν_w, to explicitly account for the slab depth, and in which the neutral axis depth is limited to $x/d = 0.20$ to be consistent with the initial assumption.

$$V_R \geq V_{min} = (\zeta \cdot V_c + V_w) = \left[\zeta (1.125 k_c + 0.375) + \frac{10}{d_0}\right] u_{crit} d \quad (2.128)$$

where $k_c = x/d \leq 0.2$ and $d_0 = \max(d; 100)$.

This model has been extended to eccentric loads (Fourtsadakis 2020) and to steel fiber reinforced concrete (SFRC) slabs without shear reinforcement (Rodriguez-Serrano 2021).

2.4 Effects of in-plane tensile stresses on the shear capacity of RC elements

Reinforced concrete slabs are structural components widely used in both bridges and buildings, due to their great versatility and ease of construction. These structural elements are mainly subjected to bending and shear, but in some cases in practice, in-plane tensile stresses may arise and act simultaneously with the out-of-plane design loads. For instance, this situation may arise in top slabs of box girder bridges subjected to hogging bending moments, decks of tied arch bridges, floor slabs under seismic loads, restrained shrinkage or thermal effects, etc. The effect of tension on the shear strength of reinforced concrete elements has not been exhaustively studied throughout the last decades, but it is gaining attention within the last years.

First widely known studies on the effect of tension on the shear strength of RC elements were carried out in the United States, after the partial collapse of a military warehouse in 1955 commented in section 2.2.2. As part of the investigation conducted after that event (Elstner *et al.* 1957), two rectangular beams without stirrups were tested in shear subjected to tension in the spanning direction, showing up to a 50% shear strength reduction for an axial tensile stress of 1.4 MPa in comparison with the control specimens tested without tension (Fig. 2.63c). The tested specimens were not heavily reinforced, having a flexural reinforcement ratio of 0.42%. Due to such a small amount of longitudinal reinforcement, the post-cracking capacity was very low and failure occurred soon after first cracks formed. In the next decade, similar experiments were conducted at the University of Washington. (Mattock 1969) studied the influence of the shear span to depth ratio a/d, reinforcement ratio ρ and concrete compressive strength f_c on the shear strength of rectangular RC beams subjected to axial tension. As can be seen in (Fig. 2.63a), a clear trend was not observed but in general grater reinforcement ratios leaded to greater shear capacities.

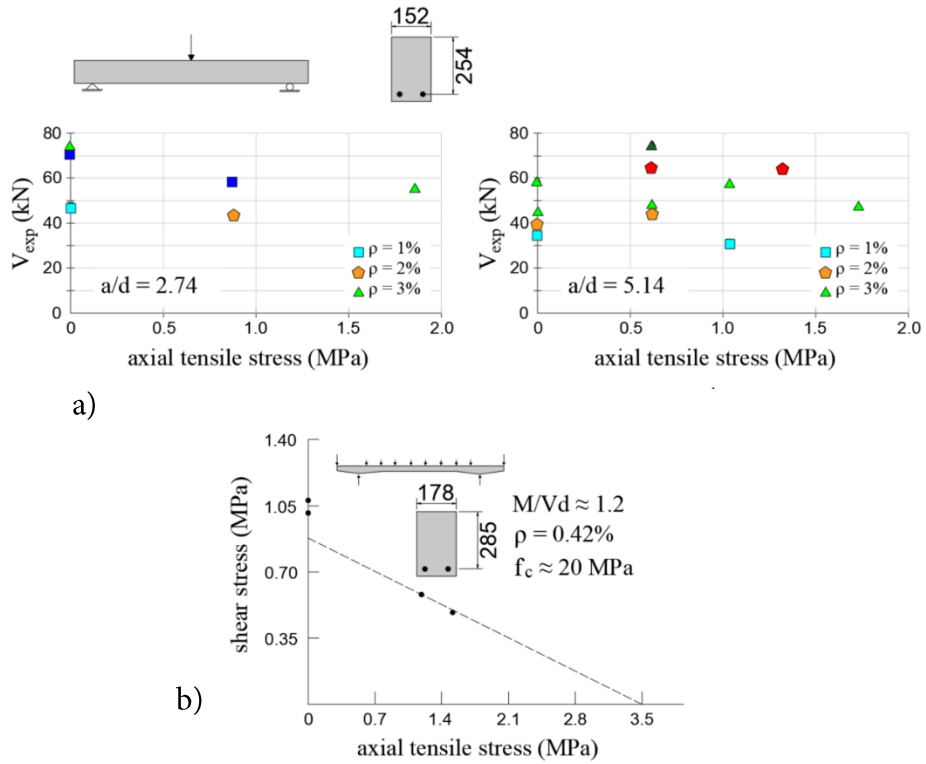

Figure 2.61: Experimental shear strength as a function of the axial tensile strength. a) Mattock *et al.* (1969) (Light color → $f_c \approx$ 30MPa; dark color → $f_c \approx$ 60MPa); b) Elstner *et al.* (1957).

Two years later, Haddadin *et al.* (1971) studied the effectiveness of the shear reinforcement in T-beams subjected to axial tension, concluding that it does not reduce the contribution of the stirrups to the shear strength. Tests were conducted in simply supported and partially restrained beams, but no significant difference on the shear behavior was observed. It is noticeable that, after the premature failure of one of the tested specimens subjected to tension, it was recommended that the shear carried by the concrete should be considered equal to zero if the normal tensile stresses were greater than $0.33\sqrt{f_c}$ (f_c in MPa). This recommendation was incorporated into the ACI-318 building code, in which the concrete contribution to the shear strength was reduced linearly to zero as tensile stresses on the member increase to 3.4 MPa. At the same time, in another investigation carried out at the Imperial College (Regan 1971), rectangular beams, with a longitudinal reinforcement ratio of 1.46% and $f_c \approx$ 30 MPa, subjected to different levels of tensile stresses,

showed a moderate reduction on the shear strength with increasing tension, with a 12% decrement for the maximum tensile stress of 2.6 MPa applied (Fig. 2.64). All these results started to highlight the importance of the amount of longitudinal reinforcement on the shear strength of RC elements subjected to axial tension. A greater amount of reinforcement leads to narrower cracks and deeper compression head for a particular tension level, which contribute to enhance the shear strength.

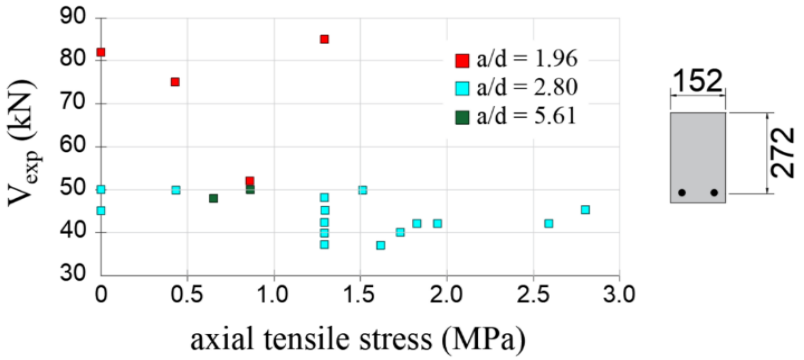

Figure 2.64: Experimental shear strength as a function of the axial tensile strength. Adapted from Regan (1971).

In the early 1980s, two experimental campaigns conducted at Cornell University (Abrams 1979; Jau *et al.* 1982) for the U.S Nuclear Regulatory Commission studied the effects of Biaxial tension on the punching-shear strength of RC slabs. Several 1200 x 1200 x 150 mm slabs with varying reinforcement ratios in the two orthogonal directions were tested up to punching failure for different values of in-plane biaxial tensile stresses. As can be seen in Fig. 2.65a, for slabs with greater reinforcement ratios, the punching strength was not significantly affected. Type-C slabs, which had the lowest reinforcement ratios (ρ_x = 1.36% and ρ_y = 0.77%), were the most affected by the external tension, with an average decrement close to 15% in the punching strength for an in-plane tensile stress about 2.5 MPa. In the same period of time, Regan (1983) presented the results of an experimental campaign on the punching-shear strength of one-way and two-way slabs subjected to unidirectional in-plane tensile forces (Fig. 2.65b). Slabs were symmetrically reinforced with a tensile reinforcement ratio of ρ = 1.3%. An average 15% decrement of the ultimate load for an in-plane tensile stress of 3.95 MPa was reported.

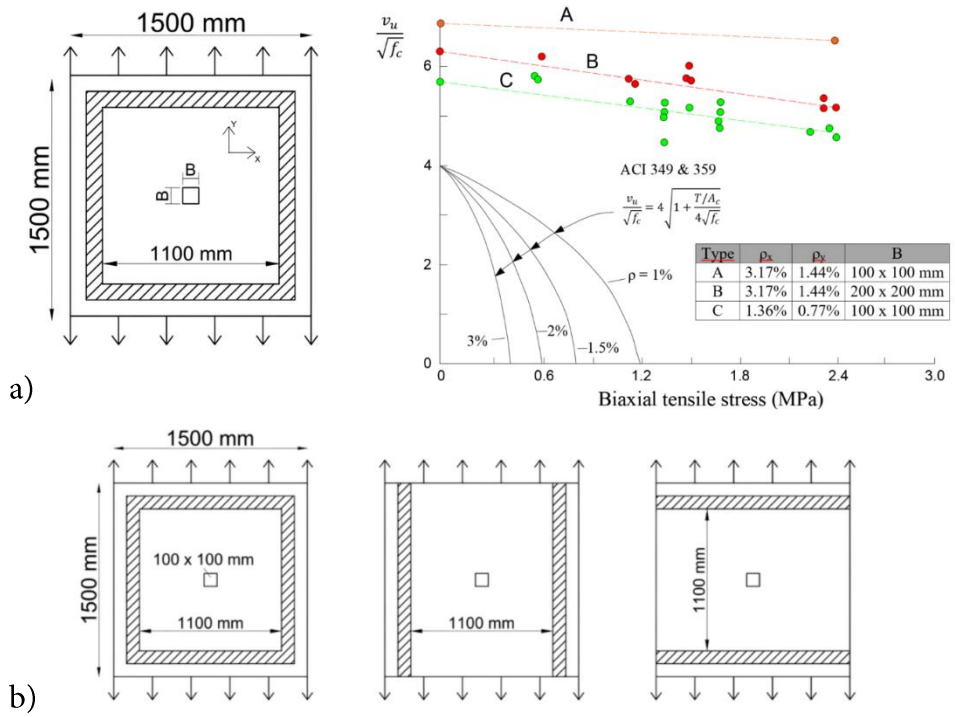

Figure 2.63: Punching test in slabs subjected to in-plane tension: a) Jau et al. (1982); b) Regan (1983).

In the late 1980s, as part of the validation of the Modified Compression Field Theory, an experimental campaign was carried out at the University of Toronto (Bhide and Collins 1989) where twenty-four square panels of 890 mm sides and 70 mm thickness were subjected to different combinations of in-plane shear v and tension σ_t. Panels were reinforced only in the longitudinal direction with a reinforcement ratio ρ_x of 1% or 2%, depending on the element, with the bars uniformly distributed along the element depth. It was experimentally observed, as the MCFT had predicted, that panels had considerable post cracking shear capacity provided that the longitudinal reinforcement ratio prevents excessive widening of the cracks (Fig. 2.66). Panels with ρ_x = 1% showed moderate influence of tension on the shear strength up to values of σ_t close to 2 MPa, decreasing from that point onwards, until reaching the uniaxial tensile strength of 4.5 MPa (Fig. 2.66a). Panels with ρ_x = 2% showed an average 20% decrement of the shear strength when $\sigma_t \approx 4.5$ MPa and a 37% when $\sigma_t \approx 7$ MPa (Fig. 2.66b), highlighting once again the

importance of the amount and distribution (the more uniform along the cross-section depth, the better) of longitudinal reinforcement.

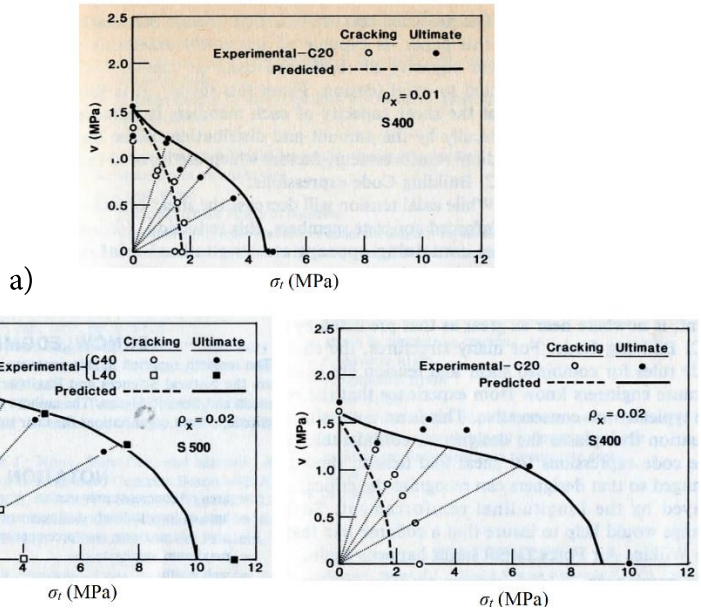

Figure 2.66: Comparisons of experimentally observed and analytically predicted shear-tension interaction diagrams: a) ρ = 1%; b) ρ = 2%. Bhide and Collins (1989).

Similar trends were observed in another two experimental campaigns carried out several years later at the same laboratory. (Adebar and Collins 1995) tested beam-like panels of 1600 x 310 x 290 mm with longitudinal reinforcement ratios ρ_x of 1% or 2% subjected to combined bending moment, shear and axial tension (Fig. 2.67). Xie *et al.* (2011) tested three panels equal to those tested by Bhide and Collins with ρ_x = 1.56%. A 5% decrement on the shear was obtained for a normal tensile stress of 3.04 MPa, whereas a 23% decrement was measured for $\sigma_t \approx$ 7.4 MPa.

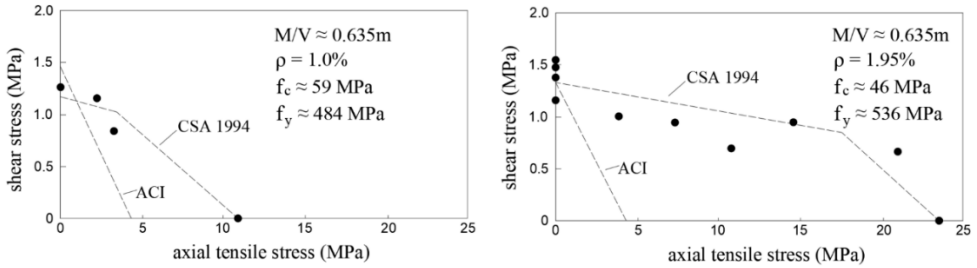

Figure 2.67: Influence of axial tension on the shear resistance of specimens without shear reinforcement. Adebar and Collins (1995).

More recently, laboratory tests were conducted at the Technical University of Denmark (Jorgensen *et al.* 2013) in beams reinforced symmetrically using high performance steel (f_y = 1027 MPa) with a longitudinal tensile reinforcement ratio ρ = 0.88%. Tested beams with a/d = 2.25 showed almost no influence of tension on the shear strength for tensile stresses up to 7.5 MPa and surprisingly only a 20% decrement for an average tensile stress of 13 MPa. Similar behavior was observed in beams with a/d = 2.75, which presented more scatter for values up to 8MPa and a moderate reduction for tensile stresses up to 13 MPa. Results, presented in Fig. 2.68a, were compared to the Eurocode-2 predictions, showing that for some of the tension levels applied, EC-2 predicts a total loss of shear capacity. The use of high-performance concrete (f_c > 75 MPa) has also been studied (Fernández-Montes *et al.* 2015) In this case, T-shaped beams with partial restraint to the rotation at the support were tested under the simultaneous action of shear and axial tension. Biggest decrements of the shear capacity were observed in high strength concrete beams (about a 33% decrement for longitudinal tensile stresses $\sigma_t \approx$ 2.5 MPa regardless the reinforcement ratio), whereas for normal concrete the loss of strength was more moderate (Fig. 2.68b). In all the specimens the longitudinal reinforcement was concentrated close to the tension face.

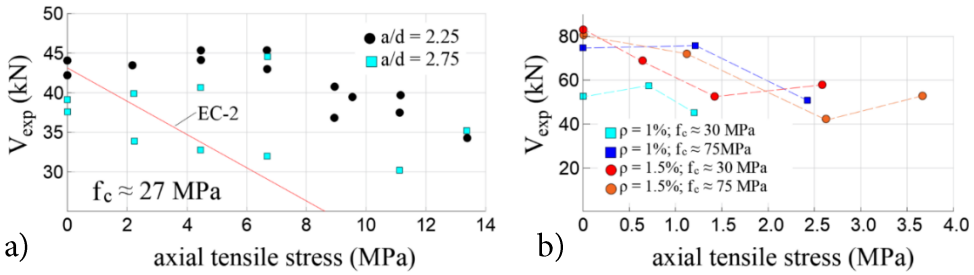

Figure 2.68: Influence of axial tension on the shear capacity: a) high performance steel (Jorgensen *et al.* 2013); b) high strength concrete. Montes *et al.* (2015).

First shear tests carried out in slabs subjected to uniaxial in-plane tension took place at the University of Lyon few years ago (Bui *et al.* 2017b) Slabs were simply supported on their four sides and subjected to a point load close to one of the supports. The external in-plane tension was applied perpendicular to that support (Fig. 2.69a). All the tested slabs, reinforced non-symmetrically with a tensile longitudinal reinforcement ratio of ρ = 1.22%, showed almost

no influence of the longitudinal tensile stress for σ_t up to 0.65 MPa. However, a significant average reduction of a 27% was observed for σ_t = 1 and 1.2 MPa (Fig. 2.69b).

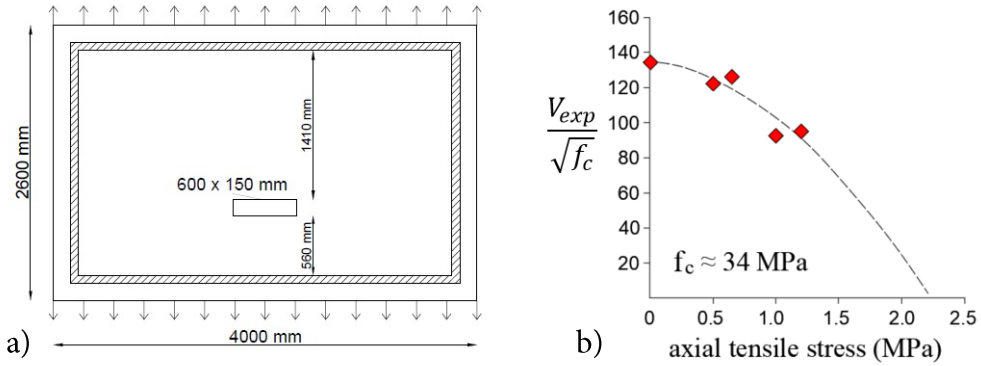

Figure 2.69: Tests conducted at the University of Lyon: a) Geometry of the slabs; b) influence of axial stress on the ultimate shear capacity. Bui *et al.* (2017b).

Finally, an extension of the Critical Shear Crack Theory for axis-symmetric punching (see section 2.3.4.2) to the particular case of in plane tensile stresses was recently presented (Deifalla 2021). In a simplified way, it was considered that a slab can be analyzed as the superposition of two sections: one subjected to tension on the steel reinforcements and one subjected to bending moment, as shown in Fig. 2.70. Hence, the analysis can be conducted using the CSCT for pure punching-shear without axial tension but using a modified value of the yield strength of the reinforcement given by Eq. (2.129), The failure criterion of the CSCT was slightly modified to better fit the experimental results of slabs subjected to punching and in-plane tension (Eq. (2.130)), and a simplified expression for the modified load-rotation curve of the slab was also proposed (Eq. (2.131)). The modified value of the yield strength of the reinforcement must be also used to check the flexural capacity of the cross-section, which may limit the punching-shear strength. The model showed good accuracy when compared to the experimental tests, with a ratio V_{exp}/V_R = 1.05 with a coefficient of variation equal to 29%.

$$f_y' = f_y\left(1 - \frac{f_s}{f_y}\right) \tag{2.129}$$

$$\frac{V_R}{b_0 d\sqrt{f_c}} = \frac{3/4}{\alpha_s\left(1 + 15\frac{\psi'' d}{16 + d_g}\right)} \tag{2.130}$$

$$\psi'' = 1.5\frac{r_s}{d}\frac{f_y'}{E_s}\left(\frac{\alpha_s V}{V_{flex}}\right)^{3/2} \tag{2.131}$$

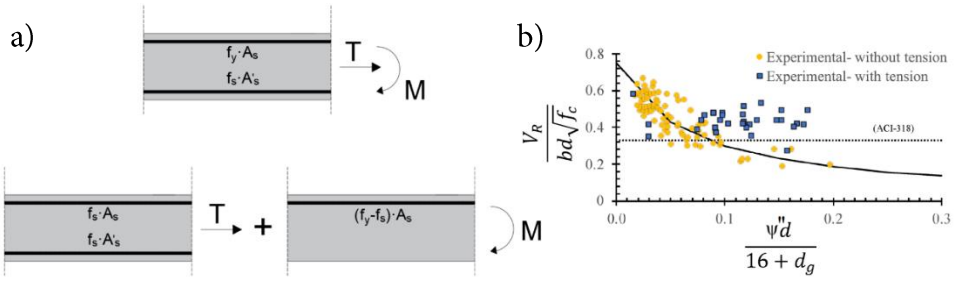

Figure 2.70: CSCT for slabs subjected to in plane tension: a) Superposition of sections; b) Failure criterion. Deifalla (2021).

2.5 Codes on shear

The following code provisions for one-way shear and punching-shear for RC elements without shear reinforcement are revised in this section: Eurocode-2 (EN CEN 2005), Model Code 2010 (CEB-*fib* 2010) and ACI 318-19 (ACI Committee 318 (2019)). These codes use very different expressions for the shear provisions, which reflects the lack of consensus on the shear capacity of members without shear reinforcement. Eurocode 2 and ACI 318-19 are based on semi-empirical approaches, while Model Code 2010 is based on the Modified Compression Field Theory for one-way shear and on the Critical Shear Crack Theory for two-way shear.

2.5.1 Eurocode 2

The provisions found in the Eurocode-2 are similar to those proposed in the Model Code 1990 (CEB-FIP 1990), which were based on the work carried out by Zsutty (1968), who after a regression evaluation of 151 slender shear tests, identified the concrete strength f_c, the longitudinal reinforcement ratio ρ and the shear slenderness a/d as the governing influences on the shear

capacity and proposed Eq. (2.132) for its evaluation. Few years later, Zsutty (1971) added an equation to account for the arch effect in short beams (Eq. (2.133)). None of these expressions incorporated a size effect factor, since the experimental database only included tests up to a cross-section height of 500 mm.

$$V_R = 2.2\left(\rho f_c \frac{d}{a}\right)^{1/3} b_w d \tag{2.132}$$

$$V_R = 2.2\left(\rho f_c \frac{d}{a}\right)^{1/3} \left(\frac{2.5}{a/d}\right) b_w d \tag{2.133}$$

One-way shear

Eurocode-2, in section 6.2.2, indicates that the design value for the shear resistance of an RC element without shear reinforcement, $V_{Rd,c}$ [MPa], is given by Eq. (2.134), with a minimum value given by Eq. (2.135):

$$V_{Rd,c} = \left(\frac{0.18}{\gamma_c} k(100\rho_l f_c)^{1/3} + k_1\sigma_{cp}\right) b_w d \geq \left(v_{min} + k_1\sigma_{cp}\right) b_w d \tag{2.134}$$

$$v_{min} = 0.035\left(1 + \sqrt{\frac{200}{d}}\right)^{3/2} \cdot \sqrt{f_{ck}} \tag{2.135}$$

where:

- γ_c is the safety coefficient for the material.
- k is the size effect factor, given by: $k = 1 + \sqrt{200/d} \leq 2$ (d in mm).
- f_{ck} (MPa) is the characteristic compressive strength of concrete.
- ρ_l is the tensile longitudinal reinforcement ratio defined as: $\rho_l = A_{sl}/b_w d \leq 0.02$.
- A_{sl} is the area of the tensile reinforcement that passes ≥ (l_{bd} + d) beyond the considered cross section (mm^2).
- b_w is the smallest width of the cross section in the tension zone (mm).
- The effect of the normal axial stresses acting in the cross-section is taken into account through the additive term $k_1 \cdot \sigma_{cp}$, where:

- k_1 is a factor equal to 0.15.
- σ_{cp} is the axial stress acting in the cross-section defined as: $\sigma_{cp} = N_{ED}/A_c \leq 0.2$.
- N_{ED} is the axial force in the cross-section due to loading or prestressing ($N_{ED} > 0$ for compression) (N_{ED} in N)
- A_c is the area of concrete cross-section (mm^2).

It is remarkable that EC-2 considers that the increment of shear strength due to a compression force *C* is equal to the reduction in shear strength due to a tensile force of the same magnitude, despite the response of concrete in one case or in the other one is radically different.

Clause (6) of section 6.2.2 of the EC-2 states that for elements with loads applied on the upper side of the member within a distance $0.5d \leq a_v \leq 2d$ to the edge of the support, the contribution of the load to the design shear force V_{ED} may be multiplied by a factor $\beta = a_v/2d$ (Regan 1998). To apply this factor it is required that the flexural reinforcement is fully anchored at the support. For $a_v < 0.5d$, a value of $a_v = 0.5d$ must be used. Nevertheless, the shear force V_{ED} calculated without the reduction factor β should always fulfil the following requirement:

$$V_{ED} \leq 0.5 \nu b_w d \tag{2.136}$$

$$\nu = 0.6\left(1 - \frac{f_{ck}}{250}\right) \tag{2.137}$$

Regarding one-way slabs, EC-2 does not provide a particular expression for the calculation of the shear effective width, so proposals included in national annexes, as the ones introduced in section 2.3.4.1, may be used.

Punching-shear

Section 6.4.4 provides an expression for the calculation of the punching shear strength of slabs and column bases without shear reinforcement, $V_{Rd,c}$ [MPa], which is the same expression used for one-way shear but replacing the term b_w by the length of the control perimeter u_1 (Fig. 2.71).

$$V_{Rd,c} = \left(\frac{0.18}{\gamma_c}\left(1 + \sqrt{\frac{200}{d_{eff}}}\right)(100\rho_l f_c)^{1/3} + k_1\sigma_{cp}\right)u_1 d_{eff} \geq (v_{min} + k_1\sigma_{cp})u_1 d_{eff} \tag{2.138}$$

The main differences between both expressions are:

- d_{eff} is the mean value of the effective depth of the reinforcement in each orthogonal direction: $d_{eff} = (d_x + d_y)/2$.
- ρ_l is the geometric average between the reinforcement ratio of both orthogonal directions: $\rho_l = \sqrt{\rho_x \cdot \rho_y} \leq 0.02$. ρ_x and ρ_y should be calculated as mean values taking into account a slab width equal to the column width plus 3d each side.
- σ_{cp} is the mean value of the normal stresses acting in each orthogonal directions: $\sigma_{cp} = (\sigma_{cp,x} + \sigma_{cp,y})/2$.
- k_1 is a factor in this case equal to 0.1.
- u_1 is the length of the control perimeter placed at a distance 2d from the face of the column (mm) (Fig. 2.71).

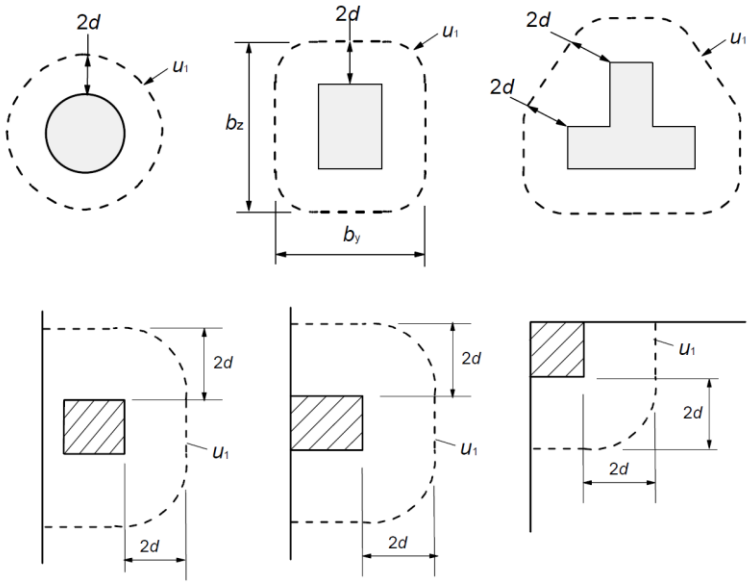

Figure 2.71: Basic control perimeters for loaded areas. EN CEN (2005).

2.5.2 Model Code 2010

The design approach used in the MC-2010 is somewhat different from other codes in terms of determining the resistance of an element to one-way shear and punching-shear. Several levels of approximation can be used, whose difference is the precision and the complexity of the operations involved. The one-way shear provisions are based on Modified Compression Field Theory

whereas the punching-shear provisions are based on the Critical Shear Crack Theory (Sigrist 2013).

One-way shear

Section 7.3.3.2 provides an expression for the contribution of the concrete to the shear strength, $V_{Rd,c}$ [MPa], given by:

$$V_{Rd,c} = k_v \frac{\sqrt{f_{ck}}}{\gamma_c} z b_w \tag{2.139}$$

Where:

- γ_c is the safety coefficient for the material.
- b_w is the smallest width of the cross section in the tension zone (mm) in the case of a beam or the effective shear width, calculated according to Fig. 2.73 in case of one-way slabs.
- f_{ck} (MPa) is the characteristic compressive strength of concrete. $\sqrt{f_{ck}} \leq 8$.
- z is the flexural lever arm (mm).
- k_v is a factor that accounts for the size effect factor and the strain effect and whose value depends on the Level of Approximation chosen. For the *LoA* I, k_v is derived from *LoA* II with the assumption that the mid-depth strain at the control section can be taken as $\varepsilon_x = 0.00125$.

$$If\ LoA = 1 \rightarrow k_v = \frac{180}{1000 + 1.25z} \tag{2.140}$$

$$If\ LoA = 2 \rightarrow k_v = \frac{0.4}{1 + 1500\varepsilon_x} \cdot \frac{180}{1000 + k_{dg} z} \tag{2.141a}$$

$$\varepsilon_x = \frac{1}{2E_s A_s} \cdot \left(\frac{M_{ED}}{z} + V_{ED} + N_{ED} \left(\frac{1}{2} \mp \frac{\Delta e}{z} \right) \right) \quad 0 \geq \varepsilon_x \geq 0.003 \tag{2.141b}$$

Where:

- N_{ED} positive for tension and negative for compression.
- $k_{dg} = 32/(16 + d_g) \geq 0.75$.
- d_g is the maximum aggregate size (mm). If $f_c > 70$ MPa → $d_g = 0$.
- V_{ED} is the design shear force at the control section

- M_{ED} is the bending moment at the control section, taken as a positive quantity.
- E_s is the reinforcement steel modulus of elasticity.
- A_s is the tensile longitudinal reinforcement area.

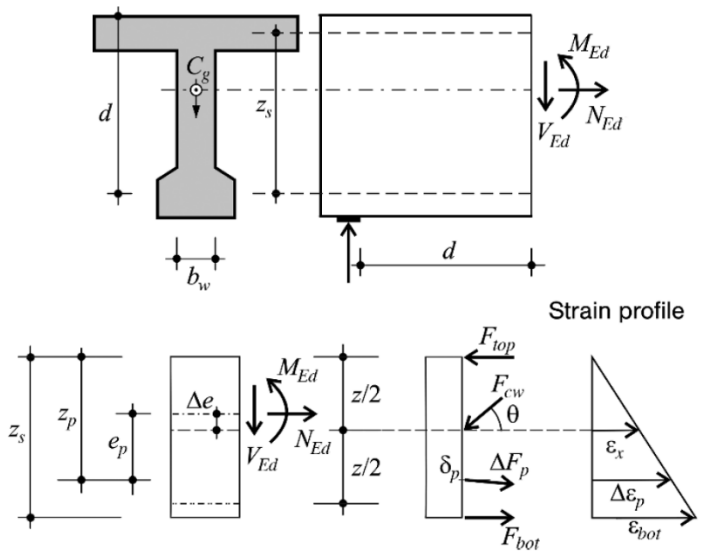

Figure 2.72: Definitions of the parameters involved in the *LoA* II. CEB-*fib* (2010).

The control section is placed at the lesser of the distances equal to d and $a_v/2$ from the face of the support. When a load is applied within a distance of $d < a_v \leq 2d$ from that point, the design shear force may be reduced by a factor $\beta = a_v/2d$. If the load is applied closer, the reduction factor must remain β = 0.5. Regarding one way slabs, the effective shear width has to be calculated according to Fig. 2.73.

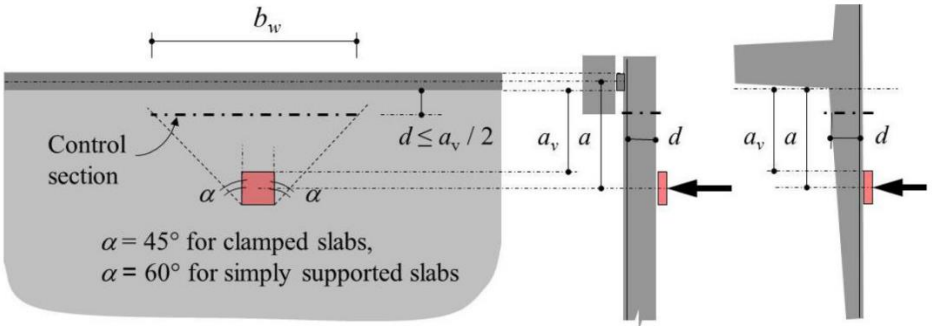

Figure 2.73: Definitions of shear effective width. CEB-*fib* (2010).

Punching-shear

Punching-shear provisions are given within the article 7.3.5. The contribution of the concrete to the punching-shear strength, $V_{Rd,c}$ [MPa], is given by:

$$V_{Rd,c} = k_\psi \frac{\sqrt{f_{ck}}}{\gamma_c} b_0 d_v \tag{2.142}$$

Where:

- b_0 is the length of the punching resisting control perimeter, usually taken at a distance $0.5d_v$ from the column face or loaded area (Fig. 2.74).
- d_v is the effective depth of the slab (mm).
- k_ψ is a parameter that depends on the rotation of the slab around the loaded area, given by:

$$k_\psi = \frac{1}{1.5 + 0.9\psi d k_{dg}} \leq 0.6$$
$$k_{dg} = 32/\left(16 + d_g\right) \geq 0.75. \tag{2.143}$$

- d_g is the maximum aggregate size (mm). If $f_c > 70$ MPa → $d_g = 0$.
- Ψ is the rotation of the slab around the loaded area for the design load, whose value depends on the Level of Approximation chosen
- *LoA* I is suitable for regular flats slabs without significant redistribution of internal forces. A safe estimation of the rotation at failure is then given by:

$$\psi = 1.5 \frac{r_s}{d} \frac{f_{yd}}{E_s} \tag{2.144}$$

- r_s denotes the position where the radial bending moment is zero with respect to the support (or point load) axis, which can be approximated by as 0.22 L_x or 0.22 L_y for the x and y directions, respectively in regular flat slabs where the ratio of the spans (L_x/L_y) is between 0.5 and 2.0.

LoA II is recommended in cases where significant bending moment redistribution is considered in the design. The slab rotation can be calculated as:

$$\psi = 1.5\frac{r_s}{d}\frac{f_{yd}}{E_s}\left(\frac{m_{Ed}}{m_{Rd}}\right)^{1.5} \tag{2.145}$$

- m_{Ed} is the average moment per unit length for calculation of the flexural reinforcement in the support strip (for the considered direction).
- m_{Rd} is the design average flexural strength per unit length in the support strip (for the considered direction).
- The width of the support strip for calculating m_{Ed} and m_{Rd} is $b_s = 1.5\sqrt{r_{s,x} \cdot r_{s,y}}$. The same value for r_s as that for Level I approximation can be adopted.

LoA III is similar to *LoA* II but r_s and m_{Ed} have to be calculated using a linear elastic (uncracked) model. In that case, the coefficient 1.5 in Eq. (2.145) can be replaced by 1.2. The width of the support strip can be calculated as in level II approximation taking $r_{s,x}$ and $r_{s,y}$ as the maximum value in the direction investigated.

In *LoA* IV, the load-rotation curve V-ψ is calculated on the basis of a non-linear analysis of the structure and accounting for cracking, tension-stiffening effects, yielding of the reinforcement and any other non-linear effects relevant for providing an accurate assessment of the structure. The ultimate load is obtained intersecting the calculated curve with the failure criterion.

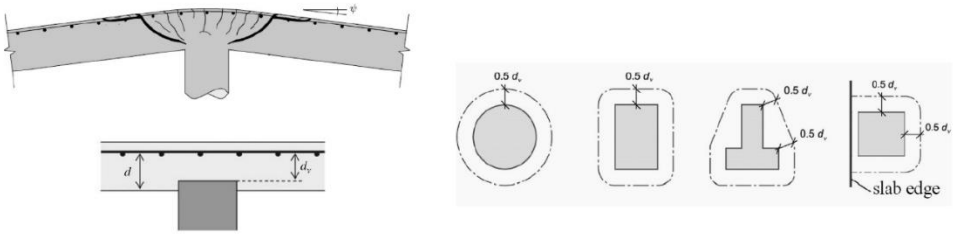

Figure 2.74: Definitions of parameters used in the punching-shear formulation. CEB-*fib* (2010).

2.5.3 ACI 318-19

The ACI 318-19 design code is mainly based on semi-empirical approaches and include a lot of rules for special design cases.

One-way shear

One-way shear provisions are found in section 22.5.5. For members without shear reinforcement, the shear capacity of concrete V_c [MPa] is given by:

$$V_c = \left[0.66\lambda_s\lambda(\rho_w)^{1/3}\sqrt{f_c} + \frac{N_u}{6A_g}\right] b_w d \qquad (2.146)$$

- λ_s is the size effect modification factor determined by $\lambda_s = \sqrt{2/(1+0.004d)} \leq 1$.
- λ is a factor for lightweight concrete. In case of normal concrete $\lambda = 1$.
- ρ_w is the tensile longitudinal reinforcement ratio $\rho_w = A_s/b_w d$.
- b_w is the smallest width of the cross section in the tension zone (mm).
- The effect of the normal axial stresses acting in the cross-section is taken into account through the additive term $N_u/6A_g$, where:
- N_u is the axial force in the cross-section, positive for compression and negative for tension (N_u in N)
- A_g is the gross area of the concrete cross-section (mm^2).

In a similar way than EC-2, ACI 318-19 considers that the increment of shear strength due to a compression force is equal to the reduction in shear strength due to a tensile force of the same magnitude. Regarding one-way slabs, in section 7.4.3, the position of the critical section is set to be placed at d from the face of the support in the case of non-prestressed slabs, where d is the effective depth, but no mention is done for the effective shear width that has to be considered. Regarding the arching action, ACI 318-19 does not provide any factor to account for the proximity of the load to the support. Instead, it recommends the use of nonlinear analysis or strut-and-tie models for members with concentrated loads within a distance twice the member depth from the support.

Punching-shear

Punching-shear provisions are presented in section 22.6.5. For two-way members without shear reinforcement, the concrete capacity is the lower value of:

$$V_c = 0.33\lambda_s\lambda\sqrt{f_c}b_0 d \quad (2.147a)$$

$$V_c = \left(0.17 + \frac{0.33}{\beta}\right)\lambda_s\lambda\sqrt{f_c}b_0 d \quad (2.147b)$$

$$V_c = \left(0.17 + \frac{0.083\alpha_s d}{b_0}\right)\lambda_s\lambda\sqrt{f_c}b_0 d \quad (2.147c)$$

- λ_s is the size effect modification factor determined by $\lambda_s = \sqrt{2/(1+0.004d)} \leq 1$.
- λ is a factor for lightweight concrete. In case of normal concrete λ = 1.
- β is the ratio of long to short sides of the column, concentrated load or reaction area.
- α_s is 40 for interior columns, 30 for edge columns, and 20 for corner columns.
- b_0 is the length of the control perimeter placed at a distance equal to d/2 from the periphery of the loaded area considered.

ACI 318-19 proposes two expressions to calculate the punching shear strength of a slab with an axial compression load due to prestressing, but it does not mention the case of axial tension.

2.6 Significance of the conducted research

Despite the exhaustive research work carried out since the beginning of the XXth century and the large amount of rational models developed throughout the years, the shear behavior of reinforced concrete elements is still not fully clear, and will probably remain as topic of research for the next decades. The complex kinematics and the different contribution of the widely accepted shear resisting actions, which depend, among other parameters, on the load level and the geometry of the specimens, are part of those

uncertainties that have provoked the lack of consensus that currently exist around the shear problem in structural engineering. Obviously, it is impossible to provide experimental evidence for all the different geometries and load cases that may be found in real practice. Hence there is a need of safe and as sound as possible rational models that capture the global shear behavior of reinforced concrete elements and can be adapted for other situations than those exhaustively experimentally studied.

In this context, this thesis aims to shed some light on the shear behavior of reinforced concrete slabs subjected to point loads. On the one hand, part of the work carried out during this investigation deals with shear in one way slabs supported on linear supports. In spite of the large amount of mechanical models derived from different approaches, only a few are intended for slabs, and the current one-way-shear code formulations are often empirical and validated with beam tests, so its applicability to one way slabs may be questionable. Thanks to the experimental work conducted in the las two decades, a significant database of test results is now available, which has allowed to develop and verify a new mechanical model to predict the shear strength of RC one-way slabs without shear reinforcement. It takes into account a significant number of variables involved in the phenomenon and is applicable to is applicable to simply supported slabs, cantilever slabs and situations with partial restraint to the rotation. The model is divided into two sub-models, one for loads applied close to supports, where the direct transmission of the load to the support plays an important role in the shear strength and a second one for loads applied away from supports where the possibility of a shear failure is assumed to coexist whit the possibility of what has been called one-way punching failure. Both sub-models showed good accuracy when compared to the available test results.

On the other hand, the second part of the investigation deals with the shear behavior of reinforced concrete slabs subjected to the simultaneous action of in plane tensile stresses and out-of-plane point loads. This load case has not been exhaustively studied throughout the years, and codes usually incorporates the effect of normal stresses as an additive term to the shear strength, sometimes assuming that the increment of shear strength due to a compression force is equal to the reduction in shear strength due to a tensile force of the same magnitude, despite the response of concrete in one case or

in the other one is radically different. To contribute to gain insight into these aspects of shear design, extending the mechanical model recently developed at UPC for the prediction of the punching-shear strength of two-way slabs to the case of in-plane tensile forces was a feasible option.

In addition to that, the particular case of one-way simply supported slabs subjected to transverse tensile stresses has been studied. Code provisions are mostly intended for beams, as commented above, where axial stresses are always applied in longitudinal (spanning) direction. However, if these expressions are used to calculate the shear strength of a one-way slab, axial loads may exist in the longitudinal and in the transverse direction. If the latter is the case, it is not clear whether those axial stresses have to be taken into account or neglected. Only a single test of these characteristics was found in literature and, despite much more research is needed in order to study this particular case with a mechanical model, a new set of tests will help to understand the overall behavior of these elements under this particular loading condition.

Chapter 3

Shear strength of one-way slabs subjected to concentrated loads

3.1 Introduction

A mechanical model has been developed to predict the shear strength of reinforced concrete slabs under concentrated loads. For the sake of simplicity, it has been divided into two sub-models, one for loads applied close to the supports and another for loads applied away from the support. Both models take into account a significant number of variables involved in the phenomenon, such as the clear shear span, the concrete compressive strength, the reinforcement ratio, the effective depth, the load spreading angle, the size effect and the size of the loaded area. It is applicable to simply supported slabs, cantilever slabs and situations with partial restraint to the rotation, such as intermediate supports. It has been validated with a database of 133 shear test (90 for loads close to the support and 43 for loads away from the support) in slabs subjected to a single concentrated load in different supporting conditions, yielding results on the safe side and showing low scatter. A parametric analysis of the model is also presented, detailing how the different involved variables affect the shear strength. These results, along with some simplified expressions for the shear strength calculation, provide a useful tool for the assessment of the shear strength of RC solid slabs in daily engineering.

3.2 Motivation

Adequacy of the ageing European road network to the current traffic conditions and loads has been subject of different studies throughout the past decades. As part of that road network, plenty of reinforced concrete bridges were built in the 1960s and 1970s. These bridges are still in service, subjected to traffic loads bigger than those at the time of design. In order to verify that these bridges are still adequate for the current traffic loads, some European

countries started to assess the capacity of different categories of bridge types. The results of these initial studies indicated that, in the case of reinforced concrete solid slab bridges, the shear strength requirements set by the current regulations are not met by a significant number of this kind of structures. However, no shear failure or excessive cracking has been observed, which may indicate that the current simplified design rules are not taking all load-bearing mechanisms into account.

In this context, to gain insight into this phenomenon and in order to avoid unnecessary retrofitting or replacement of existing RC slab bridges, a significant number of experimental campaigns have been carried out throughout the past decades, with the main goal of improving the shear strength assessment of this kind of structures (Regan, 1982; Lubell, 2006; Coin and Thonier, 2007; Natário et al. 2014; Lantsoght, 2013a; Bui et al. 2017; Rombach and Henze, 2017; Reissen et al. 2017; Havolnik et al. 2020; Dantas et al. 2020) among others. Thanks to the work of all these researchers, a significant database of test results is now available, which has allowed the authors to develop and verify a new mechanical model to predict the shear strength of RC solid slabs without shear reinforcement supported on linear supports and subjected to concentrated loads.

3.3 Proposed mechanical model for the prediction of the shear strength of one-way RC slabs subjected to point loads close to the support

3.3.1 Proximity of the load to the support

As has been explained in section 2.3.4.1 Shear span to effective depth ratio, it is widely accepted that the clear shear span to effective depth ratio av/d affects the way in which the different resisting actions contribute to the shear strength. When $a_v/d < 2.5\sim3$, a certain direct transmission from the load to the support exists, and arching action is dominant, whilst when $a_v/d \geq 3$, direct transmission can be neglected. The proposed model uses the clear shear span av as a parameter, as it corresponds to a D region, instead of the shear span a, used in some shear models for beams (Fig. 2.44), because the effective depth d is in general smaller in slabs than in beams, and depending on the

size of the loading plate, there may be a significant difference between the *a/d* and a_v/d ratios. Eurocode-2 (EN CEN 1992) and Model Code 2010 (CEB-fib 2010) consider a load to be placed close to a support when $a_v/d \leq 2$, but recent research on this topic suggests that direct transmission effects in slabs may exist for values of av/d up to 3, which is the limit value adopted for this model (Fig. 2.47). For this reason, all test where $a_v/d \leq 3$ have been selected from the available database. All the cases where $a_v/d > 3$ are out of the scope of this model and will be studied in section 3.4

3.3.2 Load spreading angle

When a slab supported on a linear support is subjected to a concentrated load, only a certain part of the slab's width contributes to the shear strength, the so called effective width. A comprehensive overview of this topic may be found in section 2.3.4.1 Effective shear width and width of the slab. For its calculation, this model assumes a transverse load spreading schema based on the French code (FD-P 2013) proposal (Fig. 2.41a) with a modified value of the spreading angle α. The election of the French load spreading schema is based on several studies, (Lantsoght et al., 2014; Bui et al., 2017; Reissen et al., 2017; Dantas and El Debs 2019) which conclude that the French proposal yields better results and lower scatter when it is used along with the simplified formulation of the codes in force, in comparison with other different options studied. Nevertheless, conservative results are obtained if a value of $\alpha = 45^{o}$ is used.

The effective width in one-way slabs for different support conditions has been also studied be means of non-linear finite elements analysis (Vaz Rodriguez et al., 2008; Reissen and Hegger 2012; Belletti et al. 2014; Lantsoght et al., 2015). All these authors coincide in that the horizontal spreading angle is slightly greater than 45 degrees. A statistical analysis using the model presented herein and different values of α was performed using the available databank. Best results, in terms of accuracy and safety, where obtained for α ranging from 51 to 53 degrees. Based on this information, and for the sake of simplicity, since the model is intended to be valid for different degrees of the restraint to the rotation at the considered support, ranging from zero to full restraint, the mean value of the angles proposed in Model Code 2010 (Fig.

2.41c) for simply supported and fully clamped slabs have been assumed, resulting in $\alpha = 52.5^{o}$ (Fig. 3.1).

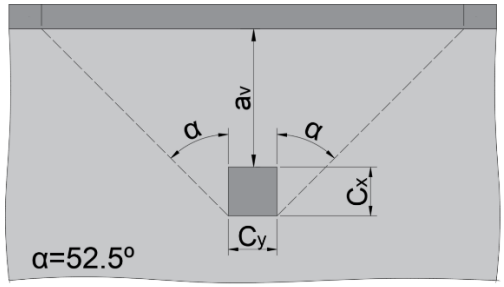

Figure 3.1: Load spreading schema adopted in the model.

3.3.3 Extension of the CCCM to RC slabs without shear reinforcement subjected to concentrated loads close to support

Considering the adopted hypothesis commented above, the shape of the failure surface in one-way slabs is similar to the one assumed in the base models for beams, but taking into account that the horizontal load spreading from the load pad to the support. According to Fig. 2.46, when $a_v/d \leq 3$, for simply supported slabs the critical crack can be assumed to start at the inner face of the support (Fig. 3.2a) whereas for clamped slabs it is assumed to start at the inner face of the load pad (Fig. 3.2b). In both cases, the critical section, where failure occurs, is assumed to be located where the critical crack reaches the neutral axis depth.

The distance βd is the horizontal projection of the first branch of the critical crack, in the tensile part of the slab, whose value is set by the geometrical assumptions. Assuming $cot\ \theta \approx \frac{a_v}{d}$:

$$\beta d = (d - \mathrm{x})\, cot\ \theta = \left(1 - \frac{\mathrm{x}}{d}\right) a_v \tag{3.1}$$

where x is the length of the un-cracked zone, which is taken equal to the neutral axis depth. To account for the increment on the neutral axis depth x due to the proximity of the load to the support (Fig. 3.3), a parabolic variation

of x is assumed between $a_v/d = 3$, ($x = x_0$, B-region) and $a_v/d = 0$ ($x_1 \approx 0.8d$), resulting:

$$\frac{x}{d} = \frac{x_0}{d} + \left(0.8 - \frac{x_0}{d}\right)\left(1 - \frac{a_v/d}{3}\right)^2 \tag{3.2}$$

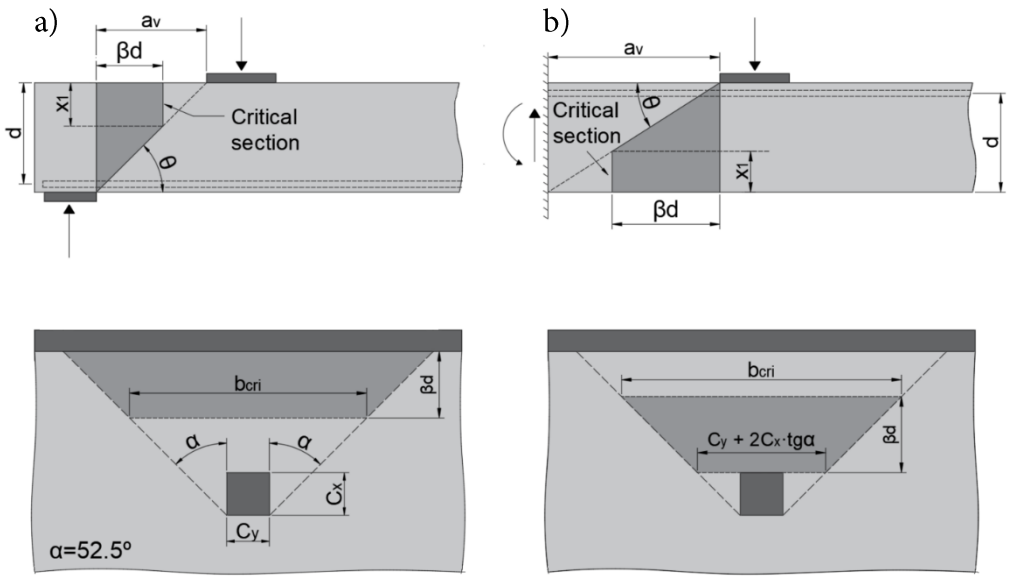

Figure 3.2: Position of the critical section: a) simply supported slab; b) cantilever slab.

As a consequence of these assumptions, the position of the critical section is known, and so is its effective width bcri, given by the next two equations. The first one for the case of simply supported slabs and the second one for clamped slabs. For the former case, the deeper the neutral axis, the wider the critical section, whereas for the latter case, is just the opposite.

$$b_{cri} = C_y + 2(C_x + a_v - \beta d)\tan\alpha \leq b_{slab} \tag{3.3a}$$

$$b_{cri} = C_y + 2(C_x + \beta d)\,tan\,\alpha \leq b_{slab} \tag{3.3b}$$

where C_y and C_x are the dimensions of the loaded area in parallel and perpendicular directions to the support (Fig. 3.1), and bslab is the slab width.

The free body considered for the equilibrium equations is the one enclosed by the section where the critical crack starts, the critical section and the critical crack itself. For simply supported slabs, the total bending moment

at the section where the critical crack starts has been considered equal to zero. For clamped slab, the value of the bending moment per unit length at the inner face of the load pad has been studied by means of a linear finite element analysis. Reinforced concrete structures are highly non-linear, but nonlinear FE analysis require large computation times when exhaustive parametric studies are conducted. Therefore, a linear elastic FE analysis was carried out with the help of Simulia Abaqus software (Dassault Systems Simulia Corp., 2014). Shear deformable shell element S4 has been used for the analysis. In order to take into account the slab's behavior after flexural cracking, appropriate values of the Poisson's ratio ν and the shear modulus G must be selected. For this study, values proposed by Natario (2015) $\nu = 0$ and $G = E_c/16$ have been adopted, where E_c is the concrete Young's modulus. For the geometry of the modeled slab, average values from the slabs of the database have been adopted. Three different sizes ($C = d$, $C = 1.5d$, $C = 2d$) and four different positions ($a_v = 0.5d$, $a_v = 1d$, $a_v = 2d$ and $a_v = 3d$) of a square loading plate have been analyzed. The study showed that the distance from the inner face of the loading plate to the contraflexure point l_0 mostly depends on the C/d ratio (Fig. 8), and is not significantly affected by the a_v/d ratio except for low values of a_v/d, where the bending moment is in general small. For $C = 1.5d$ and $C = 2d$, which are sizes more representative of real situations, contraflexure point lies within $0.2d$ when $a_v/d \geq 1$ (Negative values mean that the contraflexure point lies behind the inner edge of the plate).

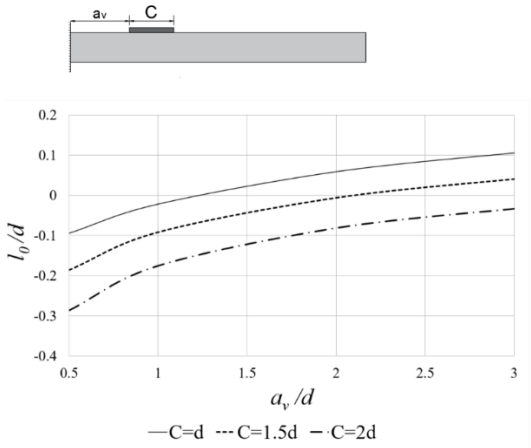

Figure 3.3: Evolution of the distance l_0 from the edge of the loading plate to the contraflexure point for different values of a_v.

On the basis of the obtained results, the value of the bending moment per unit length at the inner face of the load pad is expected to be small as it is close to the contraflexure point. For the sake of simplicity, bending moment per unit length is going to be neglected at the section where the critical crack starts. This way, the same equilibrium equations are derived for both simply supported and clamped slabs (Fig. 3.4).

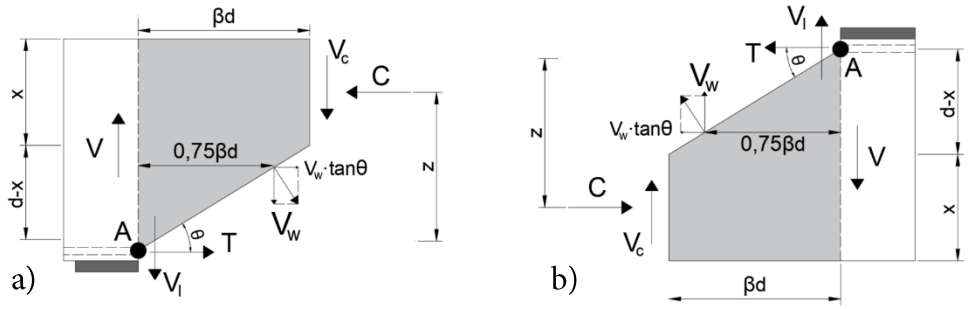

Figure 3.4: Free body diagram: a) simply supported slabs; b) cantilever slabs.

For supports with partial restraint to the rotation, as is the case of intermediate supports of continuous slab bridges, it has been reported (Regan 1982; Islam, Pam & Kwan, 1998; Reissen et al., 2018) that the shear strength is higher and influenced by the position of the contraflexure point within the shear span, reaching its maximum value when this point is placed half way between the axis of the support and the load (see section 2.3.4.1). In the present model, the influence of the degree of restraint is taken into account through the shear span, which is defined as the ratio between the maximum moment and the maximum shear in the region between the load and the support. According to this definition, the shear span results to be the maximum between the distance from the contraflexure point to the inner face of the load pad a_{v1} and the distance from the contraflexure point to the inner face of the support a_{v2} (Fig. 3.5), where $0 < \lambda_M < 1$ correspond to the situation where this point exists. This also has to be taken into account in the calculation of the size effect factor ζ (Eq. (2.74)).

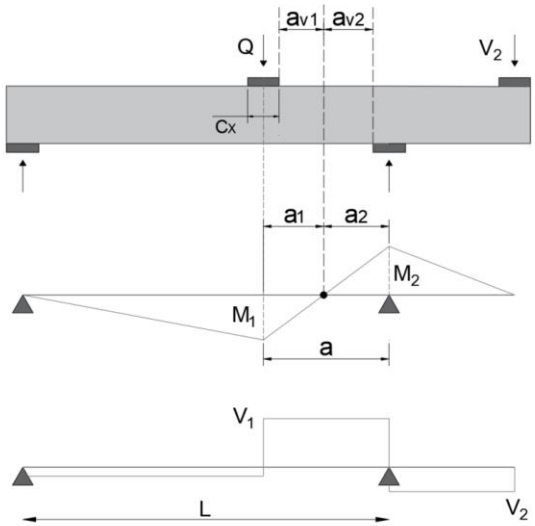

$$\lambda_M = \frac{M_2}{Q \cdot a}$$

$$a_1 = a \cdot \frac{1 - {}^{a}/_{L}}{\frac{\lambda_M}{1-\lambda_M} + 1 - {}^{a}/_{L}}$$

$$a_{v1} = \left(a_1 - {}^{C_x}/_{2}\right); \quad a_{v2} = a_v - a_{v1}$$

$$a_v = \max\left(a_{v1}; a_{v2}\right)$$

Figure 3.5: Definition of the shear span for slabs with partial restraint to the rotation.

From the equilibrium of forces and moments, the following equations are derived:

$$C = \mathrm{T} + V_w \cdot \tan\theta \tag{3.4}$$

$$\mathrm{V} = V_c + V_w + V_l \tag{3.5}$$

$$C \cdot z = V_c \beta d + V_w 0.75 \beta d (1 + \tan^2\theta) \tag{3.6}$$

In Eq. (3.6), a value of $0.75\beta d$ for the horizontal lever arm of the resultant of the residual stresses across the critical crack has been adopted, as in the CCCM for non-slender beams (see section 2.3.3.6 *CCCM-NS*). For the lever arm in flexure z, a similar parabolic variation as for x is assumed between $a_v/d = 3$, ($z = d\text{-}x/3$, B-region) and $a_v/d = 0$ ($z \approx 0.6d$), resulting:

$$z = d - \frac{\mathrm{x}}{3} + \left(0.6d - \left(d - \frac{\mathrm{x}}{d}\right)\right)\left(1 - \frac{{}^{a_v}/_{d}}{3}\right)^2 \tag{3.7}$$

From Eq. (3.5), the model assumes that the total shear force resisted V_R is equal to the addition of the vertical resultant of the residual tensile stresses through the critical crack V_w and the total shear resisted in the compression head at the critical section V_c, scaled by a factor ζ (see section 2.3.3.6 *CCCM* and Eq. (2.74)) that takes into account the size effect. This model neglects dowel action contribution V_l in specimens without shear reinforcement due

to spalling of the concrete cover. This equation may be expressed in a dimensionless way by the following expression:

$$V_R = (\zeta \cdot V_c + V_w) = (\zeta \cdot v_c \cdot f_{ct} b_{cri} d + v_w \cdot f_{ct} b_w d) = \left(\zeta \cdot v_c + \frac{b_w}{b_{cri}} v_w\right) f_{ct} b_{cri} d \quad (3.8)$$

where b_{cri} is the effective width at the critical section and b_w is the effective width at the section where the resultant of the residual stresses is applied. The term b_w/b_{cri} accounts for the different width between both sections. For the shear transferred across the crack v_w, Eq. (3.9) and (3.10) proposed in the MASM and Eq. (3.11) proposed in the CCCM-NS have been adopted. V_c is obtained by integration of the tangential stresses in the compression head at the critical section, and its ultimate value will be reached when the principal stresses at the point of maximum damage satisfy the equation of the tension-compression branch of the Kupfer and Gerstle (1973) failure envelope given by Eq. (3.12). As derived in the CCCM, the ultimate value of V_c is given by Eq. (3.12), where normal compressive stresses are considered negative.

$$V_w = \frac{0.425 \sin^2 \theta \cdot f_{ct}}{E_c \cdot \varepsilon_s} \cdot \left(1 + \frac{2 \cdot G_f \cdot E_c}{f_{ct}^2 \cdot d}\right) b \cdot d \quad (3.9)$$

$$G_f = 0.028 \cdot f_c^{0.18} \cdot d_g^{0.32} \quad (f_c \, in \, MPa; \; d_g in \, mm; \; G_f in \, N/mm) \quad (3.10)$$

$$\varepsilon_s = \frac{V \cot \theta}{A_s E_s} \quad (3.11)$$

$$\frac{\sigma_1}{f_{ct}} + 0.8 \frac{\sigma_2}{f_c} = 1 \rightarrow R_t = \frac{\sigma_1}{f_{ct}} = (1 - 0.8 \frac{\sigma_2}{f_c}) \quad (3.12)$$

$$v_c = \frac{V_c}{f_{ct} b_{cri} d} = 0.682 \frac{x_1}{d} R_t \sqrt{1 - \frac{\sigma_x + \sigma_z}{f_{ct} \cdot R_t} + \frac{\sigma_x \sigma_z}{f_{ct}^2 \cdot R_t^2}} \quad (3.13)$$

The value of the concrete compressive strength f_c has been limited to a maximum value of 40 MPa in this model. Some researchers who studied the influence of f_c in the shear strength of RC slabs (Kani, 1967; Angelakos, Bentz & Collins, 2001; Lantsoght et al., 2013) observed that the strength barely increases from medium to high values of f_c. This may be related to the fact that for high level of longitudinal compressive stresses in the compression head, high transverse tensile stresses due to Poisson effect arise, thus reducing the compression strength in the direction normal to the section considered and counteracting the enhancement due to the increment of f_c. In fact, the CCCM for beams limits the compression strength to 60 MPa for the same

reason, but in this case, this effect is enhanced due to the opening of the flow of stresses from the point load to the support. See section 2.3.4.1 *Concrete compressive strength* for more details.

The last step to calculate V_c is to relate normal stresses σ_x and σ_z with the internal forces, and therefore, with the external actions. Vertical stresses σ_z are generated by the vertical compression due to the proximity between the load and the support, producing a confining effect that may increase the shear stress capacity of the fibres of the compression chord. The effect of such vertical compressive stress is sketched in Fig. 3.6. For simply supported slabs, a triangular distribution for σ_z is adopted. This assumption has been made because one support is much closer to the load than the other, which provokes a non-symmetrical spreading of the vertical stresses (Fig. 3.6a). For cantilever slabs, a constant distribution is adopted for simplicity (Fig. 3.6b). For the former case, the value of σ_z is obtained by assuming a spreading angle of the point load equal to θ from the load pad, whereas in the latter case vertical stresses are assumed to spread with an angle θ from reaction at the support.

Vertical stress may be computed for simply supported and cantilever slabs using Eq. (3.14), with the corresponding values of L_x and L_y given by Fig. 3.6:

$$\sigma_z = \frac{\gamma \cdot V}{\frac{1}{2} \cdot L_x \cdot L_y} \cdot \psi_{ad} = \frac{\gamma \cdot (v_c + \frac{b_w}{b_{cr}} v_w)}{\frac{1}{2} \cdot L_x \cdot L_y} \cdot f_{ct} b_{cri} d \cdot \psi_{ad} \tag{3.14}$$

where $\psi_{ad} = 1\text{-}a_v/3d \leq 1$ is a stress interpolation factor in terms of a_v/d, that varies from 0 to 1. It provides continuity between loads applied close to the support ($a_v/d \leq 3$) and the rest of the cases. $\gamma = Q/V$ is the ratio between the applied load and the shear at the considered support.

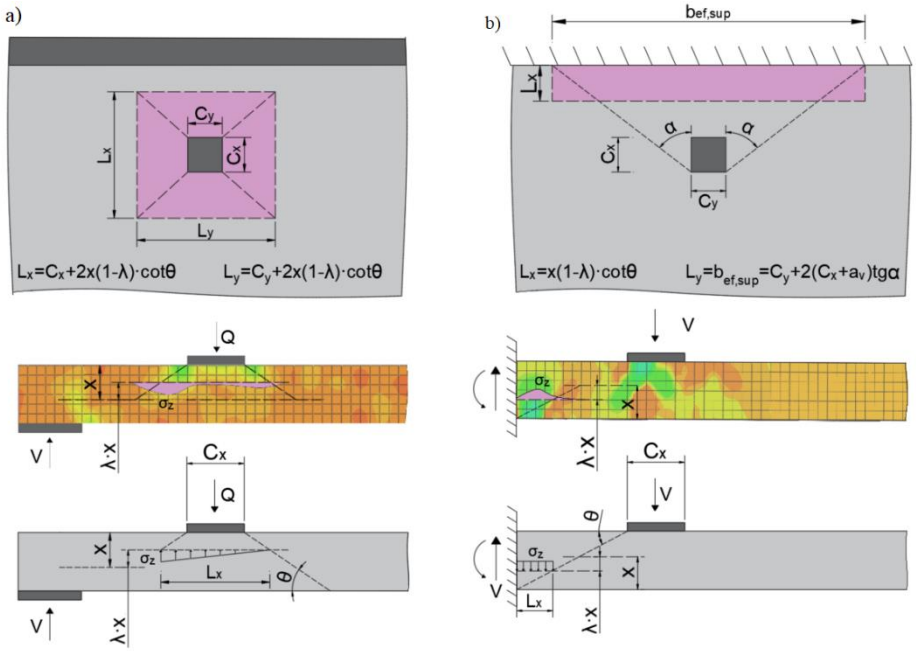

Figure 3.6: Distribution of confining stresses σ_z: a) simply supported slabs; b) cantilever slabs.

Horizontal compression stresses σ_x may be related to the shear resisted in the compression head by Eq. (3.6). The force C due to bending in the compression chord is assumed to vary from $C = 1/2\sigma_{x,max} \cdot b_{cri} \cdot x_1$ for $a_v/d = 3$ to $C \approx 0.8 \cdot \sigma_{x,max} \cdot b_{cri} \cdot x_1$ for $a_v/d = 0$. Also, the relation between the compression stress at the point of maximum damage σ_x and the maximum compression stress $\sigma_{x,max}$ varies from $\sigma_x = \lambda \cdot \sigma_{x,max}$ for $a_v/d = 3$ to $\sigma_x \approx \sigma_{x,max}$ for $a_v/d = 0$ (Fig. 3.7). A double linear interpolation is made and the following expressions are derived:

$$C = \frac{K_C}{K_\lambda} \sigma_x \cdot b_{cri} \cdot x_1 \tag{3.15}$$

$$K_C = 0.8 - \frac{0.3 \cdot a_v}{3d} \tag{3.16}$$

$$K_\lambda = 1 - \frac{a_v}{3d}(1 - \lambda) \leq 1 \tag{3.17}$$

If the value of C from Eq. (3.15) is substituted into Eq. (3.6), an expression for σ_x is obtained:

$$\sigma_x = \frac{\frac{K_\lambda}{K_C}\left(V_c \cdot \beta d + V_w \cdot 0{,}75\beta d \cdot (1+\tan^2\theta)\right)}{x_1 \cdot z \cdot b_{cri}} = \frac{\frac{K_\lambda}{K_C}\left(v_c \cdot \beta + \frac{b_w}{b_{cri}} v_w \cdot 0{,}75\beta \cdot (1+\tan^2\theta)\right)}{\frac{x_1}{d}\cdot\frac{z}{d}} f_{ct} \quad (3.18)$$

Then, substituting the values of σ_x and σ_z in Eq. (3.13), a general formula is obtained that can be solved for v_c in a iterative way. This way the value of v_w and finally the shear strength V_R are obtained following the iterative schema presented in section 2.3.3.6 *The Multi-Action Shear Model (MASM).*

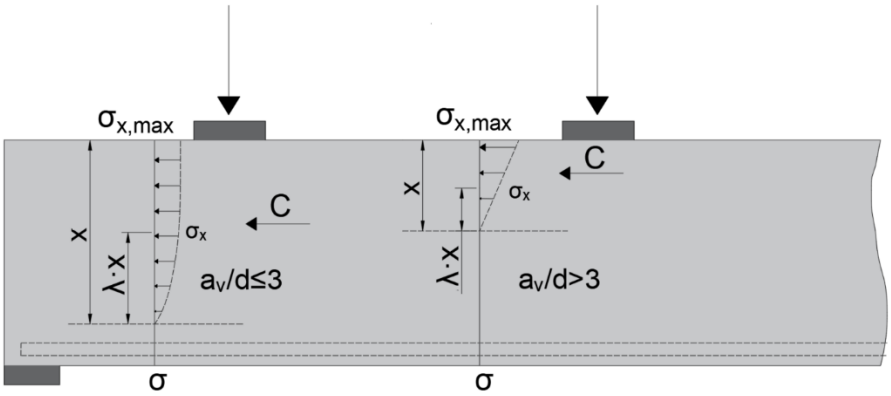

Figure 3.7: Change in the normal stresses distribution with the proximity of the load to the support.

3.3.4 Validation of the proposed model with the available database

Thanks to all the experimental campaigns carried out throughout the las decades, a significant database of shear test on RC slabs supported on linear supports is now available. For the validation of this model, only un-cracked slabs, subjected to a single concentrated load with $a_v/d \leq 3$, width $b \geq 1$ m and a loading plate with a minimum side length of 100 mm have been selected. In total, 90 experimental tests met the parameters: 45 simply supported slabs, 24 cantilever slabs and 21 slabs with partial restraint to the rotation at the support. The ratio between the experimental results and those predicted by the proposed model V_{exp}/V_R, for each support condition and in total, is presented in Table 3.1. The full database is included in appendix A.

A general good agreement is observed between the predictions and the experimental results, in terms of mean and scatter: V_{exp}/V_R =1.127, CoV =

0.121 for simply supported slabs, V_{exp}/V_R =1.132, CoV = 0.166 for cantilever slabs and V_{exp}/V_R =1.165, CoV = 0.168 for slabs with partial restraint to the rotation at the support. Globally, V_{exp}/V_R =1.137, CoV = 0.145 for all the slabs considered. The results obtained do not present a significant variation for the three different static schemas, which indicates that the hypotheses adopted in each case are adequate, as well as the assumption of the common spreading angle α for all the cases. Figure 3.8 shows the ratio V_{exp}/V_R as a function of a_v/d, of the amount of longitudinal reinforcement ρ, of the concrete compressive strength f_c and of the ratio of the length of the loading plate to the effective depth of the slab C_x/d for each case.

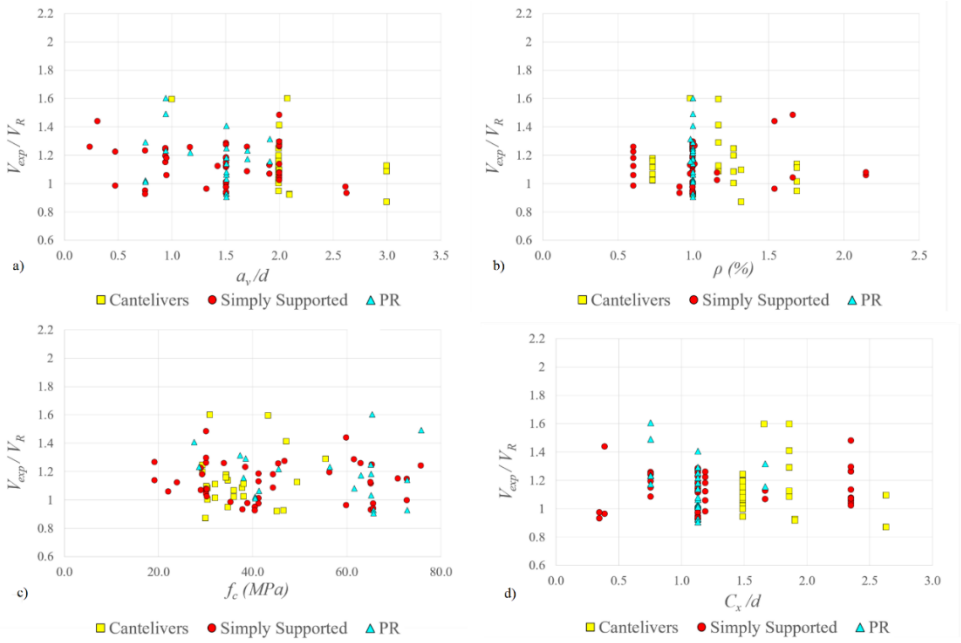

Figure 3.8: Comparison between predictions and test results in terms of different variables: a) a_v/d ratio; b) amount of tensile longitudinal reinforcement ρ; c) concrete compressive strength f_c; d) C_x/d ratio.

Table 3.1. Comparison between model predictions and test results

	Simply supported (SS)	Cantilever	Partial restraint (PR)	All slabs
Nº tests	45	24	21	90
V_{exp}/V_R	1.127	1.132	1.165	1.137
Std. deviation (σ)	0.137	0.188	0.196	0.165
CoV (δ)	0.121	0.166	0.168	0.145
min	0.925	0.869	0.907	0.869
max	1.480	1.596	1.622	1.622
Percentile 5%	0.933	0.918	0.907	0.920

As can be seen in Fig. 3.8a, the accuracy of the model is good over the whole range of values of a_v/d. This indicates that the model captures the enhancement on the shear strength due to the proximity of the load to the support and that the assumption of considering the direct transmission effects for values of $a_v/d \leq 3$ is appropriate. Fig. 3.8c shows that the precision of the model seems to be independent of the concrete compressive strength, since similar mean and scatter are obtained for medium strength concretes and high strength concretes, confirming that limiting the maximum concrete compressive strength to 40 MPa is a realistic assumption, although no data is available for high strength concrete cantilever slabs. Finally, attending to Fig. 3.8b and 3.8d, it also seems that the accuracy of the proposed model is independent of the longitudinal reinforcement ratio ρ and the C_x/d ratio respectively. However, to ensure that the model captures well the effect of these parameters, more tests are required using a wider range of values of the influencing parameters, since most of those included in the database are concentrated around a few values.

3.3.5 Parametric analysis of the model

In this section, the influence on the model predictions of several variables is going to be analysed. Specifically, the concrete compressive strength f_c, the

longitudinal reinforcement ratio ρ, the a_v/d ratio, the effective depth d, the width of the slab b and the width of the loading plate C_y. For this purpose, the obtained shear capacities V_R are going to be compared with a reference strength V_{R0}, corresponding to the shear strength of a slab where all the studied parameters are set equal to control values. These control values correspond to average values of the slabs of the available database. Minimum, maximum and control values adopted for each parameter are summarized in Table 2, along with the shear strength ratio obtained for the minimum and maximum values of each variable. When one of the parameters is studied, the rest are kept constant and equal to their control values. Figure 14 summarizes the results of the study for both cantilever and simply supported slabs. The length of the loading plate C_x has been kept constant and equal to 250 mm for all the analysis.

Table 3.2. Adopted values for the parametric analysis

Variable	Min. Value	Control value	Max. Value	V_{Rmin}/V_{R0}		V_{Rmax}/V_{R0}	
				SS	Cant	SS	Cant
f_c (MPa)	15	35	80	0.63	0.59	1.08	1.09
ρ (%)	0.5	1	3.1	0.76	0.85	1.54	1.24
a_v/d	0.4	2	3	2.2	1.79	0.67	0.89
d (mm)	100	350	750	0.33	0.34	3.99	3.16
b (mm)	1000	2500	4250	0.65	0.44	1.00	1.00
C_y (mm)	150	250	2500	0.98	0.94	1.46	1.49

As can be seen in Fig. 3.9a, the shear strength increases with the concrete compressive strength for low values of f_c, as reported by Moody *et al.* (1955a) and Bui et al. (2017), but it remains constant once it reaches the threshold value of 40 MPa selected for the model. Fig. 3.9b shows that increasing the reinforcement ratio has a favourable effect on the shear strength, which is in agreement with observed behaviour in several experimental campaigns (see section 2.4.3.1 *Reinforcement ratio and layout*). However, it is interesting to note that simply supported slabs are more affected by this parameter than

cantilever slabs. This is because increasing ρ increases the neutral axis depth, which in simply supported slabs leads to an increment in the width of the critical section, thus enhancing even more the shear strength, whereas in cantilever slabs, it leads to a reduction of the width of the critical section, and both effects slightly offset.

Fig. 3.9c shows how the a_v/d ratio affects the shear strength. The closer the load to the support, the higher the shear strength, but as in the case of ρ, simply supported slabs are more affected than cantilevers. The reason is the same: approaching the load to the support leads to an increase of the vertical confining stresses and to an increment of the neutral axis depth, which provokes a slight reduction in the width of the critical section in the case of cantilever slabs. Fig. 3.9d shows the great influence of the effective depth d in the total shear strength, despite the size effect factor. This is mainly because the a_v/d ratio has been kept constant in this comparison, and greater clear shear spans are obtained for higher values of d, which leads to greater effective widths. The divergence between both curves starting at a value of $d \approx 500$ mm is because the width of the critical section stops increasing for cantilever slabs, as it reaches the control value for the width of the slab.

The effect of increasing the width of the slab is shown in Fig. 3.9e. When the slab's width is greater than the maximum effective width reachable at the critical section for the control values of the rest of the variables, the shear strength stops increasing and remains constant. When the width of the slab is reduced, the shear strength decreases almost linearly with the width. Cantilever slabs are affected earlier by this reduction, because the control section is closer to the support, and therefore is wider than in simply supported slabs. Finally, Fig. 3.9f shows the effect of increasing the width of the loading plate (dimension parallel to the support) while its length is kept constant. Shear strength increases until the width of the critical section equals the control value for the width of the slab. Vertical confinement stresses are more affected by the size of the loading plate in the case of simply supported slabs than in the case of cantilever slabs, decreasing with increasing values of C_y, and that is the reason why the curve presents a lower slope and slightly decreases from the point of maximum strength in the former case.

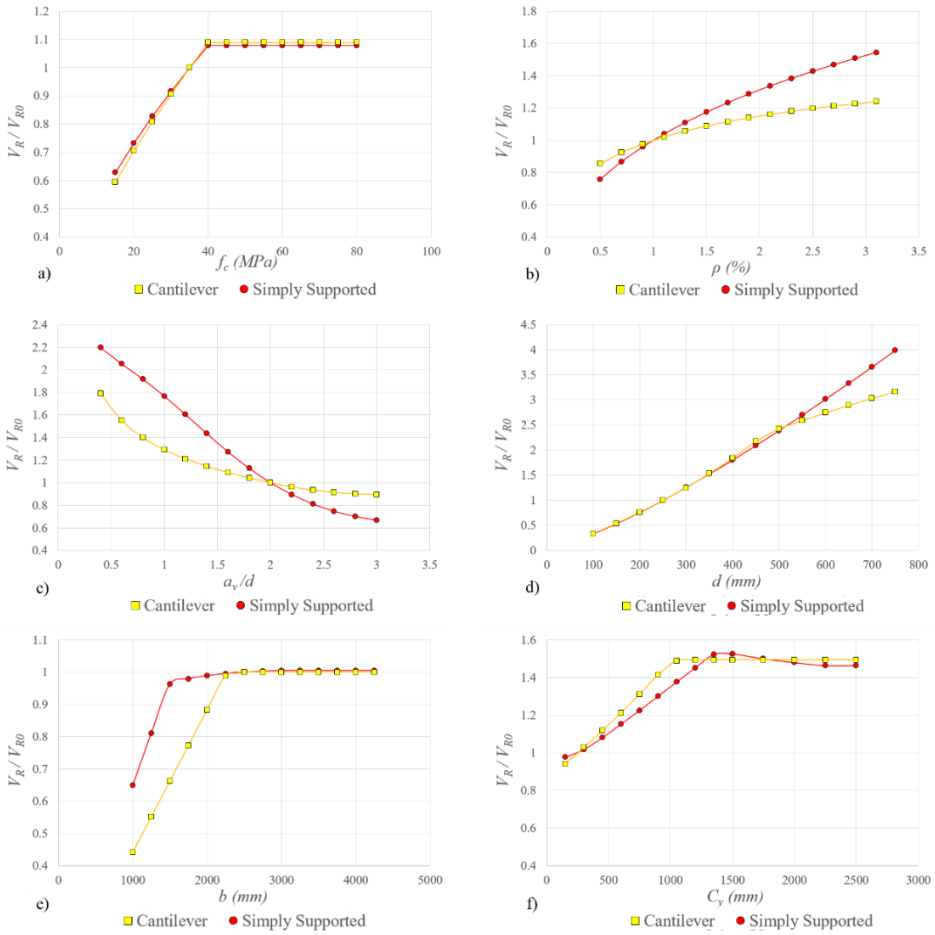

Figure 3.9: Evolution of the strength predicted by de model as a function of different variables: a) concrete compressive strength f_c; b) amount of longitudinal tensile reinforcement ρ; c) a_v/d ratio; d) effective depth d; e) width of the slab b; f) width of the loading plate C_y.

3.3.6 Simplified expressions

After a statistic analysis of the model, the following simplified expressions for simply supported slabs, cantilever slabs, and slab with partial restraint to the rotation at the support Eq. 3.19a, Eq. 3.19b and Eq. 3.19c are proposed in order to easily estimate the shear strength, without solving the equations of the model in an iterative way, where x_0 is the value of the neutral axis depth in pure flexure in slender situation and a_v corresponds to the real distance between the inner face of the loading plate and the inner face of the support

in all three cases. The uniaxial tensile concrete strength f_{ct} used in the derivation of the model has been replaced by the concrete compressive strength f_c following the relationship proposed in the Eurocode-2: $f_{ct} = 0.3 f_c^{2/3}$ $(f_c \leq 40MPa)$.

$$V_R = 0.3 \cdot \zeta \left[\left(0.84 - 0.21\frac{a_v}{d}\right) + \left(1 - \frac{a_v}{3d}\right)^2 \cdot \frac{x_0}{d} \right] f_c^{2/3} b_{cri} d \qquad (3.19a)$$

$$V_R = 0.3 \cdot \zeta \left[\left(0.47 - 0.058\frac{a_v}{d}\right) + \left(1 - \frac{a_v}{3d}\right)^2 \cdot \frac{x_0}{d} \right] f_c^{2/3} b_{cri} \qquad (3.19b)$$

$$V_R = 0.3 \cdot \zeta \left[\left(0.84 - 0.21\frac{a_v}{d}\right) + 2.65\left(1 - \frac{a_v}{3d}\right)^2 \cdot \frac{x_0}{d} \right] f_c^{2/3} b_{cri} d \qquad (3.19c)$$

These expressions have been applied to the selected slabs of the database and compared to the values obtained solving the equations of the model. Obtained results are summarized in Table 3.3. As can be seen, enough accuracy is attained with the simplified expressions, even though the scatter slightly increases in comparison to the model. However, more experimental results are required to validate them over a larger range of the main variables affecting this phenomenon.

Table 3.3. Comparison between simplified equations predictions, model predictions and test results

	Simply supported (SS)		Cantilever		Partial restraint (PR)		All slabs	
Nº tests	45		24		21		90	
	Model	Simp.	Model	Simp.	Model	Simp.	Model	Simp.
V_{exp}/V_R	1.127	1.158	1.132	1.175	1.165	1.139	1.137	1.158
Std. deviation (σ)	0.137	0.166	0.188	0.216	0.196	0.253	0.165	0.200
CoV (δ)	0.121	0.143	0.166	0.184	0.168	0.222	0.145	0.173
min	0.925	0.892	0.869	0.901	0.907	0.869	0.869	0.869
max	1.480	1.568	1.596	1.785	1.622	1.768	1.622	1.785
Percentile 5%	0.933	0.916	0.918	0.915	0.907	0.888	0.920	0.903

3.3.7 Comparison with code provisions

To conclude, results obtained with both the model and the simplified expressions are compared to those obtained using Eurocode-2, ACI 318-19 and Model Code 2010 provisions for one-way shear (see section 2.5). For EC-2 and ACI 318-19, French load spreading schema has been used, with values of $\alpha = 45^o$ and $\alpha = 52.5^o$. In the case of Model Code 2010, values of α provided in its formulation are used, adopting $\alpha = 60^o$ for the case of simply supported slabs with partial restraint to the rotation. Results of the comparison are summarized in Table 3.4.

In general, results obtained with the CCCM and the simplified expressions are more accurate than those obtained using code provisions. Among the codes, MC-2010 (LoA II) and EC-2 with $\alpha = 52.5^o$ are the best options, followed by EC-2 with $\alpha = 45^o$ and MC-2010 (LoA I). As far as ACI 318-19 concerns, its formulation yields highly conservative results with large scatter , and seems not the most suitable method for assessing the shear strength of RC slabs under concentrated loads close to the support.

Table 3.4. Comparison between simplified equations, model predictions and code provisions.

	Simply supported (SS)		Cantilever		Partial restraint (PR)		All slabs	
Nº tests	45		24		21		90	
	V_{exp}/V_R	$CoV\ (\delta)$	V_{exp}/V_R	$CoV\ (\delta)$	V_{exp}/V_R	$CoV\ (\delta)$	V_{exp}/V_R	$CoV\ (\delta)$
CCCM	1.127	0.121	1.132	0.166	1.165	0.168	1.137	0.145
CCCM simpl.	1.158	0.143	1.175	0.184	1.139	0.222	1.158	0.173
EC-2 α=45º	1.569	0.316	1.379	0.180	1.656	0.156	1.539	0.263
EC-2 α=52.5º	1.331	0.296	1.106	0.182	1.391	0.162	1.285	0.259
ACI α=45º	2.615	0.522	1.765	0.320	2.762	0.329	2.423	0.480
ACI α=52.5º	2.203	0.495	1.416	0.326	2.301	0.300	2.016	0.466
MC-2010 (LoA I)	1.879	0.211	2.648	0.194	2.083	0.163	2.131	0.247
MC-2010 (LoA II)	1.127	0.284	1.382	0.198	1.257	0.159	1.225	0.246

3.3.8 Summary

A theoretical model for the shear strength of RC slabs, linearly supported and subjected to concentrated loads close to the support ($a_v/d \leq 3$), has been described and verified with the results of experimental campaigns carried out throughout the last decades. The developed model has been derived from the Compression Chord Capacity Model for slender and non-slender beams, by identifying both the differences in the behavior between beams and one-way slabs and the main effects of the proximity of the load to the support, incorporating them into the governing equations. The following conclusions can be drawn from the performed studies:

- The model accounts for a significant number of variables involved in the phenomenon, such as the clear shear span, the concrete compressive strength, the reinforcement ratio, the effective depth, the load spreading angle, the size effect and the size of the loaded area. It is applicable to simply supported slabs, cantilever slabs and slabs with partial restraint to the rotation at the support

- Good accuracy has been found when comparing the model predictions with the test results available, with a mean value (MV) of the ratio V_{exp}/V_R =1.127, and CoV = 0.121 for simply supported slabs, MV of V_{exp}/V_R =1.132, CoV = 0.166 for cantilever slabs and MV of V_{exp}/V_R =1.165, CoV = 0.168 for slabs with partial restraint to the rotation at the support. Globally, MV of V_{exp}/V_R =1.137, CoV = 0.145 for the 90 slabs considered. Furthermore, 95% of the results have a V_{exp}/V_R ratio greater than 0.92. Thus, all the assumptions of the model, including considering the direct transmission effects from a value of a_v/d = 3 and a common horizontal spreading angle α = 52.5º seem to be appropriate.

- For the case of slabs with certain degree of restraint to the rotation, the position of the contraflexure point between the load and the support influences the shear strength of the slabs. In these cases, according to its definition, the clear shear span a_v results to be the maximum between the distance from the contraflexure point to the inner face of the load pad a_{v1} and the distance from the contraflexure point to the inner face of the support a_{v2}, and this is the value of a_v that has been adopted in the formulation.

- The parametric analysis of the model carried out in section 3.3.4, along with the simplified equations presented in section 3.3.5, are a useful tool for the design and assessment of the shear strength of reinforced concrete slabs in daily engineering. Results yielded by the simplified expressions are similar to the ones obtained using the model but with slightly more scatter (Globally, MV of V_{exp}/V_R=1.137 CoV = 0.145 for the model and MV of V_{exp}/V_R =1.158 CoV = 0.173 for the simplified expressions). Anyhow, obtained values are safe, since 95% of the results have a V_{exp}/V_R ratio greater than 0.90. These expressions allow to easily calculate the shear strength of a slab, without solving all the equations of the model in an iterative way, and the parametric analysis gives an insight into the influence of different parameters on the shear strength of a specimen, which may be useful in the conception and design of new structures.
- Both the general and the simplified methods developed provide more accurate predictions of the 90 tests results, included in the available database, than those obtained using codes provisions. MC-2010 (*LoA II*) and EC-2 with $\alpha = 52.5^{o}$ are the best options, followed by EC-2 with $\alpha = 45^{o}$ and MC-2010 (*LoA I*). As far as ACI 318-19 concerns, since its formulation does not include a factor to take into account the proximity of the load to the support, it yields the most conservative results which also present large scatter.

3.4 Point loads applied away from supports

This section presents a theoretical model for the prediction of the shear and punching-shear strength of one-way reinforced concrete slabs subjected to concentrated loads for the cases where no direct transmission of the load to the support can be considered. It is an extension of the Compression Chord Capacity Model for shear in beams and punching-shear in two-way slabs, and complements the work carried presented in the previous section. Based on observations made in the experimental campaigns mentioned earlier, the model assumes the possibility of two different failure modes (Fig. 3.10). In mode-I or shear failure, failure is considered to occur when the maximum vertical shear stress is reached in a section placed between the load and the support, parallel to the latter, over a certain width, the so called effective width. Mode-II or punching-shear failure is a local failure due to excessive vertical shear stresses around the load along a control perimeter, produced by

the initial spreading of the load into the slab. The value of the maximum shear stresses and the position of the critical sections for each case are derived in this section. The model is applicable to simply supported slabs, cantilever slabs and situations with partial restraint to the rotation, such as intermediate supports and has been validated using a database of 43 shear tests in slabs subjected to a single concentrated load in different supporting conditions. A parametric analysis is also presented, detailing how the different involved variables affect the shear strength and the predicted failure mode, helping to gain insight into this phenomenon.

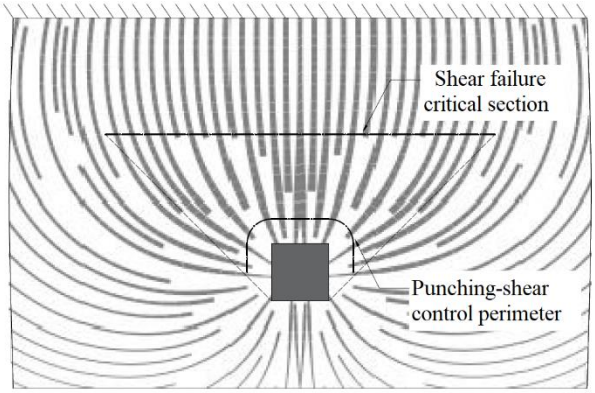

Figure 3.10: Lines representing the shear flow in a one-way slab (obtained with FEM) showing the difference between shear failure and punching-shear failure.

3.4.1 Mode-I: Shear failure

The model derived in this section for this failure mode is based on the Multi Action Shear Model (MASM) and the Compression Chord Capacity Model (CCCM) for shear in slender beams (see section 2.3.3.6 *MASM* and *CCCM*).

3.4.1.1 Load spreading angle

The horizontal load spreading schema adopted for this failure mode is the same as the one adopted for the case of point loads applied close to the support. However, if no limit value is established, as the concentrated load goes away from the support, the effective shear width increases indefinitely,

until it reaches the full width of the slab for a certain value of the a_v/d ratio, depending on the geometry of the loading plate and the slab, and a threshold value must be established in order to obtain accurate results (Lantsoght *et al.* 2013b; Dantas and El Debs 2019; Havolnik *et al.* 2020). This phenomenon has been studied by means of the linear finite element model introduced in section 3.3.2. A cantilever slab and a simply supported slab have been analyzed, both with an effective depth equal to 200 mm and subjected to a square concentrated load of 300 x 300 mm, which are average values of the slabs from the available database. Length and width have been selected in such a way that a load placed at a distance $a_v = 8d$ correspond to mid-span and its theoretical effective width at the support $b_{eff,sup}$ is lower than the whole width of the slab, resulting in a 3500 x 6000 mm slab.

As can be seen in Fig. 3.11 and Table 3.5, when a_v/d is equal to 3, according to the FEA results, the effective shear width at the support $b_{eff,sup}$ is slightly overestimated using the spreading angle of $\alpha = 52.5°$ in both cases. However, when a_v/d ratio is increased to 5 and to 8, the measured effective shear width is much smaller than the values expected if no threshold value is adopted, and tends to the theoretical effective width at the support corresponding to $a_v/d = 3$, $b_{eff,3d}$, with less than 5% difference. The curves have been obtained using the definition of effective shear width shown in Fig. 2.42 in sections separated $0.05d$ within the clear shear span. Thus, the model assumes that the effective shear width stops increasing from a distance equal to three times the effective depth from the inner face of the load pad, and remains constant beyond this point (Fig. 3.12). This threshold value is in good agreement with the observations made in the above-mentioned studies, and must be always lower than or equal to the width of the slab $b_{eff,3d} \leq b_{slab}$.

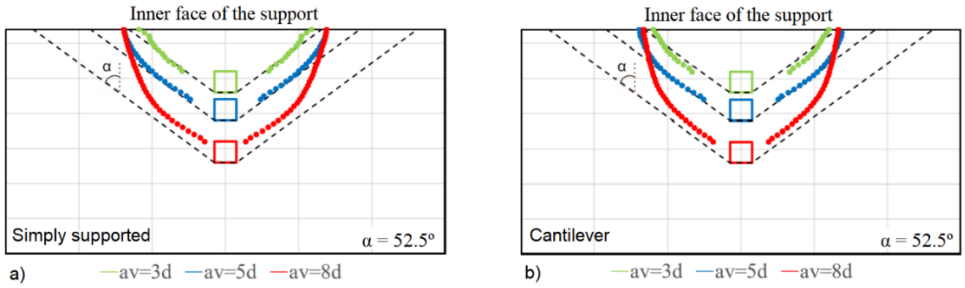

Figure 3.11: Evolution of the effective shear width between the load and the support for different values of the clear shear span a_v: a) Simply supported slab; b) Cantilever slab.

Table 3.5. Ratio between measured effective width at the support and assumed effective width at the support for $a_v = 3d$

	$b_{eff,sup}/b_{eff,3d}$	
	Simply supported	Cantilever
$a_v = 3d$	0.888	0.905
$a_v = 5d$	1.045	1.046
$a_v = 8d$	1.045	1.003

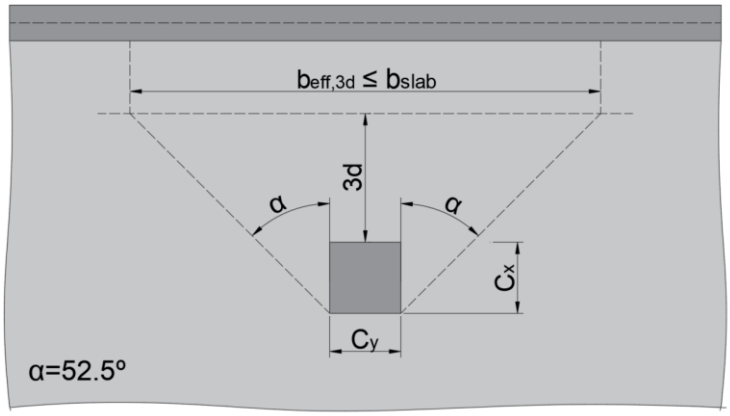

Figure 3.12: Load spreading schema adopted by the model, with a maximum value of the effective width reached at three times the effective width from the inner face of the load pad.

3.4.1.2 Failure surface

The shape of the failure surface is similar to the one assumed in the model for loads applied close to the support. However, the section where the critical crack starts, for both simply supported and cantilever slabs, is not known in advance. This model adopts the hypothesis from the CCCM that, at the time shear failure takes place, the critical crack starts at the section where the bending moment law equals the cracking moment.

For cantilever slabs, the FE model presented before has been used to study the possible location of this section. Three different sizes ($C = d$, $C = 1.5d$, $C = 2d$) and positions ($a_v = 3d$, $a_v = 5d$, $a_v = 8d$) of a square loading plate ($C = C_x = C_y$) have been analyzed. In general, positive longitudinal bending moments are found underneath the loading plate, as can be seen in Fig. 3.13a for the particular case of $C = 1.5d$. However, the distance l_0 from the edge of the plate to the zero bending moment point is more affected by the size of the plate than by the clear shear span (Fig. 3.13b), laying within $0.3d$ for the three sizes studied. (Negative values mean that the contraflexure point lies behind the inner edge of the plate). Thus, the critical shear crack is expected to start at some section close to the edge of the loading plate. For the shake of simplicity, the model assumes that for cantilever slabs the critical crack starts at the inner face of the loading plate, which is a conservative assumption, since it leads to narrower critical sections (Fig. 3.14a).

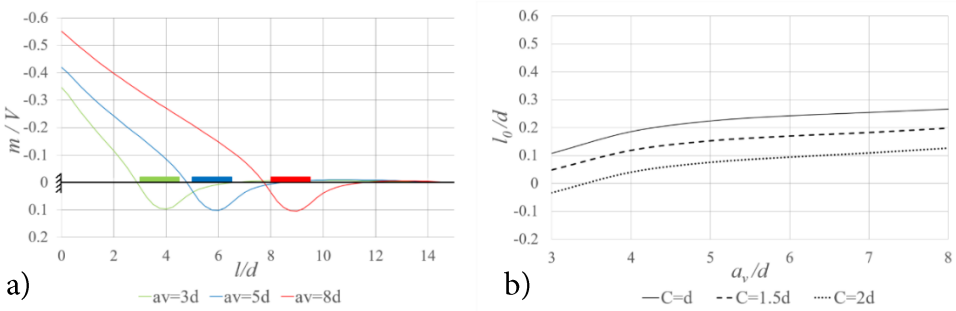

Figure 3.13: a) Dimensionless longitudinal bending moment in the cantilever slab for $C = 1.5d$; b) Evolution of the distance l_0 from the edge of the loading plate to the contraflexure point for different values of a_v.

As far as simply supported slabs concern, the section where the moment per unit width m equals the cracking moment per unit width m_{crack} cannot be estimated from the shape of the longitudinal bending moment diagram. Assuming that at a particular cross-section placed at a distance l from the face of the support (Fig. 3.14b), the total bending moment is given by Eq. (3.20), and considering that for a rectangular cross section the cracking moment is given by Eq. (3.21), the position where the critical crack starts l_{crack} is given by Eq. (3.23), which depends on the total shear V at the support and on the considered flexural effective width $b_{eff,fl}$ of that section. In general, transverse

flexural cracks are reported to appear on the sides of the tested slabs, so for the validation of the model $b_{eff,fl} = b_{slab}$ is considered. In both simply supported (SS) and cantilever slabs, the critical section, where failure occurs, is assumed to be located where the critical crack reaches the neutral axis depth.

$$M = V \cdot l \tag{3.20}$$

$$M_{crack} = \frac{f_{ct} \cdot b_{slab} \cdot h^2}{6} \tag{3.21}$$

$$l_{crack} = \frac{f_{ct} \cdot b_{slab} \cdot h^2}{6 \cdot V} \tag{3.22}$$

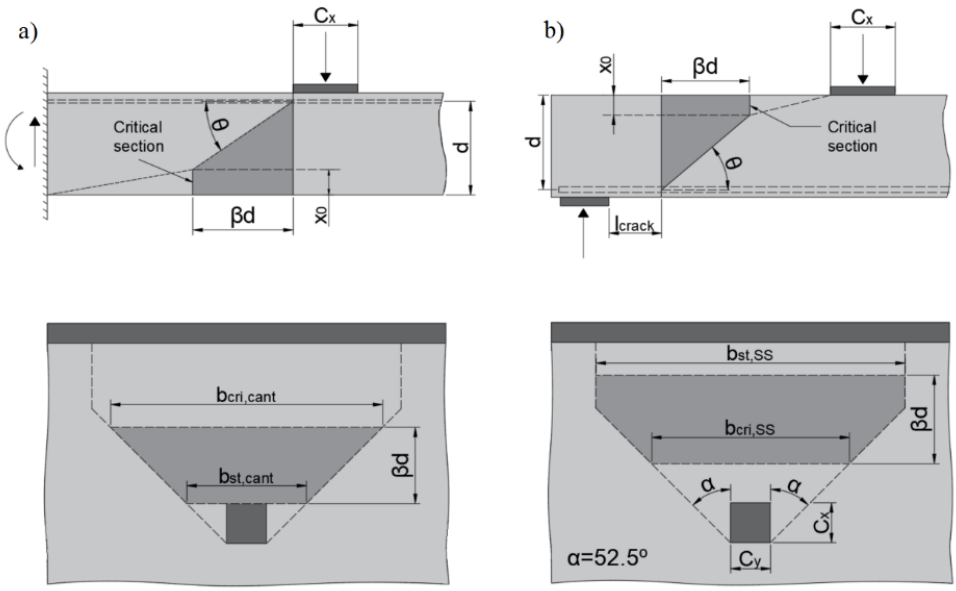

Figure 3.14: Position of the critical section: a) cantilever slab; b) simply supported slab.

The distance βd is the horizontal projection of the first branch of the critical crack, in the tensile part of the slab, whose value is assumed to be equal to 0.85*d*, according to the CCCM and to the available images and drawings of longitudinal saw cuts made on tested slabs (Vaz Rodrigez *et al.* 2008; Rombach and Henze 2017; Reissen *et al.* 2018). As a consequence of these assumptions, the position of the critical section may be established according to the layouts given in Figure 7. As far as slabs with partial restraint to the

rotation at the support concern, the same considerations as in the case of loads applied close to the supports are taken into account (see Fig. 3.5).

3.4.1.3 Equilibrium equations

The free body considered for the equilibrium equations is the one enclosed by the section where the critical crack starts, the critical section and the critical crack itself. On the basis of the above assumptions, the same equilibrium equations are derived for both simply supported and clamped slabs, differing only in the value of the width of the enclosing sections of the free body (Fig. 3.15).

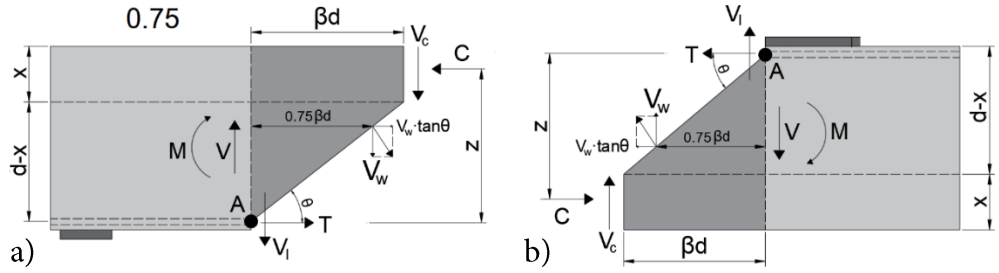

Figure 3.15: Free body diagram: a) simply supported slab; b) cantilever slab.

From the equilibrium of forces and moments at point A, the following equations are derived:

$$C = \mathrm{T} + V_w \cdot \tan\theta \tag{3.23}$$

$$\mathrm{V} = V_c + V_w + V_l \tag{3.24}$$

$$C \cdot z = M + V_c \beta d + 0.75 V_w \beta d (1 + tan^2\,\theta) \tag{3.25}$$

where a value of $0.75\beta d$ for the horizontal lever arm of the resultant of the residual stresses across the critical crack has been adopted, according to the CCCM, and M represents the total bending moment acting over the effective shear width at the starting section of the critical crack. In the case of cantilever slabs, M results in a small value and may be neglected. From Eq. (3.24), the model assumes that the total shear force resisted is equal to the addition of the vertical resultant of the residual tensile stresses through the critical crack

Vw and the total shear resisted in the compression head at the critical section *Vc,* scaled by a factor ζ (see section 2.3.3.6 *CCCM* and Eq. (2.74)) that takes into account the size effect. This model neglects dowel action contribution V_l in specimens without shear reinforcement due to spalling of the concrete cover. This relationship is expressed in a dimensionless way in Eq. (3.26).

$$V_R = (\zeta \cdot V_c + V_w) = (\zeta \cdot v_c \cdot f_{ct} b_{cri} d + v_w \cdot f_{ct} b_w d) = \left(\zeta \cdot v_c + \frac{b_w}{b_{cri}} v_w\right) f_{ct} b_{cri} d \qquad (3.26)$$

where b_{cri} is the effective width at the critical section and b_w is the effective width at the section where the resultant of the residual stresses is applied. The term b_w/b_{cri} accounts for the different width between both sections. For the shear transferred across the crack v_w, Eq. (2.60a) proposed in the MASM may be used. As in the CCM, V_c is obtained by integration of the tangential stresses in the compression head at the critical section, and its ultimate value will be reached when the principal stresses at the point of maximum damage satisfy the equation of the tension-compression branch of the Kupfer's failure envelope given by Eq. (3.12). As derived in the CCCM, the ultimate value of V_c is given by Eq. (3.12). The same consideration regarding the limiting value of the concrete compressive strength f_c to a maximum value of 40 MPa introduced in the model for loads applied to the support has been adopted in this model.

The last step to calculate v_c is to relate normal stresses σ_x and σ_z with the internal forces, and therefore, with the external actions. Vertical stress σ_z is assumed to be equal to zero, as no vertical confinement at the critical section is considered. Horizontal compression stress σ_x at the point of maximum damage may be related to the shear resisted in the compression head by rearranging terms of Eq. 3.25 and assuming a linear elastic behavior in the uncracked concrete zone. Following the derivation detailed in section 2.3.3.6 *MASM* and taking into account that the effective shear width varies along the critical crack, Eq. (3.27) is derived, where b_{st} if the effective shear width of the slab at the section where the critical crack starts. Then, substituting the values of σ_x and σ_z in Eq. (3.12), a general formula is obtained that can be solved for v_c in a iterative way, so the value of the shear strength V_R may be calculated.

$$\frac{\sigma_x}{f_{ct}} = \frac{0.85\left(m_{crack} \cdot \frac{b_{st}}{b_{cri}} + v_c \cdot \beta + \frac{b_w}{b_{cri}} v_w \cdot 0.75\beta \cdot (1 + tan^2\,\theta)\right)}{\frac{x}{d} \cdot \left(1 - \frac{x}{3d}\right)} \qquad (3.27)$$

3.4.2 Mode-II: Punching-shear failure

The mechanical model presented for this failure mode is based on the Compression Chord Capacity Model for punching-shear in slabs (Mari *et al.* 2018). A full explanation of the CCCM-Punching may be found in section 2.3.4.2 *CCCM-Punching.*

3.4.2.1 Influence of the supporting conditions

Punching-shear failure is a local failure around the point load due to excessive vertical shear stresses produced by the initial spreading of the load into the slab. However, despite it is regarded as a local phenomenon, it is affected by the global behavior of the structural element. In this regard, cantilever slabs behave in a different way in comparison with classic punching-shear theories. This issue has been analyzed with the help of the FE model presented herein.

When a cantilever slab is subjected to a point load, bending moments parallel to the support generate tensile stresses in the bottom face of the slab. However, bending moments parallel to the span generates compression stresses in the bottom face between the load and the support, as showed in Fig. 3.13a, which is the area where shear stresses are higher. This means that the critical crack is more likely to develop from a flexural crack at the top face of the slab in this zone, as have been observed experimentally, and a punching-shear failure as such is unlikely to occur except maybe for punctual loads applied in a small area close to the free edge of the slab. Thus, cantilever slabs are not considered for this failure mode.

3.4.2.2 Failure surface

As far as simply supported slabs concern, punching-shear strength is evaluated using the CCCM for punching but assuming some simplifications in order to consider the one-way behavior of the whole specimen. Global one-way behavior provokes an irregular distribution of shear per unit length along the control perimeter, not only because different stiffness between the longitudinal (spanning) direction and the transverse direction, but also because of the difference in the total shear force transmitted to each side of the loading plate in the longitudinal direction, which depends on the position

of the point load within the span. Fig. 3.16 shows shear flows and distribution of shear forces and bending moments acting along the control perimeter for three different positions of the load within the span: $a_v/d = 3$, $a_v/d = 5$ and $a_v/d = 8$ (mid-span). The FE model presented previously has been used for this analysis.

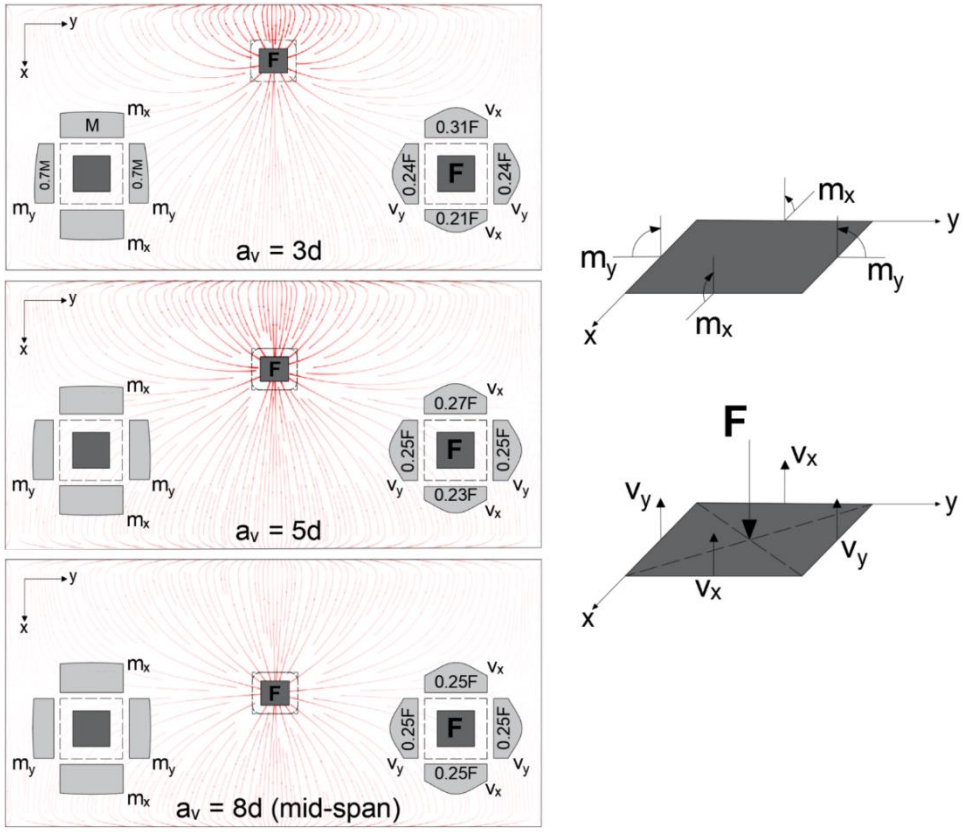

Figure 3.16: Shear flows and distribution of shear forces and bending moments per unit length along the control perimeter for three different positons of the point load.

Since simply supported slabs are statically determinate structures, total shear transferred to each support has to satisfy the global equilibrium conditions always. This means that for the cases where the point load is applied closer to one support than to the other, depending on the length of the span, average shear stress may be significantly higher along the part of the control perimeter faced to the closest support than along the rest of the perimeter, as shown in Fig. 3.16. Thus, the model assumes that a partial failure punching cone develops in the most stressed zone (Fig. 2.39b), whilst average

shear stress along the rest of the control perimeter may remain below its ultimate value, if the load is not applied close to the mid-span.

To account for this behavior, the model adopts a three-sided control perimeter (Vaz Rodriguez *et al.* 2008), with round corners for the case of rectangular loading plates, placed at a distance equal to 0.5*d* from the loading plate, as in the CCCM-Punching and common design codes such as Model Code 2010 and ACI 318-19 (Fig. 3.17). This way, punching-shear failure is considered to occur when the total shear force transferred to the closest support V equals the total shear force resisted by this half of the control perimeter V_R. This approach implies that punching-shear failure is not governed only by the total force applied F, as is usual in axis-symmetric punching models, but also by its position within the shear span, as in one-way shear models. As the load moves away from the support, total shear force at both supports tend to equalize, diminishing shear stresses along the most loaded part of the control perimeter, therefore increasing the total force F necessary to provoke punching-shear failure and increasing the possibility of a flexural failure.

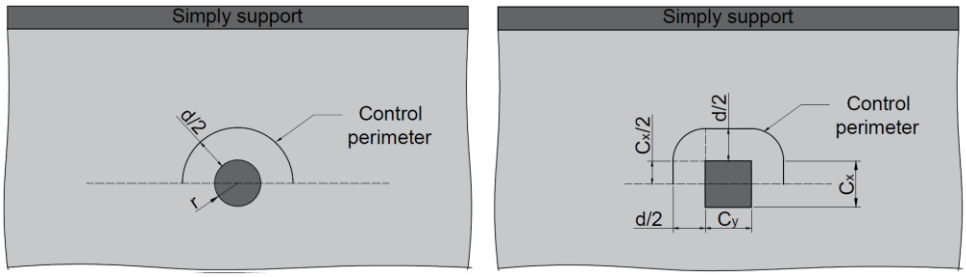

Figure 3.17: Control perimeter considered by the model: a) Circular load; b) Rectangular load.

3.4.2.3 Multi-axial stress state in the slab compressed chord

As detailed in in section 2.3.4.2 *CCCM-Punching*, vertical stresses σ_z in the vicinity of the column enhance the capacity of the concrete of the compression zone to resist shear. To account for the global one-way behavior of the slab, the distribution of σ_z adopted in the model for loads applied close

to the support, for the particular case of simply supported slabs has been adopted. Regarding the in-plane tangential normal stresses σ_φ the conservative value of $m_\varphi / m_r = 1.5$ derived for the CCCM-punching can be used. However, the effect of such confining stresses is moderate, since a tri-axial compressive stress is never reached, because the normal stresses in the compression zone of the slab are always accompanied by shear stresses, generating always a tensile principal stress. Consequently, failure will take place in a compression-compression-tension state of principal stresses (Fig. 2.59a). In order to account for this phenomenon, a modified tension-compression branch of the Kupfer's biaxial failure envelope is adopted (Fig. 2.59b), in which the confined concrete compressive strength f_{cc} is used instead of the regular compressive strength f_c, so that a higher shear stress is needed to reach failure. The Eurocode-2 (EN-CEN 2005) provision for f_{cc} is adopted (Eq. (2.112)), where for the confinement stress σ_{cc} the mean value between the vertical and tangential stresses is used.

3.4.2.4 Equilibrium equations

On the basis of the diagrams showed in Fig. 3.16, bending moment along the control perimeter is greater in the side faced to the closest support than in the lateral sides. This difference leads to a greater ultimate shear stress along the side parallel to the support since, as derived in the CCCM, greater bending moments lead to greater compressive stresses in the compression head, thus to a greater shear strength. However, shear and moment redistributions take place from the longitudinal to the transverse direction for advanced load stages, as reported in Sagaseta *et al.* 2011, 2014, due to uneven cracking in both directions. Shear redistributions increase the percentage of total shear transmitted to the lateral sides of the control perimeter (Fig. 2.54), while bending moment redistributions increase the ultimate shear strength in the lateral sides, reducing it along the side faced to the support. Both types of redistribution contribute to a more uniform distribution of the acting shear stresses and the ultimate shear stress along the three-sided control perimeter. As simplification, the model considers a constant value of the bending moment and average values of the reinforcement ratio $\rho = {(\rho_l + \rho_t)}/{2}$ and the effective depth $d = {(d_l + d_t)}/{2}$ in the longitudinal and transverse directions along the control perimeter. Thus, neutral axis depth x and compressive force

C acting on the compression head are constant along the control perimeter. From the equilibrium of forces and moments in the free body of Fig. 3.18, the following equations are derived:

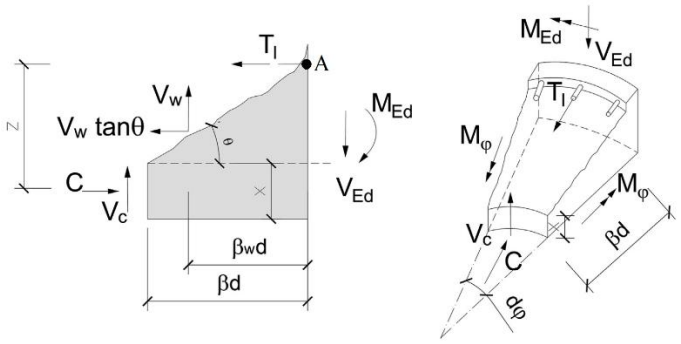

Figure 3.18: Forces in a portion of the slab above the critical crack.

$$C = \mathrm{T} + V_w \cdot \tan\theta \tag{3.28}$$

$$\mathrm{V} = V_c + V_w \tag{3.29}$$

$$C \cdot z + m_\varphi \cdot d\varphi \cdot \beta d = m_{cr}\frac{r_{crack}}{r_{crit}} + V_c \beta d + V_w \, {}^2\!/_3 \, d(1 + \tan^2\theta) \tag{3.30}$$

where the differential term $m_\varphi \cdot d\varphi \cdot \beta d$ due to the tangential moment can be neglected, βd is the horizontal projection of the critical crack, in the tensile part of the slab, whose value $\beta = \frac{0.5 \cdot \left(1 - \frac{x_0}{d}\right)}{x_0/d}$ is derived from the geometrical assumptions, and value of $2/3\beta d$ for the horizontal lever arm of the resultant of the residual stresses across the critical crack β_w has been adopted, according to the CCCM-Punching. Similarly to the shear failure model, from Eq. (3.29), the punching-shear model assumes that the total shear force resisted V_R is equal to the sum of the vertical resultant of the residual tensile stresses through the critical crack V_w and the total shear resisted in the compression head V_c, scaled by the size effect factor ζ (Eq. (2.74)). This equation may be expressed in a dimensionless way by the following expression:

$$V_R = (\zeta \cdot V_c + V_w) = (\zeta \cdot v_c + v_w) f_{ct} u_{cri} d \tag{3.31}$$

where u_{cri} is the length of the considered control perimeter (Fig. 3.17). Shear transferred across the crack v_w is in general a small value in comparison with v_c and the average value of $v_w = 0.05$ considered in the CCCM-Punching has

been adopted. Shear resisted at the compression head v_c is given by Eq. (3.32). Full derivation of this expression may be found in section 2.3.4.2 *CCCM-Punching*. In the same way than for the shear failure mode, the ultimate shear strength will be reached when the principal stresses at the point of maximum damage satisfy the equation of the modified tension-compression branch of the Kupfer's failure envelope (Eq. (3.12)).

$$v_c = 0.682\zeta \frac{x_0}{d} R_t \sqrt{1 - \frac{\sigma_r + \sigma_z}{f_{ct} \cdot R_t} + \frac{\sigma_r \sigma_z}{f_{ct}^2 \cdot R_t^2}} \tag{3.32}$$

Again, the last step to calculate v_c is to relate normal stresses σ_r and σ_z with the internal forces, and therefore, with the external actions. According to CCCM-Punching, σ_r is given by Eq. (3.33), whereas for σ_z, as commented before, the value adopted in the model for loads applied close to the support, for the particular case of simply supported slabs has been adopted. Then, substituting the values of σ_r and σ_z in Eq. (3.32), a general formula is obtained that can be solved for v_c in an iterative way. This way the value of the punching strength V_R is obtained.

3.4.2.5 Validation of the proposed model with the available database

Statistical analysis

Thanks to all the experimental campaigns carried out throughout the last decades, a significant database of shear tests on solid RC slabs supported on linear supports is now available. For the validation of this model, only slabs subjected to a single concentrated load placed at $a_v/d \geq 3$, width $b_{slab} \geq 1$ m and a loading plate with a minimum side length of 100 mm and a maximum aspect ratio $C_y/C_x = 3$ have been selected. In total, 43 experimental tests met the parameters: 22 simply supported slabs, 16 cantilever slabs and 5 slabs with partial restraint to the rotation at the support. The ratio between the experimental results and those predicted by the proposed model V_{exp}/V_R, for each support condition, is presented in Table 3.6 and Fig. 3.18. When the two possible failure modes are considered, as is the case of simply supported slabs and slabs with partial restraint to the rotation, V_R corresponds to the lowest

of the two strength values obtained. The full database and values of the shear strength obtained for each failure mode can be found in Appendix A.

A general good agreement is observed between the predictions and the experimental results, in terms of mean and scatter: $V_{exp}/V_R = 1.12$, $CoV = 0.16$ for simply supported slabs, $V_{exp}/V_R = 1.12$, $CoV = 0.12$ for cantilever slabs and $V_{exp}/V_R = 1.16$, $CoV = 0.11$ for slabs with partial restraint to the rotation. Globally, $V_{exp}/V_R = 1.12$, $CoV = 0.14$ for all the slabs considered. The results obtained do not present a significant variation for the three different static schemas, which indicates that the hypothesis adopted in each case are adequate, as well as the assumption of a common load spreading angle α for all the cases.

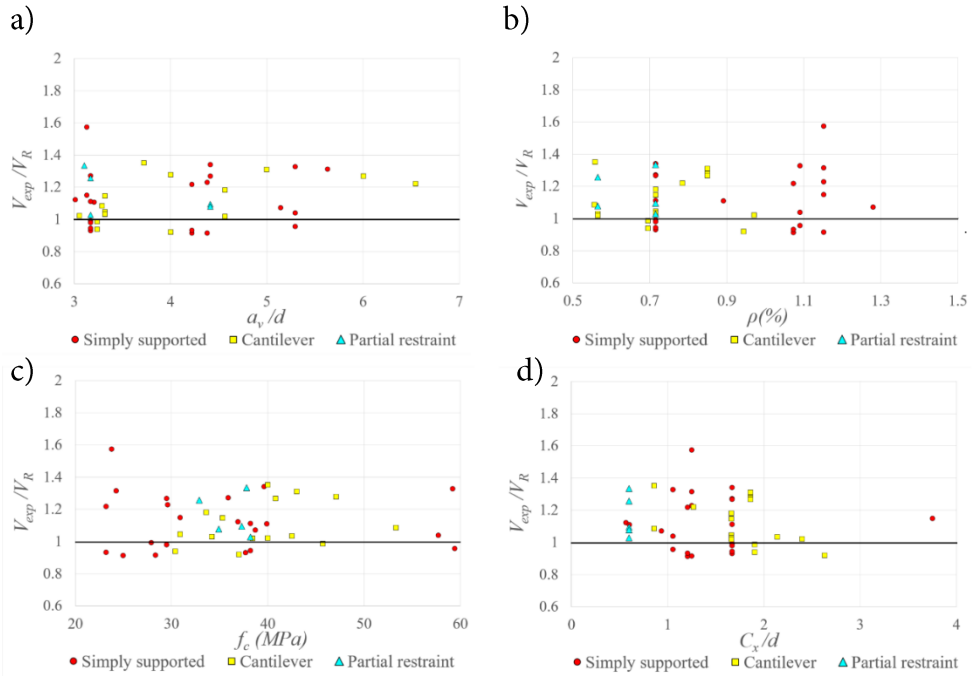

Figure 3.19: Comparison between predictions and test results in terms of different variables: a) a_v/d ratio; b) average reinforcement ratio ρ; c) concrete compressive strength f_c; d) C_x/d ratio.

Table 3.6. Comparison between model predictions and test results

	Simply supported (SS)	Cantilever	Partial restraint (PR)	All slabs
Nº tests	22	16	5	43
V_{exp}/V_R	1.12	1.12	1.16	1.12
Std. deviation (σ)	0.18	0.14	0.13	0.16
CoV (δ)	0.16	0.12	0.11	0.14
min	0.91	0.92	1.03	0.91
max	1.57	1.35	1.34	1.57
Percentile 5%	0.92	0.93	1.04	0.92

Failure mode prediction

For the case of simply supported slabs and slabs with partial restraint to the rotation, if the model predictions for the failure mode is compared to the reported failure mode, 78% of the times it is correctly predicted. The failure mode given by the model for the slabs of the database have been studied in terms of the a_v/d ratio, the average amount of longitudinal reinforcement ρ_l, concrete compressive stress f_c and width of the loading plate to width of the slab C_y/b_{slab} ratio.

Fig. 3.20a shows that punching failure dominates when $a_v/d \geq 5$, whereas not a clear trend is observed for the rest of the cases, with both failure modes being predicted. Regarding the amount of longitudinal reinforcement, both failure modes may be obtained when $\rho_l \approx 1\%$. For higher values, more punching than shear failures are predicted, but more tests are required using a wider range for this parameter, since tests included in the database are concentrated around a few values (Fig. 3.20b). The failure mode seems to be independent of the concrete compressive strength (Fig. 3.20c), since both failure modes are obtained throughout the whole range of available values of this parameter. Finally, Figure 13d shows that when $C_y/b_{slab} < 0.15$, punching-shear failure clearly dominates. For $0.15 \leq C_y/b_{slab} < 0.25$ it seems to be a transition between both failure modes, although almost no data is available, and shear failure becomes dominant when $C_y/b_{slab} \geq 0.25$. These observations are in good agreement with the experimentally obtained failure modes.

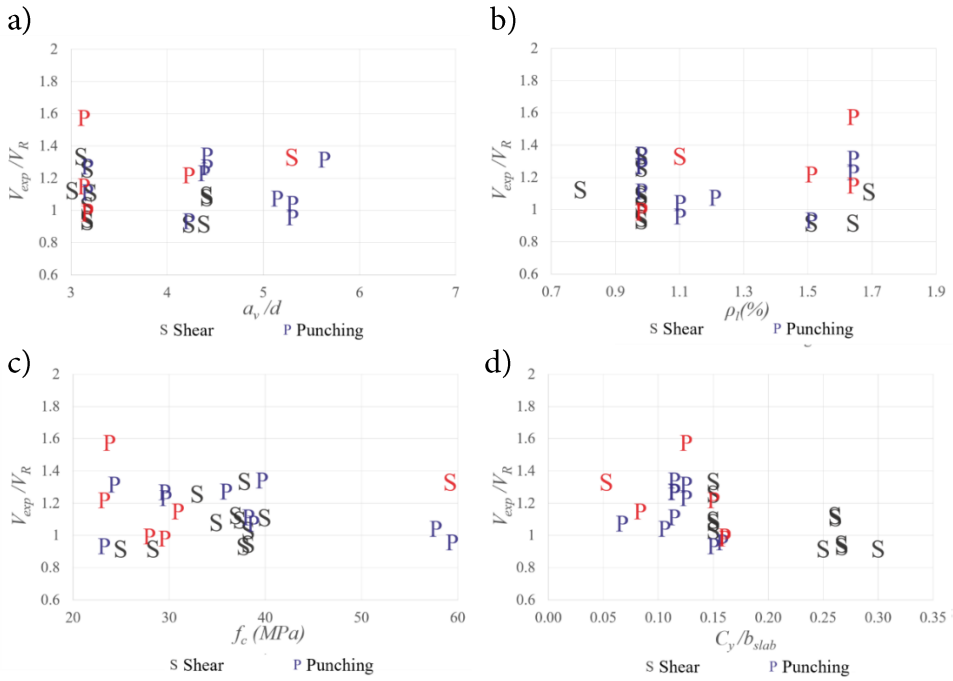

Figure 3.20: Failure mode prediction for simply supported and partially restrained slabs in terms of different variables: a) a_v/d ratio; b) amount of longitudinal reinforcement ρ_l; c) concrete compressive strength f_c; d) C_y/b_{slab} ratio. Red color means a mismatch between the model prediction and the observed failure mode.

Comparison with codes

To conclude, results obtained with the model are compared to those obtained using Eurocode-2, ACI 318-19 and Model Code 2010 LoA II expressions for one-way shear and punching-shear (see section 2.5). In the case of one-way shear, for EC-2 and ACI 318-19 provisions, French load spreading schema for the calculation of the effective shear width has been used, with values of $\alpha = 45^o$ and $\alpha = 52.5^o$. In the case of Model Code 2010, values of α provided on its formulation are used, adopting $\alpha = 60^o$ for the case of simply supported slabs with partial restraint to the rotation.

Two comparisons have been carried out. In the first one, summarized in Table 3.7, no threshold value for the effective shear width has been considered in one-way shear, and the punching-shear strength has been assessed taking into account the total force applied and the whole control perimeter defined in each code. In the second one, summarized in Table 3.8, the threshold value for the effective shear width considered in the proposed model has been

applied except for the MC-2010, since it sets the position of the critical section explicitly. Regarding punching-shear, it has been evaluated considering the three-sided control perimeter defined in Fig. 3.17, placed at the distance from the loading plate adopted in each code and taking into account only the shear force transferred to the nearest support. In both comparisons, V_R corresponds to the minimum value between the one-way shear and the punching-shear strength. To be coherent with the proposed model, for cantilever slabs, only one-way shear failure has been considered.

In general, the proposed model seems to be the most suitable option for assessing the one-way shear and punching-shear strength of one way slabs. When no threshold value for the shear effective width is adopted, one-way shear strength yielded by EC-2 and ACI 318 formulations yield too high values, and the ultimate capacity of the slab is usually limited by the punching-shear strength. This can be observed in the results obtained for cantilever slabs, where punching-shear failure has not been considered and the ratio V_{exp}/V_R is on the unsafe side. No significant influence of the load spreading angle is observed, since in most of the cases the shear effective width is limited by the width of the specimen when the load is applied away from the support. Model Code 2010 yields the best results among codes when no special consideration are taken into account.

Limiting the value of the maximum effective shear width and using a three-sided control perimeter significantly improves the safety of the results obtained with EC-2, keeping an acceptable level of accuracy. However, they are still unsafe for the case of cantilever slabs. ACI 318 is not significantly affected by this considerations, and Model Code 2010 slightly improves the accuracy of the results.

Table 3.7. Comparison between model predictions and code provisions. Case I: no threshold value for one-way shear effective width and whole control perimeter for punching-shear.

	Simply supported (SS)			Cantilever			Partial restraint (PR)			All slabs		
Nº tests	22			16			5			43		
	V_{exp}/V_R	*CoV (δ)*	*% match*	V_{exp}/V_R	*CoV*	*% match*	V_{exp}/V_R	*CoV*	*% match*	V_{exp}/V_R	*CoV (δ)*	*% match*
CCCM	1.12	0.16	73	1.12	0.11	-----	1.16	0.12	100	1.12	0.14	78
EC-2 α=45º	1.03	0.18	82	0.75	0.16	-----	1.03	0.19	80	0.93	0.23	81
EC-2 α=52.5º	1.00	0.16	86	0.62	0.17	-----	0.91	0.12	60	0.79	0.28	81
ACI α=45º	1.69	0.32	64	1.00	0.17	-----	1.34	0.25	100	1.39	0.38	70
ACI α=52.5º	1.66	0.35	64	0.83	0.18	-----	1.13	0.18	100	1.29	0.45	70
MC-2010 (LoA II)	1.47	0.24	77	1.30	0.17	-----	1.21	0.15	100	1.38	0.22	81

Table 3.8. Comparison between model predictions and code provisions. Case II: threshold value for one-way shear effective width and three-sided control perimeter for punching-shear.

	Simply supported (SS)			Cantilever			Partial restraint (PR)			All slabs		
Nº tests	22			16			5			43		
	V_{exp}/V_R	*CoV (δ)*	*% match*	V_{exp}/V_R	*CoV*	*% match*	V_{exp}/V_R	*CoV*	*% match*	V_{exp}/V_R	*CoV (δ)*	*% match*
CCCM	1.12	0.16	73	1.12	0.11	-----	1.16	0.12	100	1.12	0.14	78
EC-2 α=45º	1.30	0.21	68	0.87	0.12	-----	1.19	0.14	20	1.01	0.19	59
EC-2 α=52.5º	1.30	0.18	68	0.70	0.14	-----	1.19	0.14	20	0.85	0.22	70
ACI α=45º	1.72	0.21	64	1.17	0.13	-----	1.47	0.17	100	1.49	0.31	70
ACI α=52.5º	1.70	0.32	77	0.94	0.14	-----	1.35	0.16	20	1.38	0.39	67
MC-2010 (LoA II)	1.41	0.29	77	1.33	0.17	-----	1.21	0.14	100	1.35	0.24	81

3.4.2.6 Summary

A theoretical model for the shear strength of RC slabs, linearly supported and subjected to concentrated loads away from the support ($a_v/d \geq 3$), has been described and verified with the results of experimental campaigns carried out throughout the last decades. The developed model proposes two possible failure modes, shear and punching-shear, derived from both the Compression Chord Capacity Model for slender beams and the CCCM for axisymmetric punching-shear respectively, by identifying the differences in the behavior between beams, two-way and one-way slabs, and incorporating them into the governing equations in each case. The following conclusions can be drawn from the performed studies:

- The model accounts for a significant number of variables involved in the phenomenon, such as the clear shear span, the concrete compressive strength, the reinforcement ratio, the effective depth, the load spreading angle, the size effect and the dimensions of the loaded area. It is applicable to simply supported slabs, cantilever slabs and slabs with partial restraint to the rotation at the support.
- Good accuracy has been obtained when comparing the model predictions with the test results available, with a mean value of the ratio V_{exp}/V_R =1.12, and CoV = 0.16 for simply supported slabs, MV of V_{exp}/V_R =1.12, CoV = 0.12 for cantilever slabs and MV of V_{exp}/V_R =1.16, CoV = 0.11 for slabs with partial restraint to the rotation at the support. Globally, MV of V_{exp}/V_R =1.12, CoV = 0.14 for the 43 slabs considered. Furthermore, 95% of the results have a V_{exp}/V ratio greater than 0.92.
- Failure modes trends predicted by the model are in agreement with the experimental observations for the analyzed variables. When $a_v/d \geq 5$ or $C_y/b_{slab} \leq 0.15$, model predictions are mostly punching failures, as observed experimentally, whereas shear clearly dominates when $C_y/b_{slab} \geq 0.25$. No significant influence of the concrete compressive strength or the longitudinal reinforcement ratio has been observed experimentally nor in the model results.
- In comparison with the analyzed design codes, the proposed model provides the best results when predicting the ultimate capacity of the slabs included in the available database in terms of safety and accuracy. As far as codes concern, best results are obtained with Model Code 2010 *LoA* II.

Eurocode-2 yields unsafe results if no threshold value for the effective shear width is used, whereas ACI 318 yields quite conservative results and presents the highest scatter.

Chapter 4

Punching-Shear strength of two-way slabs subjected to concentrated loads and in-plane tension

4.1 Introduction

Reinforced concrete slabs are structural components widely used in both bridges and buildings, due to their great versatility and ease of construction. These structural elements are mainly subjected to bending and shear, but in some cases in practice, in-plane tensile stresses may arise and act simultaneously with the out-of-plane design loads. For instance, this situation may happen in top slabs of box girder bridges subjected to hogging bending moments, decks of tied arch bridges, or floor slabs subjected to horizontal loads, where skew compression fields going from the loaded side to the restraining columns of the opposite side may generate tensile stresses in the perpendicular direction, as shown in Fig. 4.1. The phenomenon of punching shear has been extensively studied over the years, both theoretically and experimentally (*fib* 2001; 2017). However, few studies have been carried out regarding punching-shear when there are tensile forces in the mid-plane of the slabs, so that further research is needed to quantify the effects of such forces on the capacity of the slabs.

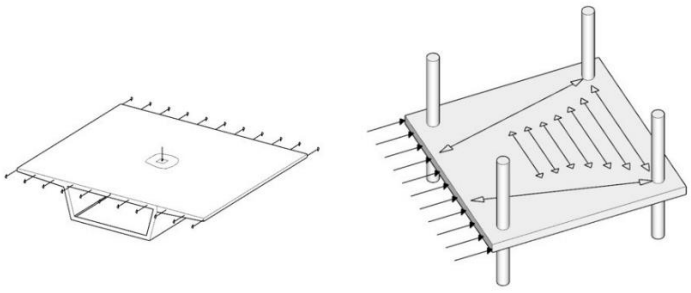

Figure 4.1: Situations found in practice of RC slabs subjected simultaneously to a point load and in-plane tension.

Two experimental campaigns were carried out at Cornell University in the late '70 and early '80 (Abrams 1979; Jau *et al.* 1982), in the context of an investigation for the U.S Nuclear Regulatory Commission, where several 1.2 x 1.2 x 0.150 m reinforced concrete slabs subjected to bi-axial tension (Fig. 4.2a) were tested in punching. In the same period of time, P.E. Regan (1983), presented the results of three 1.5 x 1.5 x 0.125 m slabs subjected simultaneously to unidirectional in-plane tension and an out-of-plane concentrated load on its center, all of them with different support scheme (Fig. 4.2b). More recently, experimental studies have been conducted by Bui *et al.* (2017b) regarding the influence of uniaxial tension on the shear strength of 2.6 x 4 x 0.3 m simply supported concrete slabs subjected to concentrated loads close to the support (Fig. 4.2c). All these studies concluded that axial tensile stresses reduce punching and shear strength respectively.

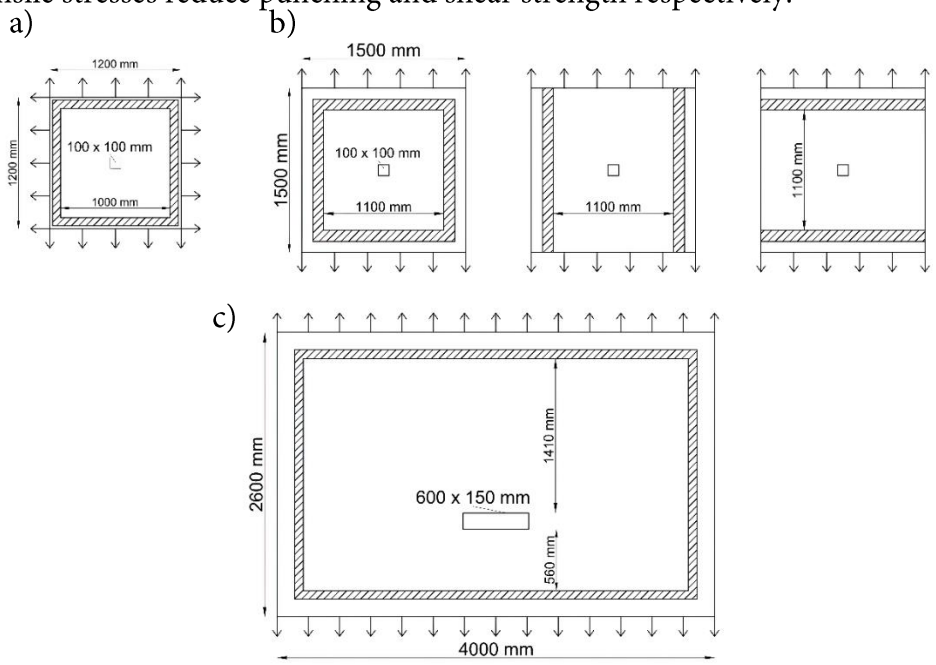

Figure 4.2: Geometry of the specimens tested by: a) Abrams (1979); b) Regan (1983); c) Bui *et al.* (2017b).

In this context, an extension of the CCCM-Punching (*see section 2.3.4.2 The Compression Chord Capacity Model for axis-symmetric punching*) has been developed to account for the effects of tensile forces on the shear resisting actions. The fundamentals of the modifications carried out are

explained and new equations are derived and validated with the results of the experimental campaigns found in literature. A comparison of the strength predictions obtained using the proposed model and code provisions included in section 2.5 is also presented. In addition to that, as part of this investigation, an experimental campaign, detailed later in this chapter, was carried at the Laboratory of Technology of Structures and Materials of the Universitat Politècnica de Catalunya (UPC), with the goal of providing experimental evidence and contributing to the model validation for the particular case of uniaxial in-plane tension.

4.2 Proposed mechanical model for the prediction of the punching-shear strength of two-way RC slabs subjected to point loads and in-plane tensile forces

4.2.1 Effects of tension on the punching-shear behaviour

In order to extend the CCCM-Punching (Mari *et al.* 2018) to account for the influence of in-plane tension, first, the effects of such tension on the mechanics of the slabs should be identified. These effects are at least the following:

1) The crack width increases due to the presence of a tensile force, so the aggregate interlock in the critical crack and, therefore, the shear resisted by the web, decreases. Such effect does not affect the assumption of the original model of a very small web contribution.

2) The angle θ of inclination of the cracks may be affected by the presence of a tensile force. However this variation is considered to be small, as failure takes place inside a D-region subjected to a complex multi-axial state of

stresses. Hence, the inclination of the crack and the position of the control perimeter have been assumed to not be affected, and the hypotheses of the original model have been adopted.

3) The presence of a tensile force reduces the depth of the neutral axis, thus reducing the contribution of the compressed chord.

4) For a given bending moment, M, the tensile force decreases the compression stress in the un-cracked chord, thus reducing its ability to transmit shear stresses.

5) The axial tensile force increases the tensile stresses in the flexural reinforcement. Therefore, it is possible that for a tensile force that produces concrete cracking, a premature yielding takes place in the longitudinal reinforcement parallel to the tension direction.

4.2.2 Derivation of the new set of equations

The neutral axis depth x, in a section subjected to a bending moment M and an axial tensile force T, according to Marí *et al.* (2017), can be approached by:

$$x = x_0 \left(1 - 0.1 \frac{T \cdot d}{M}\right) \tag{4.1}$$

where d is the effective depth and x_0 is the neutral axis depth in pure flexure, without tensile force. The influence of the tensile force T on the compression stresses acting on the un-cracked concrete chord can be obtained by including the tensile force in the equilibrium equations of a slice of slab (Eq. (4.2) to Eq. (4.4)), as indicated in Fig. 4.3.

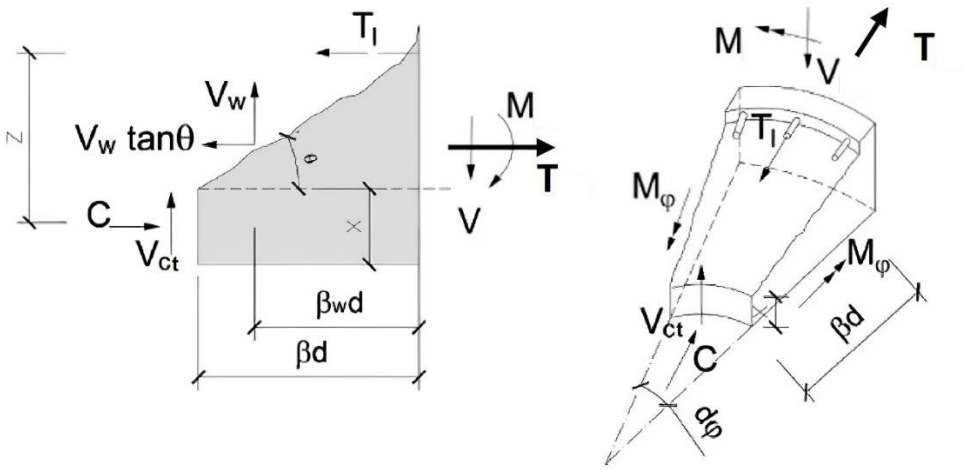

Figure 4.3: Forces acting on a differential slice of slab, including in-plane tensile forces.

$$C = T_l + V_w \cdot \tan\theta - \mathrm{T} \tag{4.2}$$

$$\mathrm{V} = V_{ct} + V_w \tag{4.3}$$

$$C \cdot z + m_\varphi \cdot d\varphi \cdot \beta d = m_{cr}\frac{r_{crack}}{r_{crit}} + V_{ct}\beta d + V_w\beta_w d(1+\tan^2\theta) - 0.5 \cdot \mathrm{T} \cdot z \tag{4.4}$$

where the differential term $m_\varphi \cdot d\varphi \cdot \beta d$ due to the tangential moment can be neglected. The distance βd is the horizontal projection of the critical crack, in the tensile part of the slab, for which the value of $\beta = \frac{0.5\cdot\left(1-\frac{x}{d}\right)}{x/d}$ from the CCCM-Punching has been adopted. V_{ct} is the shear resisted in the compression zone and V_w is the vertical resultant of the residual tensile stresses through the critical crack, whose horizontal lever arm is assumed to be $\beta_w d = 2d/3$, as in the original model. From Eq. (4.4), adopting the hypothesis for the position of the point of maximum damage at the critical section, located at a distance $\lambda = 0.425x$ from the neutral axis, and a linear distribution of normal stresses in the compression zone, the normal stress in the radial direction at the critical point is given by Eq. (4.5), where $z = d - x/3$ has been adopted as the flexural lever arm.

$$\sigma_r(\lambda) = \frac{2\lambda C}{xz} = \frac{2\lambda(m_{cr}\frac{r_{crack}}{r_{crit}} + V_c\beta d + V_w\beta_w d(1+\tan^2\theta) - 0{,}5\mathrm{T}\left(d-\frac{x}{3}\right))}{x(d-\frac{x}{3})} \quad (4.5)$$

The fundamental equations of the model are those that allows obtaining the shear stress at the critical point of the compressed chord at failure. This occurs when the principal stresses at the point of maximum damage reach the modified Kupfer failure envelope (Fig. 2.61). Then, considering the assumed parabolic distribution of shear stresses in the compression zone, the shear force resisted in this area in the presence of in-plane tensile force, V_{ct}, is obtained by integration of the shear stresses, what is straightforward and can be expressed in a dimensionless form by:

$$v_{ct} = \frac{V_{ct}}{f_{ct}bd} = 0.682\cdot\frac{x}{d}\cdot\frac{\sigma_1}{f_{ct}}\sqrt{1-\frac{\sigma_r+\sigma_z}{\sigma_1}+\frac{\sigma_r\sigma_z}{\sigma_1^2}} = 0.682\frac{x}{d}R_t\sqrt{1-\frac{\sigma_r+\sigma_z}{f_{ct}\cdot R_t}+\frac{\sigma_r\sigma_z}{f_{ct}^2\cdot R_t^2}} \quad (4.6)$$

where x/d is the neutral axis depth and R_t is the ratio between the principal tensile stress and the tensile strength at the critical point, which is provided by the modified modified Kupfer and Gerstle's envelope equation in the tension-compression branch given by Eq. (4.7). The value of σ_z to be used in Eq. (4.6) can be obtained, according to the CCCM-Punching, from Eq. (4.8). For the sake of simplicity, since V_w is much smaller than V_{ct}, and an average minimum value of $v_w = V_w/(f_{ct}\cdot u_{cri}\cdot d) = 0.05$ has been considered.

$$\frac{\sigma_1}{f_{ct}} + 0.8\frac{\sigma_2}{f_{cc}} = 1 \rightarrow R_t = \frac{\sigma_1}{f_{ct}} = (1 - 0.8\frac{\sigma_2}{f_{cc}}) \quad (4.7)$$

$$\frac{\sigma_z}{f_{ct}} = 1.25\frac{V}{f_{ct}\pi r_{crit}^2} = 2.5\frac{(v_c+v_w)}{r_{crit}/d} \quad (4.8)$$

These three expressions comprise a system of non-linear equations that has to be solved iteratively. Once v_{ct} is obtained, according to the equilibrium of vertical forces acting on the considered free body (Eq. (4.3)), the total shear resisted V_{Rt} is equal to the addition of V_w and V_{ct}, which have to be scaled by a factor ζ (Eq. (2.76)) that takes into account the size effect, so $V_{Rt} = (\zeta\cdot V_{ct} + V_w) = (\zeta\cdot v_{ct} + v_w)\cdot f_{ct}\cdot u_{cri}\cdot d$, where u_{crit} represents the length of the control perimeter. The shear span a, to be used in the size effect parameter, can be estimated as the average distance from the position of the line of zero radial bending moment to the center of the column. This model neglects dowel

action contribution in specimens without shear reinforcement due to spalling of the concrete cover. In the following equations, the value of the external tension is expressed in relation to the tensile force producing the cracking of the slab's cross-section, or $T_{cr} = A_c \cdot f_{ct}$, with A_c being the composite concrete and steel area of the cross-section of the slab and f_{ct} the concrete tensile strength. This way, if v_{ct} is plotted as a function of x_0/d for different values of the ratio T/T_{cr}, a close to a linear relationship can be observed (Fig. 4.4). According to this, the model predicts that the higher the tensile force, the lower is the shear resisted. After a statistical analysis, Eq. (4.9) was derived, which accurately approaches the values obtained solving the model equations. For this simplified expression, the tensile strength of concrete f_{ct} can be estimated from the compressive strength using the expression provided in the Eurocode-2 ($f_{ct} = 0.3 f_c^{2/3}$). It is important to highlight that when T = 0, Eq. (4.9) is equal to the simplified expression derived in the CCCM-Punching (Eq. (2.127)).

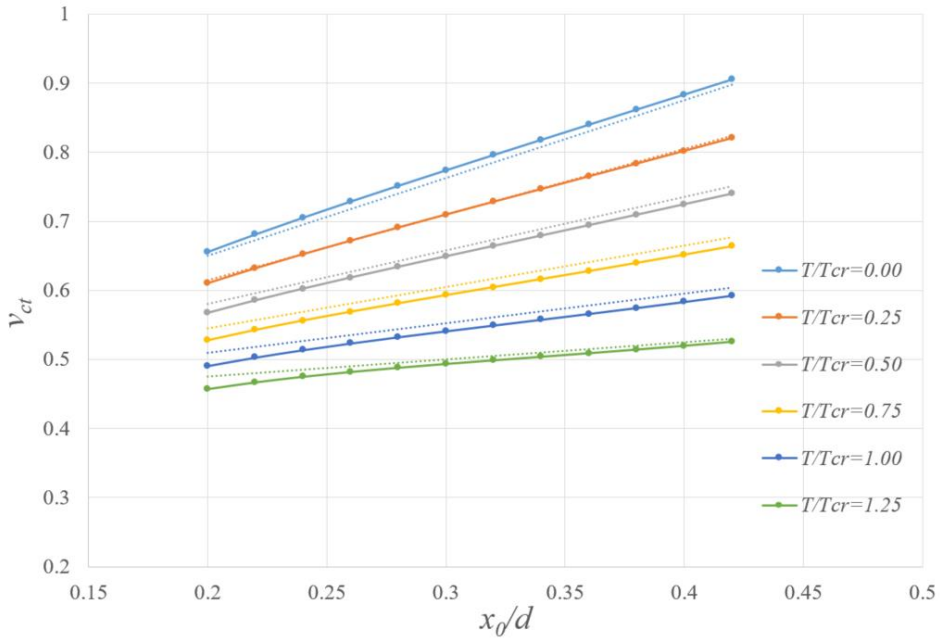

Figure 4.4: Dimensionless shear carried by the un-cracked concrete chord v_{ct} as a function of the x_0/d ratio for different values of T/T_{cr}. Dotted lines represent the simplified expression.

$$V_{Rt} = \mathrm{V}_{ct} + V_w = \zeta \left(\left(1.125 - 0.85 \frac{T}{T_{cr}} \right) \frac{x_0}{d} + 0.425 \right) \cdot f_{ct} \cdot u_{crit} \cdot d \qquad (4.9)$$

For values of $T>T_{cr}$, the contribution of the concrete to resist tension is not considered, being the tensile force resisted only by the reinforcement, whose stress increases considerably, and the maximum punching-shear capacity may be limited by the yielding of the reinforcement. The effect of in-plane tensile forces is considered by using a reduced steel strength in the tension direction, given by:

$$f_y^* = f_{y-} \frac{T}{A_s} \qquad (4.10)$$

Due to this reduction, the punching strength associated to reinforcement yielding, V_y, may become dominant, diminishing even more the strength and stiffness of the slab. In that case, the punching shear strength of slabs subjected to in-plane tensile forces is given by:

$$V_{Rt} \leq V_y \approx 2\pi f_y^* d^2 \left(1 - \frac{\rho f_y^*}{2 f_c} \right) \qquad (4.11)$$

In the case of slabs subjected to uniaxial in-plane tensile forces, Eq. (4.9) must be applied only to the part of the control perimeter affected by the tensile stresses, which is approximately half of the total perimeter, as is shown in Fig. 4.5. Then, the shear resisted along the control perimeter $V_{Rt/2}$, may be estimated as the mean value of the shear force resisted in the faces affected and non-affected by the tensile stresses, obtained using Eq. (4.9) with the corresponding value of the external tension T (Eq. (4.12)). In this case, if Eq. (4.11) is not satisfied, V_{Rt} has to be replaced by V_y in Eq. (4.12).

$$V_{R,t/2} = \frac{V_R}{2} + \frac{V_{Rt}}{2} = \zeta \left(\left(1.125 - 0.425 \cdot \frac{T}{T_{cr}} \right) \cdot \frac{x_0}{d} + 0.425 \right) \cdot f_{ct} \cdot u_{crit} \cdot d \qquad (4.12)$$

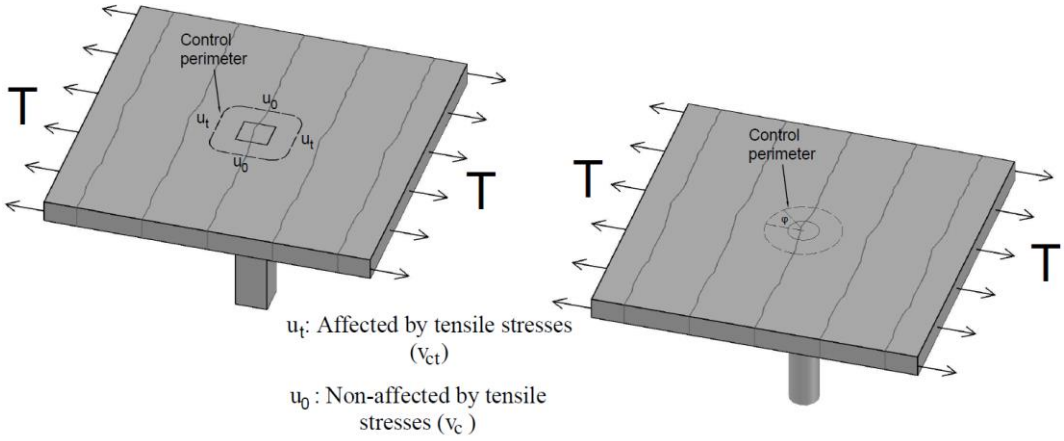

Figure 4.5: Parts of the control perimeter affected and non-affected by tensile stresses in the case of uniaxial in-plane tension.

The effect of the yielding of the reinforcement is shown in Fig. 4.6 for the particular case of uniaxial tension and considering $f_{ct} \approx 3$ MPa ($f_c = 30$ MPa). As can be seen, for high reinforcement ratios parallel to the tensile force ($\rho_l \geq 0.013$), a moderate linear reduction of the punching-shear capacity takes place, since failure is governed by Eq. (4.9). However, as ρ_l decreases, for certain value of T/T_{cr}, the reduction of the punching strength increases, since yielding of reinforcement takes place prior to punching failure and the ultimate capacity in the direction of the in-plane tension is governed by Eq. (4.11). This fact may happen even for $T<T_{cr}$ for low reinforcement ratios ($\rho_l < 0.011$). Furthermore, it can be observed that for $T=T_{cr}$, another change of slope of the curves takes place, since the slab cracks under the tensile force and a sudden increment of tensile stress in the reinforcement occurs. This fact also takes place even for higher reinforcement ratios ($\rho_l \geq 0.013$), although in these cases the increment of stress in the reinforcement does not provoke yielding. Finally, a minimum punching strength is reached (bottom horizontal line) of value $V_{Rt/2}/V_R = 0.5$, which corresponds to the shear resisted by the portion of the control perimeter parallel to the tensile forces, not affected by tensile stresses.

In case of slabs supported on circular columns, either subjected to biaxial or uniaxial tension, both the tensile force per unit length normal to the

control perimeter and the neutral axis depth depend on the angle φ (see Fig. 4.5). In that case, the punching strength should be obtained by integration of the shear per unit length obtained for each value of the angle φ along the control perimeter. However, parametric studies carried out showed that the error made using in a simplified way a square control perimeter of the same length is 1% for T/T_{cr} = 0.25 and 5% for T/T_{cr}= 1

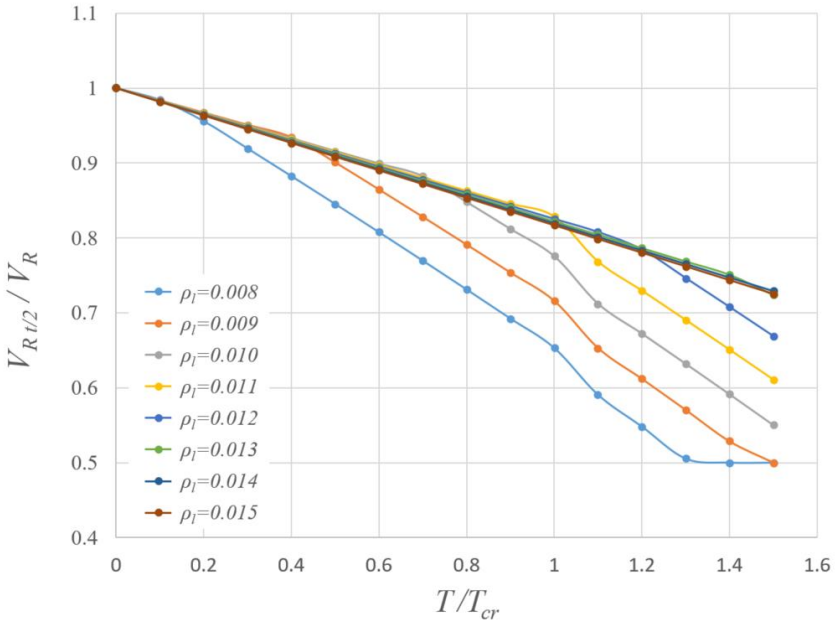

Figure 4.6: Influence of ρ_l on the reduction of the shear punching strength as *T/Tcr* increases for the unidirectional tension case.

4.3 Validation of the model

4.3.1 Experimental campaign

4.3.1.1 Specimens tested

In order to validate the model for the particular case of uniaxial in-plane tension, a set of 5 slabs of 1650 x 1650 x120 mm were cast at the Laboratory of Technology of Structures and Materials of the Universitat Politècnica de Catalunya (UPC). The dimensions of the slabs tested were based on the punching-shear tests performed by El-Salakawy *et al.* (1997) and Adetifa and

Polak (2005), and try to represent approximately a continuous building slab supported by an orthogonal column grid of 3.75 m of span length in the two orthogonal directions. The slabs were supported on 8 points placed at the vertices of a regular octagon, equidistant 765 mm from the center of the punching vertical point load, which was applied on its center. Even though the thickness of the specimens may be slightly small to represent deck-slab of bridges or actual floor slab, this size was selected to give continuity to the two experimental campaigns mentioned above, which have been a starting point for the present experimental campaign.

The slabs were subjected to tension in their plane in only one direction, through 10 post-tensioning bars 25mm in diameter and 600mm in length, with a maximum allowable tensile stress f_{pu}=1050 MPa, partially embedded in 2 opposite faces (5 bars on each side) (Fig. 4.7 and Fig. 4.8). These bars connected the slabs to the tensioning system in order to apply the tensile force to the specimens. Although most of the tension was transmitted to the concrete by bond, anchors were placed at the embedded end of the bars for greater safety. The value of the external tension applied during the tests, as previously mentioned, is measured in relation to the tensile force producing the cracking of the slab or $T_{cr} = A_c \cdot f_{ct}$, with A_c being the composite concrete and steel area of the cross-section of the slab and f_{ct} the tensile concrete strength. Averaging the values of the tensile strength obtained from characterization tests (Table 4.2), $T/T_{cr} = 1$ approximately correspond to σ_t = 3.3 MPa. The specimens were designed so that punching failure takes place before flexural failure up to a value of $T = 1.5T_{cr}$, having computed the ultimate punching capacity using some of the code formulations included in section 2.5.

The slabs were reinforced with two steel meshes arranged on the upper and lower faces (Fig. 4.8). In the direction parallel to the external tension applied, the same amount of reinforcement was placed on the upper and lower faces in all the slabs (A1, B1, A2, A3, A4). This reinforcement consisted of Φ12 mm bars spaced 105 mm in slabs type A (ρ_l= 0.011) and Φ16 mm bars spaced 105 mm in slab B1 (ρ_l = 0.020).

In the direction perpendicular to the applied tension, on the lower face, an assembly consisting of 12mm bars spaced 100 mm was arranged in all cases (ρ_t = 0.013), while 12 mm bars spaced 200 mm were arranged on the upper

face. Additional reinforcing bars were placed in the vicinity of the post-tensioning bar anchors, as a measure of local reinforcement. The tensile reinforcement ratio and effective depth of each type of slab are shown in Table 4.1. The large amount of longitudinal reinforcement in specimen B (ρ_l = 2%) may give place to higher values of the contribution of aggregate interlock and dowel action to the punching strength than usual in practical cases. However, the experimental results of slab B can be adequate to identify how the increment of reinforcement ratio affects the structural response and to verify how theoretical models account for the above mentioned effects on the punching shear resisting mechanisms.

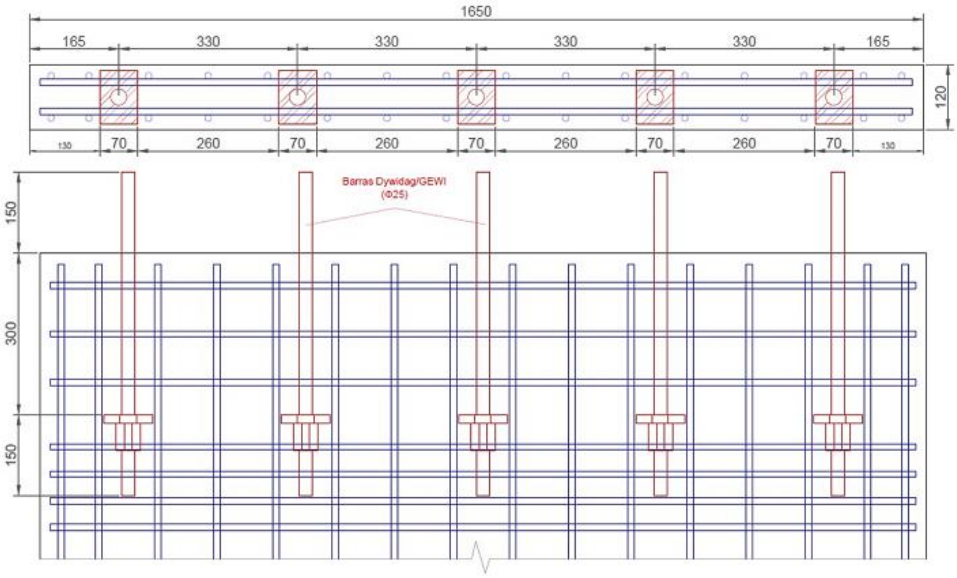

Figure 4.7: Position of post-tensioning bars inside the slab.

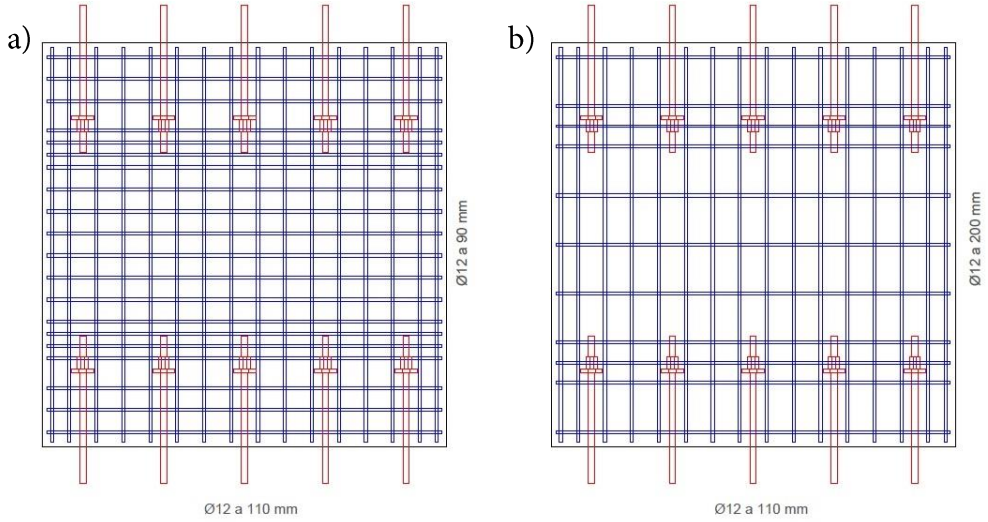

Figure 4.8: Reinforcement layout of "type A" slabs. a) Tension side. b) Compression side.

The punching load was transmitted to the slab through a 145 x 145 x 30 mm steel plate located in its center. Due to the configuration of the

experiment, the slabs were tested face down with respect to their real position in a building slab, in which the reaction of the column goes upwards and the tensile reinforcement is arranged on the upper face. The slabs were cast using ready-mixed concrete from a local supplier. Normal strength class C30/37 with crushed limestone aggregate with a maximum size of 10 mm was used. To characterize the concrete before each punching test, standard compression (UNE-EN 12390-3), splitting (UNE-EN 12390-6) and elastic modulus (UNE-EN 12390-13) tests were performed. The specimens were reinforced with deformed bars of B500-S steel. Yield stress and elastic modulus of each diameter of reinforcing steel (UNE-EN ISO 6892-1) were also characterized. Results are shown in Table 4.2.

Table 4.1. Reinforcement ratios and effective depths of the tension side reinforcement.

	Parallel to tension			**Perpendicular to tension**		
Slab type	**Reinforcement area (mm^2)**	**Reinforcement ratio**	**Effective depth (mm)**	**Reinforcement area (mm^2)**	**Reinforcement ratio**	**Effective depth (mm)**
A	1810	0.0108	99	1810	0.0130	87
B	3217	0.0197	97	1810	0.0133	85

Table 4.2. Mean values of material properties.

Concrete

Test Ref.	T/T_{cr}	fc (Mpa)	fct (Mpa)	Ec (Gpa)	d_max (mm)	Age (days)
A1	0	37.6	3.38	29.2	10	160
B1	0.44	37.7	3.41	29.8	10	225
A2	0.69	35.9	3.05	28.3	10	204
A3	1.02	37.4	3.13	29.0	10	183
A4	1.26	36.7	3.36	30.3	10	218

Steel

Diameter (mm)	fy (MPa)	Es (MPa)
10	525.9	216.3
12	535.9	210.7
16	536.8	201.6

4.3.1.2 Test set-up

Four out of the five tested specimens were subjected to different levels of tensile stresses, while the control slab was left un-tensioned. To introduce the tensile force in the slabs, an auxiliary steel structure, whose plan dimensions were 2500 x 2840mm, was built. This structure consisted of a rectangular steel frame surrounding the slab, as shown in Fig. 4.9. On both sides parallel to the tensile forces, the frame consisted of a single HEB 300 profile, while on both perpendicular faces it was formed by two HEB 300 profiles arranged in parallel and separated four centimeters, to allow the passage of bars (extensions) connected to the above mentioned bars partially embedded in the slab. On one of these faces, a passive anchor for the tensioning bars was used whereas they were prestressed from the other end, with the help of force-

controlled hollow jacks connected to the extension bars (Fig. 4.10). The steel structure was set at the appropriate height with the help of four height-adjustable supports designed for the experimental campaign and located under each of the four corners of the frame. For safety reasons, once the desired external force value was reached, the bars were anchored and the jacks were disconnected from them. This fact caused a small loss of the tensile force during the test that was quantified by the arranged instrumentation. The theoretical loads to be applied and the values measured during the tests are shown in Table 4.3.

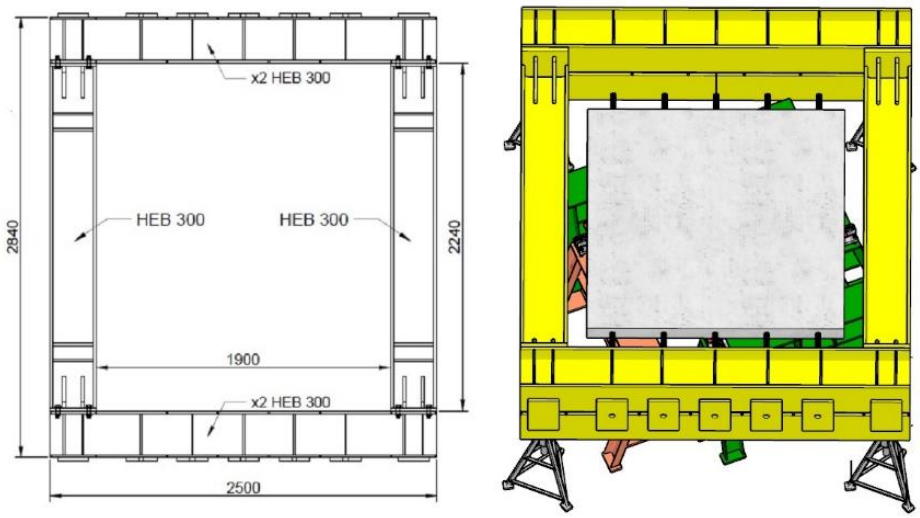

Figure 4.9: Steel frame used to apply tensile force to the slabs.

a) b)

Figure 4.10: a) Jacks placed at the active anchorage. b) Passive anchorage.

Table 4.3. Values of the tensile force applied at each test.

Test Ref.	Type of slab	T/T_{cr} before disconnecting jacks	T/T_{cr} at the test beginning	T/T_{cr} at failure
A1	A	0.00	0.00	**0.00**
B1	B	0.50	0.46	**0.44**
A2	A	0.80	0.71	**0.69**
A3	A	1.10	1.09	**1.02**
A4	A	1.40	1.37	**1.26**

To introduce the punching load, a hydraulic jack anchored in a loading frame, rigidly fixed to the floor slab, was used. Eight 120 x 120 mm load cells were placed at the slab supports to measure the reactions, arranged in a circle centered with respect to the center of the loading frame. A piece of rubber 120 x 120 x 20 mm was placed over each of the cells to ensure smooth contact with the slabs. The 8 load cells were supported on 4 rigid easels arranged in such a way that the distance between the mid-points of two opposite supports was 1530 mm. To cause the punching of the slab, a 145 x 145 x 30 mm steel loading plate was used, under which a thin layer of fine aggregate was placed to ensure regular contact between the upper face of the slab and the plate (Fig. 4.11). Due to the small distance between the bars protruding from the slabs and the steel frame, the evolution of the reaction force yielded by the nearest load cells to the frame was closely monitored in order to observe a possible interaction between both elements. Only in the test with the highest tensile force, and also the highest deflection, a slower increment of those reactions was observed close to the end of the loading stage, which may indicate some contact between the protruding bars and the frame. This interaction resulted in a slight decrement of these reaction forces, about a 5% of the mean reaction at each support, at the failure load. Therefore, this effect has been neglected.

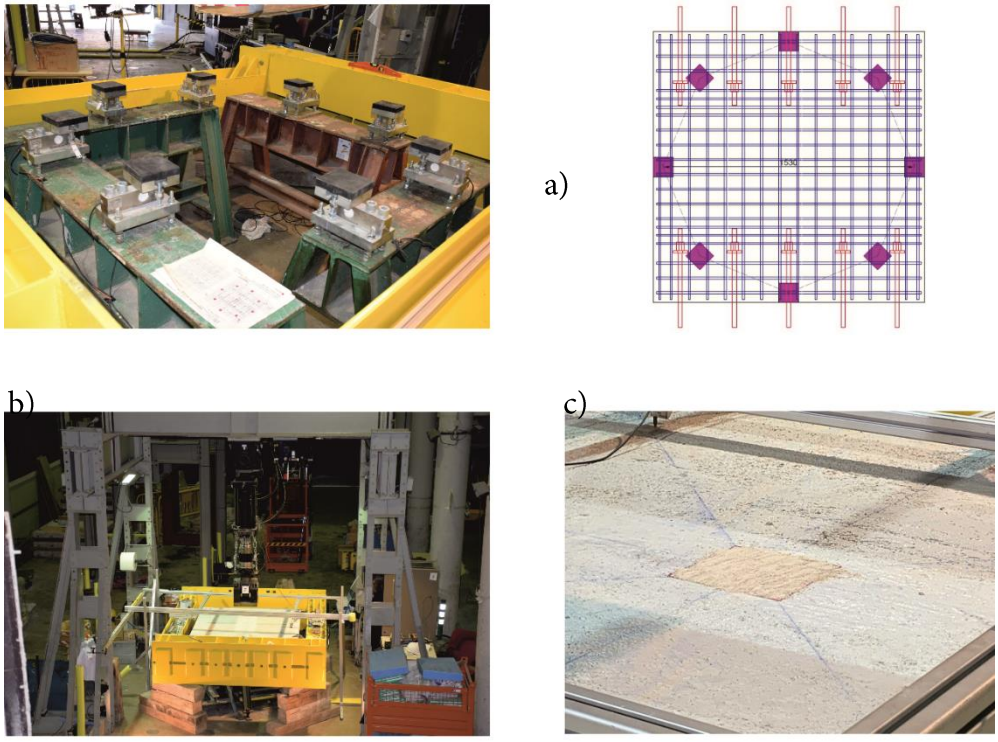

Figure 4.11: a) Support scheme. b) Hydraulic jack used to apply the punching load. c) Fine aggregate layer placed below the loading plate.

4.3.1.3 Instrumentation

Load cells of 50 kN were used as supports of the slab in the position given in Figure 8. In addition, hollow load cells of 500 kN were used in the post-tensioned bars, (in both active and passive anchors), in order to measure the in-plane tensile force applied to the slab. To control the deformation and the entry of the reinforcement into plastic regime, 32 strain gauges were distributed throughout the slab, 24 of which were placed in the reinforcement parallel to the tension and 8 in the perpendicular reinforcement, also in the central section (Fig. 4.12). In addition, a 75 mm displacement transducer was placed in the center of the lower face to measure the vertical displacement at the center of the slab, jointly with the internal linear variable displacement transducer (LVDT) of the loading frame. Finally, 8 LVDTs on the upper side of the slab were located, in the vertical of each support, to control their descent and subtract their mean value from the displacements measured in the center of the slab.

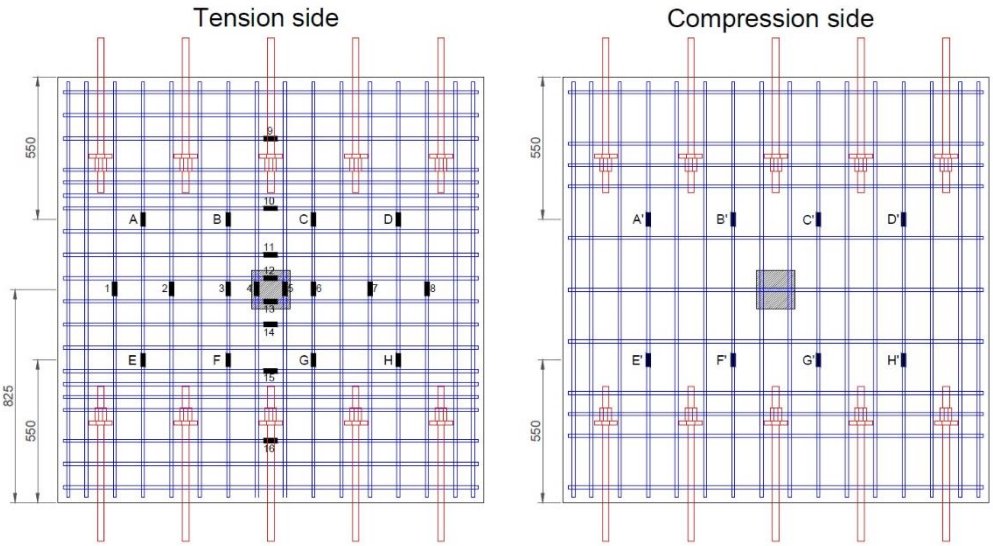

Figure 4.12: Position of strain gauges on the reinforcement.

4.3.1.3 Test procedure

First, the tensile force, given in Table 4.3, was introduced in the slabs and, subsequently, the point load was incrementally applied up to the punching-shear failure. In all cases, two levels of the out-of-plane load were previously applied, one up to 20% of the predicted ultimate load (P_u) and another up to 40% of P_u. Both loads were maintained for 100 seconds and served to accommodate all the elements involved in the test and to check that the instrumentation was properly working. Once the second test load ended and the slab was unloaded, the test up to failure was started, applying the load by a controlled displacement at a rate of 0.001mm/s. Taking account of the stretching of bars and the loading stages, average test duration was about two and a half hours. In support of the experimental campaign, a finite element model was developed, using as reference the one developed at the University of Waterloo (Canada) by Genikomsou and Polak (2015). This model was initially used to predict the tests results and to design the auxiliary structures of loading and support.

Once the first test was performed over the reference slab A1, the numerical model was calibrated with the obtained result (Fig. 4.13) and used to predict

the results of the rest of Type-A slabs, under different tensile force levels. With respect to the Type B slab, only a single test was performed with a tensile force of $T/T_{cr} = 0.5$. Then, since there was not reference slab of type B, the same numerical model was also used to predict the punching-shear capacity of a Type B control ($T/T_{cr} = 0$) slab, as shown in Table 4.4. Details of the numerical simulations performed will be explained later in this chapter.

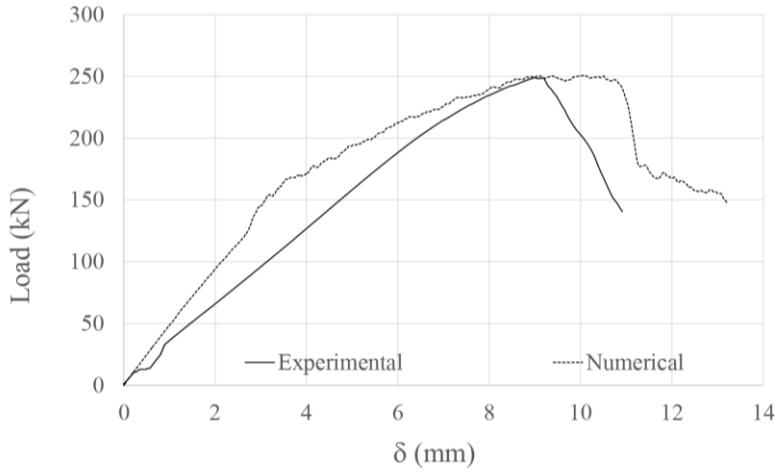

Figure 4.13: Load-deflection curve of the type-A control slab obtained experimentally and with FEA.

Table 4.4. Punching-shear strength of both types of control slabs.

Type of slab	Punching shear strength (kN)	Type of analysis
A	249.1	Lab. Test

B	263.9	FEM

4.3.2 Experimental results

4.3.2.1 Ultimate loads

The main interest of the experimental campaign was to observe the variation of the ultimate punching-shear load as a function of the tensile force applied to the slabs. For this purpose, the load-displacement curves of each one of the tests are analyzed in this section, together with that obtained for the control slab. Fig. 4.14 and Table 4.5 show the punching-shear failure load of each test and also their relationship with that of the control slab. As can be seen, there is a notable and progressive reduction in the failure load with respect to the value obtained in the control slabs. The maximum reduction was 28% for $T = 1.26\ T_{cr}$. The decreasing trend is practically linear with the applied tensile force and is accentuated in cases where the applied tensile force is greater or equal than T_{cr}. This is possibly due to the fact that when the value of T_{cr} is exceeded, cracking of the concrete occurs and, at the crack, the entire value of the applied external tension is resisted by the reinforcement, which significantly increases its stress, reducing its contribution to the punching strength. Fig. 4.15 shows the load vs. displacement at the center or slab curves for all type-A specimens. The previous explanation can also be applied to the increase in the ultimate displacement as long as the tensile force increases. The premature yielding of the reinforcement decreases the stiffness of the specimen and, therefore, an increase in the deflection occurs.

This effect is captured by the model, as explained in section 4.2. As observed in the theoretical curve calculated with the parameters of type-A slabs shown in Fig. 4.16, for values of the external force close to $T_{cr} = 1$, the punching shear strength associated to reinforcement yielding, V_y (Eq. (4.12)) becomes dominant over V_{Rt} (Eq. (4.10)) in the stressed direction. For this reason the slope of the curve decreases from that point onwards. A similar analysis has been made for slab Type B, in which this effect is not observed, because after cracking, the remaining capacity of the reinforcement $f_y^* = f_y - T/A_s$ is higher than in type-A slabs. Therefore, the contribution of the longitudinal reinforcement to the punching shear strength is enough to keep V_{Rt} as the dominant failure load in the stressed direction.

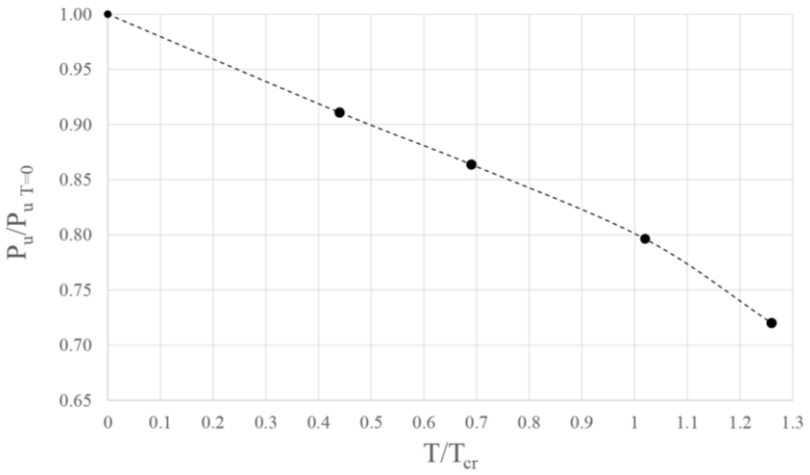

Figure 4.14: Relative decrement of the punching strength to the tensile force applied.

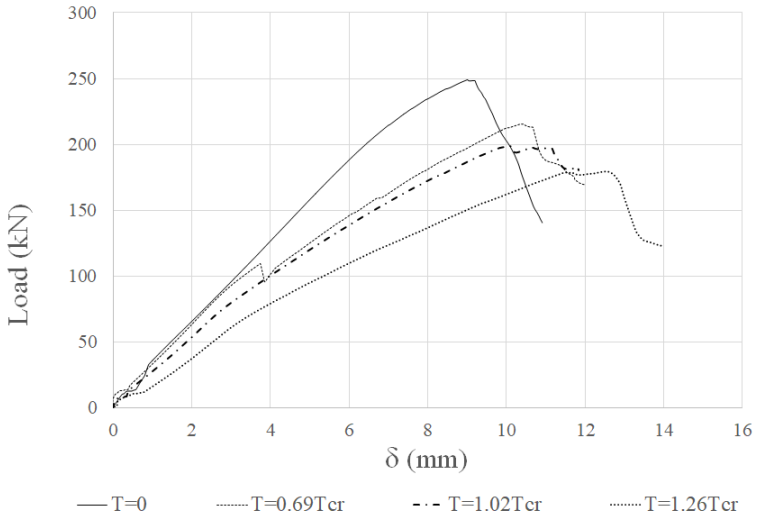

Figure 4.15: Load-deflection curves of the four type-A specimens.

Table 4.5. Experimental results.

Test Ref.	Slab type	T/T_{cr} at failure	Punching load (P_u) (kN)	$P_u/P_{control}$
A1	A	0	249.13	**1**
B1	B	0.44	240.4	**0.911**
A2	A	0.69	215.2	**0.864**
A3	A	1.02	198.4	**0.796**
A4	A	1.26	179.4	**0.720**

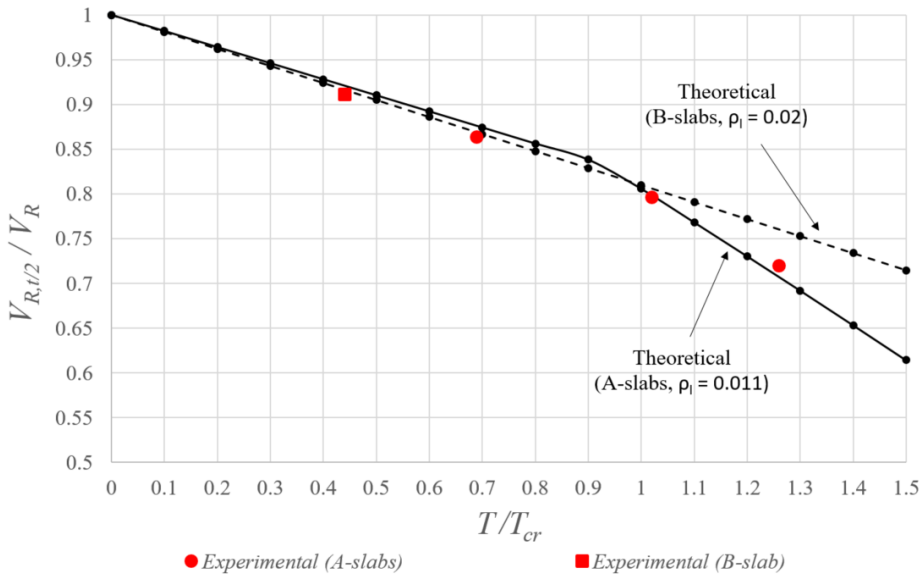

Figure 4.16: Theoretical and experimental punching shear strength vs. relative tensile force applied T/T_{cr}

Fig. 4.17 shows the state of cracking at the bottom face of the slabs at failure for some of the tests carried out (tensile forces are in the vertical direction). As observed, the crack pattern area increases in the dimension perpendicular to the tensile forces, as the applied tensile force increases.

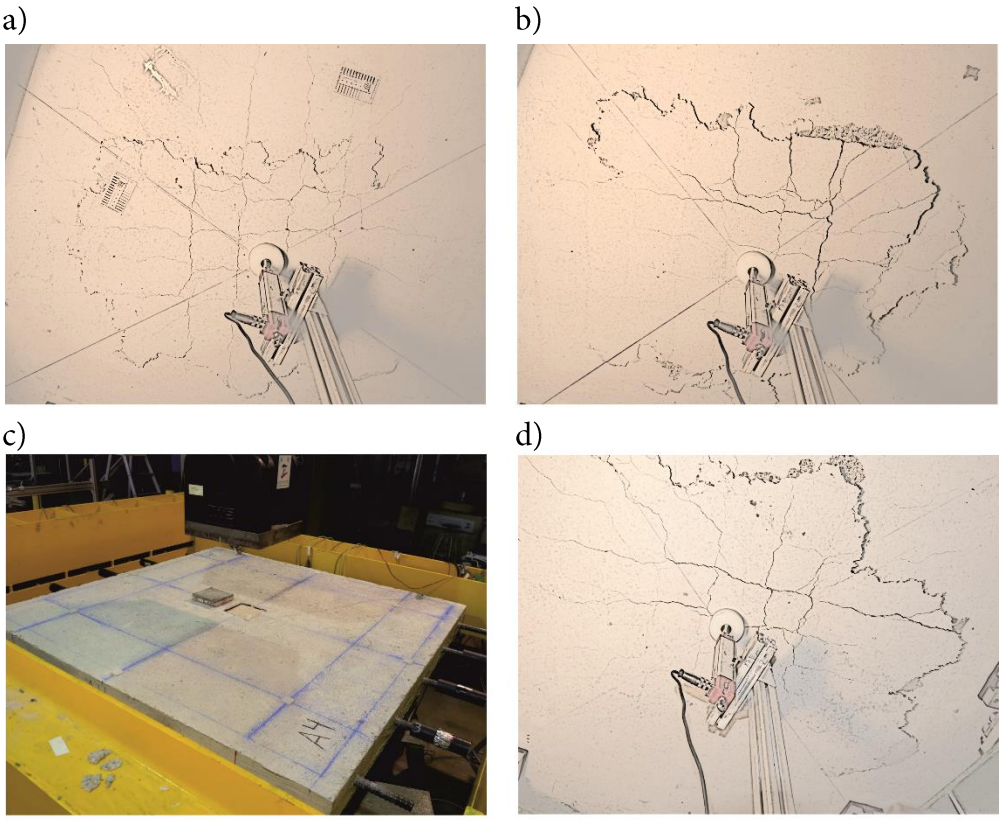

Figure 4.17: Final crack pattern of the slabs: a) T=0; b) T=0.69T_{cr}; c) T=1.26 T_{cr} (Top face); d) T=1.26 T_{cr}. Tensile force applied in vertical direction in the photographs.

4.3.2.2 Strains in the reinforcement

In order to study the evolution of the strains in the reinforcement at the central area of the slabs, a set of strain gauges was specifically placed on both the reinforcement parallel to the external tensile force and perpendicular to it (gauges 3 to 6 and 11 to 14 respectively). Firstly, the data yielded by the gauges glued to the reinforcement parallel to the external force was closely monitored during the tensioning stage, to ensure a homogenous distribution of the tensile stresses along the mid-section of the slabs prior to the beginning of the punching test. When the tests were running, the main goal of the strain gauges was to control the moment of yielding of the reinforcement parallel to the tensile force. If yielding takes place for a punching load close to the failure load, it may be assumed that yielding of the reinforcement is not influencing the punching strength, and thus and VRt prevails over Vy. On the other hand,

if yielding of the reinforcement takes place in an early stage of the punching test, a flexural-punching failure occurs, and Vy prevails over VRt.

Fig. 4.18 shows the moment of yielding of the longitudinal reinforcement in all the type-A slabs. In the control slab (T=0), yielding occurred at a load level very close to the failure load. For the case of T/Tcr = 0.69, the average strain in the reinforcement reached the yielding strain when the load applied was an 88% of the failure load. In the other two cases, where T/Tcr = 1.02 and T/Tcr = 1.26 the average strain in the reinforcement reached the yielding strain when the load applied was a 58% and a 42% of their respective failure loads.

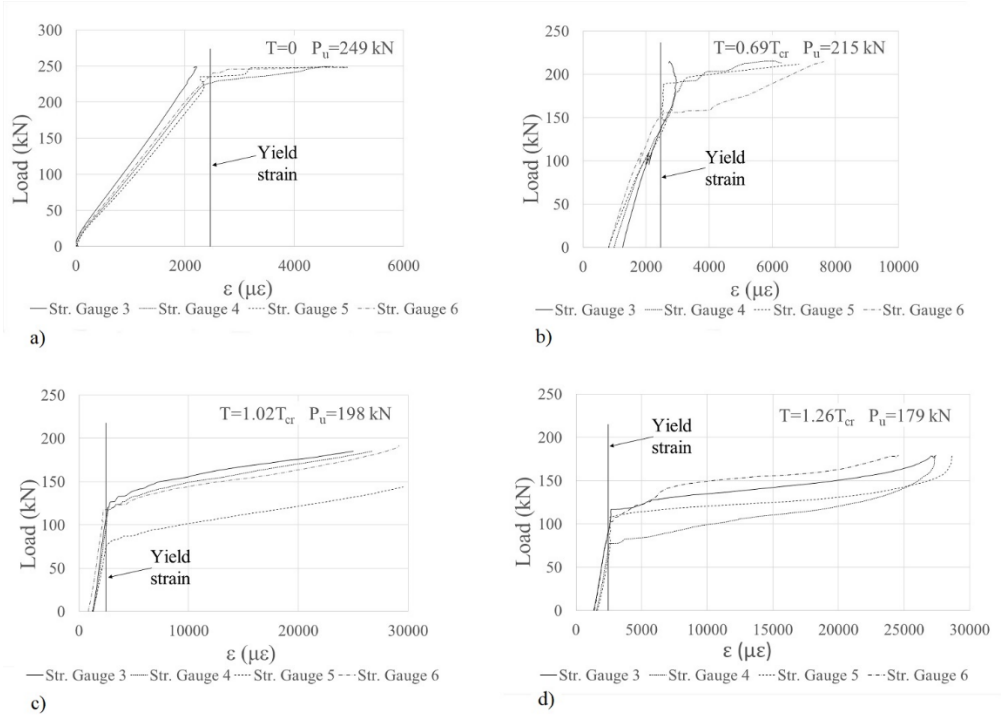

Figure 4.18: Evolution of strains in the longitudinal reinforcement: a) T=0; b) T=0.69T_{cr}; c) T=1.02T_{cr}; d) T=1.26T_{cr}.

Fig. 4.19 shows the evolution of the average strains of the reinforcement located in the central part of the slab in both directions. In the control slab, both reinforcements presented similar values of strain during the whole test, reaching yielding for a punching load very close to the failure load. For the

case of T/T_{cr} = 0.69, the slope of the force-strain curve of the perpendicular reinforcement increased a 14% when the parallel reinforcement reached yielding. This slope incremented by 11% for T/T_{cr} = 1.02 and by 14% for T/T_{cr} = 1.26.

In addition to that, Fig. 4.20 shows the comparison between the mean reactions measured at the load cells closest to the sides of the slab perpendicular to the external force (longitudinal reaction) and at the closest ones to the sides parallel to the external force (transverse reaction). As can be seen for values of $T = 0$ and T/T_{cr} = 0.69, the evolution of the reactions barely changes after the yielding of the reinforcement parallel to the external force. However for T/T_{cr} = 1.02 and T/T_{cr} = 1.26 an increment in the transverse reaction and a decrement of the longitudinal reaction with respect to the mean reaction occurs, more accentuated in the case of T/T_{cr} = 1.26. These behaviors may indicate that there was a moment redistribution process in the specimens subjected to high axial load levels, which may occur without collapse due to the static indeterminacy of two way slabs. In summary, the observed experimental behavior corroborates the assumptions of the model related to the effects of the in-plane tensile forces on the punching shear strength.

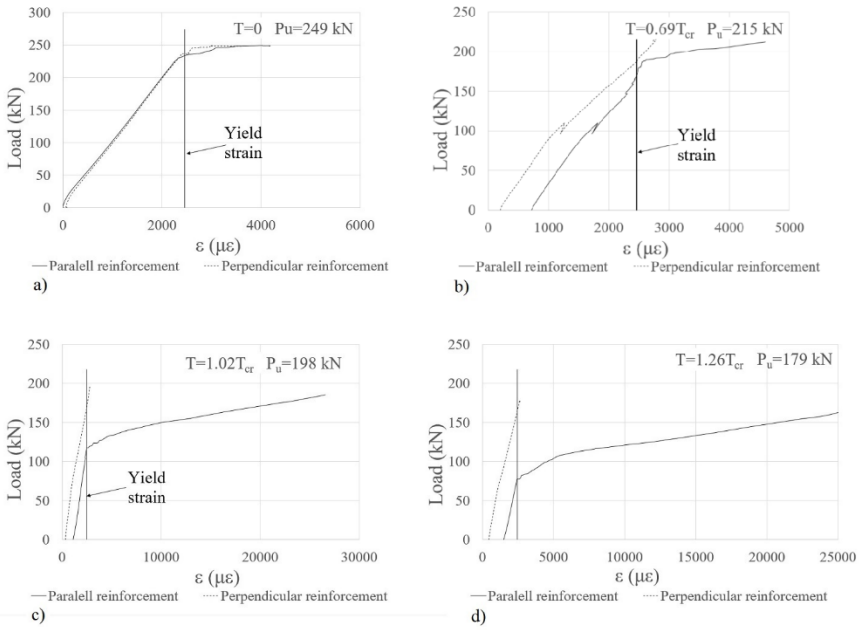

Figure 4.19: Relationship between strains in the reinforcement parallel and perpendicular to the tensile force. a) T=0; b) T=0.69T_{cr}; c) T=1.02T_{cr}; d) T=1.26T_{cr}.

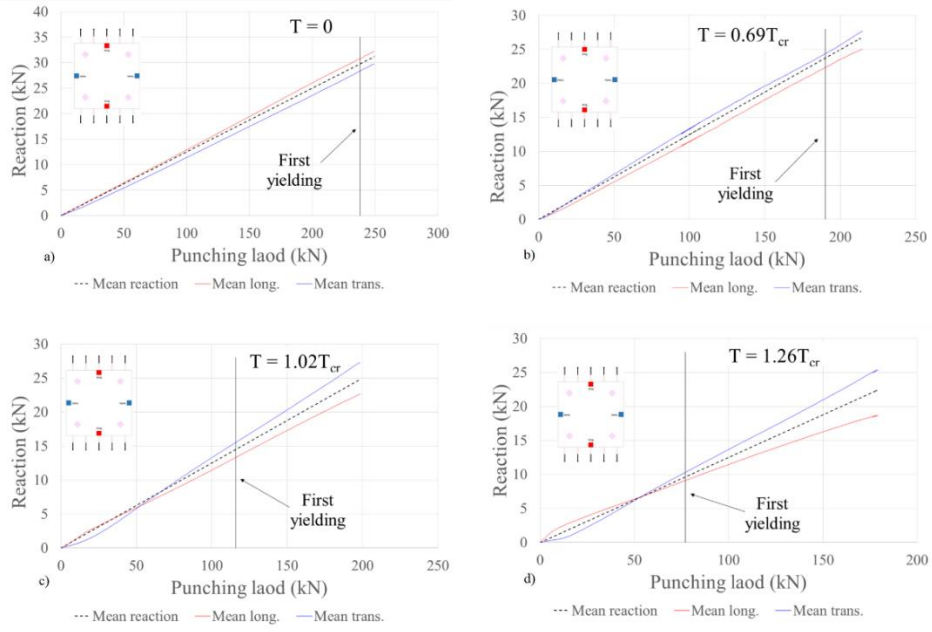

Figure 4.20: Evolution of the longitudinal and transverse reaction during the tests. a) T=0; b) T=0.69T_{cr}; c) T=1.02T_{cr}; d) T=1.26T_{cr}.

4.3.3 Model prediction of the experimental test found in literature and comparison with design codes provisions

Table 4.6 summarizes the comparison of the punching-shear strength predictions of all slabs tested in the experimental campaign described above, the ones tested at Cornell University (Abrams 1979; Jau *et al.* 1982) and the two specimens tested by Regan (1983) in approximately axisymmetric supporting conditions, using the simplified expressions proposed in Section 4.2.2 and those available in the Eurocode-2 (EN CEN 2005), the Model Code 2010 (CEB-*fib* 2010) (see section 2.5) and the ACI 349-06 (ACI Committee 349 (2007)) "Code Requirements for Nuclear Safety Concrete Structures" which contents the following expression for the punching strength of slabs subjected to membrane stresses.

$$V_{c1} = \left(2 + \frac{4}{\beta_c}\right) \cdot \left(1 + \frac{0.25 \cdot f_{m1}}{\rho_1 \cdot f_y}\right) \cdot \sqrt{f_c} \cdot b_1' \cdot h \quad if \quad f_{m1} \leq 0.9 \cdot \rho_1 \cdot f_y \tag{4.13a}$$

$$V_{c1} = 0.5 \cdot \sqrt{f_c} \cdot h \quad if \quad f_{m1} > 0.9 \cdot \rho_1 \cdot f_y \tag{4.13b}$$

$$V_{c2} = \left(2 + \frac{4}{\beta_c}\right) \cdot \left(1 + \frac{0.25 \cdot f_{m2}}{\rho_2 \cdot f_y}\right) \cdot \sqrt{f_c} \cdot b_2' \cdot h \quad if \quad f_{m2} \leq 0.9 \cdot \rho_2 \cdot f_y \tag{4.13c}$$

$$V_{c2} = 0.5 \cdot \sqrt{f_c} \cdot h \quad if \quad f_{m2} > 0.9 \cdot \rho_2 \cdot f_y \tag{4.13b}$$

$$V_c = V_{c1} + V_{c2} \tag{4.13e}$$

Where the ultimate punching shear capacity V_c is equal to the sum of the strength in each one of the two considered orthogonal directions, V_{c1} and V_{c2}, β_c is a constant depending on the shape of the column, f_m is the membrane stress and b_1' and b_2' are the portions of the control perimeter considered in each direction. In the case of tensile membrane stresses, f_m is considered negative.

For the comparison, all safety factors have been removed from the original formulations, and reported mean values of the materials strength and the actual applied loads have been used. The main characteristics of Regan's and

Cornell's slabs are summarized in Appendix A. Regan's specimens were 1.5 m square and 125 mm thick (Fig. 4.21a) and have been considered simply supported on their four sides for the calculations, despite the testing set up may have introduced some restriction to the rotation at the supports. Cornell's specimens were 1.2 m square and 150 mm thick simply supported on their four sides (Fig 4.21b).

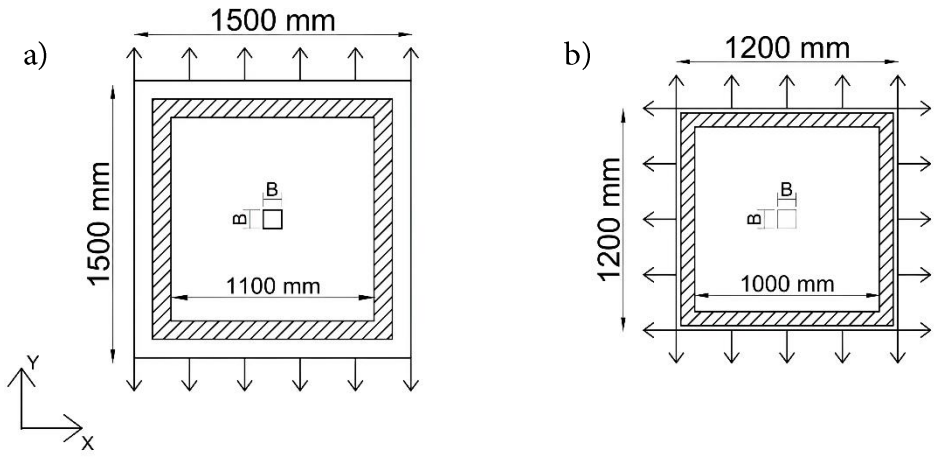

Figure 4.21: a) Regan's and b) Cornell's slabs dimensions.

Eurocode-2 predictions were calculated using Eq. (2.138), which accounts for the effects of normal stresses with the additive term σ_{cp}. Regarding ACI, the formulation presented in section 11.12.2.3 of ACI 349-06 has been selected (Eq. (4.13)) rather than the formula of section 22.6.5 of ACI 318-19 (ACI Committee 318 (2019)), which does not incorporate the effect of axial forces. Finally, Level of Approximation II has been used for Model Code 2010 predictions. In this case, the effects of tensile stresses have been introduced in the calculation of the slab's rotation ψ, (Eq. (2.145)), through term m_{Rd}, which has been calculated taking account of the applied tensile force. To calculate the term m_{Ed}, Eq. (7.3-71) of MC-2010 has been used, considering no eccentricity of the resultant of the shear forces with respect to the centroid of the control perimeter. Therefore, $m_{Ed} = V_{Ed}/8$, being V_{Ed} actually the punching strength of each slab ($V_{Ed} = V_{Rd}$). Thus, Eq. (4.14) has been solved iteratively for each value of the external applied load.

$$V_{Rd} = \frac{1}{1.5 + 0.9k_{dg} \cdot d \cdot 1.5 \cdot \frac{r_s}{d}\frac{f_y}{E_s} \cdot \left(\frac{\frac{V_{Rd}}{8}}{m_{Rd}}\right)^{1.5}} \sqrt{fc} \cdot b_0 \cdot d \tag{4.14}$$

Regarding code predictions, in uniaxial tension, best results are yielded by EC-2, followed closely by MC-2010, whereas for biaxial tension, best results are yielded by MC-2010, followed by EC-2. ACI 349-06 yields more conservative results in both cases. As far as CCCM concerns, it seems to be the best prediction method for uniaxial tension. Unfortunately, the available database of this type of tests is scarce, and needs to be extended with future research on this topic. For biaxial tension both CCCM and MC-2010 yield similar average results P_{exp}/P_{model} = 1.126 and 1.121 respectively), but CCCM has a slightly lower coefficient of variation than MC-2010 (9.76 % and 12.72 % respectively). Globally, best results are given by the CCCM with an average value of P_{exp}/P_{model} = 1.11 and a coefficient of variation of 9.32%, with a minimum value of 0.939 and a maximum value of 1.498. Table 4.6, along with Fig. 4.22 summarize the results of the comparison. Full comparison can be found in Appendix A.

Table 4.6. Comparison of the ultimate load predictions.

	P_{exp}/P_{CCCM}	P_{exp}/P_{EC2}	P_{exp}/P_{ACI}	P_{exp}/P_{MC10}
Mean Uniaxial	1.053	1.135	1.329	1.146
CoV Uniaxial (%)	2.847	4.706	10.705	7.150
Max.	1.105	1.205	1.482	1.280
Min.	1.008	1.040	1.102	1.019
Mean Biaxial	1.126	1.245	1.535	1.121
CoV Biaxial (%)	9.757	10.480	10.283	12.718
Max.	1.498	1.539	1.786	1.506
Min.	0.939	0.977	1.209	0.870
Total Mean	1.113	1.225	1.497	1.126
Total CoV (%)	9.320	10.380	11.577	11.808

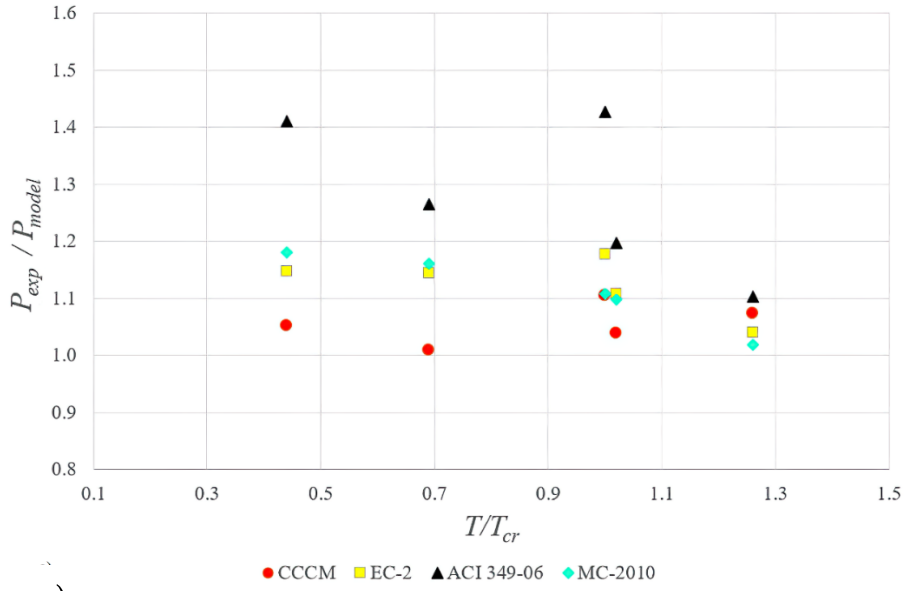

a)

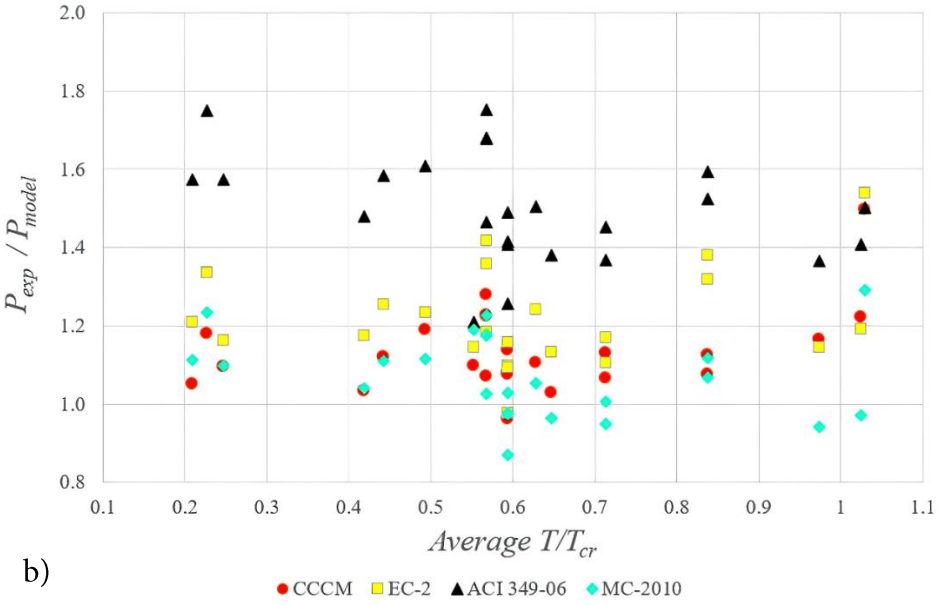

b)

Figure 4.22: Comparison of ultimate loads obtained with each design method. a) Uniaxial tension b) Biaxial tension.

4.3.4 Numerical simulations

In addition to help in the design of the tests setup, the numerical model mentioned before was used to contrast the values of the punching strength obtained with the proposed model in the particular case of uniaxial tension. Numerical simulations were performed for T/T_{cr} ranging from 0 to 1.5, including the values used in the experimental tests conducted as part of this investigation. The numerical analysis was carried out with the help of Simulia Abaqus software (Dassault Systems Simulia Corp. 2014).

4.3.4.1 Model generation

Taking into account the existing double symmetry, both in geometry and loading, only a quarter of each slab was simulated, considering the corresponding boundary conditions in both symmetry planes. Given the similarity of the dimensions of the specimens tested with those of Adetifa and Polak (2005), the recommendations of Genikomsou and Polak (2015) regarding the size of the element and the type of element used for concrete and reinforcement have been followed. For concrete, cubic elements of 8 nodes (C3D8R) have been used to reduce the computational cost and to avoid obtaining excessively rigid results, while for the reinforcing bars, linear beam elements of 2 nodes (B31) have been used. The reinforcing bars were considered perfectly bonded to the concrete. The size chosen for the concrete elements was 20 mm, so that 6 elements were arranged along the 120 mm of the slab edge. The supports of the slab were simulated by means of non-linear springs (SPRING A), with a very high stiffness in compression and practically zero stiffness in tension, thus allowing the partial lifting of the slab and avoiding the appearance of undesired tensile reactions (Fig. 4.23) The introduction of tensile forces was simulated in the model by applying the loads directly to the nodes located in the area of the anchor plates of the post-tensioning bars, while for the punching load, a displacement was imposed on the nodes located on the upper face of the slab, under the surface occupied by the load plate.

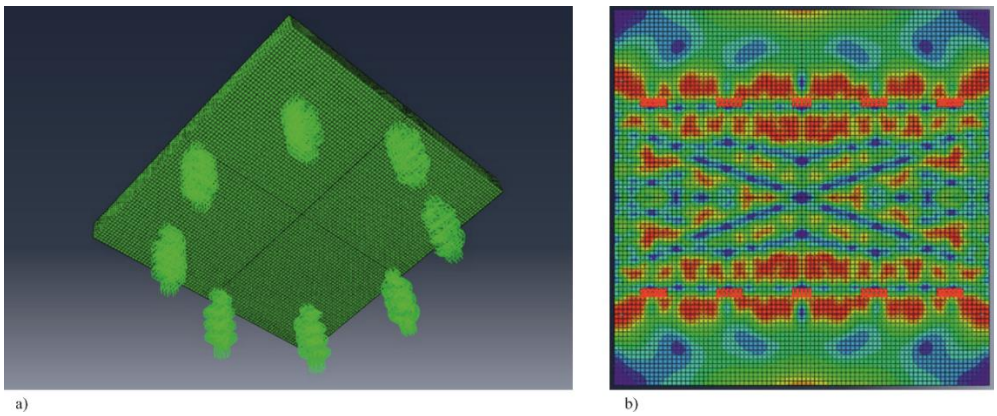

Figure 4.23: Modelling techniques: a) Springs simulating the supports; b) cracks (in blue) in the slab after applying the tensile force (in vertical direction in the picture) at the selected nodes.

Abaqus offers two different packages to perform this type of simulations: Abaqus / Standard, for static analysis, and Abaqus / Explicit, for quasi-static analysis. Up to a certain value of the applied external tension ($T/T_{cr} \leq 0.8$), the results obtained with one or another form of analysis were quite similar (Fig. 4.24). The main difference was the time needed to perform the simulation, being more than 3 hours in the case of Abaqus / Standard and approximately half an hour in the case of Abaqus / Explicit. From $T/T_{cr} = 1$, simulations with Abaqus / Standard began to show convergence problems, so it was decided to conduct the study with Abaqus / Explicit.

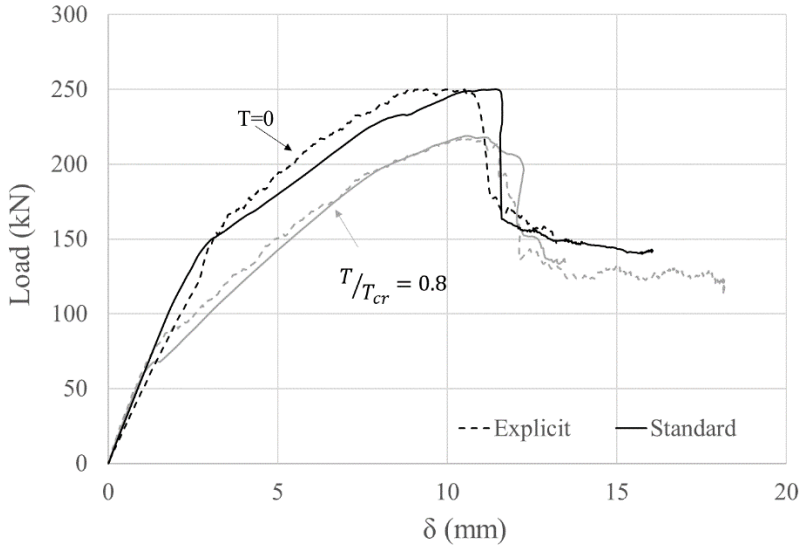

Figure 4.24: Comparison between load-deflection curves obtained with Abaqus/Standard and Abaqus/Explicit for T=0 and T/T_{cr}=0.8.

4.3.4.2 Materials

To simulate the behavior of concrete, the Concrete Damaged Plasticity model (Lubliner *et al.* 1988; Lee and Fenves 1998) was chosen, which requires the definition of the uniaxial constitutive equations in compression and tension, in addition to the definition of a yielding surface. For compression, a linear behavior of up to 40% of f_c (σ_{c0}) was considered. To define the elastic response, only the modulus of elasticity (E_c) and the Poisson ratio (ν) are needed. The modulus of elasticity is that obtained in the corresponding characterization test (see Table 4.2), while for ν, as Abaqus considers it a fixed value throughout the whole simulation process, including the post-cracking regime, a value $\nu = 0$ was chosen.

To take into account the non-linear behavior in compression, the Hognestad parabolic constitutive equation was chosen (Fig. 4.25a). The values of ε_{c0} and ε_{cu} correspond to those proposed in Table 3.1 of Eurocode-2, with $\varepsilon_{c0} = 0.002$ and $\varepsilon_{cu} = 0.0035$. For the tensile behavior, the model proposed in section 5.1.8.2 of the Model Code 2010 was selected, which considers a linear behavior up to f_{ct}, and a bilinear softening branch governed by the fracture energy of the material (Fig. 4.25b). The value of the fracture energy adopted is given in Eq. (2.68b), proposed in Marí *et al.* (2014) as a modification of that provided by the Model Code 2010 to account for the maximum aggregate size of concrete, which in this case was 10 mm.

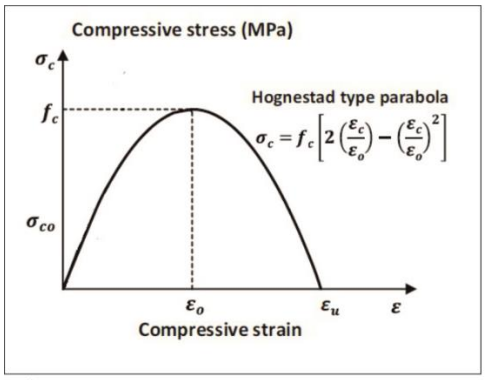

a)

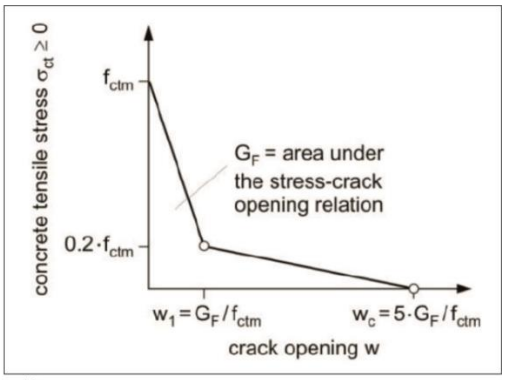

b)

Figure 4.25: Uniaxial compressive stress-strain relationship for concrete. b) Uniaxial tensile stress-crack width relationship for concrete.

The behavior of concrete in tension must be introduced in ABAQUS trough a stress-strain relationship, so it is necessary to transform the stress-crack opening given by Model Code (Fig. 4.25b) into a stress-strain curve. For this purpose, the crack opening is divided by the characteristic length of the element (l_c), defined as the average dimension of a finite element, in this case the length of an edge of a cubic element. Thus, the softening of the tensile branch, is given by $\varepsilon_{ct} = \varepsilon_{cr} + w / l_c$, where ε_{cr} is the concrete strain corresponding to the tensile strength, f_{ct}. The values used to define the yielding surface, collected in Table 4.7, were modified from those proposed in Genikomsou and Polak (2015) to adjust the simulation of the type-A control slab to the results obtained in the laboratory. For the steel reinforcement, a uniaxial bilinear stress-strain diagram was used, considering perfect plasticity. The yield stress and the modulus of elasticity used were those extracted from the characterization tests and collected in Table 4.2.

Table 4.7. Parameters defined for the Concrete Damaged Plasticity.

Dilation (ψ)	**Eccentricity (ε)**	**σ_{b0}/σ_{co}**	***K***	**Viscosity (μ)**
37.5	0.1	1.16	0.8	0

4.3.4.3 Results

A comparison between the load-displacement curves obtained by the numerical simulations and those obtained in the tests is shown in Fig. 4.26. As can be also seen in Table 4.8, quite accurate results were obtained in terms of the ultimate load.

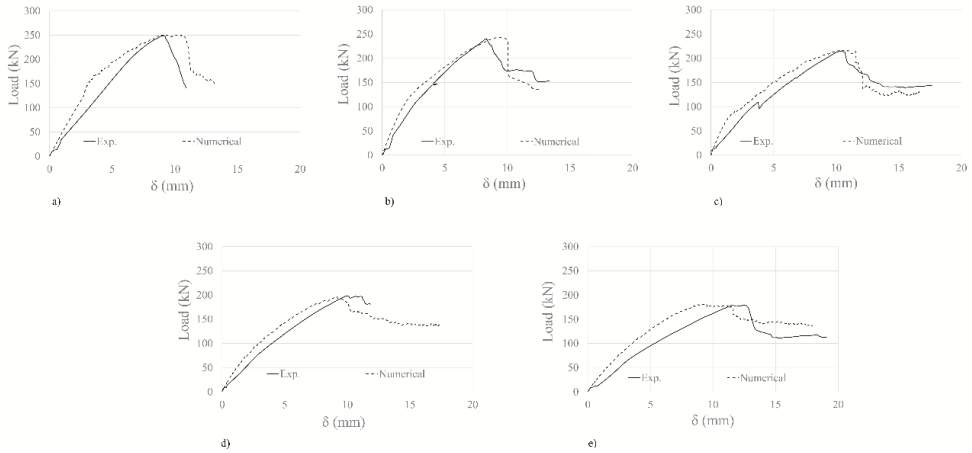

Figure 4.26: Comparison between load-deflection curves obtained with the numerical model and in the laboratory tests for a) T=0; b) T/T_{cr}=0.44; c) T/T_{cr}=0.69; d) T/T_{cr}=1.02; e) T/T_{cr}=1.26.

Once it was verified that the numerical model correctly reproduced the results obtained in the laboratory tests, simulations with reinforcement ratios corresponding to type A slabs, were performed for other values of T/T_{cr} up to a maximum of T/T_{cr} = 1.5. Table 4.9 and Fig. 4.27 show that the numerically obtained punching-shear capacity decreases as T/T_{cr} increases. The experimental results are also included in the plot. As can be seen, the relative decrease of strength obtained for type B slab (T/T_{cr} = 0.44) fits the obtained curve quite well. Thus, no favorable effect of having a greater amount of reinforcement in the direction parallel to the tensile force was observed for this load level. Nevertheless, the amount of reinforcement parallel to tension may play a significant role in the punching-shear capacity for higher values of the external tension.

Table 4.8. Comparison between numerical and experimental results.

Test Nº	T/T_{cr}	P_u (Numerical) (kN)	P_u (Experimental) (kN)	$P_u/P_{control}$ (Numerical)	$P_u/P_{control}$ (Exp.)	Δ (%)
1	0	250.3	249.13	**1**	**1**	------
2	0.44	243.3	240.4	**0.922**	**0.911**	**+1.21**
3	0.69	220.3	215.2	**0.880**	**0.864**	**+1.85**
4	1.02	203.5	198.4	**0.785**	**0.796**	**-1.38**
5	1.26	182.2	179.4	**0.723**	**0.720**	**+0.42**

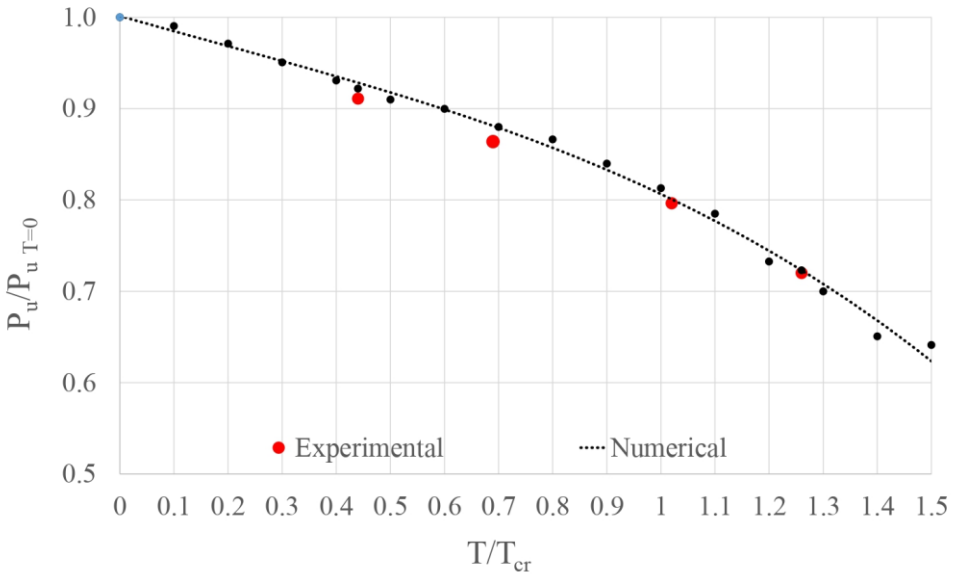

Figure 4.27: Comparison of the relative decrement of the punching strength to the tensile force applied obtained numerically and in laboratory tests.

Finally, cracking patterns obtained for different values of applied external tension are presented in Fig. 4.28, where the variation thereof can be seen as the external tension is increased.

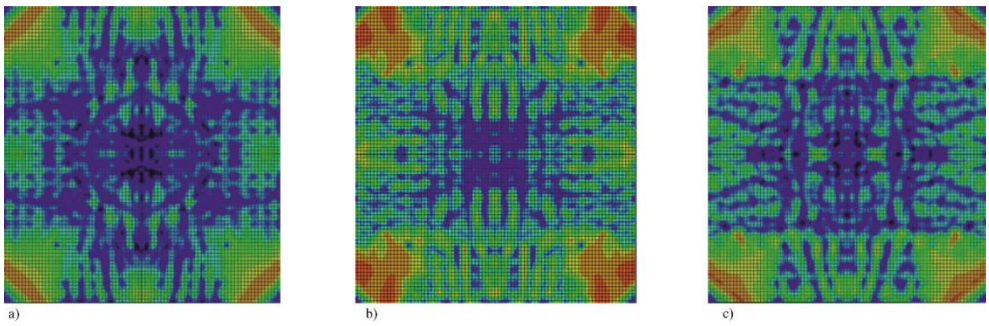

Figure 4.28: Cracking pattern at failure for a) T=0; b) T/T_{cr}=0.7; c) T/T_{cr}=1.26; (Tensile force applied in vertical direction)

4.4 Summary

A mechanical model for the shear punching strength of RC flat slabs subjected simultaneously to concentrated loads and in-plane tensile forces, has been described and verified with the results of previously carried out experimental campaigns. The developed model has been derived from the

Compression Chord Capacity Model for punching-shear, by identifying the main effects of in-plane tensile forces on the punching shear resisting mechanisms and failure modes, and incorporating them into their governing equations. The following main conclusions can be drawn from the studies performed:

- The following main effects of in-plane tensile forces on the punching shear strength of slabs, have been identified:
- A reduction of the neutral axis depth, and the corresponding reduction of the contribution of the compression chord to the shear strength.
- An increment of the tension in the longitudinal reinforcement and, by equilibrium, a decrement of compression stress in the un-cracked concrete chord, thus reducing its shear transfer capacity.
- A possible premature cracking of concrete, due to a high level of pure tension, that considerably increases the tensile stress in the longitudinal reinforcement.
- An increment of the critical crack width, that reduces the transfer capacity of shear and residual tensile stresses, along the crack.

- Simple and accurate design equations have been derived, showing that the shear transfer capacity of the compressed chord linearly decreases as a function of the ratio T/T_{cr}, where T is the applied tensile force and T_{cr} is the force that produces cracking in the concrete.
- The model has been able to accurately reproduce the results of an experimental campaign carried out by the authors, on 5 slabs subjected to a concentrated load and different levels of unidirectional in-plane tensile forces. The experimentally observed behaviour has been captured both qualitatively and quantitatively, with an average error on the prediction of the ultimate load of 5%.
- When a high tensile force T is applied, the increment of tensile stress in the longitudinal reinforcement due to the tensile force may be such that yielding of the reinforcement under increasing concentrated load may occur prior to punching failure, thus reducing the punching strength. Such phenomenon usually occurs for $T>T_{cr}$. However, for low reinforcement ratios, it can also occur for $T<T_{cr}$.
- The above described phenomenon is captured by the model, in which such failure is associated to the load that produces yielding in the flexural reinforcement in both directions, when yielding takes place. The relationship between the ultimate load and the ratio T/T_{cr} results approximately bilinear, with higher slope when premature yielding of the longitudinal reinforcement takes place.
- If additional reinforcement is placed to resist the applied tensile force, even in case that the section cracks ($T>T_{cr}$), the increment of stress in the longitudinal reinforcement may not be enough to produce yielding prior to the punching failure, thus contributing to avoid the "extra" reduction of punching strength.
- Predictions of punching-shear-tension tests results, available in the literature, were made with the proposed CCCM model and with different theoretical models included in design codes (EC-2, ACI 349-06, MC-2010 (LoA II)). It was showed that the best results are yielded by the proposed model (mean error of 5.3% (CoV=2.85%) for the case of uniaxial tension and 12.6% (CoV=9.76%) for biaxial tension). Among the Codes provisions, EC-2, provides the best predictions for uniaxial tension (mean error of 13.5% (CoV=4.71%) whereas MC-2010 provides the best results for biaxial tension

(mean error of 12.1% and CoV=12.72%). Mostly all the predictions of the ultimate load are conservative, being the ACI 349-06 predictions the most conservative ones.

Chapter 5

Shear strength of one-way slabs subjected to concentrated loads and transverse in-plane tension

5.1 Introduction

This chapter presents the results of the experimental campaign carried out to investigate the effects of in-plane transverse tensile forces on the shear strength of linearly supported one-way "RC slabs without shear reinforcement, subjected to concentrated loads. A total of 5 half scale slabs (1650 x 1650 x 120 mm), subjected simultaneously to different levels of in-plane tensile forces and a concentrated load were tested up to failure. The clear shear span to effective depth ratio a_v/d was equal to 3 in all tests, to minimize the effects of the direct transmission of the load to the closest support, the so called arching action. Code formulations are, in general, intended for beams, where only longitudinal axial stresses may take place in practice, and is often not clear how to proceed when predicting the effects of transverse tensile forces on the shear strength of one-way slabs.

5.2 Transverse in-plane tension in design codes shear provisions.

Shear provisions included in two of the most internationally accepted codes, such as Eurocode-2 (EN CEN 2005) and ACI 318-19 (ACI Committee 318 (2019)) are reviewed in this section. Additional information may be found in section 2.5.

Eurocode-2, in section 6.2.2, indicates that the design value for the shear resistance $V_{Rd,c}$ is given by Eq. (5.1), with a minimum value given by Eq. (5.2), where γ_c is the safety factor for concrete; $k = 1 + \sqrt{200/d} \leq 2$ is the size

effect factor; ρ_l is the amount of longitudinal tensile reinforcement ($\rho_l \leq 0.02$); b_w is the smallest width of the cross-section in the tensile area (mm); f_{ck} is the characteristic concrete compressive strength (MPa) and d is the effective depth of the cross-section (mm).

$$V_{Rd,c} = \left(\frac{0.18}{\gamma_c} \cdot k \cdot \sqrt[3]{100 \cdot \rho_l \cdot f_{ck}} + k_1 \cdot \sigma_{cp}\right) \cdot b_w \cdot d \tag{5.1}$$

$$V_{Rd,c} = \left(0.035 k^{3/2} \cdot f_{ck}^{1/2} + k_1 \cdot \sigma_{cp}\right) \cdot b_w \cdot d \tag{5.2}$$

The effect of axial stresses on the shear strength is included through the term $k_1 \cdot \sigma_{cp}$, where $k_1 = 0.15$ and $\sigma_{cp} = N_{Ed}/A_c$, being N_{Ed} the axial load applied in the cross-section, with negative sign in the case of tension, and A_c is the area of the concrete cross-section. It is remarkable that EC-2 considers that the increment of shear strength due to a compression force C is equal to the reduction in shear strength due to a tensile force of the same magnitude, despite the response of concrete in one case or in the other one is radically different. Another important aspect of this formulation is that it is intended mostly for beams, where axial stresses are always applied in longitudinal (spanning) direction. However, if these expressions are used to calculate the shear strength of a one-way slab, axial loads may exist in the longitudinal and in the transverse direction. If the latter is the case, it is not clear whether those axial stresses have to be taken into account or neglected. The experimental campaign presented in this chapter tries to provide some insight into this issue.

ACI 318-19 provides different sets of equations to calculate the shear strength, depending on the type of element and loading. Chapter 7: *"One way slabs"* refers to section 22.5 for the calculation of the concrete contribution to the shear strength V_c. Within this section, it is pointed out that the effect of axial tension due to creep and shrinkage shall be considered in calculating V_c, and it is recommended that if there is uncertainty about the magnitude of the axial tension, it is desirable to design shear reinforcement to resist the total shear. For elements without shear reinforcement, and assuming normal weight concrete ($\lambda = 1$), Table 22.5.5.1 of ACI Code provides Eq. (5.3) for the one-way shear strength of non-prestressed members, where $\lambda_s = \sqrt{2/(1 + 0.004d)} \leq 1$ is the size effect factor; ρ_w is the amount of

longitudinal tensile reinforcement; f_c' is the specified concrete compressive strength (MPa); b_w is the web width (mm) and d is the distance from the extreme compression fiber to centroid of longitudinal tensile reinforcement (mm).

$$V_c = \left[0.66 \cdot \lambda_s \cdot (\rho_w)^{1/3} \cdot \sqrt{f_c'} + \frac{N_u}{6A_g}\right] \cdot b_w \cdot d \qquad (5.3)$$

In this case, the effect of axial stresses is included trough the term $N_u/6A_g$, where N_u is the axial force normal to the cross section acting simultaneously with the shear force ($N_u < 0$ for tension) and A_g is the gross area of concrete. In the same way as Eurocode-2, ACI 318-19 considers the increment of shear strength due to a compression force equal to the reduction in shear strength due to a tensile force of the same magnitude. According to the definition of N_u, it seems that it is intended for axial forces parallel to the spanning direction, and it is not clear what to do in the case of a one-way slabs subjected to axial tension in the transverse direction.

In this context, an experimental campaign has been carried out at the Laboratory of Technology of Structures and Materials of the Universitat Politècnica de Catalunya (UPC), whose main goal was to identify and quantify the effect of unidirectional in-plane tension forces perpendicular to the spanning direction on the one-way shear strength of RC slabs.

5.3 Experimental campaign

5.3.1 Specimens tested

A total of five 1650 x 1650 x 120 mm slabs, simply supported on two parallel linear supports, were cast at the Laboratory of Technology of Structures and Materials of the Universitat Politècnica de Catalunya (UPC). The dimensions of the slabs tested in the context of this experimental campaign were conditioned by punching-shear tests conducted as part of this thesis (see section 4.3.1), since it was intended to reuse the tensioning system built for that occasion. In order to ease the placement, alignment and removal of the whole set-up within the portal frame where the main hydraulic jack of the laboratory is installed, the point load was decided to be applied at the center of the slabs. This way, one of the supports was moved inwards so a

clear shear span to effective depth ratio a_v/d equal to 3 was attained. The opposite support was also moved slightly inwards in order to avoid a flexural failure. The final dimensions of the set-up are and the supporting system are shown in Fig. 5.1.

The specimens were subjected to tension in their plane, only in the direction parallel to the supports, through 10 post-tensioning bars 25mm in diameter and 600mm in length (Fig. 5.2), partially embedded in 2 opposite faces (5 bars on each side) connected to the tensioning system. Although most of the tension was transmitted to the concrete by bond, anchors were placed at the embedded end of the bars for greater safety. The value of the external tension applied during the tests is measured in relation to the tensile force producing the cracking of the slab's cross-section, or $T_{cr} = A_c \cdot f_{ct}$, with A_c being the composite concrete and steel area of the cross-section of the slab and f_{ct} the concrete tensile strength. Averaging the values of the tensile strength obtained from characterization tests (Table 5.2), $T/T_{cr} = 1$ approximately corresponds to $\sigma_t = 3.2$ MPa.

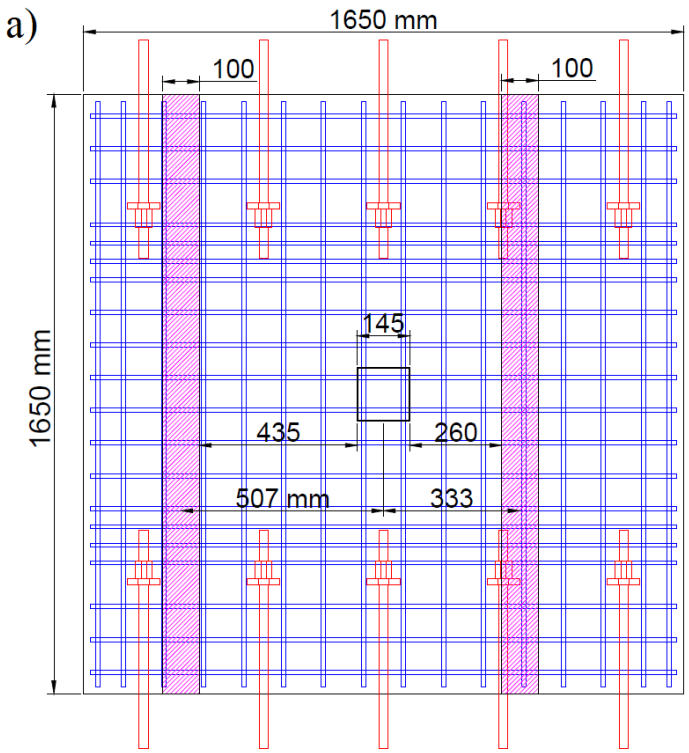

b)

Figure 5.1: Experimental set-up: a) dimensions of the specimens; b) bottom view of a tested specimen.

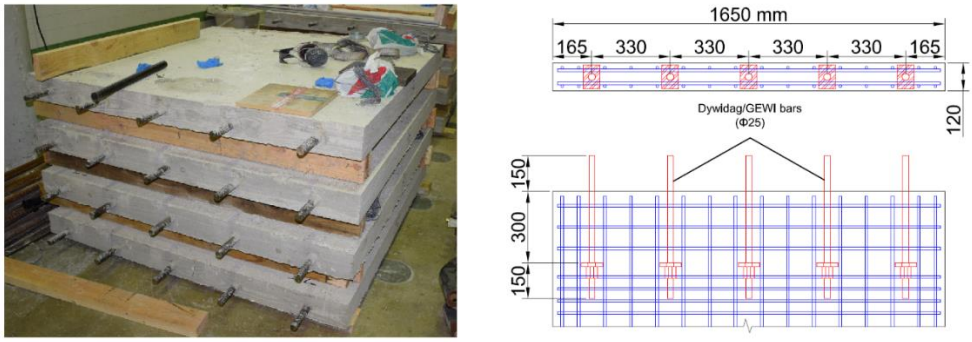

Figure 5.2: Position of post tensioning bars inside the slabs.

The slabs were reinforced with two steel meshes arranged on the upper and lower faces (Fig. 5.3). In the direction parallel to the external tension (transverse direction), all the tested slabs, named A4, A5, A6, A7 and B2, were symmetrically reinforced. On each face, reinforcement consisted of 12mm bars spaced 105 mm in type A slabs (ρ = 0.011) and 16mm bars spaced 105 mm in slab B2 (ρ = 0.02). In the direction perpendicular to the applied tension (longitudinal or spanning direction), on the lower face, an assembly

consisting of 12mm bars spaced 100 mm was arranged in all cases, ($\rho = 0.013$), while 12 mm bars spaced 200 mm were arranged on the upper face. Additional reinforcing bars were placed in the vicinity of the post-tensioning bar anchors, as a measure of local reinforcement. The tensile reinforcement ratio and effective depth of each type of slab are shown in Table 5.1. The amount of transverse reinforcement in specimen B2 ($\rho = 2\%$) may be higher than usual in practical cases. However, the experimental results of this specimen can be adequate to identify if the increment of the reinforcement parallel to tension significantly affects the structural response and the shear strength.

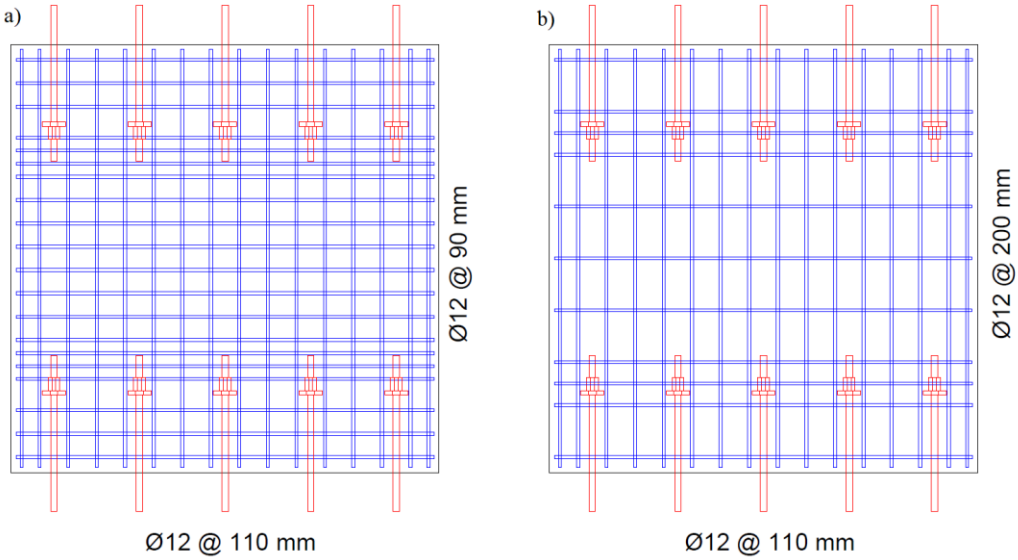

Figure 5.3: Reinforcement layout for type-A slabs: a) bottom face; b) top face.

The slabs were cast using ready-mixed concrete from a local supplier. Normal strength concrete C30/37 with crushed limestone aggregate with a maximum size of 10 mm was used. To characterize the concrete, standard compression (UNE-EN 12390-3), splitting (UNE-EN 12390-6) and elastic modulus (UNE-EN 12390-13) tests were performed. The specimens were reinforced with deformed bars of B500-S steel. Yield stress and elastic modulus of each type of reinforcing steel (UNE-EN ISO 6892-1) were also characterized. Results are shown in Table 5.2.

Table 5.1. Tensile reinforcement of the specimens.

	Parallel to tension			Perpendicular to tension		
Slab type	**Reinforcement area (mm^2)**	**Reinforcement ratio**	**Effective depth (mm)**	**Reinforcement area (mm^2)**	**Reinforcement ratio**	**Effective depth (mm)**
A	1810	0.0108	99	1810	0.0130	87
B	3217	0.0197	97	1810	0.0133	85

Table 5.2. Mean values of material properties.

Concrete

Test Ref.	**T/T_{cr}**	**fc (Mpa)**	**fct (Mpa)**	**Ec (Gpa)**	**d_max (mm)**	**Age (days)**
A4	0	36.2	3.01	28.5	10	170
B2	0.43	36.6	3.23	31.3	10	287
A5	0.70	37.5	3.27	29.8	10	277
A6	1.06	37.0	3.40	29.6	10	280
A7	1.30	35.9	3.12	30.0	10	184

Steel

Diameter (mm)	**fy (MPa)**	**Es (MPa)**
10	525.9	216.3
12	535.9	210.7
16	536.8	201.6

5.3.2 Tests set-up

Four out of the five tested specimens were subjected to different levels of in-plane tension, whilst the control slab was tested without axial force. To introduce the tensile force in the slabs, the auxiliary steel structure introduced in section 4.3.1.2, was used. This structure consisted of a rectangular steel frame surrounding the slab (Fig. 5.5a). On sides parallel to the tensile forces, the frame consisted of a single HEB 300 profile, whereas on both perpendicular faces it was formed by two HEB 300 profiles arranged in parallel and sligthly separated to allow the passage of bars (extensions) connected to the aforementioned bars partially embedded in the slab (Fig. 5.5b). On one of these faces, a passive anchorage for the tensioning bars was used while they were prestressed from the other end, with the help of force-controlled hollow jacks connected to the bars protruding from the specimens (Fig. 5.5c).

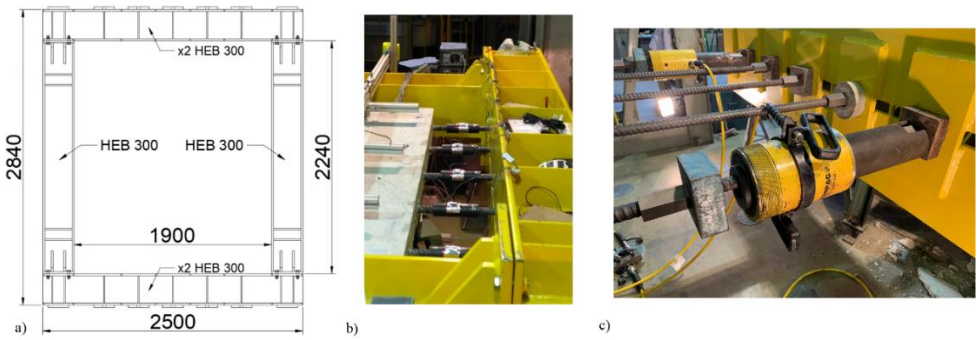

Figure 5.5: Tensioning system used to apply the axial force to the specimens: a) steel frame; b) Extension connected to the protruding bars; c) Jacks placed at the active anchorage.

The steel structure was set at the appropriate height with the help of four height-adjustable supports located under each of the four corners of the frame. For safety reasons, once the desired external force value was reached, the bars were anchored and the jacks were disconnected from them. This fact caused a small loss of the axial force during the test that was quantified by the arranged instrumentation. The theoretical loads to be applied and the values measured during the tests are shown in Table 5.3.

Table 5.3. Values of the tensile force applied at each test.

Test Ref.	Type of slab	T/T_{cr} before disconnecting jacks	T/T_{cr} at the test beginning	T/T_{cr} at failure
A4	A	0.00	0.00	**0.00**
B2	B	0.50	0.45	**0.43**
A5	A	0.80	0.73	**0.70**
A6	A	1.10	1.08	**1.06**
A7	A	1.40	1.32	**1.30**

Supporting system comprised two HEB 100 profiles 1650 mm long placed on top of five 20 x 120 mm hinged load cells used to measure the distribution of the reaction at each support (Fig. 5.6). A piece of rubber of 120 x 120 x 20 mm was placed over each of the load cells to allow the free rotation of the support. A 10 mm thick rubber strip was placed on top of the HEB 100 profiles to ensure smooth contact between the supports and the tested specimens. Load cells were supported on two rigid easels arranged in such a way that the distance between the inner face of the loading plate and the closest support was equal to $3d$ ($a_v = 3d$). To introduce the concentrated load, a hydraulic jack anchored in a loading frame, rigidly fixed to the floor slab, with a maximum capacity of 1000 kN was used. The out-of-plane load was applied to the specimens through a 145 x 145 x 30 mm steel plate, under which a thin layer of fine aggregate was placed to ensure regular contact with the upper face of the slabs.

Figure 5.6: Support system of the tested specimens.

5.3.3 Instrumentation

In addition to the load cells of 50 kN placed underneath the supports, hollow load cells of 500 kN were used in the post-tensioned bars (Fig. 5.7a), in both active and passive anchorages, in order to measure the in-plane tensile force applied to each slab. To control the possible yielding of the reinforcement, in both longitudinal and transverse direction, 8 strain gauges were distributed as shown in Fig. 5.7b. To measure the deflection underneath the point load of each specimen, a 75 mm displacement transducer was positioned at the center of the lower face, jointly with the internal linear variable displacement transducer (LVDT) of the loading frame. Finally, 3 LVDTs were placed in the vertical of each support on the upper side of the slabs, to control their descent and then, to subtract their mean value from the displacements measured in the center of the slab.

5.3.4 Test procedure

First, the tensile force, given in Table 5.3, was introduced in the slabs and, subsequently, the point load was incrementally applied on its center up to failure of the specimen. In all cases, two levels of the out-of-plane load were

previously applied and removed, one up to 40 kN and another up to 80 kN. Both loads were maintained for 100 seconds and served to accommodate all the elements involved in the test and to check that the instrumentation was properly working. Once the second test load ended and the slab was unloaded, the test up to failure was started, applying the load by a controlled displacement at a rate of 0.005 mm/s.

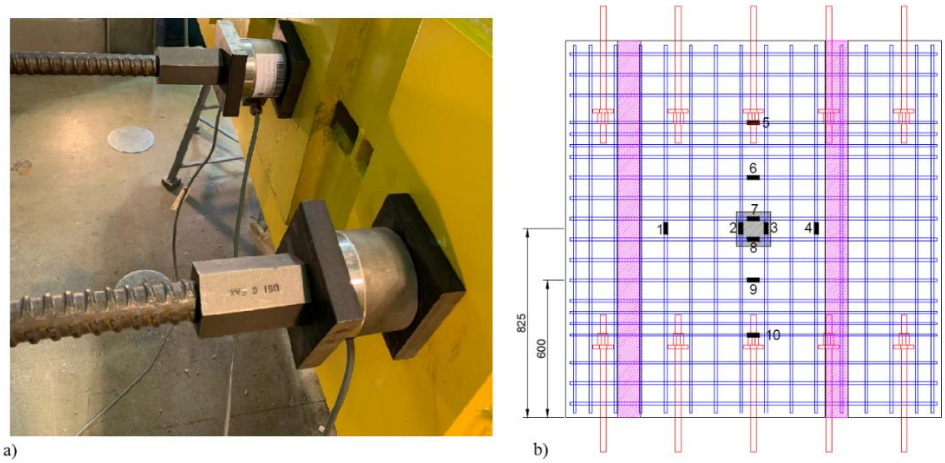

Figure 5.7: a) Hollow load cells placed at the anchorages of the tensioning bars; b) position of the strain gauges.

In support of the experimental campaign, in the same way as in the punching-shear tests presented in section 4.3, a finite element model was developed using software package Simulia Abaqus, taking as reference the above mentioned one and the recommendations given in Nana *et al.* (2017). This model was initially used to predict the tests results and to design the auxiliary structures of loading and support. Once the test on the control slab was performed, the numerical model was calibrated with the obtained result (Fig. 5.13a) and used to predict the shear strength of the rest of Type-A slabs under the corresponding value of the external force applied. With respect to Type-B slab, only a single test was performed with a tensile force of T/T_{cr} = 0.43. Then, since there was not reference slab of type B, the same numerical model was also used to predict the shear capacity of the Type B reference slab, as shown in Table 5.4. Details of the numerical simulations will be explained in later in this chapter.

5.4 Experimental results

5.4.1 Ultimate loads

The main interest of the experimental campaign was to quantify the variation of the shear strength as a function of the tensile force applied to the slabs. Fig. 5.8 shows the comparison between all the experimental load-deflection curves obtained. As can be seen, the ultimate load of all type-A slabs slowly decreases with increasing levels of the applied tensile force, with a 5.3% reduction for $T/T_{cr} = 1.3$ ($\sigma_t = 4.2$ MPa). The whole trend is showed in Fig. 5.14. Regarding slab B2, the ultimate load obtained was a 2.1% lower than that obtained for its control slab using the aforementioned FEM, confirming the trend observed with type-A slabs. Values of the ultimate load and comparison to the control slabs are summarized in Table 5.4. These results indicate that, for the tension levels applied in the laboratory tests, if this tensile force is applied in the direction perpendicular to the span, the shear strength seems to be barely affected.

Nevertheless, the external tension affected the stiffness of the specimens. Slabs A5, A6 and A7 showed similar response, which indicate that the external force cracked the concrete, but the reinforcement was able to carry all the stresses caused by the addition of transverse bending and tension. This was confirmed by the measurements provided by the strain gauges placed in both longitudinal (gauges 7 and 8) and transverse (gauges 2 and 3) reinforcement underneath the point load. No signs of yielding were observed in any of the experimental tests, which discards the possibility of a flexural failure. These measurements are in good agreement with the brittle failure observed in the load-deflection curves.

Slab B2 represents an intermediate situation, in which concrete cracks prematurely, but the higher reinforcement ratio in the transverse direction increases the global stiffness with respect to type-A slabs. It is interesting to note that slab B2 presented a higher shear strength than slab A4 (type-A control slab). Some numerical studies (Reissen and Hegger 2012) have shown a small but positive influence of the transverse reinforcement ratio on the shear strength. However, no significant influence has been observed experimentally (Lantsoght *et al.* 2013b; Bui *et al.* 2017a; Reissen *et al.* 2017). In the context of the study presented herein, the FEM predicted a 9.3%

increment of the shear strength for the type-B control slab with respect to the A4 control slab, and slab B2, tested with a tension level of T/T_{cr} = 0.43 (σ_t = 1.38 MPa), resisted a shear strength value 7.1% higher than the control slab A4.

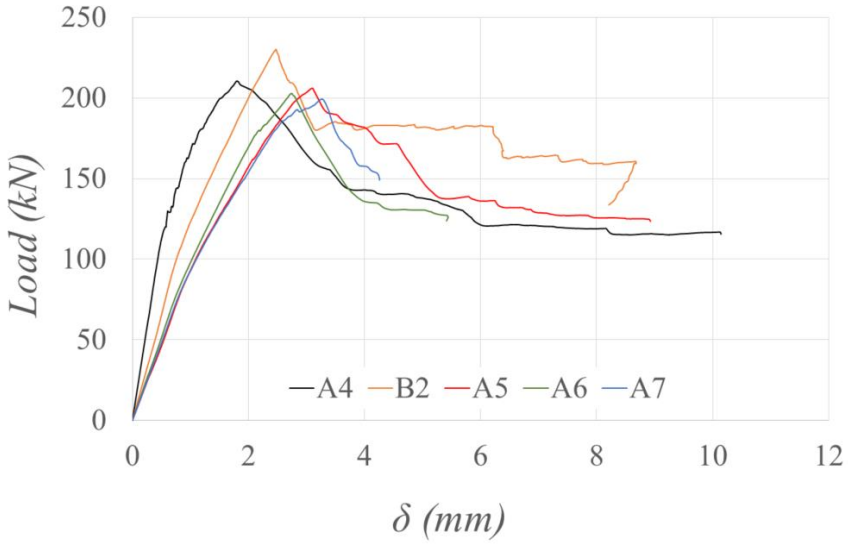

Figure 5.8: Load-deflection curves of the experimental tests.

Table 5.4. Experimental results.

Test ref.	**$V_{u,\ control}$ (kN)**	**T/T_{cr} at failure**	**Ultimate load (P_u) (kN)**	**Shear strength (V_u) (kN)**	$V_u/V_{u,control}$
A4	210.6	0.00	210.6	127.1	1
B2	230.2*	0.43	225.3	135.9	0.979
A5	210.6	0.70	206.9	124.4	0.978
A6	210.6	1.06	202.8	122.4	0.963
A7	210.6	1.30	199.4	119.6	0.947

*Obtained from FEM

Fig. 5.9 shows the state of cracking at the bottom face of the slab at failure for all the tests carried out. Auxiliary lines at 45º with the spanning direction have been superimposed as a reference. As can be observed, a crack parallel to the closest support appeared in all cases. In slabs subjected to tension, this failure crack was observed to turn and to connect with cracks parallel to the spanning direction provoked by the external force applied. Only slab A6 presented a cracking pattern that seems to be a transition between shear and punching-shear failure, since the crack parallel to the support quickly turns and partially surrounds the loading plate. Negative influence of in-plane tensile forces on the punching-shear strength of two-way slabs were observed in the experimental tests detailed in section 4.3, and this may have been the case of slab A6. However, as shown in Fig. 5.8 and Table 5.4, the load-deflection behavior and the ultimate load of this slab were in accordance with the rest of results obtained.

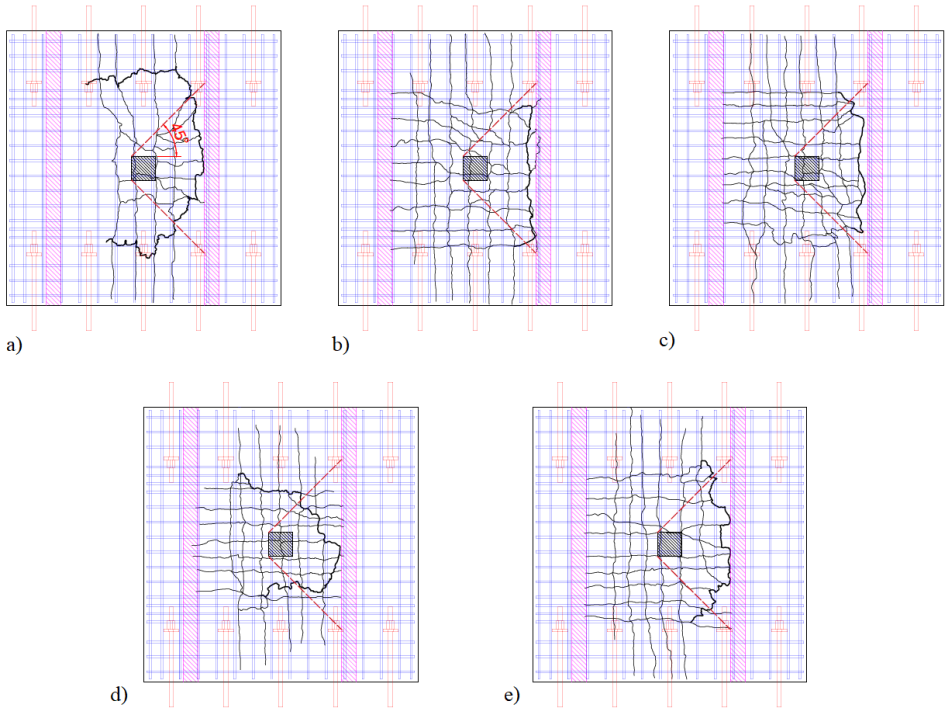

Figure 5.9: Cracking patterns at failure. a) A4 (T/T_{cr} = 0); b) B2 (T/T_{cr} = 0.43); c) A5 (T/T_{cr} = 0.7); d) A6 (T/T_{cr} = 1.06); e) A7 (T/T_{cr} = 1.3).

5.4.2 Reactions at the supports

In order to know if the external tensile force affected the distribution of the reactions at the supports, the measures yielded by the load cells supporting both HEB 100 profiles were analyzed and compared to the values obtained for the control slab. Despite only five load cells were available for each support, it was enough to capture the global behavior. Fig. 5.10 shows the distribution of the reaction at both supports for all tested type-A slabs. It can be seen that regardless the level of tensile force applied, reaction distributes more or less in the same way, with highest values measured at the center of each support and decreasing towards the free edges of the slabs. An interesting point is that, despite the clear shear span for the farthest support is equal to 5*d*, a similar trend was observed for the reaction distribution than that at the support placed at 3*d*. This is in agreement with some existing studies (Lantsoght *et al.* 2013c, Havolnik *et al.* 2020) which conclude that a limit value for the horizontal load spreading must be established in order to avoid highly un-conservative results when using the simplified formulation of the codes, and is also in line with the hypothesis adopted in the mechanical model for the prediction of the shear strength of one-way slabs subjected to point loads presented in chapter 3.

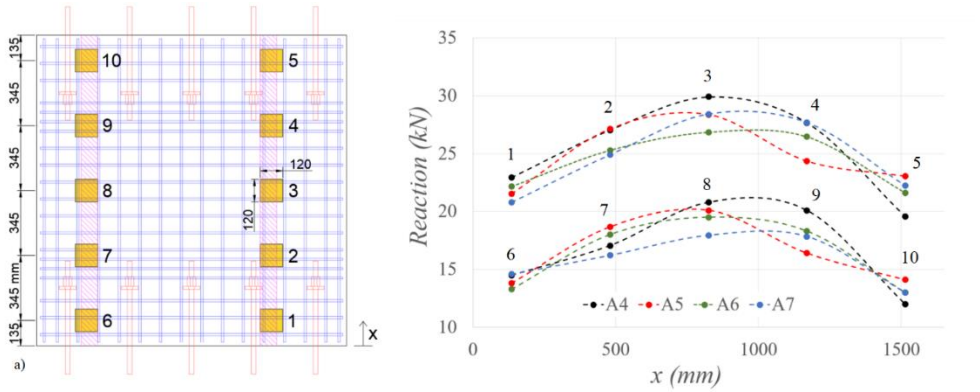

Figure 5.10: a) Position and dimensions of the load cells placed underneath the support; b) Distribution of the reaction at failure at the closest support to the point load for type-A slabs.

5.5 Numerical simulations

This section presents the numerical model developed jointly with the experimental campaign. In addition to help in the design of the test set-up, the model was also used to contrast the values of the shear strength obtained experimentally, and to perform simulations for values of the tensile force different from those applied in the experimental campaign.

5.5.1 Model generation

Taking into account the existing plane of symmetry at the middle of the slab, parallel to the spanning direction, both in geometry and loading, only half of each slab was modelled, considering the corresponding boundary conditions in the symmetry plane. The numerical model was inspired in the model developed for the experimental campaign presented in section 4.3.4, but also some of the recommendations given in Nana *et al.* (2017), such as the use of an explicit quasi-static solution, or the definition of a linear evolution of the damage parameter, in both tension and compression, were taken into account.

Regarding the type of element used, 8 nodes hexahedral elements with reduced integration (C3D8R) were selected for concrete in order to reduce the computational cost and to avoid obtaining excessively rigid results due to the linear interpolation of the displacements field. For the reinforcing bars, linear beam elements of 2 nodes (B31) perfectly bonded to concrete were used. The chosen size for the concrete elements was 20 mm, so that 6 elements were arranged along the 120 mm of the slab thickness. The same element size of 20 mm was considered for the reinforcing elements. The supports of the slab were simulated by means of non-linear springs (SPRING A), with a very high stiffness in compression and practically zero stiffness in tension, thus allowing the partial lifting of the slab and avoiding the appearance of undesired tensile reactions (Fig. 5.11a). The introduction of tensile forces was simulated in the model by applying the loads directly to the nodes located in the area of the anchor plates of the post-tensioning bars (Fig. 5.11b), while for the point load, a displacement was imposed on the nodes located on the upper face of the slab, under the surface occupied by the loading plate (Fig. 5.11c).

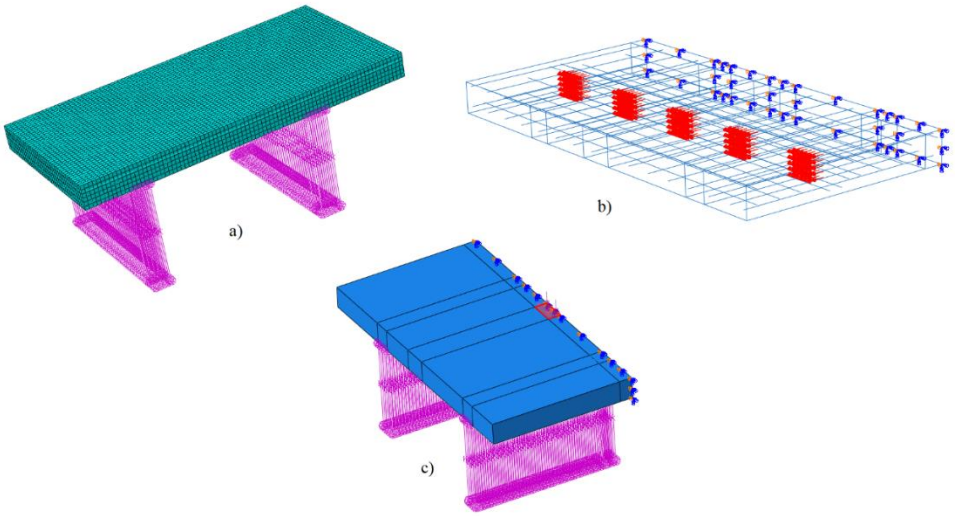

Figure 5.11: Modelling techniques: a) Mesh sizes and spring simulating the supports; b) Area of application of the tensile force; c) Imposed displacement at the point load position.

The simulations were performed by means of a quasi-static analysis, available in the Abaqus/Explicit package. This kind of analysis has several advantages in comparison to the traditional implicit method when non-linear analyses are carried out. The absence of a global tangent matrix stiffness in the explicit analysis avoids certain convergence problems and in general, it saves a substantial amount of time when performing parametric studies. To avoid dynamic instabilities, the ratio of the kinetic energy generated by the inertia forces to the internal deformation energy must be negligible, which has to be checked after each simulation.

5.5.2 Material model

The material model was similar to the one used in the model developed for the punching-shear experimental campaign. A comprehensive explanation can be found in section 4.3.4.2. Only small changes were made, such as the definition of a linear damage parameter, in both tension and compression, following the recommendations given in Nana *et al.* 2017 (Fig. 5.12). The values used to define the yielding surface of the Concrete Damaged Plasticity Model, slightly modified from those presented in Table 4.8 to adjust

the simulation of the type-A control slab to the results obtained in the laboratory, are summarized in Table 5.5.

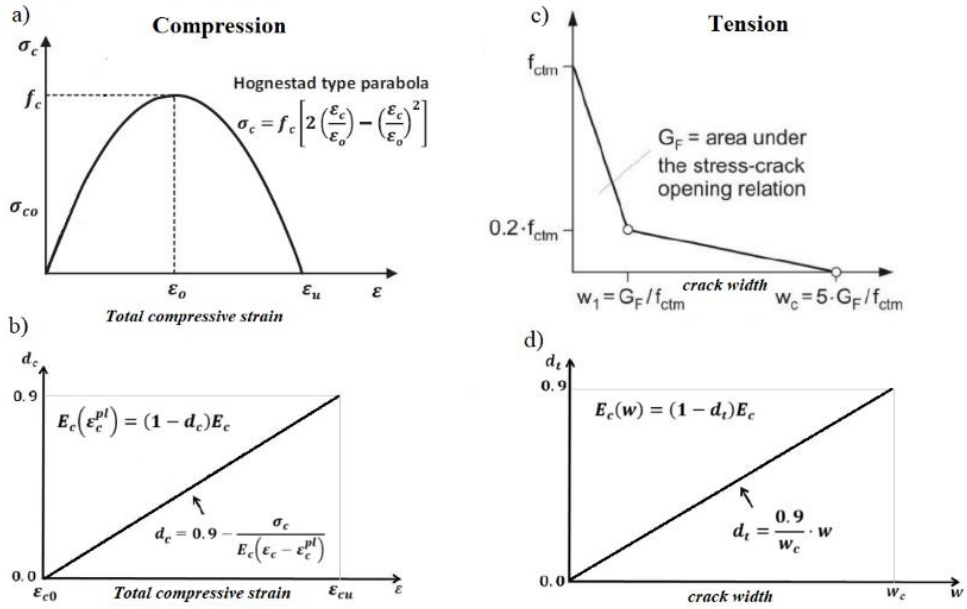

Figure 5.12: Constitutive relationships for concrete: a) Compressive behaviour; b) compressive damage; c) Tensile behaviour; d) Tensile damage.

Table 5.5. Parameters defined for the Concrete Damaged Plasticity.

Dilation (ψ)	**Eccentricity (ε)**	**σ_{b0}/σ_{co}**	***K***	**Viscosity (μ)**
36.0	0.1	1.16	0.8	0

5.5.3 Results

A comparison between the load-displacement curves obtained by the numerical simulations and experimentally is shown in Fig. 5.13. Accurate results were obtained in terms of ultimate load and deflection, despite numerically obtained shear strengths are in general smaller than the experimental ones, with an average difference of 4.46%. Results of the comparison are summarized in Table 5.6.

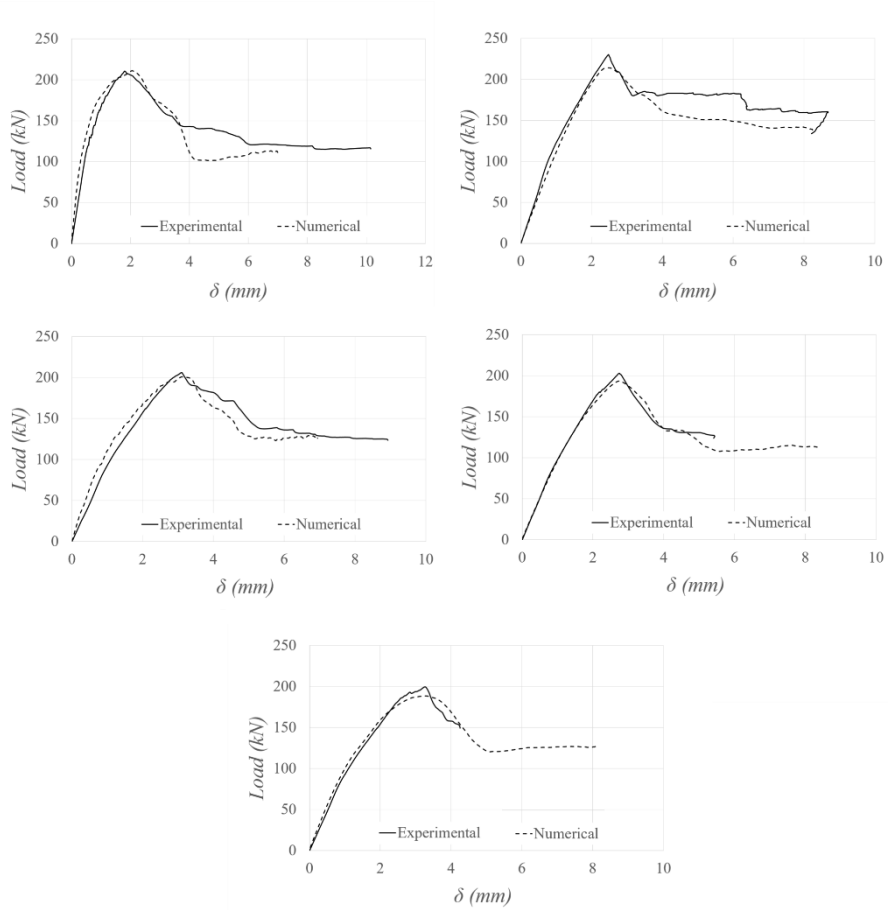

Figure 5.13: Comparison between load-deflection curves obtained with the numerical model and experimentally: a) A4 (T/T_{cr} = 0); b) B2 (T/T_{cr} = 0.43); c) A5 (T/T_{cr} = 0.7); d) A6 (T/T_{cr} = 1.06); e) A7 (T/T_{cr} = 1.3).

Table 5.6. Comparison between numerical and experimental results.

Test ref.	T/T_{cr}	P_u **(Numerical) (kN)**	P_u **(Experimental) (kN)**	$P_u/P_{control}$ **(Numerical)**	$P_u/P_{control}$ **(Exp.)**
A5	0	210.95	210.61	1	1
B2	0.43	214.03	225.30	0.930	0.979
A6	0.70	200.63	206.09	0.951	0.978
A7	1.06	193.59	202.86	0.918	0.963
A8	1.30	188.24	199.42	0.892	0.947

Once the numerical model was validated with the experimental results, simulations were performed, for type-A slabs, for other values of T/T_{cr} than those applied at the laboratory, up to a maximum of $T/T_{cr} = 1.5$ (Fig. 5.14). A linear decreasing trend is observed, with a weak interaction between shear strength in the spanning direction and tensile stresses in transverse direction. For $T/T_{cr} = 1.2$ ($\sigma_t \approx 3.8$ MPa), $P_u/P_{u,T=0}$ ratio is equal to 0.92. Beyond that point, the numerical model predicts a slightly greater reduction of the shear strength as the tensile force increases, with a 12.4% decrement when $T/T_{cr} = 1.5$ ($\sigma_t \approx 4.8$MPa). In general, numerical simulations are in agreement with the experimental results. As can be seen, B2 slab properly fits the curve obtained for type-A slabs, which may indicate that for the considered reinforcement ratios, the effect of the external tensile force on the shear strength is similar.

Fig. 5.14 also includes EC-2 and ACI 318 predictions (Eq. (5.1) and (5.3) respectively) for the reduction of the shear strength with increasing tension. For their calculation, the value of the transverse tensile stress has been used without any further consideration, assuming that longitudinal and transverse normal stresses affects the same way the shear strength. As can be seen, this approach leads to highly conservative results. For example, for $T/T_{cr} = 1.3$ ($\sigma_t \approx 4.2$MPa), EC-2 predicts a 49.2% reduction and ACI 318 a 75.3% reduction. This percentages are much greater than the 5.3% reduction observed experimentally and 10.8% reduction predicted numerically for the same level of tension. Therefore, in order to obtain closer results to those obtained experimentally and numerically, the value of the transverse tensile stress should be weighted before being used in the current code formulations.

Nevertheless, since the effect of normal stresses is an additive term in the shear strength, this factor may change for different values of the effective depth, reinforcement ratio or concrete compressive strength than those of the specimens tested. This is also the reason why ACI 318 yields more conservative results than EC-2. Both codes add the tensile stresses to the shear strength multiplying σ_t by a similar factor (0.167 for ACI and 0.15 for EC-2), but for the geometry of the tested slabs, the ratio between both codes predictions when $\sigma_t = 0$ *is* $V_{R,EC2}/V_{R,ACI} = 1.37$. Thus, in this case, for the same value of σ_t, the relative reduction of the shear strength is greater for ACI 318.

The results of the experimental campaign presented herein are more or less in line with the observations made in the only similar experiment available in literature, conducted by Regan (1983), when a 15% reduction on the strength was reported for $\sigma_t \approx 3.95$ MPa. This value is greater than the values obtained by the authors, but it is reasonable since the point load was applied at mid-span and a punching-shear failure occurred. Because of that, part of the failure surface was normal to the transverse tensile stresses and the strength of the specimen could have been more affected. However, in the experimental campaign carried out by Bui *et al.* (2017b) on slabs subjected to longitudinal tensile stresses, greater relative strength reductions up to a 27% were obtained for values of around 1.2 MPa. This greater values of strength reduction seems to highlight the different degree of affectation between transverse and longitudinal tensile stresses. In any case, the experimental evidence in slabs is scarce and more research is needed in slabs with different geometries, reinforcement ratios, reinforcement dispositions (symmetric or not) and supporting conditions.

To conclude, cracking patterns obtained for different values of the applied external tension are presented in Fig. 5.15, showing a considerable similarity with the experimentally observed crack patterns.

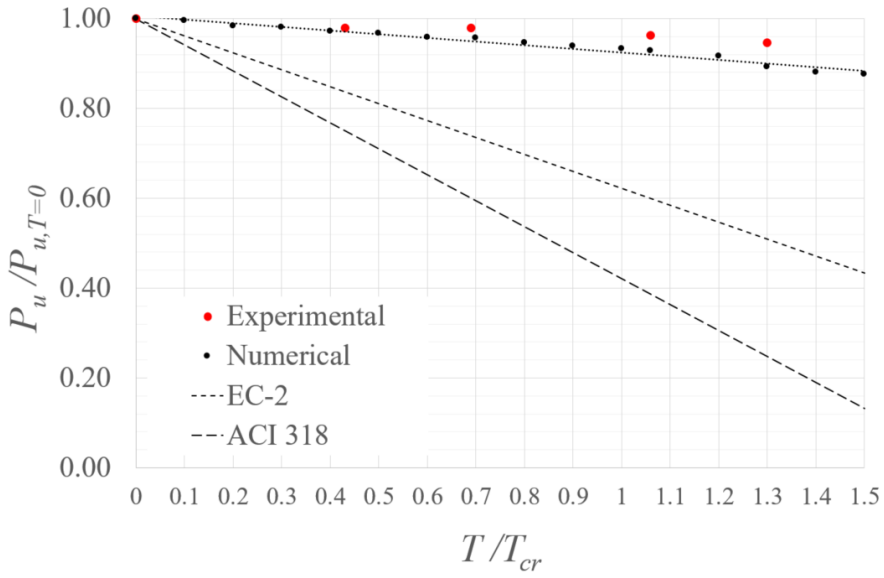

Figure 5.14: Comparison of the relative decrement of the shear strength obtained numerically, in laboratory tests and with EC-2 and ACI-318 predictions.

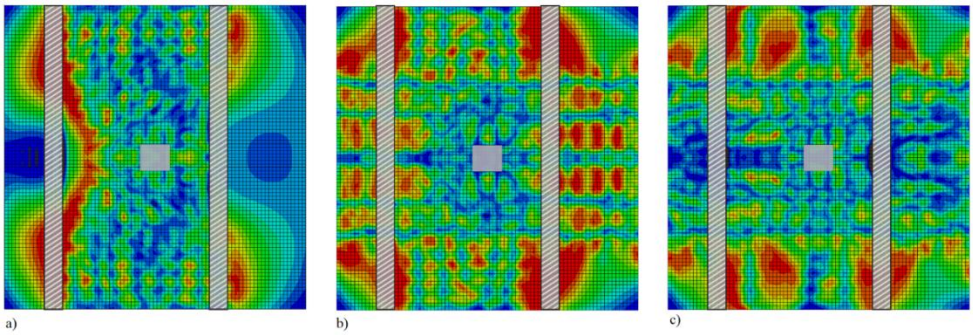

Figure 5.15: Cracking pattern at failure (red: not-cracked; green: tension softening; blue: open crack or compression): a) $T/T_{cr} = 0$; b) $T/T_{cr} = 0.7$; c) $T/T_{cr} = 1.3$.

5.6 Summary

Based on the observations made during the experimental campaign presented in this chapter, the following conclusions can be drawn:

- Code formulations are, in general, not clear about how to proceed when predicting the effects of transverse tensile forces on the shear strength of one-way slabs. It is probably due to the fact that they are originally intended for beams, where only longitudinal axial stresses may take place in practice. It is not mentioned if transverse normal stresses should be considered in the same way as longitudinal stresses or even if they may be neglected. The comparison between code predictions and experimental and numerical results carried out in this study shows that the shear strength is barely affected by the transverse tensile stresses, and neglecting its negative contribution leads only to slightly unsafe results, for the particular case of the specimens tested. On the contrary, if transverse tensile stresses are taken into account, their value should be lessened or very conservative results will be obtained.

- For the studied case of one-way slabs subjected to transverse axial tension, no significant reduction of the shear strength has been observed. An approximately linear decrement up to a 5.3% reduction on the shear strength for the highest transverse axial load applied ($\sigma_t \approx 4.2$ MPa) was obtained experimentally. These values are smaller than the relative strength reduction of the shear strength reported in tests on slabs subjected to longitudinal axial tension (27% reduction for $\sigma_t \approx 1.2$ MPa, see section 2.4), which highlights the

difference in the degree of affectation on the one-way shear strength of transverse and longitudinal tensile stresses.

- Transverse axial load affects the stiffness of the members due to premature cracking of concrete. If not enough reinforcement is provided in the transverse direction, this fact may lead to a non-fulfillment of the serviceability limit state of deformations and affect the durability of the member due to excessive crack width.
- The numerical model developed for the non-linear analysis of the tested slabs, calibrated with the experimental results of the tested reference slab (T=0), predicts an approximately linear decrement of the shear strength with increasing axial tension, as observed experimentally, but yields slightly conservative results, particularly for values of T/T_{cr} > 1.2. For the aforementioned case of the highest transverse axial load applied at the laboratory ($\sigma_t \approx 4.2$ MPa), the numerical model predicts an 11.8% reduction in the shear strength, compared to the 5.3% reduction observed experimentally.

Chapter 6

Conclusions

6.1 Summary

In this thesis, the shear behaviour of reinforced concrete one-way slabs subjected to concentrated loads and the punching-shear behaviour of RC two-way slabs subjected to the simultaneous action point loads and in-plane tension has been addressed. The development of mechanical models that properly predict the ultimate capacity of slabs under such loading conditions, along with the provision of experimental evidence for the seldom studied case of out-of-plane loads and in-plane tension was the main goals of this study.

In the case of one-way slabs subjected to concentrated loads, a mechanical model has been developed to predict the shear strength. For the sake of simplicity, it has been divided into two sub-models, one for loads applied close to the supports, where only the one-way shear failure has been considered, and another for loads applied away from the support, where the possibility of two different failure modes, one-way shear and punching-shear, has been assumed. Both models take into account a significant number of variables involved in the phenomenon, such as the clear shear span, the concrete compressive strength, the reinforcement ratio, the effective depth, the load spreading angle, the size effect and the size of the loaded area. It is applicable to simply supported slabs, cantilever slabs and situations with partial restraint to the rotation, such as intermediate supports. It has been validated with a database of 133 shear test (90 for loads close to the support and 43 for loads away from the support) in slabs subjected to a single concentrated load in different supporting conditions, yielding results on the safe side and showing low scatter. A parametric analysis of the model was also performed, detailing how the different involved variables affect the shear strength, and some simplified expressions for the shear strength calculation were provided.

Regarding the case of two-way slabs subjected to out-of-plane point loads and in-plane tension, the fundamentals of the modifications made to the

original model for axisymmetric punching previously developed at the Universitat Politècnica de Catalunya are explained and new set of simplified equations have been derived and validated with the results of the experimental campaigns found in literature. A comparison of the strength predictions obtained using the proposed model and punching-shear provisions included in some of the most widely accepted international building codes has been also presented. In addition to that, an experimental campaign was carried out in order to provide experimental evidence for the particular case of uniaxial in-plane tension and to contribute to the model validation. As an addition to the experimental works conducted, another set of experimental tests on one-way slabs subjected to concentrated loads an in-plane transverse axial tension is presented. This particular load case, barely studied throughout the last decades, represents a real situation where the interpretation of design codes may be ambiguous, since in general, shear provisions in codes are mainly intended for beams, where axial stresses are always applied in longitudinal (spanning) direction.

6.2 Conclusions

6.2.1 Literature review

- Despite the exhaustive research work carried out since the beginning of the XX century, the shear behaviour of reinforced concrete elements is still not fully clear. The lack of consensus that currently exist around the shear problem in structural engineering is a consequence of the complexity of the phenomenon.
- The basic ideas and hypotheses related to shear in RC elements, that are currently widely accepted, were developed in the first decade of the XX century. Major contributions were made by Karl Wilhelm Ritter, Emil Mörsch and Arthur Newell Talbot.
- In spite of the shear resisting actions of RC elements are more or less widely accepted, the big amount of mechanical models available in literature consider their contribution very differently. Some models try to take into account all the resisting actions, but rather complicated design equations are obtained. Other models consider a particular resisting action as the dominant mechanism, whereas the contribution of the remaining actions is considered

in a simplified way or even neglected. These models usually lead to more simplified design equations, but their applicability to all the load cases and geometries found in practice may be questionable.

- Until the last two decades, a large portion of the research conducted on the one-way shear strength of RC elements was focused on beams. Hence, most of the mechanical models found in literature and provisions given in codes are intended for these structural elements. However, it has been experimentally observed that in the case of one-way slabs subjected to concentrated loads, specific parameters such as the width of the specimen, the size of the loading plate and its position within the span affect the shear capacity and may change the failure mode.
- The effect of tensile axial forces on the shear and punching-shear capacity of RC elements has not been exhaustively studied throughout the XX century. Reported test results show that an adequate amount of reinforcement symmetrically distributed in the cross section prevents premature failures and provide the elements with a significant post-cracking capacity. In that cases, code provisions have been observed to be conservative. On the other hand, if reinforcement is not symmetric or insufficient, the shear capacity seems to be more effected.

6.2.2 Developed mechanical models

- The Compression Chord Capacity Model has demonstrated to accurately capture the complex shear and punching-shear behaviour of reinforced concrete members. In general, comparisons with laboratory tests have shown the adequacy of the model for the prediction of the shear strength in a large variety of geometries and load cases, including the extensions presented in this thesis for the particular cases of one-way slabs subjected to concentrated loads and two-way slabs subjected to concentric loads and in-plane tension. The rational and mechanical basis of the original model allows its extrapolation to more specific situations by considering the particular parameters that are involved in each case and by introducing them into the equilibrium equations and the failure criterion.

One-way slabs subjected to concentrated loads

- The theoretical model for the prediction of the shear strength of RC slabs, linearly supported and subjected to concentrated loads close to the support ($a_v/d \leq 3$), yields accurate results when compared to the test results available, with a mean value (MV) of the ratio V_{exp}/V_R=1.127, and CoV = 0.121 for simply supported slabs, MV of V_{exp}/V_R=1.132, CoV = 0.166 for cantilever slabs and MV of V_{exp}/V_R=1.165, CoV = 0.168 for slabs with partial restraint to the rotation at the support. Globally, MV of V_{exp}/V_R=1.137, CoV = 0.145 for the 90 slabs considered. Furthermore, 95% of the results have a V_{exp}/V_R ratio greater than 0.92. Thus, all the assumptions of the model, including considering the direct transmission effects from a value of a_v/d = 3 and a common horizontal spreading angle α = 52.5º seem to be appropriate.
- The parametric analysis of the model carried out in section 3.3.4, along with the simplified equations presented in section 3.3.5, are a useful tool for the design and assessment of the shear strength of reinforced concrete slabs in daily engineering. Results yielded by the simplified expressions are similar to the ones obtained using the model but with slightly more scatter (Globally, MV of V_{exp}/V_R=1.137 CoV = 0.145 for the model and MV of V_{exp}/V_R =1.158 CoV = 0.173 for the simplified expressions). Anyhow, obtained values are safe, since 95% of the results have a V_{exp}/V_R ratio greater than 0.90.
- Both the general and the simplified methods developed provide more accurate predictions of the tests included in the available database than those obtained using the analysed codes provisions. MC-2010 (*LoA II*) and EC-2 with α = 52.5º are the best options, followed by EC-2 with α = 45º and MC-2010 (*LoA I*). As far as ACI 318-19 concerns, since its formulation does not include a factor to take into account the proximity of the load to the support, it yields the most conservative results which also present large scatter.
- The theoretical model for the prediction of the shear strength of RC slabs, linearly supported and subjected to concentrated loads away from the support ($a_v/d \geq 3$), provides very good results when compared to the test results available, with a mean value of the ratio V_{exp}/V_R =1.12, and CoV = 0.16 for simply supported slabs, MV of V_{exp}/V_R =1.12, CoV = 0.12 for cantilever slabs and MV of V_{exp}/V_R =1.16, CoV = 0.11 for slabs with partial restraint to the rotation at the support. Globally, MV of V_{exp}/V_R =1.12, CoV = 0.14 for the

43 slabs considered. Furthermore, 95% of the results have a V_{exp}/V ratio greater than 0.92.

- Failure modes trends predicted by the model are in agreement with the experimental observations for the analyzed variables. When $a_v/d \geq 5$ or $C_y/b_{slab} \leq 0.15$, model predictions are mostly punching failures, as observed experimentally, whereas shear clearly dominates when $C_y/b_{slab} \geq 0.25$. No significant influence of the concrete compressive strength or the longitudinal reinforcement ratio has been observed experimentally nor in the model results.
- In comparison with the analyzed design codes, the proposed model provides the best results when predicting the ultimate capacity of the slabs included in the available database in terms of safety and accuracy. As far as codes concern, best results are obtained with Model Code 2010 *LoA* II. Eurocode-2 yields unsafe results if no threshold value for the effective shear width is used, whereas ACI 318 yields quite conservative results and presents the highest scatter.

Two-way slabs subjected to concentrated loads and in-plane axial tension

- The mechanical model for the prediction of the punching-shear strength of RC two-way slabs subjected simultaneously to concentrated loads and in-plane tensile forces, has been described and verified with the results of previously carried out experimental campaigns. The model incorporates the main effects of in-plane tension on the shear resisting actions and yields accurate results when contrasted with tests available in the literature. When compared to codes provisions, best results are obtained with the proposed model (V_{exp}/V_R = 5.3%, CoV=2.85%) for the case of uniaxial tension and V_{exp}/V_R = 12.6%, CoV=9.76% for biaxial tension.
- The model has been able to accurately reproduce the results of an experimental campaign carried out as part of this thesis on 5 slabs subjected to a concentrated load and different levels of unidirectional in-plane tensile forces. The experimentally observed behaviour has been captured both qualitatively and quantitatively, with an average error on the prediction of the ultimate load of 5%.
- The increment of tensile stress in the longitudinal reinforcement due to the tensile force is captured by the model, in which failure may be conditioned by the load that produces yielding in the flexural reinforcement in both directions. Such phenomenon usually occurs for $T>T_{cr}$. However, for

low reinforcement ratios, it can also occur for $T<T_{cr}$. The relationship between the ultimate load and the ratio T/T_{cr} results approximately bilinear, with higher slope when premature yielding of the longitudinal reinforcement takes place.

6.2.3 Experimental works

Two-way slabs subjected to concentrated loads and uniaxial in-plane axial tension

- The set of experimental axisymmetric punching-shear tests conducted on slabs subjected to unidirectional in-plane tensile forces showed a progressive reduction of the ultimate capacity of the specimens for increasing values of the external axial force. The relationship between the ultimate load and the ratio T/T_{cr} resulted approximately bilinear, with higher slope when premature yielding of the longitudinal reinforcement takes place.
- Strains measurements indicated that for the highest values of the external force applied, the longitudinal reinforcement partially yielded before the ultimate capacity was attained. After the initiation of yielding, a redistribution process took place between the longitudinal and transverse direction, confirmed by the increment of the strain rate of the transverse reinforcement and the redistribution of the reactions.
- The effect of axial tension not only affected the ultimate capacity of the specimens, but also the load-deflection response. Greater values of the external load provoked premature cracking which leaded to a loss of stiffness, increasing the ultimate deflection under the point load. For highest values of the in-plane tensile stresses, also the failure changed from brittle to slightly ductile, which resembles the reported punching-shear behaviour of low reinforced slabs. This indicates that the hypothesis of considering a reduced yielding strength of the reinforcement when the external tension cracks the concrete cross-section is appropriate in this situation.
- If additional reinforcement is placed to resist the applied tensile force, even in case that the section cracks ($T>T_{cr}$), the increment of stress in the longitudinal reinforcement may not be enough to produce yielding prior to

the punching failure, thus contributing to avoid the "extra" reduction of punching strength.

- The numerical model developed in parallel to the experimental campaign showed a similar trend to that observed experimentally, in terms of ultimate loads, deflections and cracking patterns. Simulation performed for a wide range of values of the external tension allowed to confirm the bilinear trend observed experimentally.

One-way slabs subjected to concentrated loads and transverse in-plane axial tension

- Code formulations are, in general, not clear about how to proceed when predicting the effects of transverse tensile forces on the shear strength of one-way slabs. It is probably due to the fact that they are originally intended for beams, where only longitudinal axial stresses may take place in practice. It is not mentioned if transverse normal stresses should be considered in the same way as longitudinal stresses or even if they may be neglected. The comparison between code predictions and experimental and numerical results carried out in this study showed that the shear strength was barely affected by the transverse tensile stresses, and neglecting its negative contribution leads only to slightly unsafe results, for the particular case of the specimens tested. On the contrary, if transverse tensile stresses are taken into account, their value should be lessened or very conservative results will be obtained.

- Transverse axial load affected the stiffness of the members due to premature cracking of concrete. If not enough reinforcement is provided in the transverse direction, this fact may lead to a non-fulfillment of the serviceability limit state of deformations and affect the durability of the member due to excessive crack width.

- For the studied case of one-way slabs subjected to transverse axial tension, no significant reduction of the shear strength was observed. An approximately linear decrement up to a 5.3% reduction on the shear strength for the highest transverse axial load applied ($\sigma_t \approx 4.2$ MPa) was obtained experimentally. These values are smaller than the relative strength reduction of the shear strength reported in tests on slabs subjected to longitudinal axial tension (27% reduction for $\sigma_t \approx 1.2$ MPa, see section 2.4), which highlights the

difference in the degree of affectation on the one-way shear strength of transverse and longitudinal tensile stresses.

- Regardless the level of tensile force applied, reactions distributed more or less in the same way, with highest values measured at the center of each support and decreasing towards the free edges of the slabs. Despite the clear shear span for the farthest support was equal to 5*d*, a similar trend was observed for the reaction distribution than at the support placed at 3*d*. This is in agreement with the assumption made in the one-way shear mechanical model of limiting the shear effective width to a threshold value.

The numerical model developed for the non-linear analysis of the tested slabs, calibrated with the experimental results of the reference slab, predicted an approximately linear decrement of the shear strength with increasing axial tension, as observed experimentally, but yielded slightly more conservative results, For the case of the highest transverse axial load applied, the numerical model predicted an 11.8% reduction in the shear strength, compared to the 5.3% reduction observed experimentally.

6.3 Recommendations for future research

6.3.1 Future experimental work

The big amount of parameters involved in the shear response of reinforced concrete slabs subjected to concentrated loads requires large experimental evidence to fully understand the phenomenon and check the mechanical models in a wide variety of load cases. Some of the future research may be focused on:

One-way slabs subjected to concentrated loads supported on linear supports

- Experiments to measure the horizontal load spreading angle for different positions of the load within the span in order to better understand the distribution of the shear effective width for each different supporting conditions.
- Additional experiments for different values of the a_v/d ratio in order to help to set the limit distance to start considering the arching action effects and confirm the hypothesis accepted in the proposed mechanical models.

Also, to study the transition between one-way shear failure and punching failure, which is considered an open issue.

- Experiments on slabs subjected to multiple concentrated loads to check the interaction between the loads and correctly determinate the effective shear width.
- Experiments on slabs with different effective depths, in order to check the applicability of the size effect law developed for beams used in the mechanical model.
- Experiments on slabs subjected to longitudinal axial stresses, to help to understand and model its effects on the shear resisting actions and check the possible suitability of the expressions developed for beams.
- Experiments on slabs subjected to eccentric loads in order to extend the mechanical models to incorporate this common load case.
- Experiments on slabs made with new materials such as fibre reinforced concrete, ultra-high performance concrete or lightweight aggregate concrete. Furthermore slabs reinforced with FRP or SMA materials should be also investigated to help to validate the mechanical models for repairing situations.

Two-way slabs subjected to point loads and in-plane tension

- Additional experiments on non-axisymmetric loading conditions, to study the redistribution of internal forces between the two orthogonal directions and the validity of axisymmetric models in this situations.
- Experiments with rectangular loading areas, to study the shape of the critical perimeter and its variation with the level of in-plane tension applied.
- Additional experiments with a wide range of reinforcement ratios, to study the premature yielding and the post-cracking capacity and the degree of affection on the punching-shear capacity for different values of the in-plane tension.
- Analogously to one-way slabs, experiments on slabs made with new concrete mixes or repaired with FRP or SMA.
- Additional experiments on slabs with different effective depths and a constant level of in-plane axial stress, to check if the size effect law adopted in the models may be dependent on the normal stresses.

- Experiments on slabs subjected to axial stresses of different sign in the two orthogonal directions, to study the superposition of the tensile strains generated by the compressive force in the transverse direction with the tensile strains generated by the external tension

6.3.2 Future theoretical work

One of the main advantages of the mechanical models is that they can be modified to incorporate or be adapted to new loading conditions, material properties and static schemas. Some of the possible extensions of the mechanical models presented in this thesis are:

- Punching shear of posttensioned concrete slabs, accounting for the effects of the compression stresses and the favourable effect of inclined prestressing tendons, as well he effects of in-plane tensile forces.
- Punching shear model of slabs made of steel or plastic fibre reinforced concrete, to account for the bridging effect of fibres, increasing the shear strength along the critical crack, similarly as how it has been done for shera in beams.
- Consider the effects of strengthening systems, such as post-installed studs, studying their stresses (usually lower than the yield strength), or the effects of steel or FRP plates bonded to the top of the slab or those of SMA.
- Punching shear of slabs around internal columns under eccentric load, or around columns placed in the slab perimeter, either in one side or in a corner.

References

AASHTO LRFD. Bridge design specifications and commentary. Second edition, (1998) and 2000 update. Washington DC: American Association of State Highway Transportation Official, 2000.

AASHTO LRFD. Bridge design specifications. Washington DC: American Association of State Highway Transportation Official, 2007.

ACI Committee 318. Building code requirements for structural concrete: (ACI 318-51). Farmington Hills: American Concrete Institute, 1951.

ACI Committee 318. Building code requirements for structural concrete: (ACI 318-63). Farmington Hills: American Concrete Institute, 1963.

ACI Committee 318. Building code requirements for structural concrete: (ACI 318-19); and commentary (ACI 318R-19). Farmington Hills: American Concrete Institute, 2019.

ACI Committee 346. Code Requirements for Nuclear Safety Concrete Structures and Commentary. Farmington Hills: American Concrete Institute, 2007.

ASCE-ACI Committee 426. The shear strength of reinforced concrete members // Journal of Structural Engineering. 1973 99, 6. 1091-1187.

ASCE-ACI Committee 445. Recent approaches to shear design of structural concrete // Journal of Structural Engineering. 1998 124, 12. 1375-1417.

Abrams J.H. The punching shear strength of pre-cracked reinforced concrete in biaxial tension. M.S. Thesis, Cornell University, 1979.

Adebar P., Collins M.P. Shear strength of members without transverse reinforcement // Canadian Journal of Civil Engineering. 1996. 23. 30-41.

Adetifa B., Polak M.A. Retrofit of slabs column interior connections using shear bolts // ACI Structural Journal. 2005. 102, 2. 268-274.

Alexander, S. D. B., Simmonds S.H. Ultimate strength of slab column connections // ACI Structural Journal. 1987. 84, 3. 255-261.

Alexander, S. D. B., Simmonds S.H. Bond Model for concentric punching shear // ACI Structural Journal. 1992. 89, 3. 325-334.

Amer A., Arockiasamy M., Shahawy M. Load distribution of existing solid slab bridges based on field tests // Journal of Bridge Engineering. 1999. 4, 3. 189-193.

Angelakos D., Bentz E., Collins M.P. Effect of concrete strength and minimum stirrups on shear resistance of large members // ACI Structural Journal. 2001. 98, 3. 290-300.

Bairán J.M., Marí A. Coupled model for the non-linear analysis of anisotropic sections subjected to general 3D loading. Part 1: Theoretical formulation // Computers and Structures. 2006. 84, 31. 2254-2263.

Bairán J.M., Marí A., Cladera A. Analysis of shear resisting actions by means of optimization of strut and tie models taking into account crack patterns // Hormigón y Acero. 2017. 69, 286. 197-206.

Bairán J.M., Menduiña R., Marí A., Cladera A. Shear strength of non-slender reinforced concrete beams // ACI Structural Journal. 2020. 69, 286. 277-289.

Bazant Z.P., Kim J.K. Size effect in shear failure of longitudinally reinforced beams // ACI Structural Journal. 1984. 81, 5. 456-468.

Bazant Z.P., Chen E.P. Scaling of structural failure // ASME Applied Mechanics Reviews. 1997. 50, 10. 593-627.

Bazant Z.P., Yu Q. Designing against size effect on shear strength of reinforced concrete beams without stirrups: II. Verification and calculation // Journal of Structural Engineering. 2005. 131 456-468.

Bazant Z.P., Yu Q., Gerstle W., Hanson J., Ju J. Justification of ACI 446 Proposal for Updating ACI Code Provisions for Shear Design of Reinforced Concrete Beams // ACI Structural Journal. 2007. 104, 5. 601-610.

Bazant Z.P., Yu Q. Universal size effect law and effect of crack depth on quasi-brittle structure strength // ASCE Journal of Engineering Mechanics. 2009. 91, 4. 78-84.

Belarbi, A., Hsu, T.T.C. Constitutive laws of softened concrete in biaxial tension compression // ACI Structural Journal. 1995. 92, 5. 562–573.

Belletti, B., Damoni, C., Hendriks, M.A.N., & de Boer, A. Analytical and numerical evaluation of the design shear resistance of reinforced concrete slabs // Structural Concrete. 2014. 15, 3. 317-330.

Bentz E.C. Repeating a classic set of experiments on size effect in shear of members without stirrups // ACI Structural Journal. 2005. 102, 6. 832-838.

Bentz E.C., Vecchio F.J., Collins M.P. Simplified Modified Compression Field Theory for calculating shear strength of reinforced concrete elements // ACI Structural Journal. 2006. 103, 4. 614-624.

Bentz E. C., Foster S. J. On shear in members without stirrups and the application of energy-based methods in light of 30 years of test observations. // Structural Concrete. 2019. 20, 4. 1481-1489.

Bhide, S. B., Collins, M. P. Influence of Axial Tension of the Shear Capacity of Reinforced-Concrete Members // ACI Structural Journal. 1989. 86, 5, 570-581.

Bui T.T., Abouri S., Liman A., Nana W.S.A., Tedoldi B., Roure T. Experimental investigations of shear strength of full-scale concrete slabs subjected to concentrated loads in nuclear buildings // Engineering Structures. 2017a. 131, 15. 405-420.

Bui T.T., Nana W.S.A., Abouri S., Liman A., Tedoldi B., Roure T. Influence of uniaxial tension and compression on shear strength of concrete slabs without shear reinforcement under concentrated loads // Construction and Building Materials. 2017b. 146. 86-101.

CEB-FIP. Model Code 1978. Lausanne: 1978.

CEB-FIP. Model Code 1970. London: Thomas Telford, 1991.

CEB-fib. Model Code 2010. London: Thomas Telford, 2010.

CSA. Design of concrete structures CSA A23.-94. Canadian Standard Association, 1994.

Carmona J.R., Ruiz G. Bond and size effect on the shear capacity of RC beams without stirrups // Engineering Structures. 2014. 66. 45-56.

Carmpana S., Fernández-Ruiz M., Anastasi A., Muttoni A. Analysis of shear transfer actions on one-way RC members based on measured cracking pattern and failure kinematics // Magazine of Concrete Research. 2013. 65, 6. 386-404.

Cavagnis F., Fernández-Ruiz M., Muttoni A. An analysis of the shear transfer actions in reinforced concrete members without transverse reinforcement. Structural Concrete 2017. 19, 10.

Cavagnis F., Fernández-Ruiz M., Muttoni A. A mechanical model for failures in shear of members without transverse reinforcement based on development of a critical shear crack // Engineering Structures. 2018. 157. 300-315.

Choi, K.K., Park, H.G., Wight J.K. Unified shear strength model for reinforced concrete beams – Part I: Development // ACI Structural Journal. 2007. 104, 2. 142–152.

Choi, K.K., Park, H.G., Wight J.K. Unified shear strength model for reinforced concrete beams – Part II: Verification and simplified method // ACI Structural Journal. 2007. 104, 2. 153–161.

Cladera A. Shear design of reinforced high-strength concrete beams // PhD Thesis. Universitat Politècnica de Catalunya, Barcelona, 2003.

Cladera A., Marí A. Shear design procedure for reinforced normal and high-strength concrete beams using artificial neural networks. Part I: Beams without stirrups // Engineering Structures. 2004. 26, 2, 917-926.

Cladera A., Perez J.L., Martinez-Abella F. Shear strength of RC beams. Precision, accuracy, safety and simplicity using genetic programming // Computers and Concrete. 2014. 14, 4. 479-501.

Cladera A., Marí A., Ribas C., Bairán J.M., Oller E. Predicting the shear-flexural strength of slender reinforced concrete T and I shaped beams // Engineering Structures. 2015. 101, 15. 386-398.

Cladera A., Marí A., Bairán J.M., Oller E., Duarte, N. The compression chord capacity model for the shear design and assessment of reinforced and prestressed concrete beams // Structural Concrete. 2016. 18, 2, 1017-1032.

Clark A.P. Diagonal tension in reinforced concrete beams // ACI Structural Journal. 1951. 48, 2. 145 – 155.

Coin A., Thonier H. Shear tests on reinforced concrete slabs // Annales de Bâtiment et des Travaux Publiques. 2007. 7-16.

Collins M. P., Mitchell D., Adebar P., Vecchio, F. J. A general shear design method // ACI Structural Journal. 1996. 93, 1. 36-45.

Collins M.P., Kuchma D. How safe are our large, lightly reinforced concrete beams, slabs and footings? // ACI Structural Journal. 1999. 96, 4. 482-490.

Collins M.P., Bentz E.C., Sherwood E.G., Xie L. An adequate theory for the shear strength of reinforced concrete structures // Magazine of Concrete Research. 2008. 60, 9. 635-650.

Dantas A.M.D., El Debs M.K. Shear strength analysis of slabs without transverse reinforcement under concentrated loads according to ABNT NBR 6118:2014 // Revista Ibracon de Estruturas e Materiais. 2019. 12, 3. 658-675.

Dantas A.M.D., Lantsoght E., El Debs M.K. One-way shear strength of wide reinforced concrete members without stirrups // Structural Concrete. 2020. 22, 2.

Dassault Systems Simulia Corp. Abaqus Analysis user's manual 6.14. Providence, 2014.

Deifalla A. A mechanical model for concrete slabs subjected to combined punching shear and in-plane tensile forces // Engineering Structures. 2021. 231, 15.

Doorgest J. Transition between one-way shear and punching-shear. Msc Thesis. Delft University of Technology, 2012

Drucker D.C., Prager W. Soil mechanics and plastic analysis or limit design // Quarterly of Applied Mathematics. 1952. 10, 2. 157 – 165.

Drucker D.C. On structural concrete and theorems of limit analysis // International Association for Bridge and Structural Engineering. 1961. 21. 49 – 59.

EN CEN. EN 1992 Eurocode 2: Design of concrete structures- Part 1-1: General rules and rules for buildings. Brussels: Comité Européen de Normalisation, 2005.

El-Salakawy E.F., Polak M.A., Soliman M.H. Slab-column edge connections subjected to high moments // Canadian Journal of Civil Engineering. 1997. 25, 3. 526-538.

Elstner R.C., Richard C., Hognestad E. Laboratory investigations of a rigid frame failure // ACI Structural Journal. 1957. 53, 1. 637-668.

Elstner R.C., Hognestad E. Shearing strength of reinforced concrete slabs // Journal of the American Concrete Institute. 1956. 28, 1. 29-58.

FD-P. Eurocode 2 – Calcul des Structures en béton – Guide d'application des normes NF EN 1992. France, 2013.

Fenwick R. C., Paulay, T. Mechanisms of Shear Resistance of Concrete Beams // Journal of the Structural Division – ASCE. 1968. 94, 10, 2325-2350.

Fernández-Montes D., González E., Díaz E. Influence of axial tension on the shear strength of floor joist without transverse reinforcement // Structural Concrete. 2015. 16, 2. 207-220.

Fernandez-Ruiz M., Muttoni A., Sagaseta J. Shear strength of concrete members without transverse reinforcement: A mechanical approach to consistently account for size and strain effects // Engineering Structures. 2015. 99, 15. 360-372.

fib. Punching of structural concrete slabs // *fib* Bulletin 12. 2001.

fib. Punching shear of structural concrete slabs// *fib* Bulletin 81. 2017.

fib. Towards a rational understanding of shear in beams and slabs // *fib* Bulletin 85. 2018.

Fisker J., Hagsten, L.G. Mechanical model for the shear capacity of RC beams without stirrups: A proposal based on limit analysis // Engineering Structures. 2016. 115. 220-231.

Fourtsadakis K. Punching strength of reinforced concrete slabs under eccentric loading. Msc Thesis. Universitat Politecnica de Catalunya, Barcelona, 2020.

Gastebled O.J., May I.M. Fracture mechanics model applied to shear failure of reinforced concrete beams without stirrups // ACI Structural Journal. 2001. 98, 2. 184-190.

Genikomsou A.S., Polak M.A. Finite element analysis of punching shear of concrete slabs using damaged plasticity model in ABAQUS // Engineering Structures. 2015. 98, 1. 38-48.

Goldbeck A.T. The influence of total width on the effective width of reinforced concrete slabs subjected to central concentrated loading // ACI Journal Proceedings. 1917. 12, 2. 324-333.

Gustafsson P.J., Hillerborg, A. Sensitivity in Shear Strength of Longitudinally Reinforced Concrete Beams to Fracture Energy of Concrete // ACI Structural Journal. 1988. 85, 3. 286-294.

Guruzteaga M., Oller E., Ribas C., Cladera A., Mari A. Influence of the longitudinal reinforcement on the shear strength of one-way concrete slabs // Materials and Structures. 2015. 48, 8. 2597-2612.

Haddadin M.J., Hong S.T., Mattock A.H. Stirrups effectiveness in reinforced concrete beams with axial force // Journal of the structural division (ASCE). 1971. 97, 9. 2277-2297.

Hassan A.A.A., Hossain K.M.A., Lachemi M., "Strength, cracking and deflection performance of large-scale self-consolidating concrete beams subjected to shear failure." Engineering Structures. 2010. 32, 5. 1262-1271.

Havolnik J., Vidakovic A., Vida R. Shear capacity of clamped deck slabs subjected to a concentrated load // Journal of Bridge Engineering. 2020. 25, 7. 794-802.

Hillerborg, A., Modéer, M., Petersson, P.E. Analysis of crack formation and crack growth in concrete by means of fracture mechanics and finite elements // Cement and Concrete Research. 1976. 6, 6. 773–781.

Hillerborg, A. Analysis of a single crack // Fracture Mechanics on Concrete, Development in Civil Engineering. Amsterdam: Elsevier Science Publishers. 1983. 223-249.

Hoang L.C., Nielsen M.P. Plasticity approach to shear design // Cement and Concrete Composites. 1998. 20, 6. 437-453.

Hoover C.G., Bazant Z.P. Universal size-shape effect law based on comprehensive concrete fracture tests // ASCE Journal of Engineering Mechanics. 2014. 140, 3. 473-479.

Huber P., Huber T., Kollegger J. Investigation of the shear behavior of RC beams on the basis of measured crack kinematics // Engineering Structures. 2016. 113, 41-58.

Islam M.S., Pam H.J., Kwan A.K.H. Shear capacity of high-strength concrete beams with their point of inflection within the shear span // Proceedings of the Institution of Civil Engineers: Structures and Buildings. 1998. 128. 91-99.

Jau W.C., White R.N., Gergely P. Behavior of reinforced concrete slabs subjected to combined punching and biaxial tension. U.S Nuclear Regulatory Commission, 1982.

Jorgensen H.B., Hoang L.C., Fabrin L.S., Malgaard J. Influence of high axial tension on the shear strength of non-shear RC beams // Proceedings of the International IABSE Conference. 2013. 99, 31.

Kani J.N.G. The riddle of shear failure and its solution // ACI Structural Journal. 1964. 61, 4. 441 – 467.

Kani J.N.G. Basic facts concerning shear failure // ACI Structural Journal. 1966. 63, 6. 675 – 692.

Kani J.N.G. How safe are our large concrete beams? // ACI Structural Journal. 1967. 64, 3. 128 – 141.

Karayannis C.G., Chalioris C.E.. Shear tests of reinforced concrete beams with continuous rectangular spiral reinforcement // Construction and Building Materials. 2013. 46, 86–97.

Kaufmann W., Marti P. Structural concrete: Cracked Membrane Model // Journal of Structural Engineering. 1998. 124, 12. 1467-1475.

Khuntia M., Stojadinovic, B. Shear strength of reinforced concrete beams without transverse reinforcement. // ACI Structural Journal. 2001. 98, 5, 648-656.

Kim D., Kim, W., White, R. N. Arch action in reinforced concrete beams – a rational prediction of shear strength // ACI Structural Journal. 1999. 96, 4. 586-593.

Kim W., Jeong, J. Decoupling of Arch Action in Shear-Critical Reinforced Concrete Beams. // ACI Structural Journal. 2011. 108, 4, 395-404.

Kinnunen S, Nylander H. Punching of concrete slabs without shear reinforcement // Transactions No. 158; Royal Institute of Technology, Stockholm: 1960.

Kostovos M.D., Bobrowsky, J., Eibl J. Behavior of reinforced concrete T-beams in shear. // Structural Engineer, Part B: R&D Quarterly. 1987. 65, B1, 1-10.

Kuchma D.,Wei S., Sanders D., Belarbi A., Novak L. Development of one-way shear provisions of ACI 318-19 for reinforced concrete. // ACI Structural Journal. 2019 116, 4.

Kupfer H.B., Gerstle K.H. Behavior of concrete under biaxial stresses // Journal of the Engineering Mechanics Division. 1973. 99, 4. 853–866.

Lantsoght E. Shear in reinforced concrete slabs under concentrated loads close to supports. PhD Thesis. Delft University of Technology, Delft, 2013a.

Lantsoght E., van der Veen C., Walraven, J. Shear in one way slabs under concentrated loads close to support // ACI Structural Journal. 2013b. 110, 2. 275-284.

Lantsoght E., van der Veen C., Walraven J.C. Shear capacity of slabs under a combination of loads. Fib Symposium, Israel, April, 2013c.

Lantsoght E., van der Veen C., Walraven, J. Shear in one way slabs under concentrated loads close to support // ACI Structural Journal. 2014. 111, 6. 1441-1449.

Lantsoght, E., van der Veen, C., de Boer, A., Walraven, J. Transverse load redistribution and effective shear width in reinforced concrete slabs // Heron. 2015a. 60, 3. 145-179.

Laupa A., Siess C.P., Newmark N.M. The shear strength of simple reinforced concrete beams without web reinforcement // Structural Research Series Nº 52. University of Illinois 1953.

Lee J., Fenves G.L. Plastic damage model for cyclic loading of concrete structures // Journal of Engineering Mechanics. 1998. 124, 8. 892-900.

Leonhardt F., Walther R. The Stuttgart shear tests 1961 // Cement & Concrete Association Library. Translation Nº 111. London: 1961.

Lubell A.S. Shear in wide reinforced concrete members. PhD Thesis. University of Toronto, Toronto, 2006.

Lubell A.S., Bentz E.C., Collins M.P. One-way shear in wide concrete beams with narrow supports // ASCE/SEI Structures Congress. Vancouver, 2008.

Lubell A.S., Bentz E.C., Collins M.P. Influence of longitudinal reinforcement on one-way shear in slabs and wide beams // Journal of Structural Engineering. 2009. 135, 1. 79-87.

Lubliner J., Oliver J., Oller S., Oñate E. A plastic damage model for concrete // International Journal of Solids and Structures. 1988. 25, 3. 299-326.

Marí A., Bairán J., Cladera A., Oller E., Ribas, C. Shear-flexural strength mechanical model for the design and assessment of reinforced concrete beams // Structure and Infrastructure Engineering. 2014. 11, 11. 1399-1419.

Marí A., Bairán J., Cladera A., Oller E. Shear design and assessment of reinforced and prestressed concrete beams based on a mechanical model // Journal of Structural Engineering. 2016. 142, 10.

Marí A., Cladera A., Bairán J. Effects of axial forces and prestressing on the shear strength of structural concrete members // Proceedings of the VII ACHE International Structures Conference. A Coruña, Spain, 2017.

Marí A., Cladera A., Oller E., Bairán J. A punching shear mechanical model for reinforced concrete flat slabs with and without shear reinforcement // Engineering Structures. 2018. 166. 413-426.

Mattock A.H. Diagonal tensional cracking in concrete beams with axial forces // Journal of the structural division (ASCE). 1969. 95, 9. 1887-1900.

Mohr S., Bairán J.M., Marí A. A frame element model for the analysis of reinforced concrete structures under shear and bending // Engineering Structures. 2010. 32, 12. 3936-3954.

Moody K.G., Viest I.M., Elstner R.C., Hognestad E. Shear strength of reinforced concrete beams: Part I – test of simple beams // ACI Structural Journal. 1954. 51, 4. 317-332.

Moody K.G., Viest I.M., Elstner R.C., Hognestad E. Shear strength of reinforced concrete beams: Part II – test of restrained beams without web reinforcement // ACI Structural Journal. 1955a. 51, 5. 417- 434.

Moody K.G., Viest I.M., Elstner R.C., Hognestad E. Shear strength of reinforced concrete beams: Part III – test of restrained beams with web reinforcement // ACI Structural Journal. 1955b. 51, 6. 525 - 539.

Moody K.G., Viest I.M., Elstner R.C., Hognestad E. Shear strength of reinforced concrete beams: Part IV – analytical studies // ACI Structural Journal. 1955c. 51, 7. 697- 730.

MOP. Instrucción para el Proyecto y ejecución de obras de hormigón. Burgos: Ministerio de Obras Públicas, 1939 *ACI Committee 318.* Building code requirements for structural concrete: (ACI 318-51). Farmington Hills: American Concrete Institute, 1951.

Muttoni A., Schwartz, J. Behavior of Beams and Punching in Slabs without Shear Reinforcement // Proceedings of the IABSE Colloquium, Vol. 62, Stuttgart, Germany, 1991.

Muttoni A., Fernandez-Ruiz M. Shear strength of members without transverse reinforcement as function of critical shear crack width // ACI Structural Journal. 2008. 105, 2. 163-172.

Muttoni A. Punching shear strength of reinforced concrete slabs without transverse reinforcement // ACI Structural Journal. 2008. 105, 4. 440-450.

Muttoni A., Fernandez-Ruiz M. Shear in slabs and beams: should they be treated in the same way? // *fib* Bulletin Nº 57. 2010. 105-128.

NACU. Standard Building Regulations for the Use of Reinforced Concrete. Philadelphia: National Association of Cement Users, 1910.

Nana W.S.A., Bui T.T., Liman A., Abouri S. Experimental and numerical modelling of shear behavior of full-scale RC slabs under concentrated loads // Structures. 2017. 10. 96-116.

Natario F.M., Fernández Ruiz M., Muttoni, A. Shear strength of RC slabs under concentrated loads near clamped linear supports // Engineering Structures. 2014. 76, 10. 10-23.

Natario F.M. Static and fatigue shear strength of reinforced concrete slabs under concentrated loads near linear supports. PhD Thesis. École Polytechnique Fédérale de Lausanne, Lausanne, 2015.

NEN 6720. Technische Grondslagen voor Bouwvoorschriften, Voorschriften Beton TGB 1990 – Constructieve Eisen em Rekenmethoden. The Netherlands: Norcomissie 351001, 1995.

Nielsen M.P. Limit analysis and concrete plasticity. London: Prentice-Hall, 1984.

Olonisakin, A. A., Alexander, S. D. B. Mechanism of shear transfer in a reinforced concrete beam. // Canadian journal of civil engineering. 1999. 26, 6. 810-817.

Pang, X.B., Hsu, T.T.C. Fixed-angle softened-truss model for reinforced concrete // ACI Structural Journal. 2006. 1996. 93, 2. 197–207.

Park, H.G., Choi, K.K., Wight J.K. Strain-based shear strength model for slender beams without web reinforcement // ACI Structural Journal. 2006. 103, 6. 783–793.

Perez J.L., Cladera A., Rabuñal J.R., Martinez-Abella F. Optimization of existing equations using a new Genetic Programming algorithm: Application to the shear strength of reinforced concrete beams //Advances in Engineering Software. 2012. 50. 82-96.

Regan P.E. Beams subjected to axial loads. Imperial College, London, 1971. 93-118.

Regan, P.E. Shear resistance of concrete slabs at concentrated loads close to supports // Structures Research Group, Polytechnic of Central London, UK. 1982. 1-24.

Regan P.E. Punching shear in prestressed concrete slab bridges // Structures Research Group, Polytechnic of Central London, 1983.

Regan P.E., Rezai-Jorabi H. Shear resistance of one-way slabs under concentrated loads // ACI Structural Journal. 1988. 85, 2. 150-157.

Regan P.E. Enhancement of shear resistance in short shear spans of reinforced concrete – an evaluation of UK recommendations and particularly of BD44/95 // London, University of Westminster (UK), 1998.

Regan P.E., Kennedy-Reid I.L., Pullen A.D., Smith, D.A. The influence of aggregate type on the shear resistance of reinforced concrete // Structural Engineer. 2005. 83, 23. 27-32.

Reineck K.H. Ultimate shear force of structural concrete members without transverse reinforcement derived from a mechanical model // ACI Structural Journal. 1991. 88, 5. 592-602.

Reineck K.H. Shear design in a consistent design concept for structural concrete based on strut-and-tie models // Design examples for the 1996 FIP recommendations: Practical design of structural concrete, *fib* bulletin 16. 2002. 165-186.

Reissen K., Hegger J. Shear capacity of reinforced concrete slabs under concentrated loads // 8th IABSE Congress, Seoul, South Korea, 2012.

Reissen K., Hegger J. Experimental investigations on the shear capacity of RC cantilever slabs under concentrated loads // 16th European Bridge Conference, Edinburgh, Scotland, 2015.

Reissen K., Classen M., Hegger J. Shear in reinforced concrete slabs: Experimental investigations in the effective shear width of one-way slabs under concentrated loads and with different degrees of rotational restrain // Structural Concrete. 2017. 19, 1. 36-48.

Ritter W. Die Bauwiese Hennebique //Schweizerische Bauzeitung. 1899. Bd XXXIII., Nº7.

Rodriguez-Serrano M.F. Punching of steel fiber reinforced concrete slabs. Ms Thesis. Universitat Politecnica de Catalunya, Barcelona, 2021.

Rombach G., Henze L. Shear capacity of concrete slabs without shear reinforcement under concentrated loads close to support // Proceedings of the 2017 *fib* Symposium, Maastricht, the Netherlands, June 2017.

Ruddle M.E., Rankin G.I.B., Long A.E. Mohr approach to prediction of beam shear strength // Proceedings of the Institution of Civil Engineers: Structures and Buildings. 1999. 134, 4. 363-372.

Sagaseta J., Muttoni A., Fernández-Ruiz M., Tassinari L. Non-axis-symmetrical punching shear arounf internal columns of R slabs without shear reinforcement // Magazine of Concrete Research. 2011. 63, 6. 441-457.

Sagaseta J., Tassinari L., Muttoni A., Fernández-Ruiz M. Punching of flat slabs supported on rectangular columns // Engineering Structures. 2014. 77. 17-33.

Sarkar S., Adwan O., Bose B. Shear stress contributions and failure mechanisms of high strength reinforced concrete beams // Materials and Structures. 1999. 32, 2.

Schlaich J., Schafer K., Jennewein M. Toward a consistent design of structural concrete // PCI Journal. 1987. 32, 3. 74-150.

Sherwood E.G., Lubell A.S., Bentz E.C., Collins M.P. One-way shear strength of thick slabs and wide beams // ACI Structural Journal. 2006. 103, 6. 794-802.

Sherwood E.G., Bentz E.C., Collins M.P. Effect of aggregate size on beam-shear strength of thick slabs // ACI Structural Journal. 2007. 104, 2. 180-190.

Shioya T., Iguro M., Nojiri Y., Akiyama H., Okada T. Shear Strength of Large reinforced Concrete Beams // ACI Special Publication 118. Detroit 1990. 259-280.

SIA 162. Design code for the calculation, the construction and the execution of structures in concrete, in reinforced concrete and in prestressed concrete, Code 162. Zurich, Switerland: Société suisse des ingénieurs et des architectes, 1968.

Sigrist V., Bentz E.C., Fernandez-Ruiz M., Foster S., Muttoni A. Background to the fib Model Code 2010 shear provisions – part I: beams and slabs // Structural Concrete. 2013. 14, 3. 195-203.

Talbot A.N. Test of reinforced concrete beams: resistance of web stresses series of 1907 and 1908 // Bulletin 29. University of Illinois, Engineering Experiment Station, 1909.

Taylor H.P.J. The fundamental behavior of reinforced concrete beams in bending and shear. // ACI Special Publication 42. Detroit, 1974.

Timoshenko S., and Woinowsky-Krieger S. Theory of plates and shells. New York: McGraw-Hill, 1959.

Vaz Rodriguez R. Shear strength of reinforced concrete bridge deck slabs. PhD Thesis. École Polytechnique Fédérale de Lausanne, Lausanne, 2007.

Vaz Rodriguez R., Fernandez-Ruiz M., Muttoni A., Shear strength of R/C bridge cantilever slabs // Engineering Structures. 2008. 30, 11. 3024-3033.

Vecchio F.J., Collins M.P. The Modified Compression Field Theory for reinforced concrete elements subjected to shear // ACI Structural Journal. 1986. 83, 2. 219-231.

Vecchio F.J. Disturbed Stress Field Model for reinforced concrete: Formulation // Journal of Structural Engineering. 2000. 126, 9. 1070-1077.

Vecchio F.J. Disturbed Stress Field Model for reinforced concrete: Implementation // Journal of Structural Engineering. 2001. 127, 1. 12-20.

Vintzeleou E.N., Tassios T.P. Mathematical models for dowel action under monotonic and cyclic conditions // Magazine of Concrete Research. 1986. 38, 134. 13-22.

Walraven J.C. Fundamental analysis of aggregate interlock // Journal of the Structural Division, Proceedings of the ASCE. 1981. 107, 11. 2245-2270.

Walraven J.C. Shear friction in high strength concrete // Delft University of Technology. 1995. Vol. 4. 57-65.

Westergaard H.M. Computation of stresses in bridge slabs due to wheel loads // Public Roads. 1930. Vol. 11, 1. 1-23.

Withey O.M. Test of plain reinforced concrete series of 1906 // Bulletin of the University of Wisconsin, Engineering Series. 1907. 4, 1. 1-66.

Withey O.M. Test of plain reinforced concrete series of 1907 // Bulletin of the University of Wisconsin, Engineering Series. 1908. 4, 2. 1-66.

Xie L., Bentz E.C., Collins M.P. Influence of axial stress on shear response of reinforced concrete elements // ACI Structural Journal. 2011. 108, 6. 745-754.

Yang Y., den Ujil J., Walraven J. Critical shear displacement theory: on the way to extending the scope of shear design and assessment for members without shear reinforcement // Structural Concrete. 2015. 17, 5. 790-798.

Yang Y., Walraven J., den Ujil J. Shear behavior of reinforced concrete beams without transverse reinforcement based on critical shear displacement // Journal of Structural Engineering. 2017. 143, 1.

Yu Q., Jia-Liang L., Hubler M.H., Wendner R., Cusatis G., Bazant Z.P. Comparisson of main models for size effect on shear strength of reinforced concrete and prestressed concrete beams // Structural Concrete. 2016. 17, 5. 778-789.

Zararis P.D., Papadakis G.Ch. Diagonal shear failure and size effect in RC beams without web reinforcement // Journal of Structural Engineering. 2001. 127, 7. 733-741.

Zsutty T.C. Beam shear strength prediction by analysis of existing data // ACI Journal Proceedings. 1968. 65, 11. 943–951.

Zsutty, T.C. Shear strength prediction for separate categories of simple beam tests // ACI Journal Proceedings. 1971. 68, 2. 138–143.

Appendix A: Shear tests database

A.1 Loads applied close to the support

Geometry and reinforcement

Support type	Reference	Ref-Test	a_v/d	λ_M	f_c (MPa)	f_y (MPa)	ρ_l (%)	ρ_t (%)	b (m)	C_x (mm)	C_y (mm)	d_l (mm)	d_t (mm)	L (m)
SS	Lantsoght et. al (2013)	BL1T1	1.51		65.2	537.0	1.00	0.26	1.50	300	300	265	250	3.60
SS	Lantsoght et. al (2013)	BL2T1	0.94		75.8	537.0	1.00	0.26	1.50	200	200	265	250	3.60
SS	Lantsoght et. al (2013)	BL3T1	1.51		72.8	537.0	1.00	0.26	1.50	300	300	265	250	3.60
SS	Lantsoght et. al (2013)	BM1T2	1.51		65.2	537.0	1.00	0.26	1.00	300	300	265	250	3.60
SS	Lantsoght et. al (2013)	BM2T1	0.94		70.9	537.0	1.00	0.26	1.00	200	200	265	250	3.60
SS	Lantsoght et. al (2013)	BM3T1	1.51		72.8	537.0	1.00	0.26	1.00	300	300	265	250	3.60
SS	Lantsoght et. al (2013)	BX1T1	1.51		65.1	537.0	1.00	0.26	2.00	300	300	265	250	3.60
SS	Lantsoght et. al (2013)	BX2T1	0.94		56.3	537.0	1.00	0.26	2.00	200	200	265	250	3.60
SS	Lantsoght et. al (2013)	BX3T1	1.70		63.0	537.0	1.00	0.26	2.00	200	200	265	250	3.60
SS	Lantsoght et. al (2013)	S1T1	1.70		44.4	537.0	1.00	0.13	2.50	200	200	265	250	3.60
SS	Lantsoght et. al (2013)	S2T1	1.51		44.4	537.0	1.00	0.13	2.50	300	300	265	250	3.60
SS	Lantsoght et. al (2013)	S3T1	1.51		41.3	537.0	1.00	0.26	2.50	300	300	265	250	3.60
SS	Lantsoght et. al (2013)	S4T1	1.51		41.4	537.0	1.00	0.18	2.50	300	300	265	250	3.60
SS	Lantsoght et. al (2013)	S4T2	1.51		41.4	537.0	1.00	0.18	2.50	300	300	265	250	3.60
SS	Lantsoght et. al (2013)	S5T4	0.75		38.6	537.0	1.00	0.26	2.50	300	300	265	250	3.60

Support type	Reference	Ref-Test	a_v/d	λ_M	f_c (MPa)	f_y (MPa)	ρ_l (%)	ρ_t (%)	b (m)	C_x (mm)	C_y (mm)	d_l (mm)	d_t (mm)	L (m)
SS	Lantsoght et. al (2013)	S6T4	0.75		40.5	537.0	1.00	0.26	2.50	300	300	265	250	3.60
SS	Lantsoght et. al (2013)	S6T5	0.75		40.5	537.0	1.00	0.26	2.50	300	300	265	250	3.60
SS	Lantsoght et. al (2013)	S7T1	1.51		65.7	537.0	1.00	0.26	2.50	300	300	265	250	3.60
SS	Lantsoght et. al (2013)	S7T5	1.51		65.7	537.0	1.00	0.26	2.50	300	300	265	250	3.60
SS	Lantsoght et. al (2013)	S8T1	1.51		61.6	537.0	1.00	0.26	2.50	300	300	265	250	3.60
SS	Lantsoght et. al (2013)	S9T1	0.94		65.4	537.0	1.00	0.26	2.50	200	200	265	250	3.60
SS	Lantsoght et. al (2013)	S19T2	1.17		45.5	537.0	1.00	0.26	2.50	300	300	265	250	3.60
SS	Lantsoght et. al (2013)	S25T1	1.51		46.9	537.0	1.00	0.26	2.50	300	300	265	250	3.60
SS	Cullington *et al*. (1996)	lab 1	1.32		60.0	500.0	1.50	0.00	1.00	100	100	257	NR	4.37
SS	Cullington *et al*. (1996)	lab 2	0.31		60.0	500.0	1.50	0.00	1.00	100	100	257	NR	4.37
SS	Regan (1982)	1-SS	1.43		24.0	500.0	0.60	0.21	1.20	100	100	84	77	1.15
SS	Regan (1982)	2-SS	0.95		22.2	500.0	0.60	0.21	1.20	100	100	84	77	1.15
SS	Regan (1982)	3-SS	0.48		29.0	500.0	0.60	0.21	1.20	100	100	84	77	1.15
SS	Regan (1982)	4-SS	0.24		33.9	500.0	0.60	0.21	1.20	100	100	84	77	1.15
SS	Regan (1982)	5-SS	0.95		29.3	500.0	0.60	0.21	1.20	100	200	84	77	1.15
SS	Regan (1982)	7-SS	0.48		35.4	500.0	0.60	0.21	1.20	100	200	84	77	1.15
SS	Reissen *et al.* (2018)	S35A-1	1.91		41.3	900.0	0.98	0.45	3.50	400	400	240	254	3.00
SS	Reissen *et al.* (2018)	S35A-2	1.91		29.0	900.0	0.98	0.45	3.50	400	400	240	254	3.00
SS	Coin and Thonier (2007)	5	2.00		30.2	500.0	1.50	0.42	2.50	200	1000	85	77	2.70
SS	Coin and Thonier (2007)	6	2.00		30.2	500.0	1.50	0.42	2.50	200	700	85	77	2.70
SS	Coin and Thonier (2007)	5bis	2.00		30.2	500.0	1.50	0.42	2.50	200	1000	85	77	2.70

Appendix A: Shear tests database

Support type	Reference	Ref-Test	a_v/d	λ_M	f_c (MPa)	f_y (MPa)	ρ_l (%)	ρ_t (%)	b (m)	C_x (mm)	C_y (mm)	d_l (mm)	d_t (mm)	L (m)
SS	Coin and Thonier (2007)	6bis	2.00		30.2	500.0	1.50	0.42	2.50	200	700	85	77	2.70
SS	Lubell (2006)	AT-2/1000A	2.62		39.0	465.0	0.91	0.19	1.00	152	152	439	423	2.60
SS	Lubell (2006)	AT-2/1000B	2.63		37.9	465.0	0.91	0.19	1.00	152	152	438	422	2.60
SS	Bui *et al.* (2017)	S2	2.00		30.4	567.0	1.16	0.30	2.50	200	1000	85	77	2.70
SS	Bui *et al.* (2017)	S5	2.00		30.2	567.0	1.00	0.41	2.50	200	1000	85	79	2.70
SS	Bui *et al.* (2017)	S6	2.00		19.2	567.0	1.01	0.41	2.50	200	400	85	79	2.70
SS	Bui *et al.* (2017)	S3bis	2.00		30.4	567.0	1.16	0.18	2.50	200	400	85	77	2.70
SS	Bui *et al.* (2017)	S5bis	2.00		30.2	567.0	1.00	0.41	2.50	200	1000	85	78	2.70
SS	Bui *et al.* (2017)	S6bis	2.00		19.2	567.0	1.01	0.41	2.50	200	400	85	78	2.70
cant	Rombach and Henze (2017)	1d	1.00		43.4	522.0	1.17	0.53	4.50	400	400	215	202	1.90
cant	Rombach and Henze (2017)	2d-1	2.00		47.3	522.0	1.17	0.53	4.50	400	400	215	202	1.90
cant	Rombach and Henze (2017)	2d-2	2.00		55.5	522.0	1.17	0.53	4.50	400	400	215	202	1.90
cant	Rombach and Henze (2017)	3d-1	3.00		37.8	522.0	1.17	0.53	4.50	400	400	215	202	1.90
cant	Rombach and Henze (2017)	3d-2	3.00		49.5	522.0	1.17	0.53	4.50	400	400	215	202	1.90
cant	Havolnik *et al.* (2020)	SL0.1 A	1.99		36.1	500.0	0.73	NR	2.50	250	250	168	NR	1.30
cant	Havolnik *et al.* (2020)	SL0.1 B	1.99		36.1	500.0	0.73	NR	2.50	250	250	168	NR	1.30
cant	Havolnik *et al.* (2020)	SL1.1 A	1.99		34.8	500.0	1.50	NR	2.50	250	250	168	NR	1.30
cant	Havolnik *et al.* (2020)	SL1.1 B	1.99		34.8	500.0	1.50	NR	2.50	250	250	168	NR	1.30
cant	Havolnik *et al.* (2020)	SL1.2 A	1.99		32.2	500.0	1.50	NR	2.50	250	250	168	NR	1.30
cant	Havolnik *et al.* (2020)	SL1.2 B	1.99		32.2	500.0	1.50	NR	2.50	250	250	168	NR	1.30
cant	Havolnik *et al.* (2020)	SL0.2 A	1.99		38.2	500.0	0.73	NR	2.50	250	250	168	NR	1.30
cant	Havolnik *et al.* (2020)	SL0.2 B	1.99		38.2	500.0	0.73	NR	2.50	250	250	168	NR	1.30

Support type	Reference	Ref-Test	a_v/d	λ_M	f_c (MPa)	f_y (MPa)	ρ_l (%)	ρ_t (%)	b (m)	C_x (mm)	C_y (mm)	d_l (mm)	d_t (mm)	L (m)
cant	Havolnik *et al.* (2020)	SL0.3 A	1.99		34.5	500.0	0.73	NR	2.50	250	250	168	NR	1.30
cant	Havolnik *et al.* (2020)	SL0.3 B	1.99		34.5	500.0	0.73	NR	2.50	250	250	168	NR	1.30
cant	Havolnik *et al.* (2020)	SL2.1 A	1.99		30.5	500.0	1.27	NR	2.50	250	250	168	NR	1.30
cant	Havolnik *et al.* (2020)	SL2.1 B	1.99		30.5	500.0	1.27	NR	2.50	250	250	168	NR	1.30
cant	Havolnik *et al.* (2020)	SL2.2 A	1.99		29.4	500.0	1.27	NR	2.50	250	250	168	NR	1.30
cant	Havolnik *et al.* (2020)	SL2.2 B	1.99		29.4	500.0	1.27	NR	2.50	250	250	168	NR	1.30
cant	Natário *et al.* (2014)	FN1-E	2.10		46.6	579.0	1.00	0.39	3.00	400	400	210	194	1.50
cant	Natário *et al.* (2014)	FN1-W	2.10		45.2	579.0	1.00	0.39	3.00	400	400	210	194	1.50
cant	Natário *et al.* (2014)	SN1A	2.00		30.3	547.0	1.32	0.57	3.00	400	400	152	138	1.25
cant	Natário *et al.* (2014)	SN2A	3.00		30.1	547.0	1.32	0.57	3.00	400	400	152	138	1.25
cant	Reissen *et al.* (2018)	CS35A	2.07		31.0	900.0	0.98	0.45	3.50	400	400	241	254	1.80
PR	Lantsoght et. al (2015)	BL1T2	1.51	0.26	65.2	537.0	1.00	0.26	1.50	300	300	265	250	3.60
PR	Lantsoght et. al (2015)	BL2T2	0.94	0.24	75.8	537.0	1.00	0.26	1.50	200	200	265	250	3.60
PR	Lantsoght et. al (2015)	BL3T2	1.51	0.27	72.8	537.0	1.00	0.26	1.50	300	300	265	250	3.60
PR	Lantsoght et. al (2015)	BM1T1	1.51	0.17	65.2	537.0	1.00	0.26	1.00	300	300	265	250	3.60
PR	Lantsoght et. al (2015)	BM3T2	1.51	0.20	72.8	537.0	1.00	0.26	1.00	300	300	265	250	3.60
PR	Lantsoght et. al (2015)	BX1T2	1.51	0.21	65.1	537.0	1.00	0.26	2.00	300	300	265	250	3.60
PR	Lantsoght et. al (2015)	BX2T2	0.94	0.17	56.3	537.0	1.00	0.26	2.00	200	200	265	250	3.60
PR	Lantsoght et. al (2015)	BX3T2	1.70	0.18	63.0	537.0	1.00	0.26	2.00	200	200	265	250	3.60
PR	Lantsoght et. al (2015)	S19T1	1.17	0.14	45.5	537.0	1.00	0.26	2.50	300	300	265	250	3.60
PR	Lantsoght et. al (2015)	S1T2	1.70	0.13	28.6	537.0	1.00	0.13	2.50	200	200	265	250	3.60

Appendix A: Shear tests database

Support type	Reference	Ref-Test	a_v/d	λ_M	f_c (MPa)	f_y (MPa)	ρ_l (%)	ρ_t (%)	b (m)	C_x (mm)	C_y (mm)	d_l (mm)	d_t (mm)	L (m)
PR	Lantsoght et. al (2015)	S2T4	1.51	0.23	27.6	537.0	1.00	0.13	2.50	300	300	265	250	3.60
PR	Lantsoght et. al (2015)	S3T4	1.51	0.21	41.3	537.0	1.00	0.26	2.50	300	300	265	250	3.60
PR	Lantsoght et. al (2015)	S5T1	0.75	0.20	38.6	537.0	1.00	0.26	2.50	300	300	265	250	3.60
PR	Lantsoght et. al (2015)	S6T1	0.75	0.19	40.5	537.0	1.00	0.26	2.50	300	300	265	250	3.60
PR	Lantsoght et. al (2015)	S6T2	0.75	0.22	40.5	537.0	1.00	0.26	2.50	300	300	265	250	3.60
PR	Lantsoght et. al (2015)	S7T2	1.51	0.17	65.7	537.0	1.00	0.26	2.50	300	300	265	250	3.60
PR	Lantsoght et. al (2015)	S7T3	1.51	0.20	65.7	537.0	1.00	0.26	2.50	300	300	265	250	3.60
PR	Lantsoght et. al (2015)	S8T2	1.51	0.21	61.6	537.0	1.00	0.26	2.50	300	300	265	250	3.60
PR	Lantsoght et. al (2015)	S9T4	0.94	0.21	65.4	537.0	1.00	0.26	2.50	200	200	265	250	3.60
PR	Reissen *et al.* (2018)	MS35A	1.91	0.68	37.3	900.0	0.98	0.45	3.50	400	400	240	254	3.00
PR	Reissen *et al.* (2018)	MS35A-dr	1.91	0.34	38.0	900.0	0.98	0.45	3.50	400	400	240	254	3.00

*$\boldsymbol{a_v}$: distance between the inner face of the load and the inner face of the support; $\boldsymbol{\lambda_M}$: See Fig. 3.5; $\boldsymbol{f_c}$: Cylinder concrete compressive strength; $\boldsymbol{f_y}$: yield strength of the reinforcement; $\boldsymbol{\rho_l}$: amount of longitudinal reinforcement; $\boldsymbol{\rho_t}$: amount of transverse reinforcement; $\boldsymbol{d_l}$: effective depth of the longitudinal reinforcement; $\boldsymbol{d_t}$: effective depth of the transverse reinforcement; $\boldsymbol{b}$: width of the slab; $\boldsymbol{C_x}$: dimension of the loading plate perpendicular to the support; $\boldsymbol{C_y}$: dimension of the loading plate parallel to the support; $\boldsymbol{L}$: length of the span;

Ultimate strength prediction

Support type	Reference	Ref-Test	V_{exp} (kN)	V_{exp}/V_R	$V_{exp}/V_{R,simp}$	V_{exp}/V_{EC-2} (α=45º)	V_{exp}/V_{EC-2} (α=52.5º)	V_{exp}/V_{ACI} (α=45º)	V_{exp}/V_{ACI} (α=52.5º)	V_{exp}/V_{MC10} (LoA I)	V_{exp}/V_{MC10} (LoA II)
SS	Lantsoght et. al (2015)	BL1T1	844.0	0.929	0.913	1.19	1.19	1.86	1.86	1.59	0.96
SS	Lantsoght et. al (2015)	BL2T1	1311.0	1.241	1.405	1.49	1.20	3.65	2.92	1.72	1.22
SS	Lantsoght et. al (2015)	BL3T1	907.0	0.997	0.981	1.23	1.23	1.89	1.89	1.62	1.00
SS	Lantsoght et. al (2015)	BM1T2	591.0	1.113	0.959	1.24	1.24	1.95	1.95	1.67	1.01
SS	Lantsoght et. al (2015)	BM2T1	1062.0	1.150	1.214	1.36	1.36	3.36	3.36	1.91	1.34
SS	Lantsoght *et al.* (2015)	BM3T1	607.0	1.145	0.985	1.23	1.23	1.90	1.90	1.62	1.00
SS	Lantsoght *et al.* (2015)	BX1T1	1080.0	1.127	1.156	1.34	1.14	2.10	1.78	1.53	0.92
SS	Lantsoght *et al.* (2015)	BX2T1	1259.0	1.194	1.349	1.58	1.27	4.06	3.26	1.91	1.29
SS	Lantsoght *et al.* (2015)	BX3T1	935.0	1.257	1.427	1.49	1.18	2.09	1.66	1.81	1.05
SS	Lantsoght *et al.* (2015)	S1T1	799.0	1.086	1.220	1.43	1.14	2.13	1.69	1.84	1.02
SS	Lantsoght *et al.* (2015)	S2T1	1129.0	1.178	1.208	1.59	1.27	2.66	2.13	1.90	1.09
SS	Lantsoght *et al.* (2015)	S3T1	1131.0	1.182	1.211	1.63	1.31	2.76	2.21	1.98	1.12
SS	Lantsoght *et al.* (2015)	S4T1	964.0	1.011	1.032	1.39	1.11	2.35	1.88	1.68	0.95
SS	Lantsoght *et al.* (2015)	S4T2	925.0	0.971	0.990	1.33	1.07	2.25	1.80	1.62	0.91
SS	Lantsoght *et al.* (2015)	S5T4	1544.0	1.229	1.205	1.49	1.21	5.10	4.13	2.23	1.41
SS	Lantsoght *et al.* (2015)	S6T4	1213.0	0.949	0.925	1.15	0.93	3.91	3.17	1.71	1.09
SS	Lantsoght *et al.* (2015)	S6T5	1187.0	0.925	0.905	1.13	0.91	3.82	3.10	1.67	1.07
SS	Lantsoght *et al.* (2015)	S7T1	929.0	0.973	0.994	1.15	0.92	1.80	1.44	1.29	0.78

Appendix A: Shear tests database

Support type	Reference	Ref-Test	V_{exp} (kN)	V_{exp}/V_R	$V_{exp}/V_{R,simp}$	V_{exp}/V_{EC-2} (α=45º)	V_{exp}/V_{EC-2} (α=52.5º)	V_{exp}/V_{ACI} (α=45º)	V_{exp}/V_{ACI} (α=52.5º)	V_{exp}/V_{MC10} (LoA I)	V_{exp}/V_{MC10} (LoA II)
SS	Lantsoght *et al.* (2015)	S7T5	891.0	0.938	0.954	1.10	0.88	1.72	1.38	1.23	0.75
SS	Lantsoght *et al.* (2015)	S8T1	1227.3	1.285	1.314	1.55	1.24	2.45	1.96	1.76	1.05
SS	Lantsoght *et al.* (2015)	S9T1	1325.0	1.248	1.420	1.58	1.27	3.97	3.18	1.87	1.29
SS	Lantsoght *et al.* (2015)	S19T2	1249.0	1.255	1.167	1.51	1.22	3.25	2.61	1.75	1.08
SS	Lantsoght *et al.* (2015)	S25T1	1214.0	1.273	1.299	1.68	1.34	2.78	2.22	1.99	1.15
SS	Cullington *et al.* (1996)	lab 1	620.0	0.963	1.126	1.07	1.05	1.94	1.90	1.64	0.90
SS	Cullington *et al.* (1996)	lab 2	1000.0	1.439	1.568	2.79	2.25	6.68	5.40	3.42	2.05
SS	Regan (1982)	1-SS	97.0	1.122	1.129	1.74	1.40	3.61	2.89	1.74	1.15
SS	Regan (1982)	2-SS	110.0	1.057	1.084	1.59	1.28	4.99	4.03	1.60	1.18
SS	Regan (1982)	3-SS	171.0	1.224	1.216	2.87	2.34	8.22	6.72	2.48	1.91
SS	Regan (1982)	4-SS	206.0	1.259	1.263	3.67	3.02	10.23	8.43	2.96	2.35
SS	Regan (1982)	5-SS	160.0	1.181	1.087	1.73	1.45	5.19	4.34	1.74	1.34
SS	Regan (1982)	7-SS	176.0	0.981	0.892	2.19	1.86	6.06	5.15	1.93	1.55
SS	Reissen *et al.* (2018)	S35A-1	899.0	1.127	1.100	1.43	1.15	1.93	1.55	1.69	0.91
SS	Reissen *et al.* (2018)	S35A-2	707.0	1.068	1.061	1.26	1.02	1.82	1.46	1.59	0.81
SS	Coin and Thonier (2007)	5	264.0	1.059	1.094	1.39	1.23	1.98	1.75	1.92	0.92
SS	Coin and Thonier (2007)	6	307.0	1.480	1.545	1.95	1.69	2.78	2.41	2.63	1.27
SS	Coin and Thonier (2007)	5bis	269.0	1.079	1.115	1.42	1.26	2.02	1.79	1.96	0.94
SS	Coin and Thonier (2007)	6bis	216.0	1.042	1.087	1.38	1.19	1.96	1.69	1.85	0.89
SS	Lubell (2006)	AT-2/1000A	471.0	0.975	1.171	1.08	1.08	1.44	1.44	1.58	0.83
SS	Lubell (2006)	AT-2/1000B	440.0	0.931	1.122	1.02	1.02	1.37	1.37	1.50	0.79
SS	Bui *et al.* (2017)	S2	274.7	1.073	1.082	1.57	1.39	2.24	1.98	1.99	1.02

Support type	Reference	Ref-Test	V_{exp} (kN)	V_{exp}/V_R	$V_{exp}/V_{R,simp}$	V_{exp}/V_{EC-2} (α=45º)	V_{exp}/V_{EC-2} (α=52.5º)	V_{exp}/V_{ACI} (α=45º)	V_{exp}/V_{ACI} (α=52.5º)	V_{exp}/V_{MC10} (LoA I)	V_{exp}/V_{MC10} (LoA II)
SS	Bui *et al.* (2017)	S5	305.1	1.263	1.218	1.84	1.63	2.62	2.32	2.22	1.18
SS	Bui *et al.* (2017)	S6	165.0	1.264	1.371	1.76	1.47	2.70	2.26	2.16	1.08
SS	Bui *et al.* (2017)	S3bis	174.8	1.022	1.069	1.53	1.28	2.17	1.82	1.82	0.93
SS	Bui *et al.* (2017)	S5bis	313.1	1.296	1.250	1.89	1.67	2.69	2.38	2.28	1.21
SS	Bui *et al.* (2017)	S6bis	148.1	1.134	1.231	1.58	1.32	2.43	2.03	1.94	0.97
cant	Rombach and Henze (2017)	1d	1539.7	1.596	1.785	1.68	1.37	4.42	3.59	2.94	1.84
cant	Rombach and Henze (2017)	2d-1	1024.8	1.409	1.449	1.72	1.38	2.23	1.79	3.26	1.69
cant	Rombach and Henze (2017)	2d-2	937.8	1.289	1.326	1.49	1.20	1.88	1.51	2.75	1.46
cant	Rombach and Henze (2017)	3d-1	667.9	1.084	1.132	1.00	0.80	1.34	1.07	1.88	0.95
cant	Rombach and Henze (2017)	3d-2	717.9	1.124	1.171	0.98	0.78	1.26	1.01	1.77	0.92
cant	Havolnik *et al.* (2020)	SL0.1 A	359.6	1.021	0.946	1.40	1.12	1.95	1.56	2.40	1.39
cant	Havolnik *et al.* (2020)	SL0.1 B	374.6	1.064	0.985	1.46	1.17	2.03	1.62	2.50	1.45
cant	Havolnik *et al.* (2020)	SL1.1 A	385.6	0.944	1.061	1.20	0.96	1.67	1.34	2.62	1.25
cant	Havolnik *et al.* (2020)	SL1.1 B	463.6	1.135	1.276	1.44	1.15	2.01	1.61	3.15	1.50
cant	Havolnik *et al.* (2020)	SL1.2 A	394.6	1.013	1.146	1.26	1.01	1.78	1.42	2.79	1.32
cant	Havolnik *et al.* (2020)	SL1.2 B	431.6	1.107	1.253	1.38	1.10	1.94	1.56	3.06	1.44
cant	Havolnik *et al.* (2020)	SL0.2 A	405.6	1.112	1.026	1.55	1.24	2.13	1.71	2.64	1.54
cant	Havolnik *et al.* (2020)	SL0.2 B	372.6	1.022	0.943	1.43	1.14	1.96	1.57	2.42	1.41
cant	Havolnik *et al.* (2020)	SL0.3 A	402.6	1.175	1.091	1.59	1.28	2.23	1.78	2.75	1.58
cant	Havolnik *et al.* (2020)	SL0.3 B	395.6	1.155	1.072	1.57	1.25	2.19	1.75	2.70	1.56
cant	Havolnik *et al.* (2020)	SL2.1 A	392.6	1.080	1.175	1.35	1.08	1.92	1.54	2.86	1.39

Appendix A: Shear tests database

Support type	Reference	Ref-Test	V_{exp} (kN)	V_{exp}/V_R	$V_{exp}/V_{R,simp}$	V_{exp}/V_{EC-2} (α=45º)	V_{exp}/V_{EC-2} (α=52.5º)	V_{exp}/V_{ACI} (α=45º)	V_{exp}/V_{ACI} (α=52.5º)	V_{exp}/V_{MC10} (LoA I)	V_{exp}/V_{MC10} (LoA II)
cant	Havolnik *et al.* (2020)	SL2.1 B	362.6	0.998	1.086	1.24	1.00	1.77	1.42	2.64	1.29
cant	Havolnik *et al.* (2020)	SL2.2 A	442.6	1.244	1.357	1.54	1.23	2.20	1.76	3.28	1.59
cant	Havolnik *et al.* (2020)	SL2.2 B	425.6	1.196	1.305	1.48	1.18	2.12	1.70	3.15	1.53
cant	Natário *et al.* (2014)	FN1-E	618.8	0.926	0.910	1.11	0.89	1.45	1.16	1.98	1.07
cant	Natário *et al.* (2014)	FN1-W	612.8	0.917	0.901	1.11	0.89	1.46	1.17	2.00	1.07
cant	Natário *et al.* (2014)	SN1A	489.0	1.096	1.233	1.45	1.17	2.06	1.66	2.81	1.33
cant	Natário *et al.* (2014)	SN2A	330.0	0.869	1.007	0.84	0.67	1.19	0.96	1.58	0.75
cant	Reissen *et al.* (2018)	CS35A	1057.0	1.596	1.569	1.86	1.49	2.51	2.02	3.60	1.83
PR	Lantsoght et. al (2015)	BL1T2	1119.0	1.018	0.957	1.57	1.57	2.46	2.46	2.11	1.28
PR	Lantsoght et. al (2015)	BL2T2	1586.0	1.512	1.606	1.80	1.45	4.41	3.53	2.08	1.48
PR	Lantsoght et. al (2015)	BL3T2	1035.0	0.907	0.888	1.40	1.40	2.15	2.15	1.85	1.14
PR	Lantsoght et. al (2015)	BM1T1	811.0	1.166	1.019	1.71	1.71	2.68	2.68	2.29	1.39
PR	Lantsoght et. al (2015)	BM3T2	791.0	1.120	0.964	1.61	1.61	2.47	2.47	2.12	1.30
PR	Lantsoght et. al (2015)	BX1T2	1415.0	1.251	1.199	1.75	1.49	2.75	2.34	2.00	1.21
PR	Lantsoght et. al (2015)	BX2T2	1332.0	1.245	1.393	1.67	1.34	4.30	3.44	2.02	1.37
PR	Lantsoght et. al (2015)	BX3T2	1059.0	1.176	1.268	1.69	1.34	2.37	1.88	2.05	1.19
PR	Lantsoght et. al (2015)	S19T1	1379.0	1.218	1.220	1.67	1.34	3.58	2.88	1.93	1.19
PR	Lantsoght et. al (2015)	S1T2	912.0	1.234	1.385	1.90	1.50	3.03	2.40	2.62	1.36
PR	Lantsoght et. al (2015)	S2T4	1276.0	1.392	1.385	2.11	1.68	3.81	3.05	2.73	1.45
PR	Lantsoght et. al (2015)	S3T4	1199.0	1.062	1.017	1.73	1.38	2.93	2.34	2.10	1.18
PR	Lantsoght et. al (2015)	S5T1	1679.0	1.296	1.246	1.62	1.31	5.54	4.49	2.43	1.54
PR	Lantsoght et. al (2015)	S6T1	1353.0	1.024	0.983	1.28	1.04	4.36	3.53	1.91	1.22

Support type	Reference	Ref-Test	V_{exp} (kN)	V_{exp}/V_R	$V_{exp}/V_{R,simp}$	V_{exp}/V_{EC-2} (α=45º)	V_{exp}/V_{EC-2} (α=52.5º)	V_{exp}/V_{ACI} (α=45º)	V_{exp}/V_{ACI} (α=52.5º)	V_{exp}/V_{MC10} (LoA I)	V_{exp}/V_{MC10} (LoA II)
PR	Lantsoght et. al (2015)	S6T2	1337.0	1.016	0.954	1.27	1.03	4.31	3.49	1.88	1.20
PR	Lantsoght et. al (2015)	S7T2	1046.0	0.928	0.909	1.29	1.03	2.02	1.62	1.45	0.88
PR	Lantsoght et. al (2015)	S7T3	1021.0	0.907	0.869	1.26	1.01	1.97	1.58	1.41	0.86
PR	Lantsoght et. al (2015)	S8T2	1216.0	1.080	1.031	1.54	1.23	2.43	1.94	1.74	1.04
PR	Lantsoght et. al (2015)	S9T4	1717.0	1.622	1.768	2.05	1.65	5.14	4.12	2.42	1.68
PR	Reissen *et al.* (2018)	MS35A	1283.0	1.605	1.141	2.11	1.69	2.90	2.33	2.54	1.34
PR	Reissen *et al.* (2018)	MS35A-dr	1058.0	1.034	0.992	1.73	1.39	2.37	1.90	2.08	1.10

* V_{exp}: Experimental shear strength; V_R: Predicted shear strength; $V_{R,simp}$: predicted shear strength with the simplified expressions.

A.2 Loads away from the support

Geometry and reinforcement

Support type	Reference	Ref-Test	a_v/d	λ_M	f_c (MPa)	fy *(MPa)*	d_l (mm)	d_t (mm)	ρ_l *(%)*	ρ_t *(%)*	b (mm)	C_x (mm)	C_y (mm)	L *(m)*
SS	Lubell (2006)	AW1	3.011		36.9	467	538	517	0.790	0.087	1170	305	305	3.70
SS	Lubell (2006)	AW4	3.202		39.9	467	506	485	1.690	0.093	1168	305	305	3.70
SS	Reissen *et al.* (2018)	S15B-1	3.167		37.7	900	240	254	0.980	0.450	1500	400	400	4.00
SS	Reissen *et al.* (2018)	S15B-2	3.167		38.2	900	240	254	0.980	0.450	1500	400	400	3.00
SS	Reissen *et al.* (2018)	S25B-1	3.167		27.9	900	240	254	0.980	0.450	2500	400	400	4.00
SS	Reissen *et al.* (2018)	S25B-2	3.167		29.5	900	240	254	0.980	0.450	2500	400	400	3.00
SS	Reissen *et al.* (2018)	S35B-1	3.167		35.9	900	240	254	0.980	0.450	3500	400	400	4.00
SS	Reissen *et al.* (2018)	S35B-2	3.167		38.2	900	240	254	0.980	0.450	3500	400	400	3.00
SS	Reissen *et al.* (2018)	S35C-1	4.410		39.6	900	240	254	0.980	0.450	3500	400	400	4.00
SS	Reissen *et al.* (2018)	S35C-2	4.410		29.5	900	240	254	0.980	0.450	3500	400	400	4.00
SS	Oliveira et al. (2004)	L1b	5.297		59.2	749	114	101	1.100	1.080	2280	120	120	1.50
SS	Oliveira et al. (2004)	L2b	5.297		57.7	749	114	101	1.100	1.080	2280	120	240	1.50
SS	Oliveira et al. (2004)	L3b	5.297		59.4	749	114	101	1.100	1.080	2280	120	360	1.50
SS	Regan (1983)	BD2	5.140		38.7	530	107	95	1.210	1.350	1500	100	100	1.30
SS	Regan and Rezai-Jarobi (1988)	18	4.220		24.96	670	83	75	1.510	0.636	1000	100	300	1.35
SS	Regan and Rezai-Jarobi (1988)	19	4.220		23.2	670	83	75	1.510	0.636	1000	100	150	1.35

Support type	Reference	Ref-Test	a_v/d	λ_M	f_c (MPa)	fy *(MPa)*	d_l (mm)	d_t (mm)	ρ_l *(%)*	ρ_t *(%)*	b (mm)	C_x (mm)	C_y (mm)	L *(m)*
SS	Regan and Rezai-Jarobi (1988)	22	4.380		29.6	670	80	72	1.640	0.663	1200	100	150	1.35
SS	Regan and Rezai-Jarobi (1988)	23	4.380		28.32	670	80	72	1.640	0.663	1200	100	300	1.35
SS	Regan and Rezai-Jarobi (1988)	24	3.130		30.88	670	80	72	1.640	0.663	1200	300	100	1.35
SS	Regan and Rezai-Jarobi (1988)	25	5.630		24.24	670	80	72	1.640	0.663	1200	100	150	1.35
SS	Regan and Rezai-Jarobi (1988)	26	3.130		23.76	670	80.000	72	1.640	0.663	1200	100	150	1.35
SS	Regan and Rezai-Jarobi (1988)	19R	4.220		23.2	670	83	75	1.510	0.636	1000	100	150	0.90
cant	Natário *et al.* (2015)	FN6-E	3.238		46.5	579	210	194	1.000	0.390	3000	400	400	1.50
cant	Natário *et al.* (2015)	FN6-W	3.238		45.7	579	210	194	1.000	0.390	3000	400	400	1.50
cant	Natário *et al.* (2014)	SN3A	4.000		30.4	547	152	138	1.320	0.568	3000	400	400	1.25
cant	Reissen *et al.* (2018)	CS35B-1	3.320		37	900	241	254	0.980	0.450	3500	400	400	1.80
cant	Reissen *et al.* (2018)	CS35B-2	3.320		30.9	900	241	254	0.980	0.450	3500	400	400	1.80
cant	Reissen *et al.* (2018)	CS35B-ρq	3.320		35.3	900	241	254	0.980	0.150	3500	400	400	1.80
cant	Reissen *et al.* (2018)	CS35C	4.564		34.2	900	241	254	0.980	0.450	3500	400	400	1.80
cant	Reissen *et al.* (2018)	CS35C-ρq	4.564		33.6	900	241	254	0.980	0.150	3500	400	400	1.80
cant	Reissen *et al.* (2018)	CS35B-h	3.320		38.4	900	187	254	0.980	0.450	3500	400	400	1.80
cant	Rombach and Henze (2017)	VK4V1	3.054		42.5	554	167	153	1.200	0.742	2400	400	400	1.65
cant	Rombach and Henze (2017)	4d-1	4.000		40	522	215	202	1.170	0.530	4500	400	400	1.90
cant	Rombach and Henze (2017)	5d	5.000		46.4	522	215	202	1.170	0.530	4500	400	400	1.90
cant	Rombach and Henze (2017)	6d	6.000		43	522	215	202	1.170	0.530	4500	400	400	1.90
cant	Vaz Rodrigues *et al*. (2006)	DR1c	3.722		40.8	499	350	287	0.830	0.285	10000	300	300	2.78
cant	Vaz Rodrigues *et al*. (2006)	DR2c	3.286		40	505	350	330	0.830	0.282	10000	300	300	2.78

Appendix A: Shear tests database

Support type	Reference	Ref-Test	a_v/d	λ_M	f_c (MPa)	fy *(MPa)*	d_l (mm)	d_t (mm)	ρ_l *(%)*	ρ_t *(%)*	b (mm)	C_x (mm)	C_y (mm)	L *(m)*
cant	Vaz Rodrigues (2002)	1	6.542		53.3	460	120	111	1.190	0.380	3000	152	130	1.00
CS	Reissen (2016)	MS35B	3.167	0.56	38.2	900	240	254	0.980	0.450	3500	400	400	3.00
CS	Reissen (2016)	MS35B-22	3.104	0.66	37.8	900	180	194	0.980	0.450	3500	300	300	3.00
CS	Reissen (2016)	MS35B-ρq	3.167	0.56	32.9	900	240	254	0.980	0.150	3500	400	400	3.00
CS	Reissen (2016)	MS35C	4.410	0.45	37.3	900	240	254	0.980	0.450	3500	400	400	3.00
CS	Reissen (2016)	MS35C-ρq	4.410	0.45	34.9	900	240	254	0.980	0.150	3500	400	400	3.00

*a_v: distance between the inner face of the load and the inner face of the support; d_l: efective depth of the longitudinal reinforcement; d_t: efective depth of the transverse reinforcement; λ_M: See Fig. 3.5; f_c: Cylinder concrete compressive strength; f_y: Yield strength of the reinforcement; d_l: effective depth of the longitudinal reinforcement; d_t: effective depth of the transverse reinforcement; ρ_l: longitudinal reinforcement ratio; ρ_t: transverse reinforcement ratio; C_x: dimension of the loading plate perpendicular to the support; C_y: dimension of the loading plate parallel to the support; L: length of the span;

Ultimate strength prediction: Comparison I

Support type	Reference	Ref-Test	F_{exp} *(kN)*	V_{exp} *(kN)*	*Reported failure mode*	V_{exp}/V_R	V_{exp}/V_{EC-2} *(α=45°)*	V_{exp}/V_{EC-2} *(α=52.5°)*	V_{exp}/V_{ACI} *(α=45°)*	V_{exp}/V_{ACI} *(α=52.5°)*	V_{exp}/V_{MC10} *(LoA II)*
SS	Lubell (2006)	AW1	1170.0	585.0	S-P	1.123	1.042	1.042	1.461	1.461	1.516
SS	Lubell (2006)	AW4	1450.0	725.0	SHEAR	1.110	1.028	1.028	1.410	1.410	1.881
SS	Reissen *et al.* (2018)	S15B-1	543.0	424.0	SHEAR	0.930	1.027	1.027	1.358	1.358	1.504
SS	Reissen *et al.* (2018)	S15B-2	638.0	434.0	S-P	0.945	1.047	1.047	1.381	1.381	1.529
SS	Reissen *et al.* (2018)	S25B-1	664.0	525.0	SHEAR	0.993	0.844	0.844	1.173	1.173	1.299
SS	Reissen *et al.* (2018)	S25B-2	780.0	534.0	SHEAR	0.980	0.842	0.842	1.160	1.160	1.285

Support type	Reference	Ref-Test	F_{exp} (kN)	V_{exp} (kN)	Reported failure mode	V_{exp}/V_R	V_{exp}/V_{EC-2} (α=45º)	V_{exp}/V_{EC-2} (α=52.5º)	V_{exp}/V_{ACI} (α=45º)	V_{exp}/V_{ACI} (α=52.5º)	V_{exp}/V_{MC10} (LoA II)
SS	Reissen *et al.* (2018)	S35B-1	985.0	775.0	S-P	1.273	1.052	0.861	1.403	1.115	1.207
SS	Reissen *et al.* (2018)	S35B-2	1024.0	702.0	SHEAR	1.112	0.934	0.877	1.232	0.979	1.060
SS	Reissen *et al.* (2018)	S35C-1	1166.0	820.0	S-P	1.341	0.987	0.987	1.159	1.098	1.216
SS	Reissen *et al.* (2018)	S35C-2	924.0	656.0	S-P	1.268	0.863	0.863	1.074	1.018	1.127
SS	Oliveira et al. (2004)	L1b	322.0	161.0	SHEAR	1.329	1.133	1.133	1.443	1.443	1.094
SS	Oliveira et al. (2004)	L2b	361.0	181.0	SHEAR	1.040	1.133	1.133	1.267	1.267	1.040
SS	Oliveira et al. (2004)	L3b	400.0	200.0	SHEAR	0.957	1.114	1.114	1.329	1.329	0.995
SS	Regan (1983)	BD2	261.0	131.0	SHEAR	1.072	0.674	0.629	1.755	1.755	1.157
SS	Regan and Rezai-Jarobi (1988)	18	240.0	120.0	SHEAR	0.915	1.198	1.198	2.072	2.072	1.953
SS	Regan and Rezai-Jarobi (1988)	19	222.0	111.0	SHEAR	1.219	1.135	1.135	2.363	2.363	1.874
SS	Regan and Rezai-Jarobi (1988)	22	243.0	121.5	SHEAR	1.230	1.101	0.964	2.411	2.411	1.701
SS	Regan and Rezai-Jarobi (1988)	23	250.0	125.0	SHEAR	0.916	1.006	1.006	2.125	2.125	1.646
SS	Regan and Rezai-Jarobi (1988)	24	300.0	150.0	S-P	1.149	1.173	1.173	2.442	2.442	1.892
SS	Regan and Rezai-Jarobi (1988)	25	212.0	105.8	S-P	1.315	0.897	0.897	2.324	2.324	1.709
SS	Regan and Rezai-Jarobi (1988)	26	275.0	137.5	S-P	1.574	1.655	1.324	3.045	3.045	2.235
SS	Regan and Rezai-Jarobi (1988)	19R	170.0	85.0	S-P	0.933	0.869	0.869	1.809	1.809	1.435
cant	Natário *et al.* (2015)	FN6-E	499.0	518.5	SHEAR	0.986	0.754	0.644	0.995	0.849	1.291
cant	Natário *et al.* (2015)	FN6-W	474.0	493.5	SHEAR	0.939	0.722	0.616	0.955	0.815	1.240
cant	Natário *et al.* (2014)	SN3A	318.3	328.0	S-P	0.921	0.725	0.584	1.039	0.836	1.339
cant	Reissen *et al.* (2018)	CS35B-1	571.0	601.0	SHEAR	1.046	0.782	0.626	1.037	0.829	1.388

Appendix A: Shear tests database

Support type	Reference	Ref-Test	F_{exp} (kN)	V_{exp} (kN)	Reported failure mode	V_{exp}/V_R	V_{exp}/V_{EC-2} (α=45º)	V_{exp}/V_{EC-2} (α=52.5º)	V_{exp}/V_{ACI} (α=45º)	V_{exp}/V_{ACI} (α=52.5º)	V_{exp}/V_{MC10} (LoA II)
cant	Reissen *et al.* (2018)	CS35B-2	565.0	597.0	SHEAR	1.148	0.825	0.660	1.127	0.901	1.508
cant	Reissen *et al.* (2018)	CS35B-ρq	545.0	577.0	SHEAR	1.031	0.763	0.610	1.019	0.815	1.364
cant	Reissen *et al.* (2018)	CS35C	588.0	617.0	SHEAR	1.182	0.679	0.660	0.912	0.886	1.177
cant	Reissen *et al.* (2018)	CS35C-ρq	499.0	527.0	SHEAR	1.020	0.583	0.567	0.786	0.763	1.014
cant	Reissen *et al.* (2018)	CS35B-h	475.0	499.0	SHEAR	1.034	0.906	0.723	1.249	0.996	1.556
cant	Rombach and Henze (2017)	VK4V1	487.0	487.0	S-P	1.022	0.984	0.910	1.334	1.233	1.739
cant	Rombach and Henze (2017)	4d-1	677.0	712.0	SHEAR	1.279	0.890	0.705	1.197	0.949	1.612
cant	Rombach and Henze (2017)	5d	699.0	731.1	SHEAR	1.311	0.758	0.598	0.995	0.785	1.311
cant	Rombach and Henze (2017)	6d	656.0	685.2	SHEAR	1.268	0.646	0.543	0.858	0.721	1.112
cant	Vaz Rodrigues *et al*. (2006)	DR1c	910.0	910.0	SHEAR	1.352	0.725	0.568	0.952	0.745	1.248
cant	Vaz Rodrigues *et al*. (2006)	DR2c	719.0	719.0	SHEAR	1.086	0.632	0.496	0.832	0.653	1.118
cant	Vaz Rodrigues (2002)	1	190.0	190.0	SHEAR	1.220	0.550	0.429	0.718	0.560	0.861
CS	Reissen (2016)	MS35B	856.0	746.0	SHEAR	1.029	0.992	0.788	1.309	1.040	1.126
CS	Reissen (2016)	MS35B-22	626.0	582.0	SHEAR	1.335	1.335	1.061	1.846	1.467	1.472
CS	Reissen (2016)	MS35B-ρq	897.0	782.0	SHEAR	1.256	1.093	0.970	1.479	1.175	1.272
CS	Reissen (2016)	MS35C	956.0	741.0	SHEAR	1.095	0.825	0.825	1.079	1.023	1.132
CS	Reissen (2016)	MS35C-ρq	846.0	657.0	SHEAR	1.079	0.897	0.897	0.989	0.937	1.038

*F_{exp}: Maximum point load applied; V_{exp}: Maximum shear force transmited to the nearest support; *S-P*: shear-punching failure mode;

Ultimate strength prediction: Comparison II

Support type	Reference	Ref-Test	F_{exp} (kN)	V_{exp} (kN)	Reported failure mode	V_{exp}/V_R	$V_{exp}/V_{EC\text{-}2}$ (α=45º)	$V_{exp}/V_{EC\text{-}2}$ (α=52.5º)	V_{exp}/V_{ACI} (α=45º)	V_{exp}/V_{ACI} (α=52.5º)	V_{exp}/V_{MC10} (LoA II)
SS	Lubell (2006)	AW1	1170.0	585.0	S-P	1.123	1.042	1.042	1.461	1.461	1.516
SS	Lubell (2006)	AW4	1450.0	725.0	SHEAR	1.110	1.028	1.028	1.410	1.410	1.881
SS	Reissen *et al.* (2018)	S15B-1	543.0	424.0	SHEAR	0.930	1.027	1.027	1.358	1.358	1.504
SS	Reissen *et al.* (2018)	S15B-2	638.0	434.0	S-P	0.945	1.047	1.047	1.381	1.381	1.529
SS	Reissen *et al.* (2018)	S25B-1	664.0	525.0	SHEAR	0.993	0.999	0.999	1.173	1.173	1.299
SS	Reissen *et al.* (2018)	S25B-2	780.0	534.0	SHEAR	0.980	0.997	0.997	1.160	1.160	1.285
SS	Reissen *et al.* (2018)	S35B-1	985.0	775.0	S-P	1.273	1.355	1.355	1.445	1.336	1.207
SS	Reissen *et al.* (2018)	S35B-2	1024.0	702.0	SHEAR	1.112	1.203	1.203	1.269	1.173	1.060
SS	Reissen *et al.* (2018)	S35C-1	1166.0	820.0	S-P	1.341	1.388	1.388	1.456	1.346	1.216
SS	Reissen *et al.* (2018)	S35C-2	924.0	656.0	S-P	1.268	1.225	1.225	1.350	1.247	1.127
SS	Oliveira et al. (2004)	L1b	322.0	161.0	SHEAR	1.329	1.133	1.133	1.443	1.443	0.825
SS	Oliveira et al. (2004)	L2b	361.0	181.0	SHEAR	1.040	1.136	1.136	1.270	1.270	0.772
SS	Oliveira et al. (2004)	L3b	400.0	200.0	SHEAR	0.957	1.114	1.114	1.329	1.329	0.728
SS	Regan (1983)	BD2	261.0	131.0	SHEAR	1.072	1.198	1.198	1.762	1.762	0.966
SS	Regan and Rezai-Jarobi (1988)	18	240.0	120.0	SHEAR	0.915	1.404	1.404	2.072	2.072	1.953
SS	Regan and Rezai-Jarobi (1988)	19	222.0	111.0	SHEAR	1.219	1.598	1.598	2.363	2.363	1.874

Appendix A: Shear tests database

Support type	Reference	Ref-Test	F_{exp} (kN)	V_{exp} (kN)	Reported failure mode	V_{exp}/V_R	V_{exp}/V_{EC-2} (α=45º)	V_{exp}/V_{EC-2} (α=52.5º)	V_{exp}/V_{ACI} (α=45º)	V_{exp}/V_{ACI} (α=52.5º)	V_{exp}/V_{MC10} (LoA II)
SS	Regan and Rezai-Jarobi (1988)	22	243.0	121.5	SHEAR	1.230	1.673	1.673	2.411	2.411	1.565
SS	Regan and Rezai-Jarobi (1988)	23	250.0	125.0	SHEAR	0.916	1.448	1.448	2.125	2.125	1.646
SS	Regan and Rezai-Jarobi (1988)	24	300.0	150.0	S-P	1.149	1.689	1.689	2.442	2.442	1.892
SS	Regan and Rezai-Jarobi (1988)	25	212.0	105.8	S-P	1.315	1.557	1.557	2.320	2.320	1.506
SS	Regan and Rezai-Jarobi (1988)	26	275.0	137.5	S-P	1.574	2.038	2.038	3.045	3.045	2.183
SS	Regan and Rezai-Jarobi (1988)	19R	170.0	85.0	S-P	0.933	1.224	1.224	1.809	1.809	1.435
cant	Natário *et al.* (2015)	FN6-E	499.0	518.5	SHEAR	0.986	0.785	0.644	1.035	0.849	1.291
cant	Natário *et al.* (2015)	FN6-W	474.0	493.5	SHEAR	0.939	0.751	0.616	0.994	0.815	1.240
cant	Natário *et al.* (2014)	SN3A	318.3	328.0	S-P	0.921	0.829	0.665	1.188	0.954	1.339
cant	Reissen *et al.* (2018)	CS35B-1	571.0	601.0	SHEAR	1.046	0.828	0.658	1.097	0.872	1.388
cant	Reissen *et al.* (2018)	CS35B-2	565.0	597.0	SHEAR	1.148	0.873	0.694	1.192	0.948	1.508
cant	Reissen *et al.* (2018)	CS35B-ρq	545.0	577.0	SHEAR	1.031	0.807	0.642	1.078	0.858	1.364
cant	Reissen *et al.* (2018)	CS35C	588.0	617.0	SHEAR	1.182	0.872	0.694	1.171	0.932	1.177
cant	Reissen *et al.* (2018)	CS35C-ρq	499.0	527.0	SHEAR	1.020	0.750	0.596	1.009	0.803	1.014
cant	Reissen *et al.* (2018)	CS35B-h	475.0	499.0	SHEAR	1.034	0.953	0.761	1.313	1.050	1.556
cant	Rombach and Henze (2017)	VK4V1	487.0	487.0	S-P	1.022	0.992	0.910	1.344	1.233	1.739
cant	Rombach and Henze (2017)	4d-1	677.0	712.0	SHEAR	1.279	1.044	0.832	1.403	1.119	1.612
cant	Rombach and Henze (2017)	5d	699.0	731.1	SHEAR	1.311	1.020	0.813	1.338	1.067	1.311
cant	Rombach and Henze (2017)	6d	656.0	685.2	SHEAR	1.268	0.980	0.782	1.303	1.038	1.112
cant	Vaz Rodrigues *et al*. (2006)	DR1c	910.0	910.0	SHEAR	1.352	0.848	0.666	1.112	0.874	1.248
cant	Vaz Rodrigues *et al*. (2006)	DR2c	719.0	719.0	SHEAR	1.086	0.674	0.530	0.888	0.697	1.118

Support type	Reference	Ref-Test	F_{exp} (kN)	V_{exp} (kN)	Reported failure mode	V_{exp}/V_R	V_{exp}/V_{EC-2} (α=45º)	V_{exp}/V_{EC-2} (α=52.5º)	V_{exp}/V_{ACI} (α=45º)	V_{exp}/V_{ACI} (α=52.5º)	V_{exp}/V_{MC10} (LoA II)
cant	Vaz Rodrigues (2002)	1	190.0	190.0	SHEAR	1.220	0.956	0.753	1.247	0.983	0.861
CS	Reissen (2016)	MS35B	856.0	746.0	SHEAR	1.029	1.123	1.123	1.349	1.246	1.126
CS	Reissen (2016)	MS35B-22	626.0	582.0	SHEAR	1.335	1.461	1.461	1.881	1.716	1.472
CS	Reissen (2016)	MS35B-ρq	897.0	782.0	SHEAR	1.256	1.237	1.237	1.523	1.408	1.272
CS	Reissen (2016)	MS35C	956.0	741.0	SHEAR	1.095	1.124	1.124	1.356	1.253	1.132
CS	Reissen (2016)	MS35C-ρq	846.0	657.0	SHEAR	1.079	1.019	1.019	1.243	1.148	1.038

*F_{exp}: Maximum point load applied; V_{exp}: Maximum shear force transmited to the nearest support; *S-P*: shear-punching failure mode;

A.3 Loads applied close to the support

Regan's and Cornell's slabs characteristics

	Slab	$f_{c,cyl}$ (MPa)	f_{ct} (MPa)	B (mm)	d_X (mm)	d_Y (mm)	ρ_X (%)	ρ_Y (%)	T/T_{cr} X	T/T_{cr} Y
REGAN	BD-6	38.9	3.2	100	95	107	1.360	1.208	1.00	0
	BD-8	39.7	2.7	100	95	107	1.360	1.208	0	0
CORNELL	00B8	22.3	NR	200	108.7	116.6	1.585	0.720	0.00	0.00
	08B8	22.6	NR	200	108.7	116.6	1.585	0.720	1.37	0.69
	00C4	21.7	NR	100	115.1	116.6	0.680	0.380	0.00	0.00
	08C4	23.4	NR	100	115.1	116.6	0.680	0.380	0.69	0.41
	00D8	22.9	NR	200	108.7	116.6	1.585	0.720	0.00	0.00
	09A	28.3	NR	100	108.7	116.6	1.585	0.720	0.76	0.38
	09B	28.3	NR	100	108.7	116.6	1.585	0.720	0.76	0.38
	09C	28.3	NR	100	108.7	116.6	1.585	0.720	0.76	0.38
	09D	28.3	NR	100	108.7	116.6	1.585	0.720	0.76	0.38
	06A	22.1	NR	100	108.7	116.6	1.585	0.720	0.79	0.40
	06B	22.1	NR	100	108.7	116.6	1.585	0.720	0.79	0.40
	06C	22.1	NR	100	108.7	116.6	1.585	0.720	0.79	0.40
	06D	22.1	NR	100	108.7	116.6	1.585	0.720	0.79	0.40
	06E	24.1	NR	100	108.7	116.6	1.585	0.720	0.95	0.48
	06F	24.1	NR	100	108.7	116.6	1.585	0.720	0.95	0.48
	00A	31.0	NR	100	108.7	116.6	1.585	0.720	0.00	0.00
	00B	31.0	NR	100	108.7	116.6	1.585	0.720	0.00	0.00
	09E	31.0	NR	100	108.7	116.6	1.585	0.720	1.12	0.56
	09F	31.0	NR	100	108.7	116.6	1.585	0.720	1.12	0.56
	00C	28.3	NR	100	108.7	116.6	1.585	0.720	0.00	0.00
	02A	28.3	NR	100	108.7	116.6	1.585	0.720	0.30	0.15
	04A	28.3	NR	100	108.7	116.6	1.585	0.720	0.59	0.30
	06G	28.3	NR	100	108.7	116.6	1.585	0.720	0.86	0.43
	00D	29.7	NR	100	108.7	116.6	1.585	0.720	0.00	0.00
	02B	29.7	NR	100	108.7	116.6	1.585	0.720	0.28	0.14
	04B	29.7	NR	100	108.7	116.6	1.585	0.720	0.56	0.28
	06H	29.7	NR	100	108.7	116.6	1.585	0.720	0.84	0.42
	02C	22.7	NR	100	108.7	116.6	1.585	0.720	0.33	0.17
	04C	22.7	NR	100	108.7	116.6	1.585	0.720	0.66	0.33
	08A	22.7	NR	100	108.7	116.6	1.585	0.720	1.29	0.65
	08B	22.7	NR	100	108.7	116.6	1.585	0.720	1.36	0.69

Comparison of the ultimate load predictions.

Type	Slab	T/T_{cr} X	T/T_{cr} Y	$f_{c,cyl}$ (MPa)	P_{exp} (kN)	P_{exp}/P_{CCCM}	P_{exp}/P_{EC2}	P_{exp}/P_{ACI}	P_{exp}/P_{MC10}
UNIAXIAL TENSION	A1	0	0	37.6	249.1	1.048	1.205	1.423	1.280
	BD-8	0	0	39.7	251.0	1.048	1.119	1.482	1.176
	B1	0.44	0	37.7	240.4	1.052	1.147	1.409	1.181
	A2	0.69	0	35.9	215.2	1.008	1.145	1.265	1.160
	BD-6	1.00	0	38.9	225.0	1.038	1.108	1.196	1.098
	A3	1.02	0	37.4	198.4	1.105	1.178	1.427	1.108
	A4	1.26	0	36.7	179.4	1.074	1.040	1.102	1.019
BIAXIAL TENSION	00B8	0.00	0.00	22.3	400.8	1.283	1.534	1.786	1.506
	08B8	1.37	0.69	22.6	306.0	1.498	1.539	1.503	1.290
	00C4	0.00	0.00	21.7	223.3	1.139	1.155	1.290	1.244
	08C4	0.69	0.41	23.4	185.0	1.098	1.145	1.209	1.189
	00D8	0.00	0.00	22.9	375.1	1.201	1.436	1.671	1.410
	09A	0.76	0.38	28.3	279.5	1.280	1.418	1.753	1.228
	09B	0.76	0.38	28.3	267.4	1.225	1.357	1.678	1.175
	09C	0.76	0.38	28.3	267.9	1.227	1.359	1.680	1.177
	09D	0.76	0.38	28.3	233.6	1.070	1.186	1.466	1.026
	06A	0.79	0.40	22.1	200.7	1.081	1.099	1.415	0.978
	06B	0.79	0.40	22.1	211.4	1.138	1.158	1.490	1.030
	06C	0.79	0.40	22.1	178.4	0.961	0.977	1.258	0.870
	06D	0.79	0.40	22.1	199.8	1.076	1.094	1.408	0.974
	06E	0.95	0.48	24.1	199.8	1.067	1.104	1.369	0.949
	06F	0.95	0.48	24.1	211.8	1.131	1.171	1.452	1.007
	00A	0.00	0.00	31.0	296.8	1.068	1.255	1.675	1.196
	00B	0.00	0.00	31.0	310.2	0.977	1.312	1.750	1.250
	09E	1.12	0.56	31.0	245.2	1.077	1.320	1.524	1.069
	09F	1.12	0.56	31.0	256.3	1.126	1.380	1.593	1.117
	00C	0.00	0.00	28.3	298.2	0.939	1.300	1.761	1.251
	02A	0.30	0.15	28.3	289.3	1.180	1.336	1.749	1.234
	04A	0.59	0.30	28.3	255.9	1.121	1.253	1.583	1.111
	06G	0.86	0.43	28.3	218.1	1.028	1.133	1.380	0.965
	00D	0.00	0.00	29.7	285.2	1.053	1.224	1.644	1.172
	02B	0.28	0.14	29.7	267.0	1.052	1.209	1.574	1.114
	04B	0.56	0.28	29.7	245.2	1.035	1.176	1.479	1.041
	06H	0.84	0.42	29.7	243.4	1.106	1.241	1.504	1.055
	02C	0.33	0.17	22.7	233.6	1.097	1.162	1.575	1.098
	04C	0.66	0.33	22.7	233.2	1.191	1.234	1.608	1.115
	08A	1.29	0.65	22.7	189.1	1.165	1.144	1.366	0.943
	08B	1.36	0.69	22.7	194.0	1.223	1.192	1.408	0.972
Mean Uniaxial						1.053	1.135	1.329	1.146
CoV Uniaxial (%)						2.847	4.706	10.705	7.150
Max.						1.105	1.205	1.482	1.280
Min.						1.008	1.040	1.102	1.019
Mean Biaxial						1.126	1.245	1.535	1.121
CoV Biaxial (%)						9.757	10.480	10.283	12.718
Max.						1.498	1.539	1.786	1.506
Min.						0.939	0.977	1.209	0.870
Total Mean						1.113	1.225	1.497	1.126
Total CoV (%)						9.320	10.380	11.577	11.808